# NITROGEN-DOPED CARBON NANOTUBES: CONTROLLED SYNTHESIS, PHYSICOCHEMICAL CHARACTERIZATION AND APPLICATION AS Pd CATALYST SUPPORTS IN A HYDROGENATION REACTION

LUCY MUDIWO OMBAKA

Submitted in fulfillment of the academic requirements for the degree of Doctor of Philosophy in Science in the School of Chemistry and Physics, University of KwaZulu-Natal, Durban.

February 2015

# ABSTRACT

Catalysis is a fundamental pillar in the development of a sustainable economy that is in line with the principles of green chemistry. This drives the need to develop novel catalytic systems whose activity and selectivity towards the desired products are controllable. Carbon nanotubes (CNTs) and nitrogen-doped CNTs (N-CNTs) are smart materials that are potentially novel metal catalyst supports or catalysts. Thus, it is vital to develop procedures for synthesizing CNTs and N-CNTs that utilize green principles and aid the control of the materials' physicochemical properties. CNTs and N-CNTs can be synthesized *via* a chemical vapour deposition (CVD) technique by use of organometallic compounds such as ferrocenyl derivatives as catalysts. These ferrocenyl derivatives can be synthesized by use of solvents such as benzene, ethanol and DMF, however, a 'greener' approach is to use a solvent-free synthesis.

This research focussed on utilizing a solvent-free mechanochemical approach to synthesize novel and known ferrocenyl derivatives used as new catalysts in the controlled synthesis of N-CNTs. This research also aimed at developing a synthetic procedure that yields N-CNTs with modulated physicochemical properties. Lastly, this study aimed at utilizing the N-CNTs as Pd supports (Pd/N-CNTs) and exploiting their nitrogen content or species to control the rate of nitrobenzophenone reduction.

Nitrogen- or halogen-containing ferrocenyl derivatives were synthesized *via* a solvent-free mechanochemical approach. The ferrocenyl derivatives were used as new catalysts in the CVD synthesis of N-CNTs. Halogens in ferrocenyl derivatives, or oxygen derived from ethyl benzoate, were used to control the nitrogen content and species incorporated into N-CNTs. The synthesized N-CNTs were purified and used as supports for Pd nanoparticles. Both N-CNTs and Pd/N-CNTs were characterized by using microscopy, spectroscopy and surface characterization techniques. This included transmission electron microscopy (TEM), scanning electron microscopy (SEM), X-ray photoelectron spectroscopy (XPS), powder X-ray diffraction, Fourier-transform infrared spectroscopy and temperature programmed reduction (TPR). For comparison CNTs were also synthesized, characterized and used as Pd supports. The catalytic performance of Pd/N-CNTs was evaluated in the hydrogenation of nitrobenzophenone. The effect of surface area, pressure, temperature and solvent polarity on the catalyst's performance was also evaluated.

A simple mechanochemical solvent-free technique was developed and used to synthesize eight novel and one known nitrogen/halogen-containing ferrocenyl derivatives. The

reactions were found to occur readily at ambient temperature and pressure and more so with relatively shorter reaction times compared to the known classical Knoevenagel condensation reactions. The electron-withdrawing strength of the *para*-substituent on the novel ferrocenyl derivatives influenced the yield, product selectivity and spectroscopic properties of these compounds. The X-ray structures of five new compounds were reported.

Selected 1,1′-ferrocenyldiacrylonitriles having similar structures which differ only in their *para* substituents (*para*-CN, *para*-$CF_3$ and *para*-Cl) were used as novel catalysts in the synthesis of N-CNTs. The syntheses were conducted at 850 °C by use of either acetonitrile or pyridine as the carbon and nitrogen source. Syntheses conducted by use of pyridine as a nitrogen source yielded N-CNTs and carbon spheres (CS) while those conducted with acetonitrile (external nitrogen source) yielded N-CNTs and carbon nanofibres (CNFs). Amongst the three tested catalysts, the *para*-$CF_3$ catalyst gave the highest yield of N-CNTs in either pyridine or acetonitrile. In addition, the *para*-$CF_3$ catalyst in pyridine gave N-CNTs with the highest nitrogen-doping level, that were kinked, and less thermally stable than those obtained with the *para*-CN and -Cl catalysts in pyridine. This implied that fluorine heteroatoms enhanced the nitrogen-doping of N-CNTs. Thus, the expediency of using a fluorine heteroatom to control doping of N-CNTs is reported. When using acetonitrile, both the fluorinated and chlorinated ferrocenyl derivatives yielded metal-filled N-CNTs of controllable diameters.

Another ferrocenyl derivative, (3-ferrocenyl-2-(4-cyanophenyl) acrylonitrile), and oxygen derived from ethyl benzoate were also used to synthesize aligned N-CNTs containing 6.4-15.7 wt. % of nitrogen in either acetonitrile or a solution of acetonitrile and ethyl benzoate. For comparison, N-CNTs were synthesized in toluene. The use of 3-ferrocenyl-2-(4-cyanophenyl)acrylonitrile in acetonitrile as a nitrogen and carbon source selectively yielded mainly N-CNTs, while use of toluene as a carbon source yielded both N-CNTs and CS. The addition of oxygen enhanced the nitrogen-content of N-CNTs. However, the higher nitrogen-containing N-CNTs were found to be less graphitic and showed a higher base constant ($K_b$) compared to N-CNTs synthesized without oxygen. The outer diameters of the N-CNTs decreased upon increasing the oxygen composition in the synthesis precursors from 1-4 wt. % oxygen. In addition, the alignment of N-CNTs increased upon addition of oxygen. Electrical conductivity measurements of N-CNTs showed a negative relationship between the amount of oxygen in the starting materials and the conductivity of N-CNTs. Thus, 3-ferrocenyl-2-(4-cyanophenyl)acrylonitrile and oxygen were successfully used to control the physicochemical properties of N-CNTs during synthesis. This provided a novel synthetic

approach, which was further used to selectively incorporate pyrrolic-nitrogen species into N-CNTs. The physicochemical properties of pyrrolic-N-CNTs with different pyrrolic contents were evaluated. Pd was loaded on pyrrolic-N-CNTs and the influence of pyrrolic-nitrogen on Pd species evaluated by use of XPS analysis. XPS evaluation of Pd/N-CNTs revealed that the abundance of $Pd^{2+}$ increased as the quantity of pyrrolic nitrogen increased. The increase of $Pd^{2+}$ species was accredited to the formation of stable Pd-N coordination complexes, which increased the dispersion of $Pd^{2+}$ nanoparticles. The catalytic performance of Pd/N-CNTs was tested in the hydrogenation of aminobenzophenone. Pd/N-CNTs showed a higher efficiency and selectivity towards nitro-reduction than Pd/CNTs and commercial Pd/AC. The increased efficiency was attributed to the pyrrolic-nitrogen present in Pd/N-CNTs. The catalytic performance of Pd/N-CNTs increased with increase in surface area and temperature but decreased with increase in pressure. An aprotic solvent enhanced the selective reduction of nitrobenzophenone to aminobenzophenone more than a protic solvent. In general, these Pd/N-CNTs are promising catalysts for use in industrial processes involving the selective reduction of substituted nitro-arenes to substituted anilines.

# PREFACE

The experimental work described in this thesis was carried out in the School of Chemistry and Physics, University of KwaZulu-Natal, Durban, from July 2012 to November 2014, under the supervision of Dr. Vincent O. Nyamori and Dr. Patrick G. Ndungu.

These studies represent original work by the author and have not otherwise been submitted in any form for any degree or diploma to any tertiary institution. Where use has been made of the work of others it is duly acknowledged in the text.

Sign: _____ Date: 23-02-15

Lucy M. Ombaka
Student No. 212560295

## DECLARATION 1 – PLAGIARISM

I, Lucy Mudiwo Ombaka, declare that:

1. The research reported in this thesis, except where otherwise indicated, is my original research.

2. This thesis has not been submitted for any degree or examination at any other university.

3. This thesis does not contain other persons‘ data, pictures, graphs or other information, unless specifically acknowledged as being sourced from other persons.

4. This thesis does not contain other persons' writing, unless specifically acknowledged as being sourced from other researchers. Where other written sources have been quoted, then:
   a. Their words have been re-written but the general information attributed to them has been referenced.
   b. Where their exact words have been used, then their writing has been placed in italics and inside quotation marks, and referenced.

5. This thesis does not contain text, graphics or tables copied and pasted from the Internet, unless specifically acknowledged, and the source being detailed in the thesis and in the References sections.

Signed: ……

## DECLARATION 2 - PUBLICATIONS AND CONFERENCE CONTRIBUTIONS

DETAILS OF CONTRIBUTION TO PUBLICATIONS that form part and/or include research presented in this thesis (includes manuscripts in preparation, *in press* and published articles. The details of the contributions of each author to the experimental work and writing of each publication is given).

**PUBLICATIONS**

**Publication 1**

L. M. Ombaka; P. Ndungu; V. O. Nyamori. *Usage of carbon nanotubes as platinum and nickel catalyst supports in dehydrogenation reactions*. Catalysis Today 217 (2013) 65-75.

Contributions: I planned and wrote the review paper. Drs Ndungu and Nyamori are my supervisors who provided guidance and proofread the manuscript.

**Publication 2**

L. M. Ombaka; P. G. Ndungu; B. Omondi; V. O. Nyamori. *Mechanochemical synthesis and spectroscopic properties of 1,1'-ferrocenyldiacrylonitriles: the effect of para-substituents.* Journal of Coordination Chemistry 67 (2014) 1905-1922.

Contributions: I conceptualized, designed and conducted the synthesis of the compounds, their characterization and crystal growth, and wrote the paper. Dr Owaga conducted the X-ray crystallographic experiments. Drs Ndungu and Nyamori are my supervisors who gave general guidance and proofread the manuscript.

**Publication 3**

L. M. Ombaka; P. G. Ndungu; B. Omondi; V. O. Nyamori. *Nitrogen-doped carbon nanotubes synthesized from 1,1'-ferrocenyldi-acrylonitriles: the effect of the para-substituent.* Manuscript preparation in progress.

Contributions: I synthesized and characterized the N-CNTs. I also wrote the manuscript draft. Dr Owaga conducted the X-ray crystallographic experiments. Drs Ndungu and Nyamori are my supervisors who provided guidance and proofread the manuscript.

**Publication 4**

L. M. Ombaka; P. G. Ndungu; V. O. Nyamori. *Tuning the nitrogen content and surface properties of nitrogen-doped carbon nanotubes by using a nitrogen-containing ferrocenyl derivative and ethyl benzoate.* Journal of Materials Science 50 (2015) 1187-1200.

Contributions: I designed the synthetic procedure, synthesized and characterized the materials, and wrote the manuscript. Drs Ndungu and Nyamori are my supervisors who gave guidance and proofread the manuscript.

**Publication 5**

L. M. Ombaka; P. G. Ndungu; V. O. Nyamori. *Pyrrolic nitrogen-doped carbon nanotubes: physicochemical properties, interactions with Pd nanoparticles and their role in selective hydrogenation of nitrobenzophenone.* RSC Advances 5 (2015) 109-122.

Contributions: I designed the experiments, synthesized and characterized the supports and catalysts, performed the catalytic tests and wrote the paper. Drs Ndungu and Nyamori are my supervisors who gave guidance and proofread the manuscript.

**Publication 6**

L. M. Ombaka; P. G. Ndungu; B. Omondi; V. O. Nyamori. *Chemoselective hydrogenation of nitrobenzophenone over Pd supported on nitrogen-doped carbon nanotubes.* Manuscript preparation in progress.

Contributions: I synthesized and characterized the supports and catalysts. I conducted the catalytic tests and also wrote the manuscript draft. Drs Ndungu and Nyamori are my supervisors who provided guidance and proofread the manuscript.

## CONFERENCE CONTRIBUTIONS

1. Oral presentation: Mechanochemical synthesis and spectroscopic properties of 1,1′-ferrocenyldiacrylonitriles: the effect of *para*-substituents, at the 5th International IUPAC Conference on Green Chemistry held in Durban, South Africa (August, 2014).
2. Poster presentation: Structural characterization of nitrogen-doped carbon nanotubes and Pd supported on nitrogen-doped carbon nanotubes using XRD, at the South African Powder Diffraction conference and workshop held in Johannesburg, South Africa (January 2014).
3. Poster presentation: Synthesis of nitrogen-doped carbon nanotubes as supports for Pd catalyst used in hydrogenation of nitrobenzophenone, at the 24th Annual Conference of the Catalysis Society of South Africa (CATSA) held in Port Edward, South Africa (November, 2013).
4. Poster presentation: Solvent-free synthesis of ferrocene derivatives, at the 20th EuCheMS Conference on Organometallic Chemistry held at St. Andrews, Scotland (July, 2013).

Signed: ……:…….

## ACKNOWLEDGEMENTS

I offer my wholehearted gratitude to GOD Almighty for health, strength and provision. To GOD be the glory.

My heartfelt appreciation and gratitude goes to my supervisor, Dr. Vincent O. Nyamori, for his strong mentorship, guidance and leadership during this study. His confidence in me encouraged me to settle for nothing less than excellence. I am also grateful to him for his swift response whenever I needed his assistance. I will always remember his kindness.

I sincerely thank my co-supervisor, Dr. Patrick G. Ndungu, for his guidance during this study. I thank him for his advice and constant encouragement through the toughest moments of my study.

Special thanks go to Dr. Bernard O. Owaga for his efforts and guidance through the crystallographic studies presented in this work.

I also wish to pass my genuine appreciation to Prof. Bice S. Martincigh and Dr. Nolwazi Nombona for proofreading my manuscripts and for their critical comments of the manuscripts. Prof. Bice S. Martincigh greatly instilled a logical way of thinking in me, for which I am grateful.

My deep gratitude goes to the love of my life, Dr. Ramadhan S. Mwakubambanya for his scientific and emotional support. I am grateful to him for being optimistic about my work even in the darkest hour. His faith in my work and encouragement kept me going through the whole period of study.

I thank Dr. Philani Mashazi of Rhodes University for assisting with the XPS analysis. Likewise, I thank the catalysis research group for assisting with the TPR and XRD analysis.

This work would not have been successful without the assistance of the technical staff. Therefore, I would like to particularly thank, Neal Broomhead, Anita Naidoo and Philip Christopher, for their assistance.

I wish to thank Mr. Gregory Moodley for his constant moral and spiritual support and encouragement.

I would also like to thank Rachel Oosthuizen for inducting me into the research laboratory, and the entire Nanochemistry Research Group for their constructive discussions and support.

I am deeply grateful to my mother and the rest of my family members for their moral and financial support.

Lastly, my gratefulness goes to the National Research Foundation (NRF) and the College of Agriculture, Engineering and Science, University of KwaZulu-Natal (UKZN) for funding this research. I am also grateful to the College of Agriculture, Engineering and Science for the award of PhD bursary.

## DEDICATION

This work is dedicated to my mother, my sister Lilian and to Ramadhan S. Mwakubambanya for their endless support and encouragement. May God bless you all.

# LIST OF ABBREVIATIONS

| Full meaning | Abbreviation |
|---|---|
| Activated carbon | AC |
| Approximately | *ca.* |
| Arbitrary unit | a. u. |
| Average | Ave. |
| Carbon nanotubes | CNTs |
| Carbon thirteen nuclear magnetic resonance | $^{13}$C-NMR |
| Chemical vapour deposition | CVD |
| Compare | *cf.* |
| Crystallographic information file | CIF |
| Deuterated chloroform | $CDCl_3$ |
| Dichloromethane | DCM |
| Double-walled carbon nanotubes | DWCNTs |
| Doublet | d |
| Electrospray ionisation | ESI |
| Fourier-transform infrared spectroscopy | FTIR |
| High resolution transmission electron microscopy | HRTEM |
| Inductively coupled plasma-optical emission spectroscopy | ICP-OES |
| Infrared | IR |
| Inner diameter | ID |
| Mass-to-charge ratio | m/z |
| Mass spectrometry | MS |
| Maximum | max. |
| Melting point | m.p. |
| Metal organic chemical vapour deposition | MOCVD |
| Multi-walled carbon nanotubes | MWCNTs |
| Nanoparticles | NPs |
| Nitrogen-doped carbon nanotubes | N-CNTs |

| | |
|---|---|
| Outer diameter | OD |
| Palladium supported on activated carbon | Pd/AC |
| Palladium supported on carbon nanotubes | Pd/CNTs |
| Palladium supported on nitrogen-doped carbon nanotubes | Pd/N-CNTs |
| Platinum group metals | PGMs |
| Proton nuclear magnetic resonance | $^{1}$H-NMR |
| Radial breathing mode | RBM |
| Ratio of D-band intensity to G-band intensity in Raman spectroscopy | $I_D/I_G$ |
| Scanning electron microscopy | SEM |
| Shaped carbon nanomaterials | SCNMs |
| Shaped carbon nanomaterials synthesized from fluorine containing catalyst | SCNMs-F |
| Shaped carbon nanomaterials synthesized from chlorine containing catalyst | SCNMs-Cl |
| Shaped carbon nanomaterials synthesized from cyano containing catalyst | SCNMs-CN |
| Single-walled carbon nanotubes | SWCNTs |
| Singlet | s |
| Thermal gravimetric analysis | TGA |
| Thin layer chromatography | TLC |
| Transmission electron microscopy | TEM |
| Triplet | t |
| Volume-by-volume concentration | v/v |
| Weight percent | wt.% |
| X-ray photoelectron spectroscopy | XPS |
| X-ray diffraction | XRD |

# TABLE OF CONTENTS

# CHAPTER ONE

# INTRODUCTION

The current strain on natural resources has heightened the need to develop a sustainable environment and economy, which heavily relies on green principles. Current trends are towards utilization of the twelve principles of green chemistry outlined by Anastas *et al*. [1] to achieve a sustainable industrial economy. These principles include:- waste prevention, safe synthetic methods, operating reactions at ambient pressure and temperature, elimination of toxic reagents, the use of renewable resources and use of catalytic reactions [2].

In industrial processes, catalysts facilitate faster reaction rates and increased product yields while reducing wasteful by-products [1]. This in turn reduces environmental pollution and the cost of production, which can translate into reduced product prices and higher sales profits. Therefore, the development of new catalytic systems showing controllable activity and selectivity towards a desired product is fundamental. Carbon nanotubes (CNTs) and nitrogen-doped carbon nanotubes (N-CNTs) are examples of materials that are potentially new catalysts or new metal catalyst supports, applicable in industrial processes.

CNTs are carbonaceous materials made-up of graphene sheets that are rolled-up into one-dimensional nanotubes. CNTs consisting of one graphene sheet are called single-walled CNTs (SWCNTs); those with two graphene sheets are called double walled CNTs (DWCNTs) while those with multiple graphene sheets are called multi-walled CNTs (MWCNTs) (Figure. 1). The outer diameter of CNTs ranges between 1-100 nm.

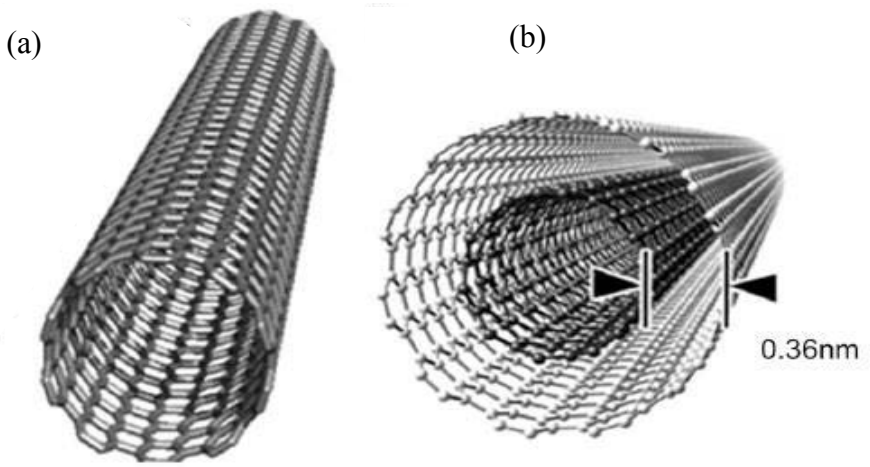


Figure 1: Schematic representation of (a) SWCNTs and (b) MWCNTs adopted from Reilly *et al*. [3].

MWCNTs (simply referred to as CNTs in this thesis) exhibit interesting properties such as strong electronic interactions with metal catalysts, high thermal stability, high tensile strength and Young‘s modulus [4]. They also show a high surface area of mesoporous nature [5]. Owing to these unique properties, CNTs are potentially smart metal catalyst supports.

Doping of CNTs with heteroatoms, like nitrogen, offers an appropriate channel for improving the electronic and physicochemical properties of CNTs [6]. The enhanced electronic and physicochemical properties of N-CNTs make them suitable for application in the field of catalysis. N-CNTs can contain different nitrogen species, such as pyridine-like, pyridine-N-oxide, pyrrole-like, carbonitrile, graphitic/quaternary and lactam nitrogens [7, 8], which are illustrated in Figure 2.

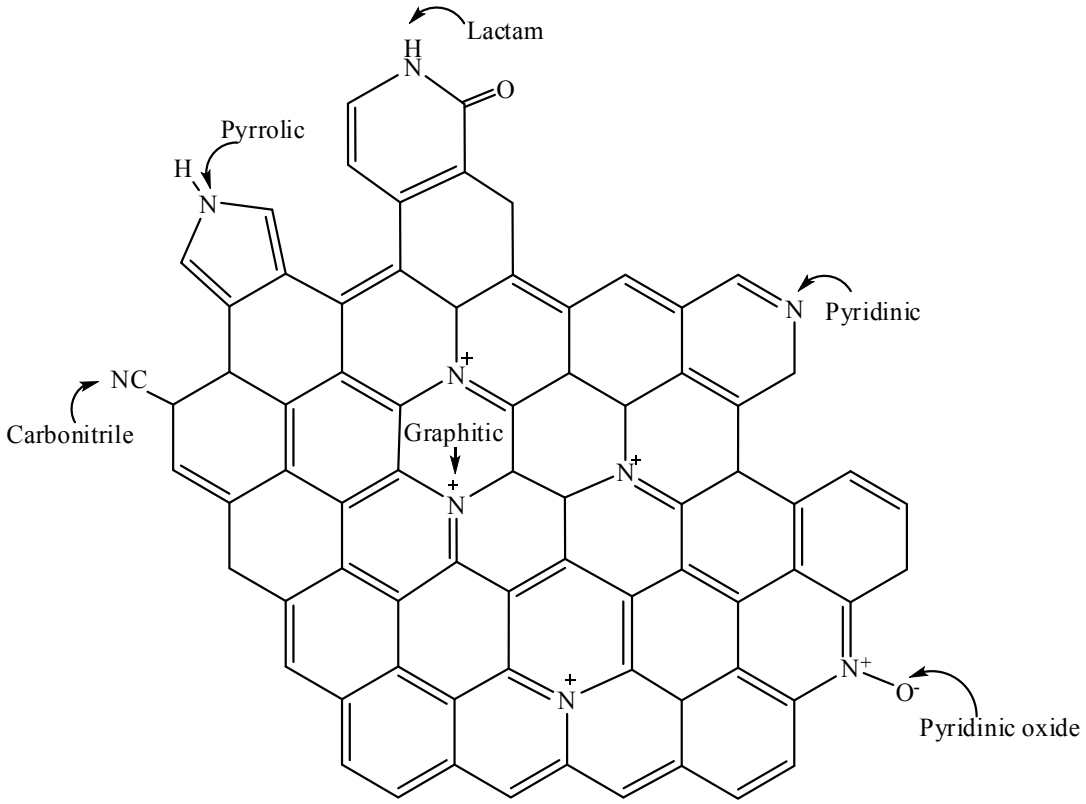


Figure 2: Graphical representation of possible nitrogen species in CNTs.

Pyridine and pyrrole nitrogen species are Lewis bases thus their presence in N-CNTs increases the amount of basic functional groups on the surface of N-CNTs [9]. These nitrogen groups also enhance the surface energy of N-CNTs [9], which can result in an enhanced catalytic activity of supported metal catalysts [10]. Doping of CNTs with nitrogen also introduces surface defects into the rather crystalline structure of CNTs. The surface

defects in N-CNTs form bamboo compartments which are usually absent in CNTs (*cf.* Figure 3a and 3b). These surface defects increase the substrate adsorption capacity and provide high-energy activation sites that can enhance the catalytic performance of supported metal catalysts. Pyridinic and pyrrolic nitrogen species also act as electron donors, which interact electronically with metal catalysts such as Pd nanoparticles (NPs) and increase the binding energy between N-CNTs and Pd NPs [11].

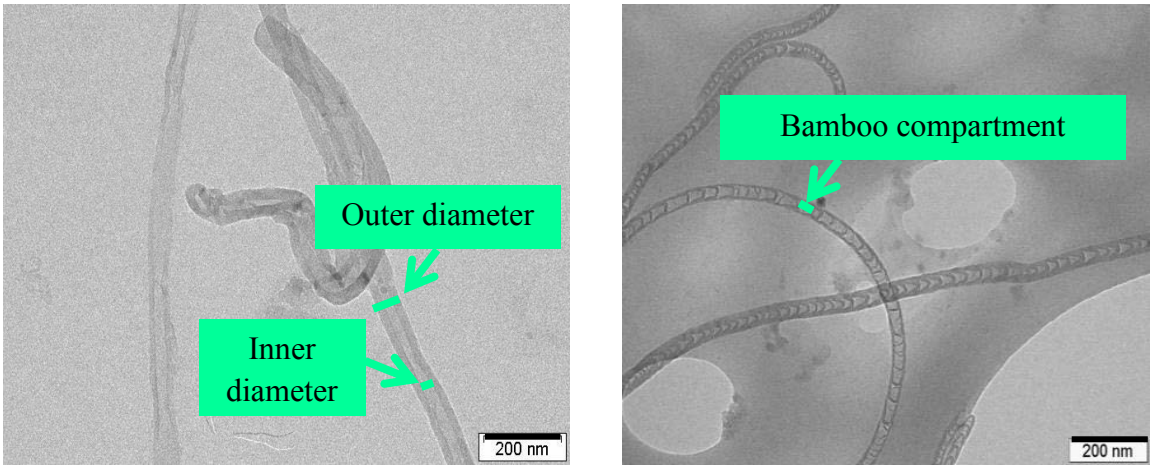


Figure 3: Micrographs of (a) CNTs and (b) N-CNTs showing bamboo compartments.

Different techniques are used to synthesize CNTs and N-CNTs; these techniques can be divided into three broad categories namely arc-discharge, laser ablation and chemical vapour deposition (CVD) techniques [4]. A key target during the synthesis of CNTs and N-CNTs is to obtain materials of uniform physical and chemical properties, such as uniform outer diameter (OD) and inner diameter (ID), and similar nitrogen species for N-CNTs. This can be achieved through manipulating various parameters employed during synthesis. One approach that can be applied to control the CVD synthesis of CNTs and N-CNTs is varying the organometallic compounds used as catalysts during synthesis. For instance, organometallic catalysts, such as ferrocene and ferrocenyl derivatives, have been used to achieve a controlled synthesis of CNTs and N-CNTs [12-14].

The ferrocenyl derivatives can be synthesized by use of solvents such as toluene [15] and dichloromethane [16]. However, a ‗greener' approach is the use of solvent-free synthesis. Solvent-free reactions can occur in the solid state, thus eliminating the use of toxic solvents, and reducing wasteful by-products. Under solvent-free conditions, reactions can be induced *via* different techniques including mechanochemical techniques, microwave irradiation and sonochemical techniques [17]. The mechanochemical approach can be accomplished by

simply milling the solid reactants together in a pyrex tube hence, it has the advantage of cost-effectiveness and a simple work-up procedure [18].

### 1.1 CVD synthesis of CNTs and N-CNTs

In the CVD technique, CNTs and N-CNTs are synthesized by use of a catalyst and a carbon/nitrogen source. To obtain CNTs a combination of nitrogen-free catalysts (for instance ferrocene) and a carbon source (such as toluene) can be used. On the other hand, to synthesize N-CNTs, a nitrogen-containing catalyst or carbon source can be used. Alternatively, a combination of a catalyst containing nitrogen heteroatoms and a carbon source can be used [13].

The growth mechanism of CNTs and N-CNTs are similar and involve the dissociation of the catalyst and carbon/nitrogen source into atoms at high temperatures. This is followed by diffusion of the carbon/nitrogen atoms into a supported metallic catalyst to form a saturated solid solution. Thereafter, the CNTs or N-CNTs precipitate out of the saturated metal catalyst to form a tube-like structure [19]. Upon depletion of the carbon source, the tube growth terminates. For N-CNTs, the nitrogen is predominantly located at the end of the tube in a ring-like fashion, which disrupts the growth process of the tube leading to closure of the tube and formation of bamboo compartments. CNTs and N-CNTs can either form through a base-or tip-growth mechanism (Figure 4) [20]. In the base-growth mechanism, the metal catalyst particle from which the tube grows is located at the bottom of the tube while in the tip-growth mechanism the catalyst is located at the top of the tube.

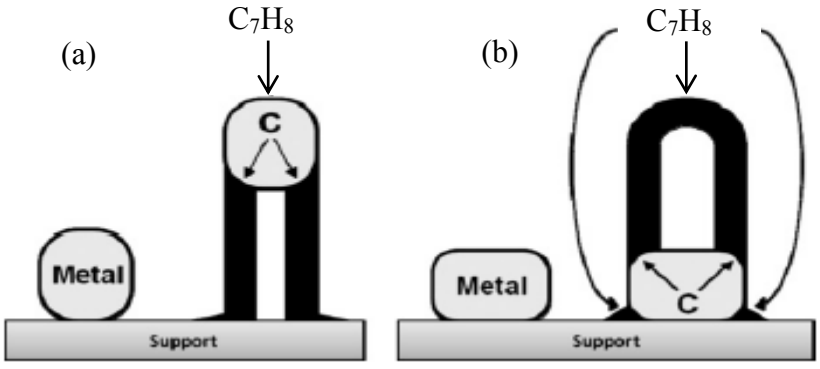


Figure 4: Graphical representation of (a) tip-growth and (b) base-growth mechanism of CNTs adopted from Shaikjee *et al*. [20]. Where, the support represents the metal catalyst support.

The OD and ID of CNTs and N-CNTs (Figure 3) influence several physicochemical properties of these materials including their metallic or semiconducting characteristics and their surface area [7, 21]. One approach useful in controlling the size of the OD and ID of CNTs and N-CNTs is the use of heteroatoms such as oxygen- and halogen- containing organic or inorganic compounds. Solvents such as methanol and water have been explored as oxygen carriers to tune the tube OD and ID [22, 23]. However, these solvents do not dissolve most organometallic catalysts and they contain -OH groups which may facilitate formation of hydrogen radicals that can retard the growth of N-CNTs [20, 22]. Thus, other oxygen- and halogen-containing organic and organometallic compounds such as esters and heteroatom-containing ferrocenyl derivatives are potentially useful in controlling the OD, ID and other physicochemical properties of these materials.

Synthesis of N-CNTs by use of the arc-discharge, laser ablation and CVD techniques usually yields N-CNTs containing a mixture of nitrogen species as displayed in Figure 2 [22, 24]. Consequently, the selective doping of CNTs with a specific nitrogen species remains a difficult task. This causes a major drawback in the commercialization of N-CNTs and evaluation of the structure-activity relationships between N-CNTs and metal catalysts.

### 1.2 Solvent-free synthesis of ferrocenyl derivatives

Owing to their volatile nature at high temperatures, ferrocene (Figure 5) and ferrocenyl derivatives are usually utilized as catalysts in the CVD synthesis of CNTs and N-CNTs [12]. Ferrocenyl derivatives containing heteroatoms such as nitrogen, oxygen, sulfur or halogens can be used to modulate the properties of CNTs and N-CNTs. For instance, nitrogen-containing 4-ferrocenylaniline (Figure 5) yielded N-CNTs with higher nitrogen contents than a mixture of ferrocene and aniline [13]. Likewise, oxygen- and sulfur-containing ferrocenyl derivatives were successfully used to control the properties of CNTs and N-CNTs [14]. Although mixtures of ferrocene and organic halogens have been used to modify the properties of CNTs, limited accounts report the use of halogen- and nitrogen-containing ferrocenyl derivatives to tune the properties of N-CNTs.


ferrocene ferrocenylaniline

Figure 5: Structure of ferrocene and ferrocenylaniline.

Ferrocenyl derivatives can be synthesized by use of various chemistry reactions involving solvent like Wittig reactions [15]. However, such ~~"in~~-solvent" syntheses have major drawbacks which include long reaction times, unnecessary separation and purification procedures, low yields, additional high cost and use of solvents with negative environmental and human effects. Hence, the cleaner and greener option to synthesis of ferrocenyl derivatives is *via* solvent-free reactions. This is because solvent-free reactions are efficient, simple, give higher yields, and eliminate the use of toxic solvents [17]. As a result, solvent-free reactions are more economical thus upholding the philosophies of green chemistry. Although, organic compounds have been widely synthesized under solvent-free conditions [17], the use of solvent-fee reactions in organometallic synthesis remains poorly researched.

### 1.3 Catalytic reactions

In industrial syntheses, catalysis is one of the extensively applied green methods used to achieve a sustainable synthesis of fine chemicals. Catalytic reactions uphold the principles of green chemistry by increasing the efficiency of producing chemicals in industries and reducing wasteful by-products. The presence of a catalyst in a reaction lowers the activation energy required for product formation thus facilitating a faster reaction rate (Figure 6).

Catalysts that are in the same phase as all the reactants are called homogeneous catalysts while those that are in a different phase from the reactants are called heterogeneous catalysts. Heterogeneous catalysts are commonly used in industrial synthesis, as they can be easily recovered and reused [25]. In view of this, it is necessary to develop sustainable and selective heterogeneous catalytic systems that optimize the synthesis of industrial chemicals. To accomplish this, an efficient metal catalyst system with a high surface-to-volume ratio, a high degree of particle dispersion and good metal-support interactions, among other properties, is necessary. Heterogeneous catalysts have been used to catalyse a variety of reactions including oxidation [26], dehydrogenation [27] and hydrogenation reactions [28].

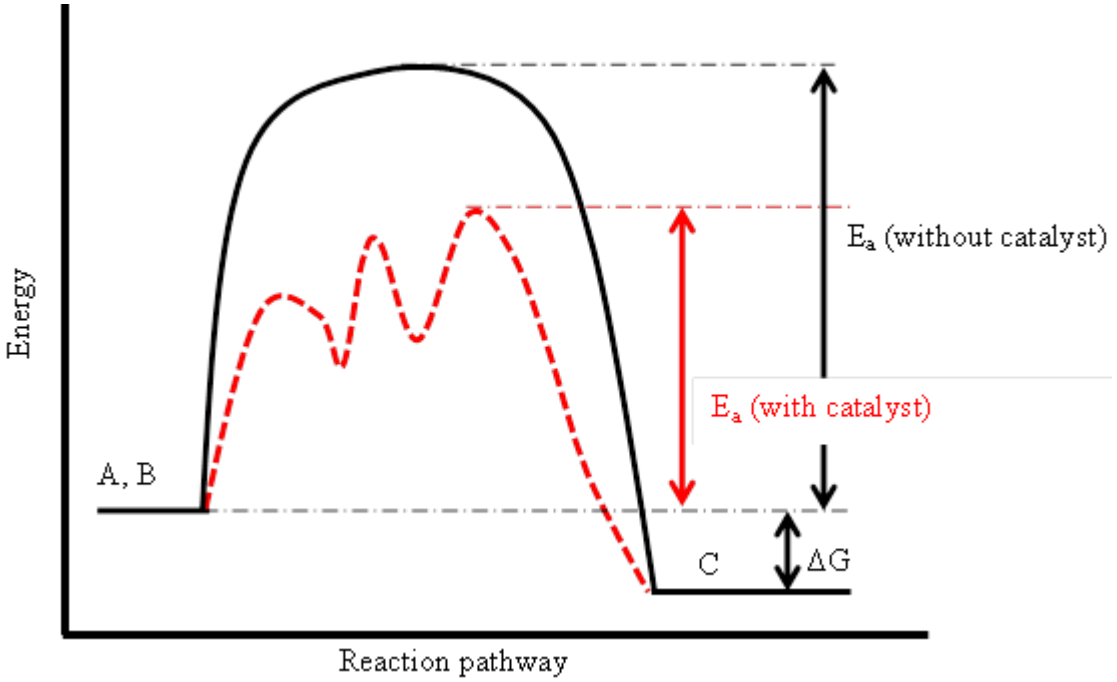


Figure 6: Activation energy of reactions with and without catalysts, where $E_a$ is the activation energy, A and B are arbitrary reactants, C is an arbitrary product and ΔG is the change in Gibbs energy.

Hydrogenation reactions involve the addition of two hydrogen atoms to a functional group acting as a hydrogen acceptor. The hydrogen source can either be hydrogen gas ($H_2$), a hydrogen donor (i.e. transfer hydrogenation) or polar substrates (i.e. electrolytic hydrogenation). Hydrogenation reactions play a vital role in the synthesis of fine chemicals [28], drug components [29] and, fuel production [30]. A common practice in hydrogenation reactions is to use noble metal catalysts such as Pd, Pt and Ni in the reactions [27, 28]. This is because noble metals contain electron holes in their d-orbitals and have lattice distances in the range of 0.36 to 0.38 nm that facilitate substrate adsorption [30].

Amongst these noble metals, Pd metal is commonly applied for hydrogenation [28] and carbon-carbon coupling reactions [28, 31]. This is due to the fact that Pd is resilient to oxidation by moisture and it easily forms Pd-H bonds [25]. Supported Pd catalysts are frequently used in the hydrogenation of several functional groups such as carbonyls, unsaturated carbon bonds and nitro-arenes.

Hydrogenation of nitro-arenes to anilines (Figure 7) is of immense industrial importance because anilines are used as precursors in the synthesis of other chemicals and for the production of pesticides [32], dyes and pharmaceutical drugs [29]. In certain cases, the nitro-arene contains other reducible functional groups, for instance, carbonyl, cyano or halogen

groups. Hydrogenation of these substituted nitro-arenes requires a selective catalyst, which will only reduce the nitro group while leaving the other functional groups unchanged. Nitrobenzophenone (NBP) is one example of a substituted nitro-arene that contains three reducible groups, namely, $NO_2$, CHO and C=C within the same molecule. The selective nitro-reduction of NBP yields aminobenzophenone (ABP), which is used to generate blue lasers and as an intermediate for synthesis of other compounds such as dehydroalanine Schiff bases [33-35]. Conventional supported Pd catalysts (such as Pd/carbon) may not show a high selectivity towards reduction of the nitro group alone (Figure 7), but may reduce other fuctional groups as well [28].

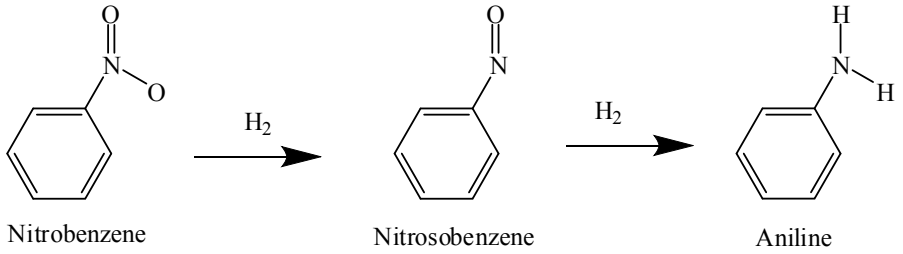


Figure 7: Proposed reaction mechanism for the reduction of nitrobenzene [10].

### 1.4 Pd supported on CNTs as a catalyst in hydrogenation reactions

Varieties of supports ranging from metal oxides to carbonaceous supports are normally used as supports for Pd. Carbonaceous supports have the advantage of easier metal recovery, as the carbon can be burnt-off to reclaim the metal catalyst. Activated carbon (AC) is an example of a carbonaceous support commonly utilized as a Pd catalyst support. However, carbon nanotubes (CNTs), that possess better physicochemical properties than AC, are increasingly being investigated as metal catalyst supports [27].

Pd supported on CNTs (Pd/CNTs) has been reported to show enhanced catalytic activity compared to Pd/AC [27]. The enhanced activity can be attributed to the previously mentioned unique physicochemical properties of CNTs, which enhance the degree of Pd particle dispersion and promote good Pd-support interactions. Many studies have been conducted on the catalytic activity of Pd/CNTs in the hydrogenation of unsaturated bonds [28]. However, not much has been reported on the use of Pd/CNTs as a catalyst in the selective hydrogenation of nitro-arenes to yield anilines (Figure 8). Thus, it is worthwhile to evaluate the potential of CNTs as novel Pd catalyst supports applied in nitro-hydrogenation reactions.

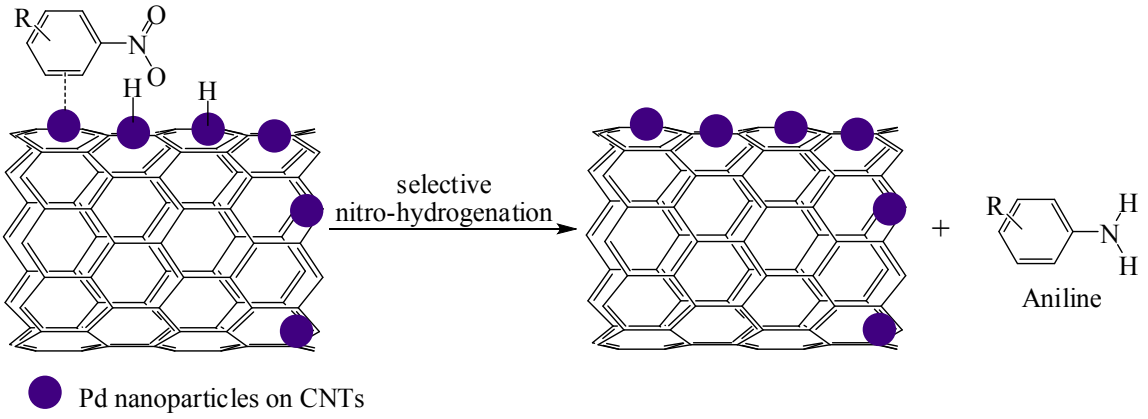


Figure 8: Schematic representation of a nitro-arene hydrogenation over Pd/CNTs.

When used as Pd catalyst supports, the performance of CNTs can further be improved by doping CNTs with heteroatoms such as nitrogen, oxygen, phosphorous and boron [11, 24]. Among these heteroatoms, doping of CNTs with nitrogen to form N-CNTs is commonly used to modify the physicochemical properties of CNTs applied as catalyst supports.

## 1.5 Pd supported on N-CNTs as a catalyst in hydrogenation reactions

N-CNTs exhibit exceptional Pd support properties such as good Pd stability, improved Pd size dispersion and an enhanced Pd activation [27]. Thus, compared with CNTs and other conventional Pd catalyst supports such as AC, N-CNTs can show enhanced catalytic performance owing to these improved properties. Since the nitrogen-species in N-CNTs are electron-rich, Pd supported on N-CNTs (Pd/N-CNTs) is strongly adsorbed onto the surface of N-CNTs, and this can lead to enhanced reaction rates [36]. In nitro-hydrogenation, an improved selectivity towards anilines over Pd/N-CNTs is possible due to the enhanced beneficial interactions between N-CNTs, Pd nanoparticles and the nitro-arene-substrate. Thus, Pd/N-CNT is potentially a smart catalyst for the hydrogenation of nitro-arenes to anilines. However, to date, limited accounts report the catalytic performance of Pd/N-CNTs in hydrogenation reactions such as the selective reduction of nitro-arenes to anilines.

## 1.6 Aim of the project

The overall aim of this study was to utilise green chemistry principles in the synthesis of novel and known halogen and nitrogen-containing ferrocenyl derivatives used as catalysts in the syntheses of N-CNTs, and to develop a controlled synthesis of N-CNTs whose nitrogen content or species modulates the selectivity of Pd/N-CNTs towards hydrogenation of nitro-

arene. The findings of this study are expected to provide insight into the controlled synthesis of N-CNTs and structure-activity relationships between Pd nanoparticles, a specific nitrogen species in the N-CNTs and the catalytic activity of Pd/N-CNTs. Hence, the specific objectives of this study were:

- To synthesize and characterize novel and known halogen- and nitrogen-containing ferrocenyl derivatives by use of a solvent-free approach.
- To synthesise and characterize N-CNTs by use of the synthesized nitrogen-containing ferrocenyl derivatives as novel catalysts. In addition, to look at the effect of other heteroatoms such as oxygen and halogens present in the ferrocenyl derivative catalysts on the synthesis of N-CNTs.
- To design a synthetic procedure that modulates the outer- and inner-diameters of N-CNTs and the type of nitrogen species incorporated into N-CNTs. Also, to investigate the physicochemical properties of the N-CNTs produced.
- To evaluate the structure-activity relationship between supported Pd nanoparticle catalysts and the particular nitrogen species incorporated into N-CNTs used as the Pd support. In addition, to evaluate the catalytic performance of Pd/N-CNTs in the hydrogenation of nitrobenzophenone to aminobenzophenone.

## 1.7 Outline of this thesis

This thesis is structured in a paper/manuscript format. Thus, all chapters excluding Chapter One (Introduction) and Chapter Eight (Conclusions) constitute a series of separate publications or manuscripts intended for submission to a particular journal. Except for Chapter One and Eight, all the other chapters are written in a format that complies with the specific journal requirements where they were published, submitted or are intended to be submitted. Hence, the thesis as a whole may not be consistent throughout in terms of style and presentation. This thesis has been structured as follows:

**Chapter One (Introduction)**

This chapter provides an overall introduction to the thesis that gives the general background information on the research as a whole and lays a foundation for the different findings reported in the thesis. The introduction also contains the research objectives and the thesis outline.

**Chapter Two (Paper 1)**

This chapter consists of a review on CNTs and N-CNTs focussing on their unique properties as platinum group metal catalyst supports. The chapter highlights the enhanced catalytic activity of platinum and nickel supported on carbon nanotubes (CNTs) compared with conventional carbonaceous and metal oxide supports used in dehydrogenation reactions. Publications in which usage of functionalized and/or pristine CNTs as metal supports reported improved selectivity to the product, and increased reactant conversion and reaction rates have been assessed. Further, the unique physical and electronic properties of CNTs that qualify them as better metal supports are mentioned; and the methods of synthesizing pristine CNTs, N-CNTs, functionalized CNTs and metal/CNTs are thoroughly outlined. The review tries to focus on current issues in catalysis such as the efficiency of CNTs and N-CNTs in catalytic dehydrogenation reactions compared with other conventional supports.

**Chapter Three (Paper 2)**

This chapter describes the use of a solvent-free mechanochemical approach for the synthesis of eight novel nitrogen- and halogen-containing ferrocenyl derivatives. A key finding in this chapter is that, depending on the acrylonitrile or diacrylonitrile substrates used, most of the products show high isolated yields with a few having low yields; however, their conversion yields could be higher in all cases.

Hence, this chapter explores the effect of the *para*-substituent on the acrylonitriles' phenyl ring on the kind of products and yields obtained, i.e. ferrocenyldiacrylonitriles, ferrocenylacrylonitriles and *bis*(ferrocenyl)diacrylonitrile. Apart from the type of substrate used, the reaction time and reactant mole ratio was investigated and found to play an important role on the product formed and the yield. The ferrocenyl derivatives were characterized by various techniques including UV-visible spectroscopy and cyclic voltammetry and they were deduced to be potentially useful for electrochromic and electron transfer studies. X-ray data analysis of some selected compounds is discussed.

In general, this chapter aimed at developing a simple mechanochemical solvent-free technique as a *greener* approach to synthesizing a range of novel ferrocenyl derivatives. This chapter also aimed at attaining a better understanding of the mechanism and the effect of the substituents on the kind of product formed, the selectivity, and yield of the reaction and the electrochemical properties of ferrocenyldiacrylonitriles. Another major focus of this chapter was to elucidate the X-ray crystallographic structures of the obtained novel ferrocenylacrylonitriles.

**Chapter Four (Paper 3)**

In this chapter, three novel ferrocenyl derivatives containing either a *para*-CN, *para*-Cl or *para*-$CF_3$ phenyl substituent, that were synthesized in Chapter Three, were used as new catalysts to synthesize N-CNTs. The focus of this chapter was on the use of the phenyl *para*-substituent on the ferrocenyl catalyst to tune the diameters and morphology of N-CNTs and to evaluate the effect of pyridine and acetonitrile as carbon sources. In addition, this chapter determined the effect of chlorine and fluorine on the nitrogen-doping levels of N-CNTs. The influence of the *para*-substituent on the X-ray crystallographic structure of ferrocenyl derivatives was determined. Both N-CNTs, carbon nanofibres (CNFs) and carbon spheres (CS) were obtained by use of the *para*-$CF_3$, *para*-CN and *para*-Cl catalysts. The presence of Cl and F in the catalysts promoted a reduction of the N-CNT ODs and IDs. Compared with the *para*-CN catalyst and the *para*-Cl catalysts, the *para*-$CF_3$ catalyst yielded more N-CNTs that were pure and contained higher nitrogen-doping levels. In this chapter, we also report the X-ray crystallographic structure of the *para*-$CF_3$ catalyst. From the crystallographic studies, it was observed that the X-ray structures of the three catalysts were influenced by the size of the *para*-substituent.

**Chapter Five (Paper 4)**

In this chapter, a solvent-free approach was used to synthesize a known nitrogen-containing ferrocenyl derivative. The synthesized ferrocenyl derivative (3-ferrocenyl-2-(4-cyanophenyl)acrylonitrile) was used as a new catalyst to successfully synthesize N-CNTs. The effect of the carbon source used was evaluated by using either toluene or acetonitrile. A key finding is that the decomposition products formed when either acetonitrile or toluene is used influences selectivity towards formation of N-CNTs.

We also present evidence that ethyl benzoate can be added up to 20 wt.% (to make at least 4 wt.% oxygen) into acetonitrile while still maintaining an effective synthesis of N-CNTs by use of 3-ferrocenyl-2-(4-cyanophenyl)acrylonitrile as the catalyst. Hence, this chapter explores the effect of oxygen derived from ethyl benzoate on the nitrogen-content, morphology and surface properties of N-CNTs. We present data indicating that, by adding a low concentration of oxygen, the nitrogen content, outer diameter, surface energy, surface basicity, alignment and conductivity of N-CNTs can be tuned. Low oxygen concentrations were observed to be favourable for the growth of well-aligned N-CNTs containing higher levels of nitrogen. Additionally, the conductivity of N-CNTs showed a correlation with the outer diameter of the N-CNTs. To date, research undertaken to modulate the

physicochemical properties of N-CNTs has focused mainly on variation of synthesis parameters such as temperature, pressure, and flow rate, among other parameters. However, the use of oxygen to modulate the physicochemical properties of N-CNTs remains unexploited and yet it is a relatively simple approach.

Hence, this chapter aimed at evaluating the expediency of using ethyl benzoate and 3-ferrocenyl-2-(4-cyanophenyl)acrylonitrile as a novel catalyst in the modulation of the physicochemical properties of N-CNTs. Additionally, this chapter aimed at gaining a better understanding of the effect of the carbon source on the selectivity towards formation of N-CNTs from a mechanistic point of view.

**Chapter Six (Paper 5)**

In this chapter, the ferrocenyl derivative synthesized in Chapter Five, together with the previously developed facile approach, was utilized to selectively incorporate pyrrolic nitrogen species into N-CNTs. The successful synthesis of pyrrolic N-CNTs containing 2.5-4.4 at. % of nitrogen *via* a CVD method is outlined. Selectivity towards formation of pyrrolic nitrogen was promoted by the use of oxygen derived from ethyl benzoate during synthesis of N-CNTs.

Although previous studies report the doping of CNTs with nitrogen, the selective doping of N-CNTs with a single nitrogen species to facilitate structure-activity relationship studies has never been reported. Thus, this chapter highlights the suitability of using ethyl benzoate as an oxygen source to modulate the type of nitrogen species incorporated into N-CNTs.

A key finding is that the physicochemical properties of N-CNTs, such as thermal stability, textural properties and surface wetness, are dependent on the amount of pyrrolic nitrogen in N-CNTs. The pyrrolic nitrogen also influenced the oxidation state of supported Pd nanoparticles, and improved interactions between Pd nanoparticles and N-CNTs resulting in better-dispersed and more stable Pd nanoparticles. Evaluation of the catalytic performance of Pd supported on pyrrolic N-CNTs (Pd/N-CNTs) in the hydrogenation of nitrobenzophenone (NBP) showed that pyrrolic nitrogen enhanced the activity and selectivity of Pd/N-CNTs. Hence, the synthesized Pd/N-CNTs are a promising catalyst for the selective reduction of NBP and other industrially important nitro-arenes such as nitrobenzene derivatives.

Therefore, the overall objective of this chapter was to utilize the oxygen heteroatom in the selective synthesis of pyrrolic-containing N-CNTs. This chapter also aimed at characterizing the physicochemical properties of pyrrolic-N-CNTs, and determining the

relationships between pyrrolic-nitrogen species and the physicochemical properties of the Pd nanoparticle catalyst. This chapter also aimed at evaluating the influence of pyrrolic-nitrogen on the catalytic activity of Pd/N-CNTs in the hydrogenation of nitrobenzophenone.

**Chapter Seven (Paper 6)**

In this chapter, further reactions of the best performing catalysts identified in Chapter Six are reported. In addition, the catalytic performance of Pd/N-CNTs synthesized by use of ferrocene is reported. These reactions highlight the effect of surface area, temperature and solvent on the catalytic performance of the catalyst. Additionally, the recyclability of the catalysts is analysed. The main finding is that increasing the surface area and temperature increases the catalytic performance of the catalyst. In addition, a protic solvent enhances the catalytic activity but not selectivity of the tested catalyst. The recycled catalysts showed good catalytic performance.

**Chapter Eight (Conclusions and future work)**

This chapter gives an overall summary of the thesis by tying together the major findings of each chapter. The main conclusions of each chapter are also related to the specific research objectives. Suggestions of possible future work emitting from the research findings are given.

## 1.8 Conclusions

A review providing fundamental information on the properties of CNTs and N-CNTs which makes them smart materials for application as Pd support for heterogeneous catalytic hydrogenation reactions is presented. A mechanochemical solvent-free approach was developed and used to synthesize novel and known nitrogen and halogen-containing ferrocenyl derivatives. The ferrocenyl derivatives were utilized as new catalysts to synthesize N-CNTs successfully. Chlorine and fluorine heteroatoms were effectively used to modulate the diameters, nitrogen-content and product distribution of N-CNTs. In addition, a novel protocol that utilizes oxygen was developed and used to tune the physicochemical properties of N-CNTs. This protocol was applied to achieve the selective synthesis of pyrrole-containing N-CNTs. The selective incorporation of pyrrolic-N-CNTs is a major break-through for the synthesis N-CNTs having a single nitrogen species. Additionally, the influence of pyrrolic nitrogen on the Pd oxidation state is presented and the resulting catalytic performance of Pd/N-CNTs is reported. Hence, this thesis presents an expedient and

'greener' approach towards the synthesis of Pd/N-CNTs whose nitrogen species controls its catalytic performance. The protocols developed have the potential to be applied in the selective incorporation of other nitrogen species into N-CNTs. The Pd/N-CNTs synthesized are potentially useful in the hydrogenation of other industrially important substituted nitro-arenes to anilines.

## References


[1] P.T. Anastas, J.C. Warner, *Green Chemistry: Theory and Practice*, Oxford University Press, Oxford, 1998.

[2] S.Y. Tang, R.A. Bourne, R.L. Smith, M. Poliakoff, Green Chem. 10 (2008) 268-269.

[3] R.M. Reilly, J. Nucl. Med. 48 (2007) 1039-1042.

[4] H. Dai, Nanotube growth and characterization, in: M.S. Dresselhaus, G. Dresselhaus (Eds.), Carbon Nanotubes Synthesis, Structure, Properties and Applications, Springler-Verlag, Heidelberg, 2001, pp. 29-51.

[5] A. Loiseau, X. Blasé, J.-Ch. Charlier, P. Gadelle, C. Journet, Ch. Laurent, A. Peigney, Synthesis methods and growth mechanism, in: A. Loiseau, P. Launois, P. Petit, S. Roche, J.-P. Salvetat (Eds.), Understanding Carbon Nanotubes, Springer-Heidelberg, 2006, pp. 49-122.

[6] J.D. Wiggins-Camacho, K.J. Stevenson, J. Phys. Chem. C 113 (2009) 19082-19090.

[7] E.M.M. Ibrahim, O.K. Vyacheslav, A. Leonhardt, S. Hampel, S. Oswald, M.H. Rümmeli, B. Büchner, Diamond Relat. Mater. 19 (2010) 1199-1206.

[8] S. Kundu, W. Xia, W. Busser, M. Becker, D.A. Schmidt, M. Havenith, M. Muhler, Phys. Chem. Chem. Phys. 12 (2010) 4351-4359.

[9] L.M. Ombaka, P.G. Ndungu, V.O. Nyamori, J. Mater. Sci. 50 (2015) 1187-1200.

[10] P. Chen, F. Yang, A. Kostka, W. Xia, ACS Catal. 4 (2014) 1478-1486.

[11] P. Chen, L.M. Chew, A. Kostka, M. Muhlera, W. Xia, Catal. Sci. Technol. 3 (2013) 1964-1971.

[12] V.O. Nyamori, S.D. Mhlanga, N.J. Coville, J. Organomet. Chem. 693 (2008) 2205-2222.

[13] E.N. Nxumalo, V.O. Nyamori, N.J. Coville, J. Organomet. Chem. 693 (2008) 2942-2948.

[14] R.S. Oosthuizen, V.O. Nyamori, Appl. Organomet. Chem. 26 (2012) 536-545.

[15] A. González, P. Vázquez, T. Torres, Tetrahedron Lett. 40 (1999) 3263-3266.

[16] N. Dwadnia, F. Allouch, N. Pirio, J. Roger, H. Cattey, S. Fournier, M.-J. Penouilh, C.H. Devillers, D. Lucas, D. Naoufal, R.B. Salem, J.-C. Hierso, Organometallics 32 (2013) 5784-5797.

[17] M. Himaja, P. Das, A. Karigar, IJRAP 4 (2011) 1079-1086.

[18] D. Braga, S.L. Giaffreda, F. Grepioni, A. Pettersen, L. Maini, M. Curzi, M. Polito, Dalton trans. (2006) 1249-1263.

[19] S. Taubert, K. Laasonen, J. Phys. Chem. C 116 (2012) 18538-18549.

[20] A. Shaikjee, N.J. Coville, Carbon 50 (2012) 3376-3398.

[21] K. Chizari, A. Vena, L. Laurentius, U. Sundararaj, Carbon 68 (2014) 369-379.

[22] G. Bepete, Z.N. Tetana, S. Lindner, M.H. Rümmeli, Z. Chiguvare, N.J. Coville, Carbon 52 (2013) 316-325.

[23] T. Thurakitseree, C. Kramberger, P. Zhao, S. Aikawa, S. Harish, S. Chiashi, E. Einarsson, S. Maruyama, Carbon 50 (2012) 2635-2640.

[24] Y. Cao, H. Yu, J. Tan, F. Peng, H. Wang, J. Li, W. Zheng , N.-B. Wong, Carbon 57 (2013) 433-442.

[25] J. Heveling, J. Chem. Educ. 89 (2012) 1530-1536.

[26] K. Pirkanniemi, M. Sillanpää, Chemosphere 48 (2002) 1047-1060.

[27] L.M. Ombaka, P. Ndungu, V.O. Nyamori, Catal. Today 217 (2013) 65-75.

[28] R.S. Oosthuizen, V.O. Nyamori, Platinum Met. Rev. 55 (2011) 154-169.

[29] H.-U. Blaser, H. Steiner, M. Studer, ChemCatChem 1 (2009) 210-221.

[30] S.-C. Qi, X.-Y. Wei, Z.-M. Zong, Y.-K. Wang, RSC Adv. 3 (2013) 14219-14232.

[31] L. Yin, J. Liebscher, Chem. Rev. 107 (2007) 133-173.

[32] A. Corma, H. Garcia, Chem. Soc. Rev. 37 (2008) 2096-2126.

[33] A.S. Saghiyan, L.A. Stepanyan, L.L. Manasyan, A.V. Geolchanyan, S.M. Djamgaryan, H.R. Ajvazyan, H.A. Panosyan, V.I. Maleev, T.F. Saveleva, Tetrahedron Lett. 21 (2010) 2638-2645.

[34] A.K. Bhowmik, S. Tan, A.C. Ahyi, J.A. Dharmadhikari, A.K. Dharmadhikari, D. Mathur, Opt. Commun. 280 (2007) 472-476.

[35] Z. Li, B. Wu, G. Su, G. Huang, Appl. Phys. Lett. 70 (1997) 562-564.

[36] G.-X. Chen, J.-M. Zhang, D.-D. Wang, K.-W. Xu, Physica B 404 (2009) 4173–4177.

# CHAPTER TWO

# USAGE OF CARBON NANOTUBES AS PLATINUM AND NICKEL CATALYST SUPPORT IN DEHYDROGENATION REACTIONS

Catalysis Today 217 (2013) 65–75

Contents lists available at ScienceDirect

Catalysis Today

journal homepage: www.elsevier.com/locate/cattod

Review

## Usage of carbon nanotubes as platinum and nickel catalyst support in dehydrogenation reactions

L.M. Ombaka, P. Ndungu, V.O. Nyamori*

*School of Chemistry, University of KwaZulu-Natal, Westville Campus, Private Bag X54001, Durban 4000, South Africa*

ARTICLE INFO

*Article history:*
Received 6 December 2012
Received in revised form 16 May 2013
Accepted 19 May 2013
Available online 15 June 2013

*Keywords:*
Carbon nanotubes
Nitrogen-doped CNT
Dehydrogenation
Platinum
Nickel

ABSTRACT

Carbon nanotubes (CNTs) as supports for metal catalysts used in dehydrogenation reactions to produce fine chemicals and hydrogen fuels are increasingly being investigated. Compared with conventional metal catalyst supports, functionalized-CNT and nitrogen-doped CNT (N-CNT) metal supports have shown enhanced reaction activity in terms of selectivity to products and conversion of reactants. This review undertakes to provide information on methods used to load metal nanoparticles (NPs) onto functionalized-CNTs and N-CNTs used as catalysts in dehydrogenation reactions. The activity of Pt/CNTs, Ni/CNTs, Pt–N/CNTs, oxygen-CNTs (O-CNTs) and phosphorus-CNTs (P-CNTs) used as catalysts in different dehydrogenation reactions are also looked at. Additionally, the morphology and electronic properties of N-CNTs that influence their performance as metal catalyst supports are discussed and prospective research areas are proposed.

# Usage of carbon nanotubes as platinum and nickel catalyst support in dehydrogenation reactions

**L.M. Ombaka, P. Ndungu, V.O. Nyamori∗**

**School of Chemistry, University of KwaZulu-Natal, Westville Campus, Private Bag X54001, Durban 4000, South Africa**

## Abstract

Carbon nanotubes (CNTs) as supports for metal catalysts used in dehydrogenation reactions to produce fine chemicals and hydrogen fuels are increasingly being investigated. Compared with conventional metal catalyst supports, functionalized-CNT and nitrogen-doped CNT (N-CNT) metal supports have shown enhanced reaction activity in terms of selectivity to products and conversion of reactants. This review undertakes to provide information on methods used to load metal nanoparticles (NPs) onto functionalized-CNTs and N-CNTs used as catalysts in dehydrogenation reactions. The activity of Pt/CNTs, Ni/CNTs, Pt/N-CNTs, oxygen-CNTs (O-CNTs) and phosphorus-CNTs (P-CNTs) used as catalysts in different dehydrogenation reactions are also looked at. Additionally, the morphology and electronic properties of N-CNTs that influence their performance as metal catalyst supports are discussed and prospective research areas are proposed.

Keywords: Carbon nanotubes, Nitrogen-doped CNT, Dehydrogenation, Platinum, Nickel

∗ Corresponding author. Tel.: +27 31 260 8256; fax: +27 31 260 3091.

E-mail addresses: lucyombaka@gmail.com (L.M. Ombaka), nyamori@ukzn.ac.za (V.O. Nyamori).

## 1. Introduction

Catalytic dehydrogenation reactions find extensive application in chemical industries and hydrogen fuel production [1,2]. It is therefore necessary to develop sustainable and selective catalytic dehydrogenation procedures that optimizes the synthesis of industrial chemicals. To accomplish this, an efficient metal catalyst system with a high surface-to-volume ratio, a high degree of particle dispersion and good metal-support interactions, among other properties, is necessary [3]. Platinum and nickel metal catalysts are well known and applied as catalysts in many industrial reactions because they show good activity under practical conditions [4]. Conventionally Pt and Ni metal catalysts are supported on carbonaceous solids or alumina to increase their activity. Such metal supports increase the distance between each catalyst particle enabling a greater exposure of substrate molecule to catalyst particles [5].

Although the use of platinum group metals (PGMs) as catalysts has been vastly studied, trends in modern chemistry are towards using PGMs supported on nanomaterials as catalysts. This technology has been shown to improve reaction selectivity profoundly [6]. Nanomaterials like CNTs, when used as metal supports form an efficient catalytic system, which prevents metal particle aggregation during reactions and accelerate reaction rates [7]. CNTs are continuously being investigated for use as catalyst supports because they possess superior catalytic support properties compared with conventional catalyst supports [8]. This can be explained by their mesoporous nature, for example, when CNTs are used as supports for metal catalysts such as Pt, they can improve the mass transfer of reactants and products leading to an enhanced reaction rate [9]. Improved selectivity towards the desired product when metal/CNT catalysts are used can be attributed to nano-confinement of the substrate molecule infused into the CNTs [10]. This is not possible for conventional supports as their surface area is not on the nano-scale. CNTs and N-CNTs exhibit either a metallic or semi-metallic nature depending on their diameter and chirality; thus, their nature ensures stronger electronic interactions with metal catalysts compared with conventional catalysts [7,11]. CNTs have a high tensile strength and Young's modulus hence, they can withstand high levels of friction during vigorously stirred reactions which would otherwise lead to mechanical deformation of conventional supports [12]. Owing to their nano-size structure, CNTs have a higher surface-to-volume ratio compared with conventional catalysts. Open ended CNTs have both their interior and exterior surfaces exposed to substrate molecules with the net effect of having every atom being exposed to two surfaces [13]. Being

carbonaceous materials, CNTs can easily be burned off to $CO_2$ and the precious metal recovered more conveniently than in conventional metal oxide supports [14].

Conventional supports like alumina are relatively mechanically and thermally unstable at high temperatures, show chemical interactions with a metal catalyst which leads to sintering of the metal particles, making it difficult to recover precious metals after use [15]. Other supports have uneven pore size and insulation properties which lead to non-uniform heat distribution during reactions [16]. However, metal oxides and carbonaceous supports are still used in numerous industrial processes and are commercially available. Alumina is commonly used as a catalyst support due to its commercial availability, while activated carbon is used in liquid phase reactions because it can be easily separated from the reaction [17]. In addition, efficient production systems that manufacture conventional supports for commercial usage have been developed. The majority of factories have also established proper systems to control the purity of conventional supports at large scale production, within a reasonable period and cost [15].

Industrial processes apply catalytic oxidative dehydrogenation to synthesize styrene, aromatic compounds, olefins, nitriles, ketones and aldehydes among other functional groups. Styrene is an important monomer that is used in the manufacture of other synthetic polymers. Styrene can be obtained by oxidative dehydrogenation of ethylbenzene over catalysts such as activated alumina, mixed-oxides and phosphates [10]. Selectivity to styrene has been shown to increase when transition metals (such as Ni, Co, *etc*.) supported on CNT are used as catalysts as opposed to conventional catalyst supports [18]. Olefins are used as industrial materials to produce completely biodegradable surfactants, which are environmentally friendly. Generally, olefins are produced by catalytic dehydrogenation of paraffins over bimetallic and trimetallic supported transition metals (such as Pt–Sn or Pt–Sn–Li) [17]. The activity of these metal catalysts in dehydrogenation of olefins was seen to improve when CNTs were used as metal supports [19].

In the present world, hydrogen is considered a source of clean and efficient energy. Hydrogen fuel can be efficiently produced by direct dehydrogenation of cycloalkanes [20] or by dehydrogenation of ammonia–borane [9]. Catalytic dehydrogenation of tetralin and decalin at temperatures of about 300 °C over Pt or Pd supported on CNTs has been shown to give a high yield of pure hydrogen and naphthalene [14]. Similarly, catalytic dehydrogenation of ammonia–borane over Pt nanoparticles (NPs) supported on CNTs has been shown to give good yields of hydrogen at temperatures as low as 70 °C [11].

Numerous research done on catalytic dehydrogenation reactions over supported Pt or Ni indicates that, reaction activity and selectivity are dependent on the nature of the metal support as well as interactions between precious metals and supports. Therefore, this review will analyze Pt and Ni metal supports used in catalytic dehydrogenation reactions with the objective of answering the following questions.

- Are CNTs, N-CNTs or functionalized-CNTs more efficient as Pt or Ni supports compared with conventional supports in catalytic dehydrogenation reactions? Apart from catalyst activity, do CNT and N-CNTs supports influence selectivity in catalytic dehydrogenation reactions?
- In what ways do the unique properties of CNTs and N-CNTs influence the catalytic activity of Pt and Ni catalysts in dehydrogenation reactions?
- How do the metal NP properties of metal/N-CNTs compare with those of metal/CNTs?

Finally, some published examples wherein Pt/CNTs and Ni/CNT catalysts are used will be reviewed.

## 2. Carbon nanotubes (CNTs)

CNTs are typical graphene sheets rolled into one dimensional nanotubes (Fig. 1) with an external diameter ranging between 1 and 100 nm [21]. CNTs can either be single-walled CNTs (SWCNTs) or multi-walled CNTs (MWCNTs), depending on the number of graphene sheets that are rolled up to form them [22].

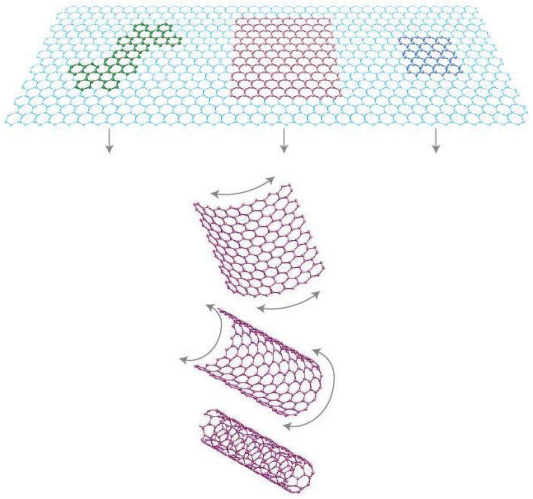

**Fig. 1**. Graphene sheet being rolled up to form a one dimensional CNT [25]

MWCNTs (Fig. 2) consist of 2–30 layers of rolled up graphene sheets; each sheet measures approximately 0.14 nm in thickness [23]. The rolled up sheets are similar to a concentric assembly of SWCNTs. The diameter of MWCNTs ranges between 2 and100 nm, while the distance between each graphene sheet is approximately 0.34 nm, which is equal to the distance between graphite layers [23]. The electronic properties of each MWCNT are equivalent to the sum of individual electronic properties of each SWCNT that makes up the MWCNT [22]. As such, MWCNTs or CNTs in general possess good electrical conductivity; they also have a high mechanical strength and very good thermal conductivity. CNTs are extensively applied in industries and research areas, this can be attributed to the fact that production of CNTs can easily be scaled up *via* a chemical vapour deposition (CVD) method [21].

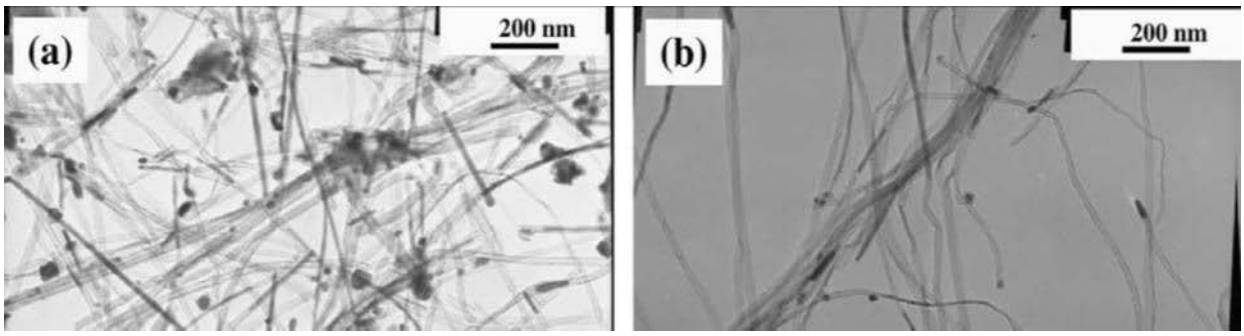


**Fig. 2**. TEM pictures of MWCNTs produced *via* a CVD method [26].

The surfaces of MWCNTs can be modified by doping with N or B to increase metal adhesion to the CNT support [21]. Functional groups (e.g. -OH or -COOH) can also be bonded to MWCNT surfaces so as to increase pore size while maintaining high surface area [24]. Thus, MWCNTs are effective as precious metal supports in catalytic reactions. In addition to catalytic applications, MWCNTs are used in various industrial appliances owing to their unique features. MWCNTs find applications in high technology coating of automobiles and aircraft, packaging, electronic devices, electrodes in chemical/electrochemical cells, biosensors, transistors, electron field emitters, lithium ion batteries and sporting materials such as tennis rackets [23]. Currently, more research is being conducted on other possible applications of MWCNTs.

## 3. Purification and functionalization of CNTs

CNTs can be synthesized *via* three major methods namely; arc discharge, laser ablation and CVD [25]. Numerous modifications of these three methods have been employed to produce CNTs with a specific desired architecture [26]. CNTs synthesized by various methods usually have closed ends and contains impurities in the form of amorphous carbon and metal NPs [27]. Thus, purification and functionalization of pristine CNTs is essential to enable modification and loading of metal NPs onto the CNTs. Purification of CNTs involves treatment with strong acids (*e.g.* $HNO_3$, $HNO_3/H_2SO_4$) which removes the amorphous carbon and oxidizes metal NPs [28]. Functionalization using aggressive acids opens the ends of CNTs and oxidizes them by introducing carboxylic (-COOH), carbonyl (-CO), and hydroxyl (-OH) groups. Incorporation of these polar groups onto the surface of pristine CNTs changes their reactivity and wetting properties. In addition, introduction of such uniform mesoporous molecular sieves anchors the catalyst metal NPs, hence minimizing sintering of the metal catalyst [29]. Mesopores also enable nanoconfinement of catalytic metal NPs, which in turn increases catalytic activity of the metals [30]. CNT functionalization can be classified into two broad categories, *i.e.* non-covalent functionalization or covalent functionalization.

### 3.1. Non-covalent functionalization

Non-covalent functionalization is based on attraction of the hydrophobic end of an adsorbed molecule to CNT walls *via* van der Waals forces or π–π interactions [31]. This type of functionalization can be performed in ionic liquids which do not interfere with the electronic structure of CNTs, as it does not involve covalent bonds. The technique is useful in the production of surfactant to exfoliate bundles of SWCNTs, wrapping of CNTs by polymers and endohedral functionalization of CNTs. The main drawback of non-covalent bonding is that it is difficult to control the functionalization system and characterize the product. Furthermore, in reactions involving other solutions the attached molecules can interact with the solution and be displaced by the solvent [31]. An example of non-covalently functionalized CNTs is CNTs functionalized with cationic polyethyleneamine and anionic citric acid [30]. When these modified CNTs were taken through various treatments selective attachment of gold NPs was realized [30].

### 3.2. Covalent functionalization

Covalent functionalization involves formation of covalent bonds between various functional groups and the sidewalls or defect sites or on tips of CNTs. Sidewall functionalization of CNTs has a greater impact in modification of CNT properties compared with tip functionalization of CNTs [32]. Covalent functionalization is irreversible and interferes with the electronic properties of CNTs causing permanent loss of double bonds on the hexagonal structures of CNTs. Covalent functionalization can be achieved by fluorination of CNTs, cycloaddition, boron adsorption and nitrogen adsorption *via* $HNO_3$, $HNO_3/H_2SO_4$ or diazonium salt. Fluorination is done by reacting the CNTs with $F_2$, HF and $IF_5$ under mild conditions to form fluoronanotubes which are very reactive and can undergo numerous substitution reactions with alkyl groups and addition reactions like Diels–Alder reactions [33]. Cycloaddition can be achieved through various reactions like 1,3-dipolar cycloaddition of azomethineylides, carbene [2+1] cycloaddition or Diels–Alder reaction *via* microwave irradiation cycloaddition [34].

## 4. Nitrogen and boron functionalization

N and B are the commonly introduced elements into the $sp^2$ carbon network of CNTs without significantly interfering with the atomic arrangement of the hexagonal rings [21]. In nitrogen-doped CNTs (N-CNTs) nitrogen can be present as a pyridinic or pyrrolic nitrogen atom [35]. The presence of nitrogen or boron in CNTs brings about major modifications in CNTs such as morphological, electrical, mechanical and oxidative properties [36]. Nitrogen or boron doping increases binding energies of transition metals, a phenomenon known as chemisorption. Boron has been noted to increase transition metal chemisorption more than nitrogen [37]. Pristine CNTs show minimal interactions with precious/transition metal NPs; usually *via* weak van der Waals forces. Metal adhesion to CNTs is significantly modified by functionalization with nitrogen or boron, which in turn increases catalyst activity [38].

When interacting with CNTs, boron is electron deficient (hole) and can either capture additional electrons from neighbouring carbon atoms or form hybridized metal-boron bonds, thus acting as an electron acceptor [39]. This enhances metal adhesion to CNTs by forming metal-boron hybrid bonds as well as enhancing the boron-carbon bonds [21], hence improving catalytic performance of metal-boron-CNTs. Nitrogen on the other hand is electron rich and thus acts as an electron donor and a base during reactions. Since electrons are known to soften the carbon-carbon bond in all $sp^2$-bonded carbon material, the extra

electrons on nitrogen tend to weaken carbon-carbon bonds in the CNTs [36]. Given that nitrogen atoms have a higher electron affinity than carbon atoms, the nitrogen species in graphite-like nitrogen-doped CNTs activate their neighbouring carbon atoms thus enhancing metal NP adhesion to carbon atoms [36,38]. In contrast, nitrogen atoms in pyridine-like nitrogen-doped CNTs enhance metal adhesion to N-CNTs by forming metal-nitrogen hybridized bonds [36].

The improved metal–CNT interactions in N-CNTs increases the catalytic performance of metal/N-CNTs. Palladium supported on N-CNTs was reported to exhibit a higher activity and selectivity compared with Pd/CNT catalysts in the hydrogenation of cinnamaldehyde to hydrocinnamaldehyde [40]. Pt/N-CNT catalyst has been shown to have good selectivity during oxidation of aniline in aqueous solutions [28]. It was also noted that Pt/N-CNT could be recycled without any loss of catalyst in terms of capacity and efficiency. As reported by Ovejero *et al*. [28] nitrogen doping significantly increased metal dispersion enabling efficient surface interactions between aniline and active sites. Very little research has been conducted on the catalytic activity of metal/B-CNTs in industrially important chemical reactions, despite the fact that boron doping increases the binding energies of transition metals to CNT supports more than nitrogen [41].

## 5. Synthesis of N-CNTs

CNTs can either be doped directly with nitrogen during synthesis (*in situ* doping) or by treating pristine CNTs with nitrogen-containing compounds (post-synthesis treatment doping) [42]. Post-synthesis treatment may be done by plasma treatment of CNTs in nitrogen gas. It can also be achieved by treating the CNTs with oxidizing agents to introduce oxygen functional groups, followed by reaction with organic amines to introduce nitrogen functional groups grafted on CNTs [43]. An example of post-synthesis treatment was done by Chetty *et al*. [44] who achieved about 4% of nitrogen atom incorporation in CNTs to produce N-CNTs in a plasma chamber. The main shortcoming of post-synthesis treatment is that it entails numerous synthetic steps, hence *in situ* doping methods are more commonly utilized in the synthesis of N-CNTs [42].

*In situ* doping procedure can be achieved by arc discharge technique [42], CVD [45] or laser ablation [46] in the presence of a nitrogen source. Of the three techniques CVD is the most common technique used to synthesize large quantities of N-CNTs successfully [42]. CVD synthesis of N-CNTs may involve usage of nitrogen containing organometallic compounds in

a suitable carbon source such as toluene [45], or nitrogen containing organic compounds in the presence of a transition metal substrate [47]. A major challenge of *in situ* doping of CNTs is attaining high percentages of nitrogen incorporation. Higher temperature techniques like laser ablation and arc discharge afford up to 33% nitrogen incorporation [48]. While, relatively lower temperature techniques like CVD and pyrolysis have been reported to yield as low as 1 at.% [49] and 7.7 at.% nitrogen incorporation [50]. Nonetheless, of the three *in situ* methods used to synthesize N-CNTs, the CVD synthesis is more widely explored. This is because CVD is suitable for large-scale production of N-CNTs, at low cost and with an easy set-up procedure which produces relatively pure N-CNTs [42]. Normally, the CNTs produced have bamboo-like structures (Fig. 3) and their growth mechanism is proposed to be similar to that of pristine CNTs [42].

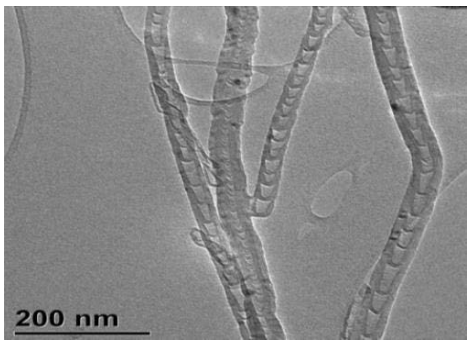


**Fig. 3**. TEM image of N-CNTs with a bamboo like structure along the tube axis [16].

At high temperatures the carbon–nitrogen precursor decomposes into nitrogen and carbon surface atoms which dissolve in the metal catalyst to form a saturated solid solution [51]. Since nitrogen and carbon atoms express different dynamics [52], metal–$C_x$ species form faster than metal–$N_x$ species and a carbon saturation is attained before nitrogen saturation leading to nucleation of carbon-rich outer walls of the CNTs before nitrogen-rich walls. This is followed by growth of nitrogen containing inner walls *via* surface diffusion. Florea *et al*. [53] noted that nitrogen containing rings are predominantly located at the end of the cap, hence saturation of the tube cap with nitrogen containing rings disrupts the tube growth process leading to closure of the tube and formation of compartments.

Just like in pristine CNT production, synthesis of N-CNTs produces nitrogen-doped amorphous carbon and nitrogen doped spheres, necessitating purification. The quality of N-CNTs formed depends on various parameters, namely nitrogen and carbon precursors, catalyst, temperature, reaction time, pressure, carrier gas flow rate among others, depending

on the reaction set-up [42]. Different combinations of the above parameters have been reported to yield different percentages of nitrogen incorporation on CNTs. Vijayaraghavan and Stevenson [54] attained 4% nitrogen-doping on CNTs using pyridine and ferrocene precursor in a CVD reactor. A higher nitrogen percentage loading ranging between 5 and 10% nitrogen atoms was achieved by passing a stream of ammonia gas along with pyridine and ferrocene precursors in a CVD reactor [54]. A yield of 0.5–5% N atomic loading in N-CNTs was also obtained using varied ammonia and ethane concentrations in a CVD reactor [55]. Amadou *et al*. [40] reported 7% incorporation of nitrogen atoms in N-CNTs synthesized in a CVD reactor using ammonia and ethane. Although several articles have been published on synthesis of N-CNTs, comparison of the different performances of the protocols is difficult since different reaction conditions are employed.

## 6. Metal loading techniques

A key issue in loading noble metals onto CNTs and N-CNTs is the surface area of metal NPs and their dispersion on CNTs. Good quality catalysts should have a high metal surface area/volume ratio and high dispersion [56]. However, pure CNTs have insufficient binding sites to aid in anchoring of metal NPs leading to poor metal dispersion. To increase metal dispersion and decrease aggregation, it is necessary that CNTs be functionalized with polar groups (such as hydroxyl and carboxylic groups) prior to metal loading [57]. Over the years several techniques have been developed to synthesize noble metal/CNT catalysts (Fig. 4) and metal NPs/N-CNT, with good dispersion, small metal size and an appreciable weight of nanoparticles loaded. Different preparation methods yield catalysts with different surface area and dispersion, hence different catalytic activities. These techniques can be classified into four broad categories, *viz*. electrochemical deposition, electroless deposition, metal nanoparticle dispersion on functionalized CNTs and physiochemical methods [58].

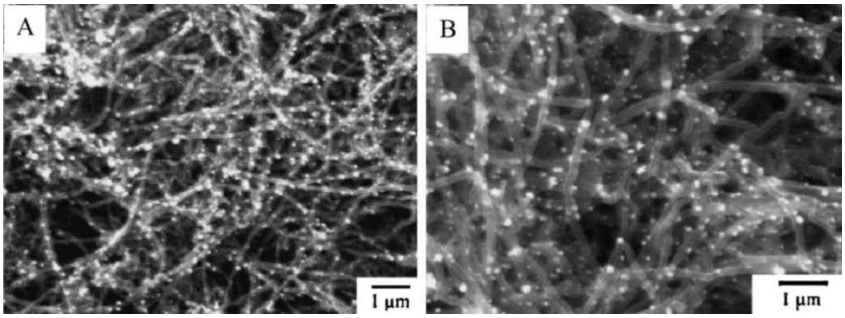


**Fig. 4**. SEM images with (A) low and (B) high magnifications of Pt/Ru/CNTs nanohybrids [27].

### 6.1. Electrochemical deposition

This method entails synthesis of metal NPs/CNTs by reduction of noble metal complexes like $H[AuCl_4]$, $H_2[PtCl_4]$ and $(NH_4)_2[PdCl_4]$ by electrons [58]. The CNTs act as a molecular conducting wire and supports for the deposition of metal NPs but do not react with the noble metal salts. Modulation of parameters such as concentration of the metal salts, nucleation potential and deposition time aids in varying the size of the noble metal NPs and their distribution on the sidewalls of CNTs [58]. Electrochemical deposition has the advantage of producing highly pure metal NPs/CNTs with good metal adhesion to the CNTs, within a short time frame [59]. Contrariwise, the main disadvantage of this method is formation of metal NPs/CNTs with large size metal NPs (between 10 and 100 nm) [60]. Precious metal NPs of diameters in the range 2–30 nm have been deposited onto CNTs using electrochemical deposition, cyclic potential scanning, and pulsed electrodeposition as seen in Table 1. Carpenter *et al*. [61] reported the preparation of nickel-carbon nanotube (Ni/CNT), where Ni loading was done on functionalized and pure CNTs by electro deposition from a Watts electrolyte. Ni/CNTs synthesized from functionalized CNTs showed better Ni homogeneity than the Ni/CNTs made from pure CNTs [61]. Wen *et al*. [62] investigated the effects of varying deposition time and current density on the morphology of nickel oxide CNTs. They reported uniformly dispersed nickel oxide particles of diameter ranging between 15 and 30 nm on CNTs.

### 6.2. Electroless deposition

Electroless deposition of NPs onto CNTs is based on a chemical process in which a chemical species having substantially lower redox potential than that of the metal nanoparticle being reduced, provides the driving force of the reactions. Studies have suggested that a direct redox reaction occurs between the metal ions and CNTs [58]. Universal application of electroless deposition is hampered by the fact that only metal ions of a redox potential higher than that of CNTs can be reduced into NPs on the nanotube support [63]. This limitation can be overcome by a procedure known as substrate-enhanced electroless deposition (SEED). SEED involves supporting carbon nanotubes with a metal substrate having a lower redox potential than that of the metal ions being reduced to NPs [58]. Owing to its simplicity, several metal NPs/CNTs have been successfully synthesized *via* this technique as summarized in Table 1. Ye *et al*. [64] have demonstrated the synthesis of Pt/Ru/Mo/graphene-CNTs catalyst using chemical reduction of metal precursors with sodium borohydride at room temperature.

### 6.3. Metal nanoparticle dispersion on functionalized CNTs

This technique utilizes the formation of covalent and non-covalent functional group on CNTs as binding sites for anchoring metal ions or metal NPs. A major disadvantage of this technique is that it leads to poor metal dispersion and large metal NPs, more so when high loading of metal is conducted [65]. The most widely applied covalent functionalization is the bonding of carbonyl and carboxyl groups onto CNT surfaces *via* treatment of CNTs with a $HNO_3$ or $HNO_3/H_2SO_4$ mixture [28]. Carbonyl and carboxyl groups act as nucleation sites for dispersion of noble metal NPs. Functionalization can also be achieved by treating CNTs with HCl, HF, $O_3$, $KMnO_4$ or $H_2O_2$ [58]. Metal NPs with sizes ranging between 2 and 5 nm have been prepared using this method (Table 1).

### 6.4. Physiochemical methods

There are numerous physiochemical methods used to load metal NPs onto CNTs. These include sputtering deposition, ion and electron beam irradiation deposition, evaporation deposition precipitation, sol–gel precipitation and metal organic CVD. The main strength of these methods is their excellent control over the size and uniformity of the noble metal NPs [58]. Sputtering deposition produces uniform-size noble metal NPs by selecting appropriate metal cathodes, controlling the current and sample exposure time. Ion and electron beam irradiation deposition is done by $\gamma$-irradiation and electron beam irradiation to homogenously disperse metal NPs [58].

Evaporation deposition precipitation is achieved by impregnating the CNTs with an aqueous solution of a metal nanoparticle salt, followed by removal of excess water by evaporation to get a solid which is dried at 373 K overnight [66]. Calcination of the solid at approximately 673 K for 4 h or in air yields metal nanoparticle/CNT. Evaporation deposition precipitation has been widely applied in loading of NPs, and a few examples are summarized in Table 1.

Another method used to precipitate metal NPs onto CNTs is the sol–gel technique. In one example metal nanoparticle/CNT catalyst were prepared *via* a series of steps; firstly, a solution of $Al(OH)_3$ was prepared by drop wise addition of liquid ammonia (1.5 M) into an $Al(NO_3)_3$ solution (0.2 M) under vigorous stirring until the pH was about 7.8 [67]. This was followed by addition of the nitrate salt of the precious metal and liquid ammonia to the $Al(OH)_3$ solution to obtain a gel in the ageing process. The material obtained was dried under supercritical conditions of ethanol followed by calcination at 400 °C.

**Table 1:** Summary of the metal particle sizes in the respective metal NP/CNT catalysts and %weight of metal loading.

| Metal NP/CNTs | Method of synthesis | Particle size in nm/%wt. of metal loading | Ref. |
|---|---|---|---|
| Pt/MWCNTs | electrochemical deposition | 60-80 | [59] |
| | cyclic potential scanning | 20 | [70] |
| | pulsed electrodeposit | 2-3 | [71] |
| | chemical reduction | 3.5, 40% | [72] |
| | ion exchange method | 3-4, 15.4% | [8] |
| | molecular layer functionalization | 2-5 | [60] |
| | | 0.1-1% | [73] |
| | wet impregnation | 0.1-1% | [74] |
| | | 20-15 | [75] |
| | Sol-gel | 2-40 | [76] |
| | MOCVD | 2-4 | [77] |
| | | 2-60 | [78] |
| Pt-Cu/CNTs | incipient wetness co-impregnation | 1% Pt-0.3% Cu | [79] |
| Pt-Na-CNTs | wet impregnation | 2-3 Pt, 5% Pt | [80] |
| Pt/CNT/carbon paper | electroless deposition | 2-4, 99.8% | [81] |
| Pt/N-CNTs | wet impregnation | 3, 48% | [82] |
| Pt–Ni/CNTs | incipient wetness co-impregnation | 2-5, 0.34% | [83] |
| | electrochemical oxidation | 60-80 | [59] |
| Pt-Ru/MWCNTs | wet impregnation | 2-3, 20% | [84] |
| | wet impregnation | 20% | [85] |
| Pt-Sn/MWCNTs | chemical reduction | 2.7, 20% | [86] |

Metal organic CVD (MOCVD) is another method used to deposit metal NPs directly on CNTs without the use of any solvent. Homogeneously dispersed metal NPs with diameters in the range of 2–4 nm have been loaded on CNTs using MOCVD as summarized in Table 1. For the metal loading, a volatile salt of the metal catalyst is mixed with CNTs to form a homogeneous mixture [68]. The mixture is then heated in an inert atmosphere to a temperature that allows the salt to decompose and the metal NPs to deposit directly onto

CNTs [69]. Since MOCVD involves fewer preparation steps, the method can be used to produce homogeneously dispersed metal NPs on CNTs at large scale.

## 7. Dehydrogenation reactions over Pt/CNT and Ni/CNT catalysts

A number of functional groups are synthesized from dehydrogenation reactions over PGMs like Pt and Ni NPs supported on CNTs. In this section, some examples of dehydrogenation reactions are discussed.

### 7.1. Dehydrogenation of ethylbenzene (EB) to styrene over Ni/CNTs

Dehydrogenation of ethylbenzene is an essential industrial process used in the production of styrene, an intermediate used to manufacture polystyrene. A key issue in the dehydrogenation of ethylbenzene (EB) to styrene is selectivity of the catalyst to styrene and the styrene yield. The performance of Ni/CNT and Ni/AC used as catalysts for dehydrogenation of ethylbenzene (EB) to styrene was evaluated [18]. Ni/CNTs with a metal loading of 9.3 wt.% exhibited higher EB conversion (72%) than both Ni/CNTs with a metal loading of 13.1% and Ni/AC with a metal loading of 10.0%, which had EB conversions of 70.7 and 55.6% respectively. It was observed that both Ni/CNTs (9.3 wt.% of Ni) and Ni/CNTs (13.1 wt.%. of Ni) had higher styrene selectivity (83.1 and 82.5% respectively) than Ni/AC (10.0 wt.% of Ni) which showed styrene selectivity of 55.8%. However, Ni/CNT (13.1 wt.% of Ni) showed the highest styrene yield at 65.7% compared with Ni/CNTs (9.3 wt.% of Ni) which had a styrene yield of 62% and Ni/AC which had a styrene yield of 52.7%.

In general, Ni/CNTs exhibited higher styrene selectivity, styrene yield and EB conversion than Ni/AC. The superior catalytic activity of Ni/CNT catalysts can be attributed to the special curvature of CNTs which results in a partial Ni-carbon covalent bond with a charge transfer from carbon to nickel NPs supported on CNTs [87]. The charge transfer from carbon to nickel may contribute towards activating the Ni NPs leading to a higher activity rate. Guo *et al*. [10] also investigated the dehydrogenation of EB over Pd/CNT as a catalysts, in their studies Pd/CNT with 2 wt.% Pd loading was used for the dehydrogenation of EB in a flow time quartz reactor. It was observed that Pd/CNT conversion of EB was at 45.7%, which was higher than the conversion of EB over Pd loaded on $Al_2O_3$ (20.7%) and $SiO_2$ (35.6%). Interestingly, the percentage conversion of EB over Pd/CNTs (45.7%) was lower than that over metal-free CNTs (64%) reported by Su *et al*. [88]. Higher activity of metal free CNTs compared with Pd/CNTs can be due to deposition of carbon layers onto the metal catalyst

during the reaction. These layers activate metal-free CNTs while they could poison Pd/CNTs, lowering their activity. However, the conversion of EB over Pd/CNTs (45.7%) was also lower than conversion of EB over Ni/CNTs (72%) [18]. On the other hand, Pd/CNTs showed a higher selectivity to styrene (100%) compared with Ni/CNTs (83.1%). In general, both Ni/CNTs and Pd/CNTs exhibited higher activity than conventional metal oxides and carbonaceous catalyst supports as shown in Fig. 5. This higher activity is accredited to the high external surface of the metal/CNT which leads to a favourable mass transfer of the reactant to the active sites, leading to the existence of active sites. High selectivity to styrene obtained over CNT-supported catalysts could be attributed to strong electronic interactions and charge transfer between metal nanoparticle and CNTs leading to high binding energies. The presence of oxygenated functional groups on the surface of functionalized CNTs also played a role in enhancing the catalytic performance of metal/CNTs [89]. This can be attributed to the fact that oxygenated functional groups increase the surface defects on CNTs, thus increasing surface reactivity sites.

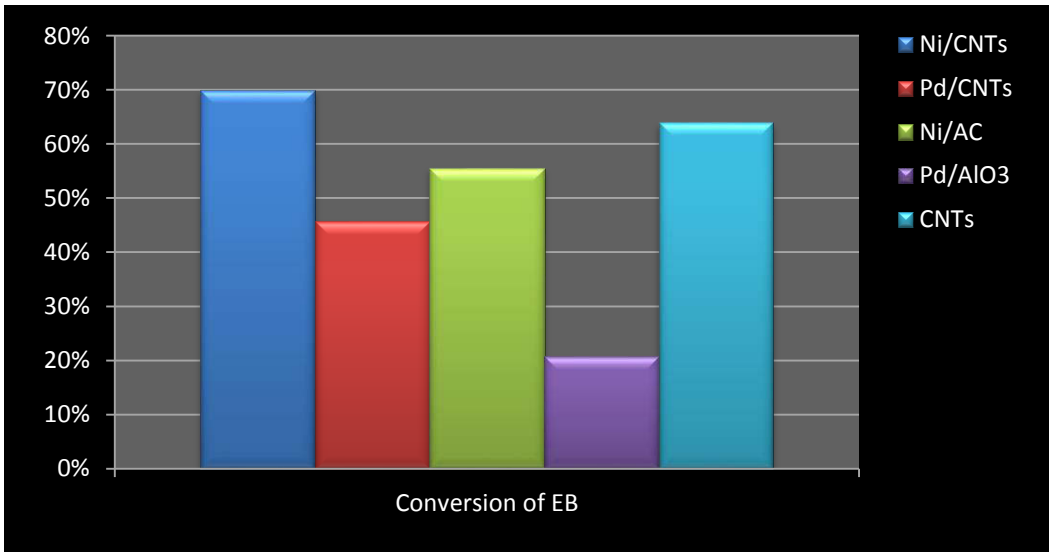


**Fig. 5**. Dehydrogenation of ethylbenzene over different metal-loaded support catalysts and different parameters.

### 7.2. Dehydrogenation of straight chain alkanes and alkenes

Dehydrogenation of straight chain alkanes to alkenes is widely applied in industries for large-scale alkene production. However this reaction is constrained by clashing reaction kinetic and thermodynamic limitations [90]. Different approaches are being studied to address these

constraints including use of CNTs as catalyst in an appropriate reactor. The application of metal/CNT hybrids as catalysts in alkane dehydrogenation has been under researched compared to application of metal free CNTs [91]. This could be attributed to the fact that CNTs on their own display an enhanced selectivity to alkenes compared with metal-based catalysts [92]. Conventionally, metals like Pt/Sn, Cr oxides and Fe oxides supported on alumina are used as catalysts in the dehydrogenation of alkanes. Frank *et al*. [93] demonstrated the catalytic activity of boron-oxygen-CNTs (B-oCNTs) and phosphorous-oxygen-CNTs (P-oCNTs) used in oxidative dehydrogenation of ethane. According to their findings, use of B-oCNT and P-oCNT catalysts drastically enhances oxidation resistance and increases ethene selectivity. Similarly, Zhang *et al*. [92] reported the high performance of P-oCNT as effective catalysts in oxidative dehydrogenation of n-butane to butene, and more so butadiene at 400 or 450 °C. In a different study, Sui *et al*. [94] showed that P-oCNT catalyst is effective in oxidative dehydrogenation of propane; they reported 42.07% propane conversion and 39.63% propene selectivity at 500 °C obtained using P-oCNT catalysts to yield high quantities of propene. Liu *et al*. [91] reported the dehydrogenation of 1-butene to butadiene over carbon nanotubes with no metal catalyst loaded. The catalytic activity of the CNTs was stable, higher and superior to metal catalyst supported on activated carbon and alumina. In general, a substantial amount of research has been conducted to conclude that surface modified CNT catalysts heighten oxidative dehydrogenation of straight chain alkanes and alkenes. The enhanced oxidative dehydrogenation of alkanes and alkenes over oxygen functionalized CNTs is attributed to oxygen groups like quinone and quinine attached to the surface of the functionalized CNTs [93]. Quinone groups attached to CNTs act as reaction sites where the alkanes are adsorbed, dehydrogenated then desorbed back upon reduction of the quinone to a hydroxyl group [91].

### 7.3. Dehydrogenation of ammonia–borane over Pt/CNT

Catalytic dehydrogenation of ammonia–borane (AB, $NH_3BH_3$) to obtain pure hydrogen is categorized as one of the efficient approaches of obtaining and storing hydrogen. Dehydrogenation of AB to release hydrogen occurs in three steps, *i.e.* the dehydrogenation of AB to polyaminoborane [PAB, $(NH_2BH_2)n$] and $H_2$, PAB to polyiminoborane [PIB, $(HNBH)n$] and $H_2$, and PIB to BN and $H_2$ [95]. Despite dehydrogenation of AB being a favourable source of hydrogen, challenges such as slow dehydrogenation kinetics, irreversibility and formation of poisonous borazine and ammonia by-products still need to be overcome. Li *et al*. [9] reported enhanced catalytic dehydrogenation properties of ammonia–

borane (AB) when Pt/CNT was used as a catalyst. The application of CNTs as Pt nanoparticle supports in dehydrogenation of AB resulted in better dehydrogenation activities and properties compared with use of Pt in various solutions [9]. This could be attributed to a combination of the synergetic catalysis of Pt/CNT NPs and nano-confinement of AB into CNT channels. The experimental results showed that dehydrogenation over Pt/CNTs occurred at lower temperature (70–190 °C) than pristine AB and significantly depressed formation of borazine the volatile by-product compared with use of Pt catalyst in various solutions [96]. Dehydrogenation reactions over Pt/CNTs were less exothermic (−2.6 kJ $mol^{-1}$) than that of pristine AB (−23.3 kJ $mol^{-1}$). The activation energy for releasing the first equivalent of hydrogen from the pristine AB (137.8 kJ $mol^{-1}$) was higher than that of AB-Pt/CNTs (~106.2 kJ $mol^{-1}$) indicating a considerable enhancement of the dehydrogenation kinetics of AB [9]. In general, nano-confinement of CNTs and nanostructure effects of CNTs activated the Pt NPs, leading to an improved dehydrogenation activity of AB. These advantages of using Pt/CNTs in AB dehydrogenation are a promising route to for production of molecular hydrogen from AB *via* a convenient renewable way.

### 7.4. Dehydrogenation of cyclohexane and methylcyclohexane

Industrial dehydrogenation of cyclohexane and methyl cyclohexane (MCH) is useful for hydrogen production and storage due to high efficiency and reversibility of the dehydrogenation reaction.

Forward reaction

$$\underset{\text{MCH}}{C_7H_{14}} \longrightarrow \underset{\text{Toluene}}{C_7H_8} + 3H_2$$

Reverse reaction:

$$C_7H_8 \longrightarrow \underset{\text{MCH}}{C_7H_{14}}$$

Conventionally, $Pt/Al_2O_3$ is used as a catalyst in commercial dehydrogenation of cyclohexane and methyl cyclohexane [4]. However, the use of $Pt/Al_2O_3$ is faced with many challenges, such as low catalytic efficiency, carbonaceous deposition and high reaction temperature [97]. Therefore, carbon nanomaterials are continuously being investigated as metal supports for this dehydrogenation process. Jian-Ping *et al*. [98] compared the activity of Pt/CNTs, Pt on hollow and mesoporous carbon NPs (Pt/HCNP and Pt/MCNP), Pt/AC and Pt/CB when used as catalysts in dehydrogenation of cyclohexane. Conversion of cyclohexane over Pt/HCNP and Pt/MCNP was noted to be higher than over Pt/AC and Pt/CB with the

same Pt loading, while conversion over Pt/CNTs was higher than over Pt/CB with similar Pt loading. Furthermore, the Pt/HCNP catalyst showed higher activity and stability than all other catalysts. The general cyclohexane percentage molar conversion followed the trend: Pt/HCNP > Pt/MCNP > Pt/AC > Pt/MWCNTs > Pt/CB, with the activity of Pt/MWCNT and Pt/CB staying at low levels with time on stream. The higher activity of Pt/HCNP was accredited to the presence of short hollow channels on HCNP which facilitated the diffusion of benzene coke formed during cyclohexane dehydrogenation thus, minimizing poisoning of the catalyst active sites [98]. Activated carbon and carbon black do not have such nano-channels hence their catalytic activity is reduced by poisoning of the active sites by benzene coke. The enhanced catalytic performance of CNP was also attributed to highly dispersed Pt NPs with smaller diameters on CNP compared to those of CNTs, AC and CB [98].

Investigations done by Wang *et al*. [74] revealed that Pt NPs supported on stacked-cone carbon nanotubes (SC-CNTs) were more active that commercial $Pt/Al_2O_3$ when used in cyclohexane and methyl cyclohexane dehydrogenation. Cyclohexane and methyl cyclohexane dehydrogenation to produce hydrogen was carried out in a fixed bed, plug-flow and stainless steel reactor. The catalytic activity and selectivity of 0.25 wt.% Pt/SC-CNTs was comparable with that of commercial 1 wt.% $Pt/Al_2O_3$ while 0.1 wt.% Pt/SC-CNTs showed a high activity and the highest efficiency for hydrogen production per metal atom. Selectivity for cyclohexane and methyl cyclohexane dehydrogenation was at 100% when 0.1–1.0 Pt/SC-CNT were used as catalysts. The percentage molar conversion of cyclohexane and hydrogen concentration produced over various catalysts decreased in the order 1% $Pt/Al_2O_3$ ≈ 1% Pt/SC-CNT ≈ 0.25% Pt/SC-CNT > 0.1% Pt/SC-CNT > 1% Pd/SC-CNT > SC-CNT. Similarly, the percentage molar conversion of methyl cyclohexane and percentage of hydrogen volume produced decreased in the order 1% $Pt/Al_2O_3$ ≈ 0.25% Pt/SC-CNT > 0.1% Pt/SC-CNT > 1% Pd/SC-CNT. Dispersion of the Pt catalyst on SC-CNTs remained high even after 6.5 h of dehydrogenation reaction while the dispersion of Pd on SC-CNTs was poor leading to lower activity rates. The activity of Pt was reported to reduce with time on stream, this can be attributed to formation of benzene and toluene coke on the active sites [74].

### 7.5. Dehydrogenation of tetralin and decalin

Cycloalkane dehydrogenation is documented as one appropriate way to store and supply pure hydrogen [19]. In addition, the aromatic by-products formed after dehydrogenation of cycloalkanes (benzene, toluene, naphthalene, *etc.*) can be re-hydrogenated to produce

cycloalkenes. Catalytic dehydrogenation of cycloalkanes is an endothermic reaction requiring high reaction temperatures; this is a major drawback to using cycloalkanes for hydrogen production. In addition, the produced aromatic by-products compete with the reactants for adsorption on the catalyst surfaces [99]. To overcome these drawbacks, studies have been conducted on the use of carbon NPs as supports for metal catalyst. Decalins (7.3 wt.% hydrogen storage capacity) and tetralins are good examples of cycloalkanes used for pure hydrogen production [19].

$$\underset{\text{Decalin}}{C_{10}H_{18}} \longrightarrow \underset{\text{Tetralin}}{C_{10}H_{12}} + 3H_2 \longrightarrow \underset{\text{Naphthalene}}{C_{10}H_8} + 5H_2$$

Direct dehydrogenation of decalins and tetralins is commonly performed over platinum and other precious metals supported on activated carbon (AC) due to the inertness of AC to side reactions. Wang *et al*. [14] studied the dehydrogenation of decalins and tetralins over Pt/SC-CNT. They also compared the dehydrogenation activity when Pt/SC-CNT was used with that of Pt, Pd, and Rh supported on carbonatious material and on alumina. It was observed that 1.0 wt.% Pt/SC-CNT catalyst showed the highest tetralin conversion (50.3%), with a hydrogen evolution rate of 5.31 mL $min^{-1}$. The highest hydrogen turnover frequency (TOF) for dehydrogenation of tetralin was observed with 0.25 wt.% Pt/SC-CNT catalyst. The trend in activity for dehydrogenation of tetralin was 1.0 wt.% Pt/SC-CNT > 1.0 wt.% $Rh/Al_2O_3$ > 1.0 wt.% $Pt/Al_2O_3$ > 1.0 wt.% $Pd/Al_2O_3$ [14].

For dehydrogenation of decalin (37.0% *cis* and 63.0% *trans*) 1.0 wt.% Pt/SC-CNT showed the highest conversion, while the Rh catalyst exhibited a lower conversion rate than when used in dehydrogenation of tetralins. In general the order of activity for decalin conversion was 1.0 wt.% Pt/SC-CNT > 1.0 wt.% $Pt/Al_2O_3$ > 1.0 wt.% $Rh/Al_2O_3$ > 1.0 wt.% $Pd/Al_2O_3$ [14]. Metal NPs supported on CNTs exhibited higher activity in the dehydrogenation of tetralins and decalins compared with metal NPs on $Al_2O_3$.

Since all catalysts used had similar metal loading percentages, the higher activity of Pt/SC-CNT can be attributed to relatively high surface area of SC-CNTs (~280 $m^2/g$) and the relatively high dispersion of Pt NPs. Pt NPs on SC-CNTs had diameters in the range of 2–4 nm, while the diameters of Pt NPs on commercial Pt/granular carbon and synthesized Pt/carbon black were (80–100 nm) and (10–15 nm) respectively [14]. The higher dehydrogenation activity of CNTs can also be attributed to favourable charge transfer from the carbon on CNTs to Pt NPs, which could have increased the activity of Pt on SC-CNT. In a similar manner, Lázaro *et al*. [19] investigated the catalytic activity of Pt/CNF for the dehydrogenation of decalins. For the dehydrogenation reaction, the catalytic activities of 1.5

wt.% Pt/CNF and 3 wt.% Pt/AC were compared. Despite Pt/AC having a higher surface area, pore volume and Pt loading than Pt/CNF which had a nine fold lower surface area, hydrogen production over Pt/CNF was found to be four fold higher than that over Pt/AC [19]. In addition, Pt/CNF was more resilient to deactivation compared with Pt/AC. This was evidenced through the gradual decrease of $H_2$ production over Pt/CNF as opposed to the rapid decrease in $H_2$ production over Pt/AC (*ca*. 50 min) [19]. CNF as metal catalyst support was seen to boost the activity of metal NPs in the dehydrogenation of cycloalkanes. The observed higher catalytic activity of Pt/CNF was ascribed to the higher dispersion of uniformly sized Pt NPs on CNF, compared to Pt NPs on AC. Additionally, high activity could be due to favourable electronic interactions between Pt and CNFs owing to the curvature of the CNF surface [87]. The faster deactivation rate of Pt/AC was due to poisoning of Pt/AC active sites during the reaction. AC contains micropores on its surface, since Pt is anchored on these micropores on AC, the carbonaceous by-products produced quickly fill this micro pores making the Pt NPs unavailable to the reactants. CNFs on the other hand have no micropores hence are more resilient to deactivation by carbonaceous by-products [19].

## 8. N-CNTs used as metal supports in selective dehydrogenation reactions

Doping CNTs with nitrogen has been shown to improve the specific surface reactivity properties of Pt/N-CNTs compared with Pt/CNTs [100]. Pt NPs loaded on N-CNTs display smaller diameters than those loaded on CNTs under similar synthesis conditions [101]. This implies that Pt/N-CNTs have a higher surface area compared with Pt/CNTs making them better catalysts. Furthermore, the size of the metal NPs loaded has been observed to be inversely proportional to the percentage of nitrogen incorporation [101]. The decrease in metal NP size loaded on N-CNTs can be attributed to enhanced surface properties such as wetness, structural defects and structural activity caused by nitrogen doping [100]. Doping CNTs with nitrogen increases the Pt nanoparticle stability on the surface of CNTs which in turn decreases metal nanoparticle migration and agglomeration in reactions [101]. Since nitrogen acts as an electron donor in N-CNTs, the extra electrons interact with the Pt nanoparticles [102] causing an increased binding energy of about 130.27 kJ $mol^{-1}$ between Pt NPs and N-CNTs [103]. An increase in percentage of nitrogen incorporation has been observed to increase further the stability of metal NPs on N-CNTs [101].

The dispersion of metal nanoparticles on CNTs has been shown to improve when CNTs are doped with nitrogen. Chen *et al*. [104] reported a better Ru dispersion on N-CNTs than on CNTs. The improved dispersion was ascribed to a decrease of Ru particle size with increase of nitrogen atom incorporation into the CNTs. Further, the presence of pyridinic nitrogen atoms in $sp^2$ hybridization states on N-CNTs allowed the un-bonded electron pair on nitrogen to complex with empty orbitals of $Ru^{3+}$ as a ligand. The formation of such a complex impeded $Ru^{3+}$ particle migration and surface diffusion resulting in lower Ru particle sintering during loading of Ru onto N-CNTs [105].

The presence of pyridinic nitrogen atoms in N-CNTs introduces basic properties onto N-CNTs surfaces [106]. As such N-CNTs containing mainly pyridinic nitrogen atoms have been reported to be effective base catalysts in reactions such as Knoevenagel condensation [107]. The application of metal free N-CNTs as a catalyst in the oxidative dehydrogenation of harmful $H_2S$ into elemental sulphur has been reported by Chizari *et al*. [108]. The desulfurization activity of N-CNTs was seen to increase when N-CNTs were supported on a silicon carbide macroscopic host. The increased desulfurization activity can be attributed to the basicity of N-CNTs and introduction of macroscopic shapes by bamboo compartment which resulted in increased interactions between the catalyst and the reactants [108]. A nitrogen doped-CNT catalyst showed high stability during the reaction even at high space velocity. Thus, N-CNTs can be applied as effective catalysts in other base catalyzed dehydrogenation reactions such as base catalyzed dehydrogenation of ammonia borane.

García-García *et al*. [109] analyzed the catalytic activity of Ru/N-CNTs and Ru/CNTs in decomposition of ammonia. They reported high yields of hydrogen production by both hybrid catalysts, with Ru/N-CNTs showing higher ammonia decomposition activity than Ru/CNTs. This findings concurs with those of Chen *et al*. [104] who also compared the catalytic activity of Ru/CNTs with that of Ru/N-CNTs in decomposition of ammonia. They reported that Ru/N-CNTs showed a higher activity than Ru/CNTs in terms of reaction rates. The higher catalytic activity of Ru/N-CNTs is attributed to the unique properties introduced into CNTs by nitrogen doping. Firstly, doping CNTs with nitrogen introduces basicity on N-CNTs and increases the electron density on N-CNTs. The increased basicity and electron density leads to activation of Ru NPs through electron transfer hence, increasing the activity of Ru/N-CNTs [109]. Secondly, the bamboo compartments introduced by nitrogen doping offers nano pores in which Ru NPs are confined, such confined NPs are possible sites for specific and improved catalytic behaviour [104]. Ovejero *et al*. [28] investigated the catalytic properties of Pt/N-CNT, Cu/N-CNT and Ru/N-CNT used in oxidation of aniline. Pt/N-CNTs

showed the highest activity with a general reactivity order of Pt/N-CNT > Cu/N-CNT > Ru/N-CNT, while, the conversion for the three catalysts decreased in the order Cu/N-CNT > Pt/N-CNT > Ru/N-CNT [28]. Although the use of N-CNTs as supports for metal catalysts significantly increases reaction activity, a number of industrial reactions have not been performed over metal/N-CNTs, some of which are listed in Table 2.

**Table 2**: Examples of dehydrogenation reactions in which the activity of Pt/N-CNT or Ni/N-CNT catalyst has not been investigated.

| Reaction | Catalyst Used | Ref. |
|---|---|---|
| dehydrogenation of paraffins to olefins | Pt, Pt-Sn | [5] |
| dehydrogenation of aliphatic amines to nitriles, imines or vinylamines | $Al_2O_3$, SiO2–$Al_2O_3$, MgO, Ga/MFI, In/MFI, Cu/MFI | [110] |
| dehydrogenation of 1,4-butanediol to γ-butyroloctane | Cu–Zn | [111] |
| | Cu–Zn–Al | [112] |
| dehydrogenation of cyclohexanol to cyclohexanone | Cu–Zn–Al | [113] |
| dehydrogenation of ethane to ethylene by $CO_2$ | Li/MgO | [114] |
| dehydrogenation of n-butanol to butylaldehyde | Cu–Zn–Ce | [115] |
| dehydrogenation of n-butanol to butylbutyrate | Cu–Zn–Ce | [115] |
| dehydrogenation of ethane to ethylene | Na/CaO | [116] |
| dehydrogenation of isobutane to isobutene | $NiO_x$/AC<br>$NiO/Al_2O_3$ | [117] |
| dehydrogenation propane to propene | $Pt/Al_2O_3$<br>$Pt/Fe_2O_3$ | [118] |

## 9. Conclusion

This review provided information on methods of loading metal NPs onto CNTs and N-CNTs. Findings from publications revealed that different methods used to load metal NPs onto CNTs and N-CNTs yield different sizes of metal NPs. It is however difficult to compare

these methods as different reaction conditions were used in different publications. Although numerous techniques have been exploited to load metal NPs onto CNTs, trends are towards the use of the MOCVD method, due to its simple work-up procedure. In addition, MOCVD can be used to load metal NPs onto CNTs and N-CNTs for commercial usage since it allows for modulation of synthesis parameters. However, more research needs to be done on how to increase the percentage of metal loading onto N-CNTs and B-CNTs.

Since alumina and AC have a higher surface area than most synthesized CNTs and N-CNTs, it would be expected that metal NPs supported on alumina and AC would show higher catalytic activity. However, this was not the case as reaction activity of Pt and Ni improved in terms of selectivity to product and reactant conversion when CNTs and N-CNTs were used as metal support compared with when AC or alumina supports. The enhanced catalytic performance of metal NPs over CNTs and N-CNTs can be attributed to the unique properties of CNTs and N-CNTs. Surface curvature of CNTs enhances the electronic properties of CNTs leading to electron and charge transfer from CNTs to metal NPs, thus promoting metal NP catalytic activity. Enhanced electronic properties of CNTs may also lead to formation of partial carbon-metal chemical bonds, which reduces metal NP migration and agglomeration leading to higher dispersion of metal NPs. The presence of hollow channels in CNTs also leads to nano-confinement of reactant molecules, which may result in improved specific catalytic behaviour. In some instances, the presence of hollow channels on CNTs facilitates quick diffusion of carbonaceous coke by-products from the catalyst active sites hence minimizing metal NP poisoning. Functionalization of CNTs with oxygen groups offers additional active sites where reactants can be dehydrogenated hence leading to synergetic catalysis between metal NPs and CNTs.

Metal NPs supported on N-CNTs showed better catalytic activity than metal NPs on CNTs. The overall order of metal support effectiveness was N-CNTs > CNTs > conventional supports. This can be attributed to increased electron density on N-CNTs, which increases basicity of N-CNTs and presence of protonated CNT-$N^+$:H sites. Increased basicity of N-CNTs enhances electron transfer from N-CNTs to metal NPs leading to activation of metal NPs and formation of chemical bonds between N-CNTs and metal NPs. The protonated CNT-$N^+$:H sites act as nucleation sites where metal NPs can also form chemical bonds with CNTs. Formation of such chemical bonds between metal NPs and N-CNTs improves metal support interactions, metal NP stability, dispersion and surface area. The morphology of N-CNTs (*i.e.* presence of bamboo and cup-end compartments) increases graphitization of N-CNTs and provides additional defect sites for anchoring metal NPs of high surface area. The

bamboo compartment also leads to improved specific reactions inside the compartments. Not much has been reported on application of metal/N or B-CNT catalysts in dehydrogenation reactions and application of functionalized N-CNTs and B-CNTs (such as oxygen or phosphorus functionalized N-CNTs and B-CNTs) as metal-free catalysts in dehydrogenation reactions hence more research is necessary in this area.

## Acknowledgements

This review was developed within the framework of the National Research Foundation (NRF) Nanotechnology Flagship Programme _Nano-architecture in the Beneficiation of Platinum Group Metals‘. We are grateful to Professors Tony Ford and Bice Martincigh for their insightful discussions on metal supports and for assisting with the proofreading of the manuscript.

## References

[1] Y. Li, D. Li, G. Wang, Catalysis Today 162 (2011) 1.

[2] N.A. Pakhomov, V.N. Kashkin, E.I. Nemykina, V.V. Molchanov, V.I. Nadtochiy, A.S. Noskov, Chemical Engineering Journal 154 (2009) 185.

[3] M. Ledoux, C. Pham-Huu, Catalysis Today 102–103 (2005) 2.

[4] M.R. Usman, Proceedings of the Pakistan Academy of Sciences 48 (2011) 13.

[5] M.M. Bhasin, J.H. McCain, B.V. Vora, T. Imai, P.R. Pujadó, Applied Catalysis A-General 221 (2001) 397.

[6] R.S. Oosthuizen, V.O. Nyamori, Platinum Metals Review 55 (2011) 154.

[7] J. Wang, G. Yin, Y. Shao, Z. Wang, Y. Gao, Journal of Physical Chemistry Letters 112 (2008) 5784.

[8] J. Wang, G. Yin, Y. Shao, Z. Wang, Y. Gao, Journal of the Electrochemical Society 154B (2007) 687.

[9] S.F. Li, Y.H. Guo, W.W. Sun, D.L. Sun, X.B. Yu, Journal of Physical Chemistry 114 (2010) 21885.

[10] X.-F. Guo, D.-Y. Jang, H.-G. Jang, G.-J. Kim, Catalysis Today 186 (2012) 109.

[11] X. Ji, R.O. Kadara, J. Krussma, Q. Chen, C.E. Banks, Electroanalysis 22 (2010) 7.

[12] H. Dai, Nanotube growth and characterization, in: M.S. Dresselhaus, G. Dresselhaus (Eds.), Carbon Nanotubes Synthesis, Structure, Properties and Applications, Springler-Verlag, Heidelberg, 2001, pp. 29-51.

[13] A. Loiseau, X. Blasé, J.-Ch. Charlier, P. Gadelle, C. Journet, Ch. Laurent, A. Peigney, Synthesis methods and growth mechanism, in: A. Loiseau, P. Launois, P. Petit, S. Roche, J.-P. Salvetat (Eds.), Understanding Carbon Nanotubes, Springer-Heidelberg, 2006, pp. 49–122.

[14] Y. Wang, N. Shah, F.E. Huggins, G.P. Huffman, Energy and Fuels 20 (2006) 2612.

[15] J. Nhut, R. Vieira, L. Pesant, J. Tessonnier, N. Keller, G. Ehret, C. Pham-Huua, M.J. Ledoux, Catalysis Today 76 (2002) 11.

[16] E. Auer, A. Freund, J. Pietsch, T. Tacke, Applied Catalysis A-General 173 (1998) 259.

[17] L. Zexiang, J. Shengfu, L. Hui, L. Chengyue, Chinese Journal of Chemical Engineering 16 (2008) 740.

[18] X. Guo, J. Kim, G. Kim, Catalysis Today 164 (2011) 336.

[19] M.P. Lázaro, E. García-Bordeje, D. Sebastián, M.J. Lázaro, R. Moliner, Catalysis Today 138 (2008) 203.

[20] P.D. Tien, T. Satoh, M. Miura, M. Nomura, Energy and Fuels 19 (2005) 2110.

[21] Y.-A. Lv, Y.-H. Cui, Y.-Z. Xiang, J.-G. Wang, X.-N. Li, Computation Materials Science 48 (2010) 621.

[22] A.K. Geim, K.S. Novoselov, Nature Materials 6 (2007) 183.

[23] M. Paradise, T. Goswami, Materials and Design 28 (2007) 1477.

[24] P. Singh, C. Samorì, F.M. Toma, C. Bussy, A. Nunes, K.T. Al-Jamal, C. Ménard-Moyon, M. Prato, K. Kostarelos, A. Bianco, Journal of Materials Chemistry 21 (2011) 4850.

[25] T. Guo, P. Nikolaev, A.G. Rinzler, D. Tomanek, D.T. Colbert, R.E. Smalley, Journal of Physical Chemistry 99 (1995) 10964.

[26] L.S. Ying, M.A. Bin Mohd Salleh, H.B. Mohamed Yusoff, S.B. Abdul Rashid, J.B.A. Razak, Journal of Industrial and Engineering Chemistry 17 (2011) 367.

[27] P.X. Hou, C. Liu, H.M. Cheng, Carbon 46 (2008) 2003.

[28] G. Ovejero, J.L. Sotelo, M.D. Romero, A. Rodríguez, M.A. Ocaña, G. Rodríguez, J. García, Industrial and Engineering Chemistry Research 45 (2006) 2206.

[29] U.M. Graham, A. Dozier, R.A. Khatri, M.C. Bahome, L.L. Jewell, S.D. Mhlanga, N.J. Coville, B.H. Davis, Catalysis Letters 129 (2009) 39.

[30] L. Jiang, L. Gao, Carbon 41 (2003) 2923.

[31] M. Tunckol, S. Fantini, F. Malbosc, J. Durand, P. Serp, Carbon 57 (2013) 209.

[32] S. Ya-Ping, F. Kefu, L. Yi, H. Weijie, Accounts of Chemical Research 35 (2002) 1096.

[33] L. Zhang, J. Yang, C.L. Edwards, L.B. Alemany, V.N. Khabashesku, A.R. Barron, Chemical Communications 3265 (2005) 3265.

[34] A. Hirsch, Angewandte Chemie International Edition in English 41 (2002) 1853.

[35] V.O. Nyamori, S.D. Mhlanga, N.J. Coville, Journal of Organometallic Chemistry 693 (2008) 2205.

[36] Y.-H. Li, T.-H. Hung, C.-W. Chen, Carbon 47 (2009) 850.

[37] P. Avouris, J. Chen, Materials Today 9 (2006) 46.

[38] A. Nieto-Márquez, D. Toledano, P. Sánchez, A. Romero, J.-L. Valverde, Journal of Catalysis 269 (2010) 242.

[39] S.A. Babanejada, R. Malekfara, S.M.R.S. Hosseini, Acta Physica Polonica A 116 (2009) 217.

[40] J.A. Amadou, K.A. Chizari, M.A. Houllé, I.A. Janowska, O.B. Ersen, D.A. Bégin, C.A. Pham-Huu, Catalysis Today 138 (2008) 62.

[41] G.-X. Chen, J.-M. Zhang, D.-D. Wang, K.-W. Xu, Physica B 404 (2009) 4173.

[42] L.F. Mabena, S.S. Ray, S.D. Mhlanga, N.J. Coville, Applied Nanoscience 1 (2011) 67.

[43] J. Li, M.J. Vergne, E.D. Mowles, W.-H. Zhong, D.M. Hercules, C.M. Lukehart, Carbon 43 (2005) 2883.

[44] R. Chetty, S. Kundu, W. Xia, M. Bron, W. Schuhmann, V. Chiril, W. Brandl, T. Reinecke, M. Muhler, Electrochimica Acta 54 (2009) 4208.

[45] E.N. Nxumalo, V.P. Chabalala, V.O. Nyamori, M.J. Witcomb, N.J. Coville, Journal of Organometallic Chemistry 695 (2010) 1451.

[46] F. Le Normand, J. Hommet, T. Szörényi, C. Fuchs, E. Fogarassy, Physical Review B 64 (2001) 2354161.

[47] M.I. Ionescu, Y. Zhang, R. Li, H. Abou-Rachid, X. Sun, Applied Surface Science 258 (2012) 4563.

[48] J. Hu, P. Yang, C.M. Lieber, Physical Review B 57 (1998) 3185.

[49] E.N. Nxumalo, V.O. Nyamori, N.J. Coville, Journal of Organometallic Chemistry 693 (2008) 2942.

[50] D. Geng, H. Liu, Y. Chen, R. Li, X. Sun, S. Ye, S. Knights, Journal of Power Sources 196 (2011) 1795.

[51] O.Y. Podyacheva, A.N. Shmakov, Z.R. Ismagilov, Carbon 52 (2013) 486.

[52] S. Taubert, K. Laasonen, Journal of Physical Chemistry C 116 (2012) 18538.

[53] I. Florea, O. Ersen, R. Arenal, D. Ihiawakrim, C. Messaoudi, K. Chizari, I.Janowska, C. Pham-Huu, Journal of the American Chemical Society 134 (2012) 9672.

[54] G. Vijayaraghavan, K.J. Stevenson, Langmuir 23 (2007) 5279.

[55] K. Chizari, I. Janowska, M. Houllé, I. Florea, O. Ersen, T. Romero, P. Bernhardt, M.J. Ledoux, C. Pham-Huu, Applied Catalysis A-General 380 (2010) 72.

[56] M. Scarselli, L. Camilli, P. Castrucci, F. Nanni, S. DelGobbo, E. Gautron, S. Lefrant, M.D. Crescenzi, Carbon 50 (2012) 875.

[57] E. Antolini, Applied Catalysis B: Environmental 88 (2009) 1.

[58] B. Wu, Y. Kuang, X. Zhang, J. Chen, Nano Today 6 (2011) 75.

[59] Z.B. He, J.H. Chen, D.Y. Liu, H.H. Zhou, Y.F. Kuang, Diamond and Related Materials 13 (2004) 1764.

[60] S.K. Cui, D.J. Guo, Journal of Colloid and Interface Science 333 (2009) 300.

[61] C.R. Carpenter, P.H. Shipway, Y. Zhu, Wear 271 (2011) 2100.

[62] B. Wen, S. Zhang, H. Fang, Rare Metals 30 (2011) 661.

[63] L. Qu, L. Dai, Journal of the American Chemical Society 127 (2005) 10806.

[64] F. Ye, X. Cao, L. Yu, S. Chen, W. Lin, International Journal of Electrochemical Science 7 (2012) 1251.

[65] X.H. Peng, J.Y. Chen, J.A. Misewich, S.S. Wong, Chemical Society Reviews 38 (2009) 1076.

[66] Y. Li, B. Zhang, X. Tang, Y. Xu, W. Shen, Catalysis Communications 7 (2006) 380.

[67] L. Piao, J. Chen, Y. Li, China Particuology 1 (2003) 266.

[68] J.-C. Hierso, R. Feurere, P. Kalck, Coordination Chemistry Reviews 178–180 (1998) 1811.

[69] V. Cominos, A. Gavriilidis, Applied Catalysis A-General 210 (2001) 381.

[70] L. Zhang, Z. Fang, G.-C. Zhao, X.-W. Wei, International Journal of Electrochem- ical Science 3 (2008) 746.

[71] X.X. Chen, N. Li, K. Eckhard, L. Stoica, W. Xia, J. Assmann, M. Muhler, W. Schuhmann, Electrochemistry Communications 9 (2007) 1348.

[72] B. Zhang, L.J. Chen, K.Y. Ge, Y.C. Guo, B.X. Peng, Chinese Chemical Letters 16 (2005) 1531.

[73] G.P. Huffman, N. Shah, Y. Wang, F.E. Huggins, Preprints of Papers-American Chemical Society, Division of Fuel Chemistry 49 (2004) 731.

[74] Y. Wang, N. Shah, G.P. Huffman, Energy and Fuels 18 (2004) 1429.

[75] H. Huang, W. Zhang, M. Li, Y. Gan, J. Chen, Y. Kuang, Journal of Colloid and Interface Science 284 (2005) 593.

[76] M. Yang, Y. Yang, Y. Liu, G. Shen, R. Yu, Biosensors and Bioelectronics 21 (2006) 1125.

[77] C. Liang, W. Xia, M. van den Berg, Y. Wang, H. Soltani-Ahmadi, O. Schlüter, R.A. Fischer, M. Muhler, Chemistry of Materials 21 (2009) 2360.

[78] V.O. Khavrus, A. Leonhardt, S. Hampel, C. Täschner, C. Müller, W. Gruner, S. Oswald, P.E. Strizhak, B. Büchner, Carbon 45 (2007) 2889.

[79] O.S.G.P. Soares, J.J.M. Órfão, M.F.R. Pereira, Industrial and Engineering Chemistry Research 49 (2010) 7183.

[80] C. Wang, G. Yi, H. Lin, Y. Yuan, International Journal of Hydrogen Energy 37 (2012) 14124.

[81] M.S. Saha, R. Li, X. Sun, Journal of Power Sources 177 (2008) 314.

[82] T. Maiyalagan, B. Viswanathan, U.V. Varadaraju, Electrochemistry Communications 7 (2005) 905.

[83] Y. Li, G.-H. Lai, R.-X. Zhou, Applied Surface Science 253 (2007) 4978.

[84] W. Li, X. Wang, Z. Chen, M. Waje, Y. Yan, Journal of Physical Chemistry B 110 (2006) 15353.

[85] J. Prabhuram, T.S. Zhao, Z.K. Tang, R. Chen, Z.X. Liang, Journal of Physical Chemistry B 110 (2006) 5245.

[86] X. Zhao, W. Li, L. Jiang, W. Zhou, Q. Xin, B. Yi, G. Sun, Carbon 42 (2004) 3251.

[87] M. Menon, A.N. Andriotis, G.E. Froudakis, Chemical Physics Letters 320 (2000) 425.

[88] D.S. Su, J.J. Delgado, N. Keller, G. Mestl, M.J. Ledoux, R. Schlögl, Catalysis Today 102–103 (2005) 110.

[89] J.J. Delgado, X. Chen, J.P. Tessonnier, M.E. Schuster, E. Del Rio, R. Schlögl, D.S. Su, Catalysis Today 150 (2010) 49.

[90] D. Sanfilippo, I. Miracca, Catalysis Today 111 (2006) 133.

[91] X. liu, D.S. Su, R. Schlögl, Carbon 46 (2008) 547.

[92] J. Zhang, X. Liu, R. Blume, A. Zhang, R. Schlögl, D.S. Su, Science 322 (2008) 73.

[93] B. Frank, M. Morassutto, R. Schomäcker, R. Schlögl, D.S. Su, ChemCatChem 2 (2010) 644.

[94] Z.-J. Sui, J.-H. Zhou, Y.-C. Dai, W.-K. Yuan, Catalysis Today 106 (2005) 90.

[95] M.A. Wahab, H. Zhao, X.D. Yao, Frontiers of Chemical Science and Engineering 6 (2012) 27.

[96] R.P. Shrestha, H.V.K. Diyabalanage, T.A. Semelsberger, K.C. Ott, A.K. Burrell, International Journal of Hydrogen Energy 34 (2009) 2616.

[97] E. Newson, H.T.P. Hottnger, R.F. Von, G.W. Scherer, T.H. Schucan, International Journal of Hydrogen Energy 23 (1998) 905.

[98] D. Jian-Ping, S. Chang, S. Jin-Ling, Z. Jiang-Hong, Z. Zhen-Ping, Journal of Fuel Chemistry and Technology 37 (2009) 468.

[99] A.C. Cooper, L.D. Bagzis, K.M. Campbell, G.P. Pez, Preprints of Papers-American Chemical Society, Division of Fuel Chemistry 50 (2005) 271.

[100] R.L.M.S. Saha, X. Sun, S. Ye, Electrochemistry Communications 11 (2009) 438.

[101] J.W.Y. Chen, H. Liu, R. Li, X. Sun, S. Ye, S. Knights, Electrochemistry Communications 11 (2009) 2071.

[102] A.S.-E.F. Coloma, J.L.G. Fierro, F. Rodríguez-Reinoso, Langmuir 10 (1994) 790.

[103] W.A.C.H. Turner, Journal of Physical Chemistry C 113 (2009) 7069.

[104] J.L. Chen, Z.H. Zhu, S.B. Wang, Q. Ma, V. Rudolph, G.Q. Lu, Chemical Engineering Journal 156 (2010) 404.

[105] H. Clavié, J.L. Petersen, S.P. Nolan, Journal of Organometallic Chemistry 691 (2006) 5444.

[106] S. van Dommele, K.P. de Jong, J.H. Bitter, Chemical Communications 4859 (2006) 4859.

[107] L. Wang, H. Jin, N. Bing, Catalysis Communications 15 (2011) 78.

[108] K. Chizari, A. Deneuve, O. Ersen, I. Florea, Y. Liu, D. Edouard, I. Janowska, C. Pham-Huu, ChemSusChem 5 (2012) 102.

[109] F.R. García-García, J. Àlvarez-Rodríguez, I. Rodríguez-Ramos, A. Guerrero- Ruiz, Carbon 48 (2010) 267.

[110] S. Kamiguchi, A. Nakamura, A. Suzuki, M. Kodomari, M. Nomura, Y. Iwasawa, T. Chihara, Journal of Catalysis 230 (2005) 204.

[111] Y.L. Zhu, H.W. Xiang, G.S. Wu, L. Bai, Y.W. Li, Chemical Communications (2002) 254.

[112] J. Yang, H.Y. Zheng, Y.L. Zhu, G.W. Zhao, C.H. Zhang, B.T. Teng, Catalysis Communications 5 (2004) 505.

[113] H.Y. Zheng, Y.L. Zhu, L. Huang, Z.Y. Zeng, H.J. Wan, Y.W. Li, Catalysis Communications 9 (2008) 342.

[114] L. Xu, S. Xie, S. Liu, L. Lin, Z. Tian, A. Zhu, Fuel 81 (2002) 1593.

[115] D. Zhang, H. Yin, R. Zhang, J. Xue, T. Jiang, Catalysis Letters 122 (2008) 176.

[116] E.V. Kondratenko, O. Ovsitser, Angewandte Chemie International Edition 47 (2008) 3227.

[117] J.F. Ding, Z.F. Qin, X.K. Li, G.F. Wang, J.G. Wang, Journal of Molecular Catalysis A: Chemical 315 (2010) 221.

[118] M.V.S. Annaland, H.A.R. Scholts, J.A.M. Kuipers, W.P.M.V. Swaaij, Chemical Engineering Science 57 (2002) 833.

# CHAPTER THREE

# MECHANOCHEMICAL SYNTHESIS AND SPECTROSCOPIC PROPERTIES OF 1,1′-FERROCENYLDIACRYLONITRILES: THE EFFECT OF *PARA*-SUBSTITUENTS

*Journal of Coordination Chemistry*, 2014
Vol. 67, No. 11, 1905–1922, http://dx.doi.org/10.1080/00958972.2014.931946

Taylor & Francis
Taylor & Francis Group

## Mechanochemical synthesis and spectroscopic properties of 1,1′-ferrocenyldiacrylonitriles: the effect of *para*-substituents

LUCY M. OMBAKA, PATRICK G. NDUNGU, BERNARD OMONDI and VINCENT O. NYAMORI*

School of Chemistry and Physics, University of KwaZulu-Natal, Durban, South Africa

(*Received 18 November 2013; accepted 1 May 2014*)

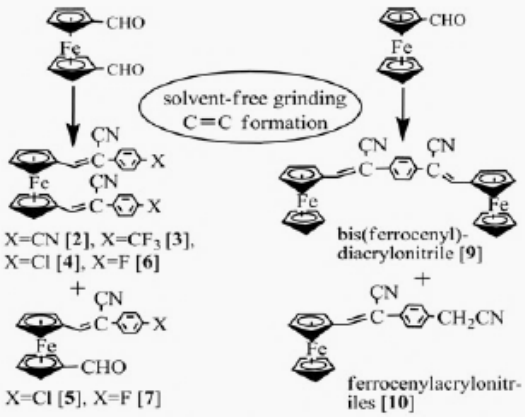


Mechanochemical synthesis of ferrocenylacrylonitriles.

An efficient and simple solvent-free mechanochemical approach for the synthesis of 1,1′-ferrocenyldiacrylonitriles was achieved by grinding together 1,1′-ferrocenedicarboxaldehyde (**1**) and phenylacetonitriles. A range of 1,1′-ferrocenyldiacrylonitriles and ferrocenylacrylonitriles (**2**–**7**) were

**Supplementary material**

The supplementary material for Chapter three is indexes as Appendix 1 located at the end of the thesis.

# Mechanochemical synthesis and spectroscopic properties of 1,1′-ferrocenyldiacrylonitriles: the effect of *para*-substituents

LUCY M. OMBAKA, PATRICK G. NDUNGU, BERNARD OMONDI and VINCENT O. NYAMORI*

School of Chemistry and Physics, University of KwaZulu-Natal, Durban, South Africa

## Abstract

An efficient and simple solvent-free mechanochemical approach for the synthesis of 1,1′-ferrocenyldiacrylonitriles was achieved by grinding together 1,1′-ferrocenedicarboxaldehyde (**1**) and phenylacetonitriles. A range of 1,1′-ferrocenyldiacrylonitriles and ferrocenylacrylonitriles (**2**–**7**) were synthesized within short reaction times, with water as the only by-product. In a similar manner, grinding together ferrocenemonocarboxaldehyde (**8**) and phenylenediacetonitrile yielded phenylene-3,3′-*bis*-(ferrocenyl)diacrylonitrile (**9**) and 3-ferrocenyl-2-(acetonitrophenyl)acrylonitrile (**10**). The yield and selectivity towards formation of ferrocenyldiacrylonitriles was strongly influenced by the electronegativity of the *para*-substituent on the phenyl ring of phenylacetonitriles. The compounds were characterized using NMR, IR, and UV–visible spectroscopy and HR-MS. Cyclic voltammetry measurements of selected compounds highlighted the role of ligands in tuning the electrochemical properties of 1,1′-ferrocenyldiacrylonitriles. X-ray crystallographic analysis highlighted the effect of the electronegativity of the *para*-substituent on the conformation of cyclopentadienyl rings attached to a ferrocenyl moiety.

Keywords: 1,1′-Ferrocenyldiacrylonitriles; 1,1′-Ferrocenedicarboxaldehyde; Solvent-free; Green chemistry; Mechanochemical

*Corresponding author. Email: nyamori@ukzn.ac.za

## 1. Introduction

Solvent-free synthesis of compounds is a growing research field in the quest for greener synthetic processes [1]. Mechanochemical synthesis of organometallic compounds, under solvent-free conditions, is of particular interest since a number of reactions can occur in the solid state [2], thereby eliminating the use of toxic solvents and reducing the overall cost of the synthesis [1]. Compared to reactions in solvents, solvent-free reactions take a shorter reaction time, exhibit higher atom economy, and allow for easier product isolation [3]. Although, numerous synthetic procedures used to synthesize compounds have been explored under solvent-free conditions [4], they remain relatively unexploited in the synthesis of ferrocenyl derivatives.

Mono- and di-substituted ferrocenyl derivatives containing substituted phenyl rings are good examples of ferrocenyl derivatives that can be synthesized via a solvent-free approach. In these compounds, the ferrocenyl moiety is an electron donor while the attached ligand is a $\pi$-electron acceptor. Such ferrocenyl derivatives are potential new materials with desirable properties for application in various fields. They could be useful in fluorescence [5], nonlinear optical devices [6], electron transfer processes [7], electrochromic devices [8], medicinal applications [9] and even as catalysts in the synthesis of shaped carbon nanomaterials such as carbon nanotubes (CNTs) [10]. Research geared towards the synthesis of nitrogen-doped carbon nanotubes (N-CNTs) using nitrogen-containing organometallic compounds as catalysts is of interest [11–13]. The incorporation of nitrogen into the graphene structure of CNTs (i.e. doping CNTs with nitrogen) has been reported to enhance both the electronic and physical properties of CNTs [14]. Hence, nitrogen-containing ferrocenyl derivatives such as 1,1′-ferrocenyldiacrylonitriles are potential organometallic catalysts for the synthesis of N-CNTs.

Under mechanochemical conditions, di- and mono-substituted ferrocenyl derivatives can be synthesized from condensation of 1,1′-ferrocenedicarboxaldehyde and ferrocenemonocarboxaldehyde, respectively, with other compounds. For example, 1,1′-ferrocenyldiimines were synthesized from the condensation of 1,1′-ferrocenedicarboxaldehyde and aromatic amines [15], while ferrocenylimines were synthesized by the condensation of ferrocenemonocarboxaldehyde and aromatic amines [16]. Similarly, *bis*-ferrocenylethenes and *bis*-ferrocenylimines have been synthesized by condensation of ferrocenemonocarboxaldehyde with phosphonium salts [17] and diaminoalkanes [18], respectively.

Although the mechanochemical reactions of 1,1′-ferrocenedicarboxaldehyde have been reported [15], the synthesis of 1,1′-ferrocenyldiacrylonitriles, in particular, has not yet been reported. In this study, a simple and efficient solvent-free procedure for synthesis of 1,1′-ferrocenyldiacrylonitriles and *bis*-ferrocenyldiacrylonitrile was achieved by mechanochemical grinding of solid reactants to obtain the desired product. Additionally, the spectroscopic, electrochemical, and X-ray crystallographic analyses of selected compounds are also discussed.

## 2. Results and discussion

### 2.1. Synthesis of 1,1′-ferrocenyldiacrylonitriles

Grinding together 1,1′-ferrocenedicarboxaldehyde **1** and substituted phenylacetonitriles in the presence of catalytic amounts of piperidine yielded a range of 1,1′-ferrocenyldiacrylonitriles (**2**, **3**, **4**, and **6**) and ferrocenylcarboxacrylonitriles (**5** and **7**) as depicted in scheme 1.

Different mole ratios of 1 : phenylacetonitrile (ca. 1 : 2 and 1 : 2.2) were used and it was noted that a mole ratio of 1 : 2.2 gave products in higher isolated product yields. Generally, the mixture containing the starting materials readily turned into a melt or a gum upon grinding at ambient temperatures. The obtained melt or gum was dried under vacuum, and IR and $^{1}$H NMR spectroscopy were used to confirm reaction completion. Formation of 1,1′-ferrocenyldiacrylonitriles was marked by disappearance of a sharp IR absorption band at ≈1650 cm$^{-1}$ (CHO) and the appearance of a strong nitrile absorption at ≈2200 cm$^{-1}$. From $^{1}$H NMR spectra, the formation of 1,1′-ferrocenyldiacrylonitriles was marked by the disappearance of a carbonyl proton resonance peak (≈10 ppm) and the appearance of an ethylene proton resonance peak (≈7.4 ppm).

The synthesis of 1,1′-ferrocenyldiacrylonitriles involved two mechanistic steps (scheme 2). First, the methylene carbon on the phenylacetonitriles was deprotonated by piperidine. Second, a Knoevenagel condensation occurred between the anionic methylene carbon and the carbonyl carbon [19].

Selectivity towards ferrocenyldiacrylonitrile formation showed a dependence on the electronegativity of the *para*-substituent on the phenyl rings. For example, *para*-substituted phenyl rings containing more electronegative groups (CN and $CF_3$) selectively

formed only 1,1′-ferrocenyldiacrylonitriles (**2** and **3**) as depicted in table 1. In contrast, the relatively less electronegative substituents (Cl and F) in the *para*-position of the phenyl ring formed both 1,1′-ferrocenyldiacrylonitriles (**4** and **6**) and ferrocenyl-carboxyacrylonitriles (**5** and **7**). This could imply that more electronegative groups stabilize the deprotonated methylene intermediate (scheme 2) more than the relatively less electronegative groups leading to selective formation of 1,1′-ferrocenyldiacrylonitriles. The stronger electronegative substituents (CN and $CF_3$) also gave larger isolated product yields compared to relatively less electronegative substituents (Cl and F). The higher isolated yields (74-78%) were comparable to those of similar compounds synthesized from 1,1′-ferrocenedicarboxaldehyde in solvents [20, 21].

Interestingly, the *para*-Cl substituted phenylacetonitrile formed ferrocenyldiacrylonitrile (**4**) as the major product, while the *para*-F equivalent did not form ferrocenyldiacrylonitrile (**6**) as the major product (table 1). This observation may suggest that the *para*-Cl substituent was more reactive than the *para*-F substituent. It is plausible that the activity difference of

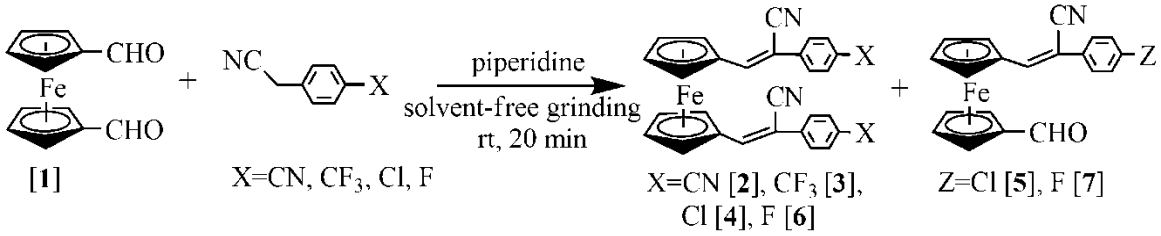


Scheme 1. Mechanochemical synthesis of 1,1′-ferrocenyldiacrylonitriles and ferrocenylcarboxacrylonitriles under solvent-free conditions.

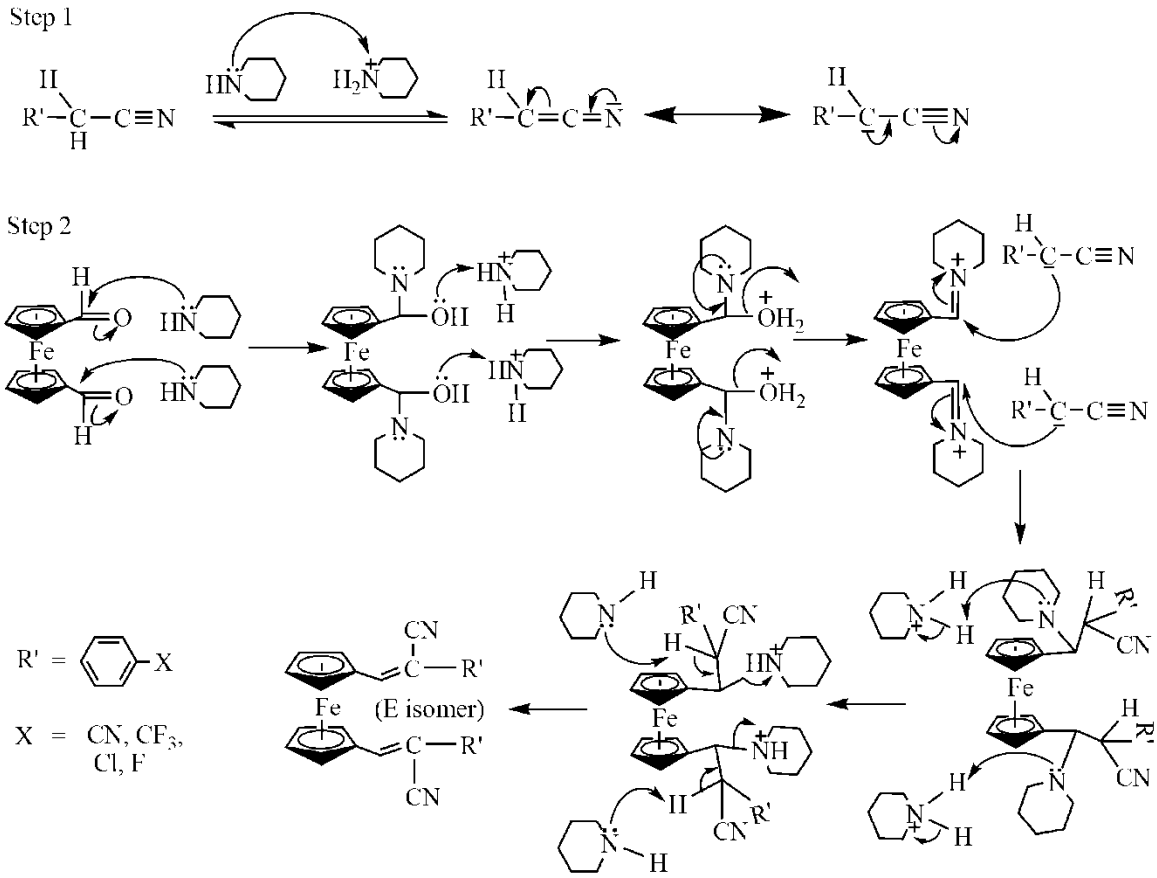


Scheme 2. Plausible reaction mechanism for formation of 1,1′-ferrocenyldiacrylonitriles.

Scheme 3. Mechanochemical reactions of 8 and phenylenediacetonitrile under solvent-free conditions.

*para*-Cl and -F substituents may be attributed to the electronegativity dipole and resonance dipole of chlorine versus fluorine when attached to a phenyl carbon [15]. Fluorine is more electronegative than chlorine and has an efficient 2p orbital that overlaps with carbon resulting in a strong resonance dipole, however, the two dipoles cancel out leading to a net dipole

of zero [22]. In the case of the chlorine substituent, with inefficient 3p–2p orbital overlap with carbon (thus resulting in a weak resonance dipole), the electronegativity dipole

Table 1. Isolated yields of 1,1′-ferrocenyldiacrylonitriles and ferrocenylacrylonitrile.*

| Compound | *Para*-substituent | Yield (%) |
|---|---|---|
| **2** | CN | 74 |
| **3** | $CF_3$ | 78 |
| **4** | Cl | 52 |
| **5** | Cl | 10 |
| **6** | F | 7 |
| **7** | F | 24 |

*Isolated yields based on 1 as the limiting reagent.

dominates over the resonance dipole leading to a net electron-withdrawing effect. Hence, the *para*-Cl substituent on the phenyl ring could give a more stable intermediate, which leads to better selectivity towards 1,1′-ferrocenyldiacrylonitrile formation, and higher isolated yields than for the *para*-F substituent.

## 2.2. Mechanochemical reactions of ferrocenemonocarboxaldehyde and phenylenediacetonitrile

*Bis*-metallocenyl compounds can be synthesized by attaching two metallocenyl moieties to a bidentate ligand or addition of another metallocene to a monodentate metallocenyl derivative. For example, Braga *et al*. [23] reported the synthesis of *bis*-ferrocenyl complexes by reacting ferrocenyl derivatives with transition metal salts. In this report, we utilize a mechanochemical approach to attach two ferrocenyl moieties to a bidentate ligand (phenylenediacetonitrile). Grinding together ferrocenemonocarboxaldehyde **8** and phenylenediacetonitrile in the presence of 1-2 drops of piperidine, and at ambient temperatures, gave phenylene-3,3′-*bis*-(ferrocenyl)diacrylonitrile **9** and 3-ferrocenyl-2-(acetonitrophenyl)acrylonitrile **10** (scheme 3).

To determine whether the reactions leading to formation of **9** and **10** were complete, $^{1}$H- and $^{13}$C NMR spectroscopy was used. From the $^{1}$H NMR spectrum, formation of **9** was marked by the disappearance of a carbonyl proton resonance (≈10 ppm) and the

appearance of an ethylene proton resonance (≈7.43 ppm). Similarly, formation of **10** was marked by the disappearance of a carbonyl proton resonance (≈10 ppm) and the appearance of an ethylene proton resonance (≈7.59 ppm) and a methylene resonance peak (≈3.75 ppm). From the $^{13}C$ NMR spectrum, the conspicuous absence of a strong carbonyl carbon resonance (≈190 ppm) marked the formation of either **9** or **10**.

To optimize the reaction conditions, different mole ratios of **8** : phenylenediacetonitrile (ca. 1 : 1, 1.4 : 1 and 2 : 1) were used. Among the three sets of mole ratios used, a mole ratio of 1.4 : 1 gave the highest yield. Since phenylenediacetonitrile was the limiting reagent, a mole ratio of 1.4 : 1 that contains an excess of phenylenediacetonitrile resulted in higher conversions of **8**-**9** and **10**. In all cases, the major product obtained was **9** while the minor product was **10**. Generally, the reaction occurred within 5-10 min of grinding. This could imply that under solvent-free conditions, phenylenediacetonitrile is less reactive than phenylacetonitrile which immediately reacts with **8** at room temperature [15]. Longer reaction times (≈20 min) favoured production of **9**, while shorter reaction times (≈5 min) yielded almost equivalent quantities of **9** and **10**. Thus, longer reaction periods allow for greater conversion of **10** into **9** until equilibrium is attained.

### 2.3. UV-visible spectroscopy

UV-visible absorption spectra of selected compounds are shown in figure 1 and the peak absorption data are summarized in table 2. All compounds exhibit absorptions in the UV and visible regions attributed to $\pi$–$\pi^*$ ligand-centered transitions and metal-ligand centered transitions, respectively [24]. A shoulder was observed in the absorption spectra of di-substituted 1,1′-ferrocenyldiacrylonitriles (**2**, **3**, and **4**, i.e. 313, 301, and 302 nm, respectively, table 2 and figure 1). In **10** and related mono-substituted ferrocenylacrylonitriles [15], similar shoulders were not observed. This could imply that electronic interactions occur between the two ligands attached to a single ferrocenyl moiety in di-substituted 1,1′-ferrocenyldiacrylonitriles. Substitution of the ferrocenyl electron donor with phenylacrylonitriles resulted in a significant red-shift of the absorption peaks. Comparison of **2**, containing a more electronegative *para*-substituent, with **4**, containing a less electronegative *para*-substituent, shows that **2** is more red-shifted than **4** (table 2). This implies that stronger electron-withdrawing groups on the phenyl *para*-position increase the electronic interactions between the ligands and the ferrocenyl moiety metal center, resulting in a

greater red-shift [25]. A comparison of **2**, containing one ferrocenyl moiety, and **9**, containing two ferrocenyl moieties, shows that **9** has a larger red-shift. Compound **9**, that exhibited a strong absorption in the UV region, has previously been reported for application in optical recording materials [26]. Thus, **2** which showed a more intense absorption in the UV region can be investigated for possible applications in optical recording materials.

The solvatochromic behaviors of **2**, **3**, and **4** were recorded in DMF, acetonitrile, and DCM (table 3). All three compounds exhibited a red-shift upon an increase of solvent

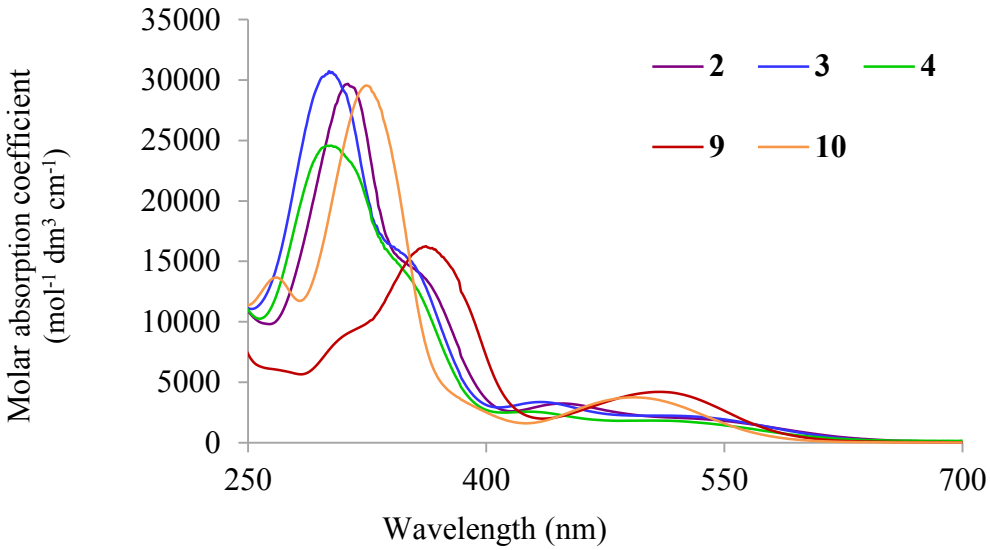


Figure 1. UV–visible spectra of **2**, **3**, **4**, **9**, and **10** in acetonitrile.

Table 2. Maximum absorption wavelength and corresponding molar absorption coefficients in acetonitrile.

| Compound | $\lambda_{max}$/nm ($\varepsilon_{max}$/mol$^{-1}$ dm$^3$ cm$^{-1}$) | | |
|---|---|---|---|
| ferrocene [38] | 435 (1276) | 324 (1120) | |
| **2** | 514 (2095) | 447 (3244) | 313 (29 679) |
| **3** | 506 (2244) | 434 (3367) | 301 (30727) |
| **4** | 505 (1831) | 427 (2567) | 302 (24 572) |
| **9** | 509 (4206) | 362 (16 251) | |
| **10** | 494 (3753) | 324 (29 537) | |

Table 3. Maximum absorption wavelength of selected 1,1′-ferr- ocenyldiacrylonitriles in DMF, dichloromethane, and acetonitrile.

| Compound | $\lambda_{max}$/nm | | |
|---|---|---|---|
| | DMF | DCM | Acetonitrile |
| **2** | 491 | 454 | 447 |
| | 319 | 317 | 313 |
| **3** | 469 | 436 | 434 |
| | 310 | 304 | 301 |
| **4** | 460 | 428 | 427 |
| | 355 | 313 | 302 |

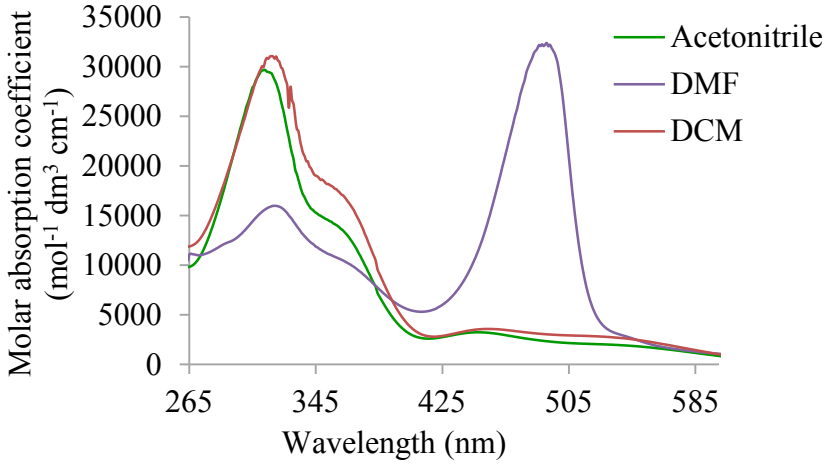


Figure 2. UV–visible spectra of **2** in acetonitrile, DMF, and dichloromethane.

polarity with **2** showing the greatest shift (figure 2). Thus, the electronegativity of the phenyl *para*-substituent influenced the dispersion interactions and the dipole-dipole interactions between the compounds and solvents [27]. Since all three compounds exhibited solvatochromic behavior, they are potentially useful for nonlinear optical studies [28].

### 2.4. Cyclic voltammetry

The redox potentials of selected compounds (table 4) showed a reversible or quasi-reversible [29] redox process within a potential range of $E_{p½} = 600 - 850$ mV. Reversibility was taken to imply that the peak potential separation ($\Delta E_p = E_{pa} - E_{pc}$) was 80 mV or less, and that the peak current ratio ($i_{pa}/i_{pc}$) was approximately one.

Table 4. Redox potentials of ferrocene and selected 1,1′-ferrocenyldiacrylonitriles.

| Compound | $E_{pa}$(mV) | $E_{pc}$(mV) | $\Delta E_p$(mV) | $p_2^1$ (mV) |
|---|---|---|---|---|
| ferrocene **[39]** | 516 | 401 | 115 | 459 |
| **2** | 859 | 818 | 41 | 839 |
| **3** | 879 | 798 | 81 | 839 |
| **4** | 834 | 763 | 71 | 799 |
| **9** | 718 | 582 | 136 | 650 |
| **10** | 657 | 592 | 65 | 624 |

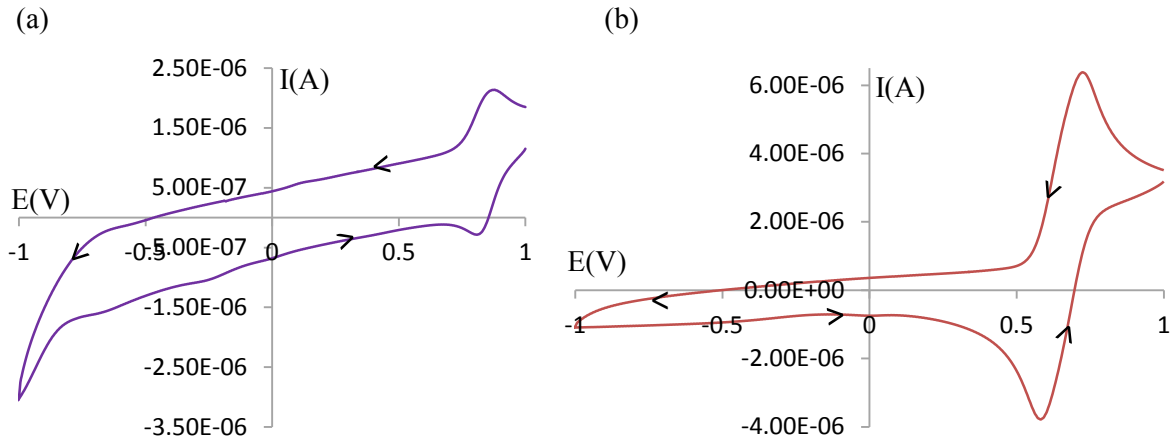


Figure 3. Cyclic voltammograms of (a) **2** and (b) **9** at a platinum working electrode, silver/silver chloride reference electrode, and at a scan rate of 100 mV $s^{-1}$ in acetonitrile.

A single reversible or quasi-reversible oxidation peak (figure 3) was observed associated with ferrocenium-ferrocene oxidation ($Fc^+$/Fc) [30]. A positive shift of the ferrocenyl redox potential was noted for substituted ferrocenyl compounds compared to free ferrocene [31].

A comparison of **2** and **4**, which differ only in their phenyl *para*-substituent, shows that *para*-CN caused a more positive shift in the redox potential of the ferrocenyl moiety compared to *para*-Cl. This implies that, as the electronegativity of the *para*-substituent increases, the positive charge on iron increases making the ferrocenyl moiety harder to oxidize [32].

Compound **2**, containing two ligands on one ferrocenyl moiety, showed a more positive redox potential than **9** which has two ferrocenyl moieties attached to one ligand. Thus, attaching two ligands onto one ferrocenyl moiety increased the donor-acceptor coupling, making it harder to oxidize the ferrocenyl moiety [33]. This can also be attributed to

a stronger electron-withdrawing effect of the ligands on the ferrocenyl moiety in **2** than in **9** [34]. Compounds **2**, **9**, and **10** showed different redox peak separation values ($\Delta_p = {}_{pa} - {}_{pc}$) indicating that the electron transfer processes and HOMO–LUMO gaps can be influenced by the number of π-acceptor ligands attached to the ferrocenyl moiety. Compound **2** has a lower $\Delta E_p$ value (41 mV) compared to that of **9** (136 mV). This could suggest that, attaching two π-electron-acceptors to one ferrocenyl moiety (**2**) increases the electron transfer process while, attaching two ferrocenyl moieties to a single *π*-electron-acceptor depresses the electron transfer process. Consequently, **9** can be studied further for applications in electron transfer processes such as molecular switches [33].

### 2.5. X-ray crystallography

The molecular structures of **2** and **4** are shown in figure 4(a) and (b), respectively, along with the atom numbering scheme. Selected bond distances and angles are compared in table 5. The two compounds are isomorphous; the difference being mainly in the β angle of 119.733(3)° in **2** and 108.902(4)° in **4**. The molecular structure of **2** features two cyanoethyl benzonitrile groups attached to two cyclopentadienyl rings of the ferrocenyl moiety in a slightly twisted fashion as opposed to the energetically favored trans conformation. In the structure of **4**, a Cl replaces both the *p*-cyano groups but also maintains the *cis* conformation.

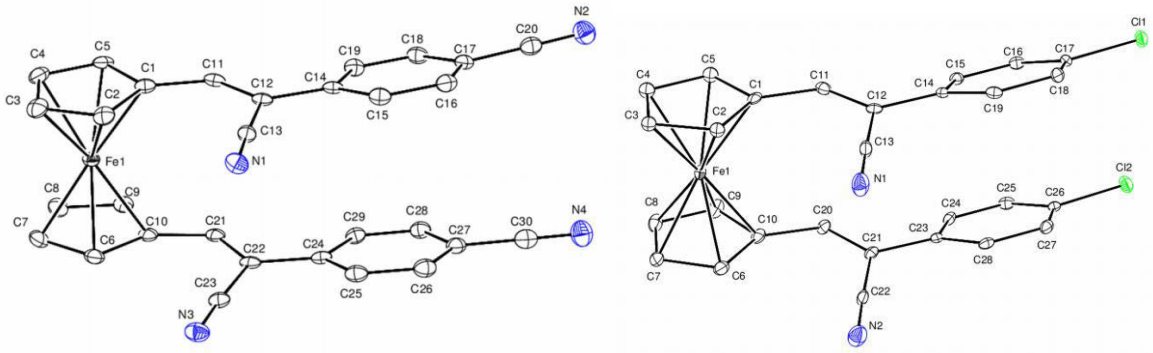


(a) (b)

Figure 4: ORTEP diagram along with the atom-numbering scheme for (a) **2** and (b) **4**. Ellipsoids are drawn at 50% probability level. Hydrogens have been omitted for clarity.

The *para*-substituents play a role in the conformations of the cyclopentadienyl rings of

the two compounds where in **2** they are staggered by 15.85(3)° from an ideal eclipsed geometry while in **4**, they have an eclipsed geometry, twisted only by an average of 0.654 (2)°. The electron-withdrawing effect of the cyano group is greater than that of the chloro substituent and therefore there is a greater decrease in the $\pi$-stacking ability of the aromatic moieties. Furthermore, the $\pi \ldots \pi$ distance of 3.644(3) Å between the phenyl rings of the benzonitrile moiety is considerably longer than that between the chlorobenzyl moieties in **4** of 3.570(3) Å. Since the substituted phenyl rings have short $\pi \ldots \pi$ distances, it therefore indicates that electrostatic and inductive effects appear to be more important [35]. For **2**, repulsive interactions dominate. There is low planarity between the cyclopentadienyl rings and the substituted phenyl rings attached to them; the planarity is slightly better in **2** than in **4**. All Fe–C bond distances and angles are within the expected ranges of similar ferrocene derivatives [36].

ORTEP drawings for **9** and **10** are shown in figure 5(a) and (b), respectively, along with the atom-numbering scheme. Selected bond distances and angles are compared in table 6. The molecular structure of **9** consists of two ferrocenyl units connected by a substituted 2-phenylacrylonitrile ligand. The configuration around the substituted 2-phenylacrylonitrile ligand is trans; the planes of the substituted cyclopentadienyl rings and the plane of the phenyl ring are unsymmetrical with dihedral angles of 28.11(7)° on one end and 42.95(6)°

Table 5. Selected bond lengths (Å) and angles (°) for **2** and **4**.

| | 2 | 4 | | 2 | 4 |
|---|---|---|---|---|---|
| C—$C_{Cp}$ | 1.448(3) | 1.453(5) | C—$C_{Cp}$ | 1.449(3) | 1.445(5) |
| C==C | 1.355(3) | 1.359(5) | C==C | 1.353(3) | 1.349(5) |
| C—$C_{Ph}$ | 1.485(3) | 1.492(5) | C—$C_{Ph}$ | 1.483(3) | 1.490(5) |
| | | | | | |
| $C_{Cp}$—C==C | 128.85(17) | 128.7(4) | $C_{Cp}$—C==C | 130.78(17) | 128.3(4) |
| C==C—$C_{Ph}$ | 124.74(16) | 122.6(4) | C==C—$C_{Ph}$ | 123.67(17) | 122.2(4) |
| C==C—$C_N$ | 120.65(17) | 121.8(4) | C==C—$C_N$ | 121.04 | 121.8(4) |
| $C_{Ph}$—*C*—$C_N$ | 114.59 | 115.6(3) | $C_{Ph}$—*C*—$C_N$ | 115.29 | 116.0(3) |
| | | | | | |
| C==C—$C_{Ph}$—$C_{Ph}$ | 165.86(18) | 156.3(4) | C==C—$C_{Ph}$—$C_{Ph}$ | 164.22(18) | 154.0(4) |

Note: $C_{Cp}$ means a carbon on a cyclopentadienyl ring; $C_{Ph}$ means carbon on a phenyl ring; CN means a carbon on a cyano group.

(a)

(b)

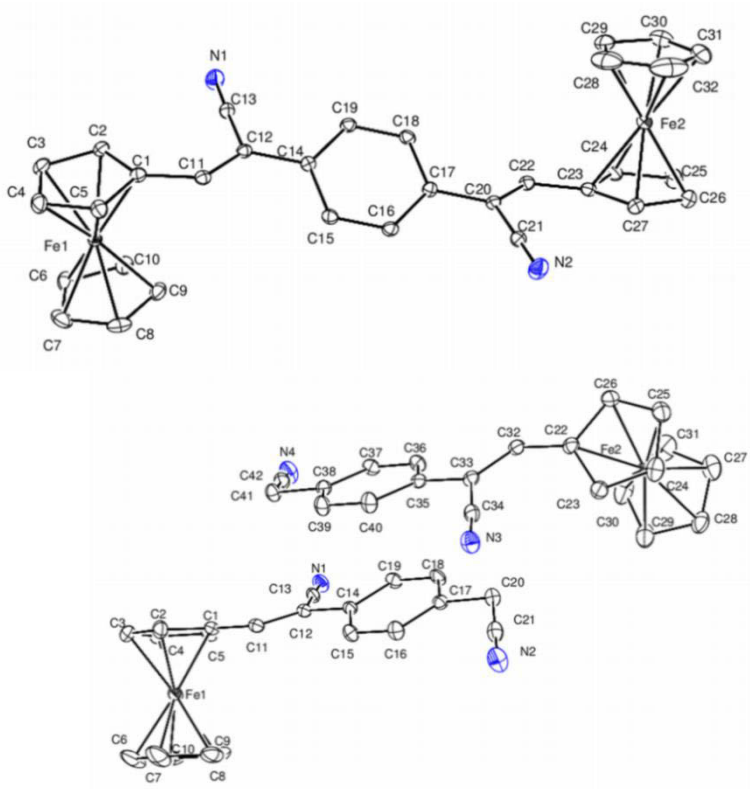


Figure 5: ORTEP diagram along with the atom-numbering scheme for (a) **9** and (b) **10**. Ellipsoids are drawn at 50% probability level. Hydrogens have been omitted for clarity.

on the other, meaning therefore that the molecule belongs to a $C_1$ point group. In addition, whereas one of the ferrocenyl moieties adopts a twisted conformation (small staggering angle of 2.12°), the other adopts an ideal staggered conformation (staggering angle of 45.99°). This lack of planarity is seen in the reduced $\pi$-conjugation in the molecule and especially along the phenylene dipropenenitrile ligand. The cyclopentadienyl rings of each of the ferrocenyl moieties are planar with a tilt angle of approximately 1.8° in one and 1.4° in the other. Compound **10** crystallizes with two molecules in the asymmetric unit, $\mathbf{10_I}$ containing Fe1 and $\mathbf{10_{II}}$ containing Fe2. The two molecules are not related by symmetry given the different orientations of the ferrocenyl moieties.

The cyclopentadienyl rings in each of the two molecules are essentially planar with angles between the set of planes of each of the rings being 0.15° and 1.56° in $\mathbf{10_I}$ and $\mathbf{10_{II}}$,

Table 6. Selected bond lengths (Å) and angles (°) for **9** and **10**.

| | **9** | **$10_I$** | | **9** | **$10_{II}$** |
|---|---|---|---|---|---|
| C—$C_{Cp}$ | 1.449(2) | 1.446(6) | C—$C_{Cp}$ | 1.448(2) | 1.448(6) |
| C==C | 1.353(2) | 1.355(5) | C==C | 1.349(3) | 1.354(5) |
| C—$C_{Ph}$ | 1.481(2) | 1.487(5) | C—$C_{Ph}$ | 1.481(2) | 1.483(5) |
| | | | | | |
| $C_{Cp}$—C==C | 129.75(16) | 127.4(4) | $C_{Cp}$—C==C | 129.36(16) | 126.7(4) |
| C==C—$C_{Ph}$ | 124.40(15) | 124.6(3) | C==C—$C_{Ph}$ | 123.32(15) | 125.6(4) |
| C==C—$C_N$ | 120.30(16) | 119.7(4) | C==C—$C_N$ | 120.67(16) | 119.4(4) |
| $C_{Ph}$—C—$C_N$ | 115.22(15) | 115.6(3) | $C_{Ph}$—C—$C_N$ | 116.01(15) | 115.1(3) |
| | | | | | |
| C==C—$C_{Ph}$—$C_{Ph}$ | -162.70(17) | -164.3(4) | C==C—$C_{Ph}$—$C_{Ph}$ | 150.73(17) | -163.4(4) |

Note: $C_{Cp}$ means a carbon on a cyclopentadienyl ring; $C_{Ph}$ means carbon on a phenyl ring; CN means a carbon on a cyano group.

Table 7. Hydrogen bonding geometry for **9** and **10** (Å/°).

| C—H…N | C—H | H…N | C…N | <C—H…N | Symmetry operator |
|---|---|---|---|---|---|
| **9** | | | | | |
| C11—H11…N2 | 0.95 | 2.51 | 3.321(2) | 143 | 1-x, -y, 2-z |
| C15—H15…N2 | 0.95 | 2.60 | 3.544(2) | 170 | 1-x, -y, 2-z |
| C22—H22…N1 | 0.95 | 2.44 | 3.317(2) | 154 | -x, -y, 1-z |
| **10** | | | | | |
| C8—H8…N2 | 1.00 | 2.61 | 3.521(7) | 152 | 1-x, 1-y, 1-z |
| C20—H20a…N1 | 0.99 | 2.40 | 3.321(5) | 155 | 1-x, -y, 1-z |
| C30—H30…N4 | 1.00 | 2.44 | 3.399(7) | 160 | 2-x, 2-y, 1-z |
| C32—H32…N1 | 0.95 | 2.49 | 3.365(5) | 154 | x, 1+y, z |
| C41—H41A…N3 | 0.99 | 2.40 | 3.322(5) | 155 | 2-x, 2-y, 1-z |

respectively. Each of the molecules has two sets of planes: the plane of the cyclopentadienyl rings [C1–C5 and C11, and C22–C26 and C32 in **$10_I$** and **$10_{II}$**, respectively] and the plane of the phenyl ring and the adjacent carbons [C14–C19 and C2 and C20; C35–C40 and C33 and C41 in **$10_I$** and **$10_{II}$**, respectively]. The nitrile groups project away from these two planes differently in each of the two molecules. In **$10_I$**, the angle between the two sets of planes is 36.82(13)° while in **$10_{II}$**, the same angle is 45.33(15)°. The cyclopentadienyl rings in the two ferrocenyl moieties adopt a slightly staggered geometry and have staggering angles that are different in the two molecules: 9.60° in **$10_I$** and 6.28° in **$10_{II}$**. Bond distances and angles do not show any significant differences between the two molecules

and are comparable to **2** and **9**, as well as to those of related structures [37].

The lattice structures of **9** and **10** are dominated by a series of C–H···N intermolecular hydrogen bonds. In **9**, these hydrogen bonds link centrosymmetrically related molecules into chains that run diagonally across the crystallographic bc plane. In the crystal structure of **10**, the C–H···N hydrogen bonds connect molecules to form layered chains of molecules that run along the crystallographic b-axis (table 7).

## 3. Conclusion

The mechanochemical synthesis of 1,1′-ferrocenyldiacrylonitriles provided an efficient approach for a range of ferrocenyl compounds. The method yielded high to moderate quantities of 1,1′-ferrocenyldiacrylonitriles depending on the electron-withdrawing group attached to the phenyl *para*-position. Selectivity towards ferrocenyldiacrylonitrile formation was favored by the presence of a strong electron-withdrawing group on the *para*-substituent of the phenyl rings. The reaction times were short and all compounds were conveniently isolated. Therefore, similar solvent-free procedures can be developed for synthesis of bimetallic compounds containing similar or different metal centers. Herein, we also demonstrate that by attaching an appropriate $\pi$-acceptor group to the ferrocenyl moiety it allows the optoelectronic properties of the ferrocenyldiacrylonitriles to be tuned. In addition, the donor–acceptor electronic interactions and electron transfer processes are enhanced when two $\pi$-acceptor ligands are attached to one ferrocenyl moiety. On the contrary, attaching two ferrocenyl moieties to a single π-acceptor reduced the electron transfer process. Hence, the redox behavior of 1,1′-ferrocenyldiacrylonitrles can be switched from reversible to irreversible by attaching an appropriate number of $\pi$-acceptor groups. The X-ray crystallographic analysis showed the different preferred solid state conformations of the ferrocenyl moiety in mono- and di-substituted ferrocenyldiacrylonitriles.

## 4. Experimental

### 4.1. General chemicals and instrumentation

Solvent-free reactions involving grinding of reactants were performed in the open air. All

reactants were used as received. Solvents used in purification of compounds and for growing crystals were dried by using standard literature methods prior to use. Aluminum-backed silica gel 60 $F_{254}$ plates were used to carry out thin-layer chromatography in solvents of varying polarity. Purification of products by column chromatography was accomplished by using silica gel 60, 0.063–0.2 mm. The melting points of various compounds were determined either by using a Bibby Stuart Scientific model SMP3 apparatus or by using a Shimadzu Differential Scanning Calorimeter (DSC 60) apparatus. Infrared spectroscopy was conducted on a Perkin Elmer Universal ATR Spectrum 100 FTIR spectrometer. $^{1}H$ and $^{13}C$ NMR spectra were recorded on a 400 MHz Bruker Ultrashield spectrometer at RT. For NMR spectroscopic analysis, samples were dissolved in deuterated chloroform and values were obtained relative to tetramethylsilane. Mass spectra of various compounds were obtained from an Agilent Technologies, 1100 series, ion-trap mass spectrometer. Electronic spectra were recorded in acetonitrile, dichloromethane, and DMF with a Perkin Elmer Lambda 35 UV–visible spectrophotometer with 10 mm path length quartz cuvettes. Cyclic voltammetry measurements were performed on a Metrohm ion analysis instrument with 757 VA Computrace software. A three-electrode configuration consisting of a rotating platinum disk working electrode rotating at 2000 rpm, platinum- wire auxiliary electrode and silver/silver chloride reference electrode was used. The voltammetry measurements were made in dry acetonitrile with $10^{-2}$ M tetrabutylammonium tetrafluoroborate as the supporting electrolyte. For the cyclic voltammetry measurements, 10 $cm^{-3}$ of solution containing approximately $10^{-3}$ M of each compound was used. A scan rate of 100 mV $s^{-1}$ was used and $E_{1/2}$ values were obtained by averaging the anodic and cathodic peak potentials.

### 4.2. Synthesis of 1,1′-ferrocenyldiacrylonitriles compounds from 1,1′-ferrocenedicarboxaldehyde; general procedure

The general procedure for synthesizing 1,1′-ferrocenyldiacrylonitriles was developed from that described by Imrie *et al*. [15]. Compound 1 (1 eq.) and substituted phenylacetonitriles (2.2 eq.) were mixed in a Pyrex tube fitted with a ground-glass joint. The compounds were thoroughly ground with a glass rod. One to two drops of piperidine was added into the Pyrex tube and the mixture was further ground at RT until a melt was formed. The Pyrex tube was sealed and placed in a shaker for approximately 20 min. To evaporate the remaining piperidine (boiling point 106 °C) and water formed as a by-product, the

samples were first dried in open air, and thereafter under a vacuum line. The products were further purified by silica gel chromatography. The formation of the products was determined using IR or NMR spectroscopy ($^{1}$H and $^{13}$C). In solid-state IR spectra, formation of the products was characterized by the disappearance of the sharp carbonyl absorption at approximately 1650 $cm^{-1}$ and the appearance of a strong nitrile absorption at approximately 2200 $cm^{-1}$, $^{1}$H and $^{13}$CNMR spectra showed the disappearance of the carbonyl resonance and the appearance of alkene resonance peaks. Pure compounds were further analyzed by mass spectrometry, microanalysis, and X-ray diffraction.

### 4.2.1. Synthesis of 1,1′-ferrocenyldi[-2(4-cyanophenyl)acrylonitrile] (2).

The general procedure described in Section 4.2 was followed by using 1,1′ferrocenyldicarboxaldehyde (**1**) (145.0 mg, 0.60 mM) and 4-cyanophenylacetonitrile (188.0 mg, 1.32 mM). Upon grinding a deep maroon paste was formed, which was dried to obtain a maroon solid. Reaction completion was monitored by using preparative TLC plates with a solvent system of hexane/diethyl ether (1:1), and the product was then purified by column chromatography with a solvent system of hexane/diethyl ether (1:1) to obtain the product as dark maroon crystals (219.0 mg, 74%) and 37.0 mg of 1,1′-ferrocenedicarboxaldehyde (1). d.p. *ca*. 325 °C; IR ($cm^{-1}$) 3182, 2926, 2852, 2213, 1608, 1587, 1510, 1452, 1417, 1371, 1319, 1251, 1180, 1035, 996, 918, 830, 819, 542, 501, 486, 456, 425; $^{1}$H-NMR spectra ($CDCl_3$) 7.55 (4H, d, *J* 8.4 Hz, ArH), 7.47 (4H, d, *J* 8.5 Hz, ArH), 7.34 (2H, s, CH), 5.08 (4H, s, $C_5H_4$), 4.65 (4H, s, $C_5H_4$); $^{13}$C NMR spectra ($CDCl_3$) 132.7, 125.3, 77.2, 73.7, 72.2; HR-MS ($C_{30}H_{18}FeN_4$) ES: [M + $H^+$] *m/z* calc. 491.0959, found 491.0969.

### 4.2.2. Synthesis of 1,1′-ferrocenyldi[-2(4-{trifluoromethyl}phenyl)acrylonitrile] (3).

The general procedure described in Section 4.2 was followed by using 1,1′-ferrocenyldi-carboxaldehyde (**1**) (145.0 mg, 0.60 mM) and 4-(trifluoromethyl)phenylacetonitrile (244.0 mg, 1.32 mM). Upon grinding a deep red paste was formed, which was dried to obtain a red solid. Reaction completion was monitored using preparative TLC plates with a solvent system of hexane/diethyl ether (1:1) and the product was then purified by column chromatography with a solvent system of hexane/dichloromethane (1:1) to obtain red crystals as the product (268.0 mg, 78%) and 31.0 mg of 1,1′-ferrocenedicarboxaldehyde (**1**). m.p. 252 °C; IR ($cm^{-1}$) 3059, 2924, 2216, 1617, 1593, 1456, 1421, 1324, 1255, 1157, 1111,

1070, 1000, 925, 824, 729, 667, 642, 621, 584, 477, 421; $^{1}$H-NMR spectra ($CDCl_3$) 7.40 (8H, q, *J* 5 Hz, ArH), 7.31 (2H, s, CH), 5.12 (4H, s, $C_5H_4$), 4.62 (4H, s, $C_5H_4$); $^{13}$C NMR spectra ($CDCl_3$) 141.4, 125.9, 124.8, 107.3, 79.1, 77.2, 73.1, 72.9; HR-MS ($C_{30}H_{18}F_6FeN_2$) ES: $[M]^+$ *m/z* calc. 576.0724, found 576.0717

### 4.2.3. Synthesis of 1,1′-ferrocenyldi[-2(4-chlorophenyl)acrylonitrile] (4) and ferrocenyl-carboxl-2(4-chlorophenyl)acrylonitrile (5).

The general procedure described in Section 4.2 was followed by using 1,1′-ferrocenyl-dicarboxaldehyde (1) (145.0 mg, 0.60 mM) and 4-chlorophenylacetonitrile (200.0 mg, 1.32 mM). Upon grinding the two substances in the presence of piperidine, the mixture formed a brown paste, which eventually turned red. Reaction completion was monitored using preparative TLC plates with a solvent system of hexane/dichloromethane (1:1). The red paste was dried, then purified by column chromatography in hexane and dichloromethane (1:1) to obtain two fractions of red solids ($R_f$ = 0.5 and 0.375) and 87.0 mg of 1,1′-ferrocenedicarboxaldehyde (**1**). Characterization of the solid obtained from the less polar fraction ($R_f$ = 0.5) gave 4 (153.0 mg, 52%) m.p. 238 °C; IR ($cm^{-1}$) 3087, 3050, 2209, 1898, 1649, 1598, 1493, 1456, 1411, 1374, 1329, 1305, 1251, 1186, 1094, 1037, 997, 917, 827, 815, 774, 745, 540, 499, 489, 437, 396; $^{1}$H-NMR spectra ($CDCl_3$) 7.22 (4H, s, ArH), 7.18 (4H, s, ArH), 7.15 (2H, s, CH), 5.06 (4H, s, $C_5H_4$), 4.56 (4H, s, $C_5H_4$); $^{13}$C NMR spectra ($CDCl_3$) 140.1, 129.1, 126.0, 79.3, 72.7, 71.5; HR-MS ($C_{28}H_{18}Cl_2FeN_2$) ES: $[M]^+$ *m/z* calc. 508.0196, found 508.0199.

Characterization of the solid obtained from the more polar fraction ($R_f$ = 0.375) gave **5** (22.0 mg, 10%) m.p.138 °C; IR ($cm^{-1}$) 3096, 2925, 2851, 2211, 1680, 1663, 1599, 1509, 1492, 1455, 1407, 1368, 1243, 1184, 1094, 1036, 1013, 997, 921, 825, 741, 485, 410; $^{1}$H-NMR spectra ($CDCl_3$) 9.93 (H, s, CHO), 7.54 (2H, d, *J* 8.4 Hz, ArH), 7.38 (2H, d, *J* 8.4 Hz, ArH), 7.18 (H, s, CH), 5.03 (2H, s, $C_5H_4$), 4.84 (2H, s, $C_5H_4$), 4.62 (2H, s, $C_5H_4$), 4.57 (2H, s, $C_5H_4$); $^{13}$C NMR spectra ($CDCl_3$) 193.3, 141.4, 134.8, 132.7, 129.4, 127.4, 126.7, 118.3, 108.3, 80.3, 78.8, 74.5, 72.7, 72.5, 71.2, 71.2, 71.1; HR-MS ($C_{20}H_{14}OClFeN$) ES: $[M+ H^+]$ *m/z* calc. 376.0192, found 376.0180.

### 4.2.4. Synthesis of 1,1′-ferrocenyldi[-2(4-fluorophenyl)acrylonitrile] (6) and ferrocenyl- carboxl-2(4-fluorophenyl)acrylonitrile (7).

The general procedure described in Section 4.2 was followed by using 1,1′-ferrocenyl-dicarboxaldehyde (**1**) (145.0 mg, 0.60 mM) and 4-fluorophenylacetonitrile (178.0 mg, 1.32 mM). Upon grinding, a red solution was formed which gradually turned into a reddish-brown solid. Reaction completion was monitored using preparative TLC plates with a solvent system of hexane/dichloromethane (1:1) and the product was then purified by column chromatography with a solvent system of hexane/diethyl ether (1:1) to obtain two fractions ($R_f$ = 0.25 and 0.125) and 100.0 mg of 1,1′-ferrocenedicarboxaldehyde (**1**). The less polar fraction was isolated as a reddish-brown solid while the more polar fraction was isolated as a red solid. Characterization of the solid obtained from the less polar fraction ($R_f$ = 0.25) gave compound **6** (20.0 mg, 7%) m.p. 214 °C; IR ($cm^{-1}$) 3052, 2921, 2851, 2212, 1604, 1593, 1510, 1456, 1418, 1372, 1311, 1281, 1265, 1236, 1163, 1107, 913, 814, 760, 725, 650, 594, 510, 480, 447, 426, 388; $^1$H-NMR spectra ($CDCl_3$) 7.32 (4H, q, *J* 3.5 Hz, ArH), 6.92 (4H, t, *J* 8.48 Hz, ArH), 7.13 (2H,s, CH), 5.03 (4H, s, $C_5H_4$), 4.56 (4H, s, $C_5H_4$); $^{13}$C NMR spectra ($CDCl_3$) 139.9, 129.8, 126.7, 126.7, 118.6, 116.0, 115.8, 107.6, 79.4, 72.6, 71.4; HR-MS ($C_{28}H_{18}F_2FeN_2$) ES: $[M]^+$ *m/z* calc. 476.0787, found 476.0789.

Characterization of the solid obtained from the more polar fraction ($R_f$ = 0.125) gave compound **7** (51.0 mg, 24%) m.p. 115 °C; IR ($cm^{-1}$) 3087, 2920, 2850, 2213, 1680, 1662, 1602, 1591, 1508, 1454, 1413, 1367, 1265, 1233, 1163, 1103, 1034, 1000, 921, 833, 763, 742, 651, 616, 593, 489, 445, 427, 398; $^1$H-NMR spectra ($CDCl_3$) 9.93 (H, s, CHO) 7.59 (2H, s, ArH), 7.12 (2H, s, ArH), 7.10 (H, s, CH), 5.03 (2H, s, $C_5H_4$), 4.84 (2H, s, $C_5H_4$), 4.62 (2H, s, $C_5H_4$), 4.56 (2H, s, $C_5H_4$); $^{13}$C NMR spectra ($CDCl_3$) 193.3, 140.8, 130.4, 127.3, 127.3, 118.5, 116.3, 116.0, 108.5, 79.0, 72.5, 71.1; HR-MS ($C_{20}H_{14}OF_1FeN$) ES: $[M]^+$ *m/z* calc. 359.0409, found 359.0412.

## 4.3. Reactions of ferrocenemonocarboxaldehyde (8) and phenylenediacetonitrile

Ferrocenemonocarboxaldehyde (**8**) (400 mg, 1.86 mM) and phenylenediacetonitrile (203 mg, 1.30 mM) were added into a Pyrex tube fitted with a ground glass joint. The mixture was thoroughly ground with a glass rod in the presence of one to two drops of piperidine. A deep red gum formed which turned into a melt upon further grinding. The Pyrex tube was sealed and placed in a shaker for 20 min. The sample was subsequently dried in air

followed by high vacuum drying to obtain a red solid. The reaction completion was monitored using preparative TLC plates with a solvent system of hexane/diethyl ether (3:2) and the product was then purified by column chromatography with a solvent system of hexane/diethyl ether (3:2) to obtain a major and a minor product and 58 mg of starting ferrocene- monocarboxaldehyde (**8**). The major product ($R_f$ = 0.325) was isolated as red crystals and identified as phenylene-3,3‘-*bis*-(ferrocenyl)-diacrylonitrile, compound **9**. The minor product ($R_f$ = 0.1) was isolated as reddish-orange crystals and identified as 3-ferrocenyl-2(acetonitrophenyl)acrylonitrile **10**. Further characterization of compound **9** gave (319.0 mg, 65%); d.p. *ca*. 275 °C; IR ($cm^{-1}$) 3107, 2212, 1594, 1457, 1408, 1363, 1275, 1249, 1106, 1033, 997, 889, 837, 813, 721, 689, 507, 482, 463,448; $^1$H-NMR spectra ($CDCl_3$) 7.62 (4H, s, ArH), 7.43 (2H,s, CH), 4.98 (4H, s, $C_5H_4$), 4.56 (4H, s, $C_5H_4$), 4.23 (10H, s, $C_5H_5$); $^{13}$C NMR spectra ($CDCl_3$) 143.6, 134.5, 125.6, 118.9, 105.8, 77.2, 71.9, 70.3, 69.9; HR-MS ($C_{32}H_{24}Fe_2N_2$) ES: $[M]^+$ *m/z* calc. 548.0638, found 548.0641.

Further characterization of compound **10** gave (152.0 mg, 30%) m.p. 151 °C; IR ($cm^{-1}$) 3094, 2934, 2212, 1919, 1783, 1594, 1515, 1456, 1408, 1361, 1320, 1268, 1249, 1191, 1104, 1049, 1032, 997, 915, 837, 813, 722, 690, 613, 481, 449, 429; $^1$H-NMR spectra ($CDCl_3$) 7.61 (2H, s, ArH), 7.59 (2H, s, ArH), 7.37 (1H, s, CH), 4.96 (2H, t, *J* 1.7 Hz, $C_5H_4$), 4.54 (2H, t, *J* 1.8 Hz, $C_5H_4$), 4.23 (5H, s, $C_5H_4$), 3.75 (2H, s, $CH_2$) $^{13}$C NMR spectra ($CDCl_3$) 144.0, 134.8, 129.8, 128.6, 125.8, 118.9, 117.4, 105.6, 77.2, 71.8, 70.3, 69.9, 23.4; *m/z* ; $[M^+]$, 352.1 HR-MS ($C_{21}H_{16}FeN_2$) ES: $[M]^+$ *m/z* calc. 352.0663, found 352.0671.

## 5. X-ray crystallography

### 5.1. Structural analysis of 2, 4, 9, and 10

Data for X-ray diffraction of **2**, **4**, **9**, and **10** were collected from APEX [38] with cell refinement of SAINT-Plus [38]. The data reduction was done by using SAINT-Plus and XPREP [38] while the structures were solved by direct methods with SHELXS9 [39] program(s). The structures obtained were refined by using SHELXL97 [39] and their molecular graphics were obtained by using ORTEP-3 [40]. The software WinGX was used to prepare material for publication [41]. The crystal data and structure refinement for 2, 4, **9**, and **10** are summarized in table 8.

Table 8. Crystallographic data and structure refinements for **2**, **4**, **9**, and **10**.

| Parameter | **2** | **4** | **9** | **10** |
|---|---|---|---|---|
| Empirical formula | $C_{30}H_{18}Fe_1N_4$ | $C_{28}H_{18}Fe_1N_2$ | $C_{32}H_{24}Fe_2N_2$ | $C_{21}H_{16}Fe_1N_2$ |
| Formula weight | 490.33 | 509.19 | 548.23 | 352.21 |
| Temperature (K) | 173(2) | 173(2) | 173(2) | 173(2) |
| Wavelength (Å) | 0.71073 | 0.71073 | 0.71073 | 0.71073 |
| Crystal system | Monoclinic | Monoclinic | Monoclinic | Triclinic |
| Space group | $P2_1/c$ | $P2_1/c$ | $P2_1/c$ | $P\bar{1}$ |
| Unit cell dim (Å/°) | | | | |
| *a*, *α* | 7.3307(4) | 7.2041(5) | 11.4369(3) | 7.2547(3), 101.730(2) |
| *b*, *β* | 25.1890(14), 119.733(3) | 23.4176(14), 108.902(4) | 28.7450(7), 93.6830(10) | 11.9787(5), 92.658(2) |
| *c*, *γ* | 13.8031(7) | 13.4176(8) | 7.5275(2) | 19.2512(9), 90.818(2) |
| *V* (Å$^3$) | 2213.2(2) | 2149.4(2) | 2469.58(11) | 1635.78(12) |
| Z | 4 | 4 | 4 | 4 |
| σ (mg/m$^3$) | 1.472 | 1.574 | 1.475 | 1.430 |
| $\mu$ (mm$^{-1}$) | 0.709 | 0.971 | 1.199 | 0.924 |
| *F*(000) | 1008 | 1040 | 1128 | 728 |
| Crystal size (mm$^3$) | 0.38x0.26x0.08 | 0.35x0.28x0.12 | 0.49x0.47x0.10 | 0.43x0.28x0.09 |
| $\theta$ range (°) | 1.88 → 25.00 | 1.74 → 26.13 | 1.78 → 28.34 | 1.08 → 28.00 |
| Index ranges | -8 → 8<br>-29 → 29<br>-16 → 16 | -8 → 8<br>-28 → 28<br>-15 → 14 | -14 → 15<br>-38 → 38<br>-10 → 10 | -9 → 9<br>-15 → 15<br>-25 → 25 |
| Reflections | 33106 | 15565 | 75646 | 49618 |
| Indep reflections | 3786[$R_{int}$ = 0.0335] | 3829 [$R_{int}$ = 0.0302] | 6131 [$R_{int}$ = 0.0366] | 7796[$R_{int}$ = 0.0292] |
| Completeness to $\theta$ %/(°) | 96.9 (25.00°) | 89.5 (26.13) | 99.5 (28.34) | 98.5 (28.00) |
| Absorption correction | Semi-empirical from equivalents | Semi-empirical from equivalents | Semi-empirical from equivalents | Semi-empirical from equivalents |
| Max & min Trans. | 0.9454 & 0.7743 | 0.8924 & 0.7274 | 0.8895 &0.5911 | 0.9214 & 06919 |
| Refinement | Full-matrix least-squares on $F^2$ | Full-matrix least-squares on $F^2$ | Full-matrix least-squares on $F^2$ | Full-matrix least-squares on $F^2$ |
| Data/restrs/para | 3786/0/316 | 3829/0/298 | 6131/0/325 | 7796/0/434 |
| GOOF on $F^2$ | 1.008 | 1.238 | 1.121 | 1.071 |
| Final R indices [I > 2 sigma(I)] | $R_1$ = 0.0296, $wR_2$ = 0.0779 | $R_1$ = 0.0572, $wR_2$ = 0.1333 | $R_1$ = 0.0316, $wR_2$ = 0.0806 | $R_1$ = 0.0593, $wR_2$ = 0.1867 |
| *R* indices (all data) | $R_1$ = 0.0364, $wR_2$ = 0.0814 | $R_1$ = 0.0595, $wR_2$ = 0.1343 | $R_1$ = 0.0398, $wR_2$ = 0.0845 | $R_1$ = 0.0663, $wR_2$ = 0.1913 |
| Largest diff. peak & hole (e.Å$^3$) | 0.339 & -0.339 | 2.298 & -0.712 | 0.452 & -0.537 | 1.758 & -0.660 |

## Supplementary material

Tables and Figures giving $^1$H and $^{13}$C NMR spectra, IR spectra and HR-MS analysis for compounds **2**, **3**, **4**, **5**, **6**, **7**, **9** and **10**. UV-visible spectrophotometric and cyclic voltammetry data for compounds **2**, **3**, **4**, **9** and **10**. CIF files and crystallographic data of compounds **2**, **4**, **9** and **10**. Responses to the various alerts from CIF validation are provided in the CIF files under the publication section, experimental refinement section.

## Acknowledgements

This research was financed by the National Research Foundation (NRF) and the University of KwaZulu-Natal (UKZN). Lucy M. Ombaka thanks the UKZN College of Agriculture, Engineering and Science for the award of a postgraduate bursary. We are also grateful to Prof. B.S. Martincigh, Dr R.S. Mwakubambanya, Godfrey Keru, and Mombeshora Tonde for their critical comments on the manuscript.

## References

[1] M. Himaja, P. Das, A. Karigar. *Int. J. Res. Ayurveda Pharm*., **4**, 1079 (2011).

[2] D. Braga, S.L. Giaffreda, F. Grepioni, A. Pettersen, L. Maini, M. Curzi, M. Polito. *Dalton Trans*., **10**, 1249 (2006).

[3] A. McCluskey, P.J. Robinson, T. Hill, J.L. Scott, J.K. Edwards. *Tetrahedron Lett*., **43,** 3117 (2002).

[4] A. Majumder, R. Gupta, A. Jain. *Green Chem. Lett. Rev.*, **6**, 151 (2013).

[5] O. Galangau, I. Fabre-Francke, S. Munteanu, C. Dumas-Verdes, G. Clavier, R. Méallet-Renault, R.B. Pansu, F. Hartl, F. Miomandre. *Electrochim. Acta*, **87**, 809 (2013).

[6] S. Venkatraman, R. Kumar, J. Sankar, T.K. Chandrashekar, K. Sendhil, C. Vijayan, A. Kelling, M.O. Senge. *Chem. Eur. J.*, **10**, 1423 (2004).

[7] O.F. Mohammed, A.A.O. Sarhan. *Chem. Phys.*, **372**, 17 (2010).

[8] P. Camurlu, Z. Bicil, C. Gültekin, N. Karagoren. *Electrochim. Acta.*, **63**, 245 (2012).

[9] S. Braga, A.M.S. Silva. *Organometallics*, **32**, 5626 (2013).

[10] V.O. Nyamori, S.D. Mhlanga, N.J. Coville. *J. Organomet. Chem.*, **693**, 2205 (2008).

[11] R.S. Oosthuizen, V.O. Nyamori. *Appl. Organomet. Chem*., **26**, 536 (2012).

[12] E.N. Nxumalo, N.J. Coville. *Mater*., **3**, 2141 (2010).

[13] E.N. Nxumalo, V.P. Chabalala, V.O. Nyamori, M.J. Witcomb, N.J. Coville. *J. Organomet. Chem.*, **695**, 1451 (2010).

[14] M.I. Ionescu, Y. Zhang, R. Li, H. Abou-Rachid, X. Sun. *Appl. Surf. Sci*., **258**, 4563 (2012).

[15] C. Imrie, P. Kleyi, V.O. Nyamori, T.I.A. Gerber, D.C. Levendis, J. Look. *J. Organomet. Chem.*, **692**, 3443 (2007).

[16] C. Imrie, V.O. Nyamori, T.I.A. Gerber. *J. Organomet. Chem*., **689**, 1617 (2004).

[17] W. Liu, Q. Xu, Y. Ma, Y. Liang, N. Dong, D. Guan. *J. Organomet. Chem.*, **625**, 128 (2001).

[18] P.E. Kleyi, C.W. McCleland, T.I.A. Gerber. *Polyhedron*, **29**, 1095 (2010).

[19] S. Yuan, Z. Li, L. Xu. *Res. Chem. Intermed*., **38**, 393 (2012).

[20] A. González, P. Vázquez, T. Torres. *Tetrahedron Lett*., **40**, 3263 (1999).

[21] N. Dwadnia, F. Allouch, N. Pirio, J. Roger, H. Cattey, S. Fournier, M.-J. Penouilh, C.H. Devillers, D. Lucas, D. Naoufal, R.B. Salem, J.-C. Hierso. *Organometallics*, **32**, 5784 (2013).

[22] P.Y. Bruice. *Organic Chemistry*, 5th Edn, pp. 683–686, Pearson Education, Upper Sadle River (2007).

[23] D. Braga, M. Polito, D. D'Addario, E. Tagliavini, D.M. Proserpio, F. Grepioni, J.W. Steed. *Organometallics*, **22**, 4532 (2003).

[24] Y. Yamaguchi, W. Ding, C.T. Sanderson, M.L. Borden, M.J. Morgan, C. Kutal. *Coord. Chem. Rev.*, **251**, 515 (2007).

[25] B. Dhokale, P. Gautam, R. Misra. *Tetrahedron Lett.*, **53**, 2352 (2012).

[26] K. Yoshiharu, M. Takashi, M. Shuichi. In *Optical recording materials sensitive to blue laser beam, publication number, 2002-002110, Patent abstracts of Japan, Kokai Tokyo Koho*, pp. 13 (2002).

[27] O.F. Mohammed, E. Vauthey. *J. Phys. Chem. A*, **112**, 5804 (2008).

[28] P. Kaur, M. Kaur, G. Depotter, S. Van Cleuvenbergen, I. Asselberghs, K. Clays, K. Singh. *J. Mater. Chem.*, **22**, 10597 (2012).

[29] W.E. Geiger, N.G. Connelly. *Chem. Rev.*, **96**, 877 (1996).

[30] V. Lakshmi, G. Santosh, M. Ravikanth. *J. Organomet. Chem.*, **696**, 925 (2011).

[31] R.S. Bayly, P.D. Beer, G.Z. Chen. In *Ferrocene Ligands, Materials and Biomolecules*, P. Štěpnička (Ed.), pp. 281–318, John Wiley & Sons, Atrium Southern Gate, Chichester (2008).

[32] L.V. Snegur, A.A. Simenel, Y.S. Nekrasov, E.A. Morozova, Z.A. Starikova, S.M. Peregudova, Y.V. Kuzmenko, V.N. Babin, L.A. Ostrovskaya, N.V. Bluchterova, M.M. Fomina. *J. Organomet. Chem*., **689**, 2473 (2004).

[33] S. Barlowa, S.R. Marder. *Chem. Commun.*, 1555 (2000).

[34] S.M. Batterjee, M.I. Marzouk, M.E. Aazab, M.A. El-Hashash. *Appl. Organometal. Chem.*, **17**, 291 (2003).

[35] F. Cozzi, J.S. Siegel. *Pure Appl. Chem*., **67**, 683 (1995).

[36] V.O. Nyamori, G. Keru, B. Omondi. *Acta Crystallogr., Sect. E: Struct. Rep. Online* **68**, 1535 (2012).

[37] D. Onyancha, V. Nyamori, C.W. McCleland, C. Imrie, T.I.A. Gerber. *J. Organomet. Chem*., **694**, 207 (2009).

[38] Bruker, *APEX2, SAINT-Plus, XPREP and SADABS. Bruker AXS Inc*., Madison, Wisconsin, USA. (2008).

[39] G.M. Sheldrick. *Acta Cryst.*, **A64**, 112 (2008).

[40] L.J. Farrugia. *J. Appl. Cryst*., **30**, 565 (1997).

[41] L.J. Farrugia. *J. Appl. Cryst.*, **32**, 837 (1999).

# CHAPTER FOUR

# NITROGEN-DOPED CARBON NANOTUBES SYNTHESIZED FROM 1,1′-FERROCENYLDIACRYLONITRILES: THE EFFECT OF THE *PARA*-SUBSTITUENT

Lucy M. Ombaka, Patrick G. Ndungu, Bernard Omondi, Vincent O. Nyamori*

School of Chemistry and Physics, University of KwaZulu-Natal, Westville Campus, Private Bag X54001, Durban, 4000, South Africa

## Abstract

Nitrogen-doped carbon nanotubes (N-CNTs) have been synthesized *via* a chemical vapour deposition technique by use of 1,1′-ferrocenylphenyldiacrylonitriles as new catalysts. Three catalysts with different *para*-substituents on the phenyl rings, namely, *para*-CN, *para*-$CF_3$ and *para*-Cl were synthesized, characterized by NMR, IR, HR-MS; single crystal X-ray analysis was conducted on the *para*-$CF_3$ catalysts. X-ray crystallographic analysis of the *para*-$CF_3$ catalysts indicates that steric factors influence the X-ray structure of 1,1′-ferrocenylphenyldiacrylonitriles. The catalysts were used for the synthesis of shaped carbon nanomaterials (SCNMs) at 850 °C by use of either acetonitrile or pyridine as carbon and nitrogen sources to yield mixtures of N-CNTs and carbon spheres (CS) when pyridine was used. The lowest percentage of CS is in the products obtained with the *para*-$CF_3$ catalysts. N-CNTs obtained from the *para*-$CF_3$ catalysts in pyridine have the highest nitrogen-doping level, show a kinked morphology and are less thermally stable compared with those synthesised by use of the *para*-CN and -Cl catalysts. This implies that fluorine heteroatoms enhance nitrogen-doping into N-CNTs. The use of acetonitrile and the *para*-CN and -Cl catalysts yields a mixture of N-CNTs and carbon nanofibres (CNFs) with less abundance of CNFs in the products obtained using *para*-Cl catalysts. However, the *para*-$CF_3$ catalyst with acetonitrile gives N-CNTs as the only shaped carbon nanomaterials. Analysis of transmission electron microscopy images reveal that iron is encapsulated into the cavities of N-CNTs synthesized from the *para*-$CF_3$ and *para*-Cl catalysts in acetonitrile. The outer and inner diameters of N-CNTs synthesized with the *para*-$CF_3$ and *para*-Cl catalysts in acetonitrile are significantly less than those of N-CNTs synthesized from the *para*-CN catalyst. **Keywords:** Nitrogen-doped carbon nanotubes, carbon nanofibres, chlorine, fluorine, ferrocenyldiacrylonitriles, chemical vapour deposition,

## 1. Introduction

Shaped carbon nanomaterials (SCNMs) such as carbon nanotubes (CNTs) are fascinating carbonaceous materials with novel physical and chemical properties [1]. Owing to their unique properties, such as high tensile strength, Young‘s modulus [2], thermal stability [3], surface area [4], and excellent electrochemical properties [5], CNTs are useful materials in the field of nanotechnology [1]. These physicochemical properties of CNTs can be enhanced further *via* nitrogen-doping to form nitrogen-doped CNTs (N-CNTs). The nitrogen species present in N-CNTs act as n-type conductors and as basic functional groups thus enhancing the electrical properties [6] and surface energy [7] of N-CNTs. Additionally, N-CNTs contain defect sites which promote their wettability and surface area [8] making them useful materials, applicable in various fields such as catalysis [1] and field emission devices [9].

Unlike other flake-like carbonaceous materials such as graphene, CNTs and N-CNTs are cylindrical and contain hollow cavities in their structures. These hollow cavities can be filled with iron to form ferromagnetic CNTs and N-CNTs [10]. Ferromagnetic CNTs and N-CNTs are used in different areas, such as electromagnetic wave absorption [10]. They can also be applied as heterogeneous catalysts with the added advantage of the ease of separating them from solutions by use of magnets [11]. Iron filled CNTs have been synthesized by using mixtures of organic halogens and ferrocene as catalysts [12]. For instance, Gui *et al*. synthesized iron-encapsulated CNTs by use of dichlorobenzene and ferrocene catalyst [13]. However, little is known about the use of halogenated ferrocenyl derivatives as catalysts in the synthesis of iron encapsulated CNTs or N-CNTs.

Ferrocene [14] and ferrocenyl derivatives [15] are frequently used as catalysts in the synthesis of CNTs and other shaped carbon nanomaterials (SCNMs) owing to their volatile nature [14, 16]. Nitrogen-containing ferrocenyl derivatives can be useful catalysts in the synthesis of N-CNTs [7]. In some instances, the use of nitrogen-containing ferrocenyl derivatives yields N-CNTs with better physical or chemical properties as opposed to the use of ferrocene dissolved in a nitrogen containing organic solvent. For example, Nxumalo *et al*. showed that the use of 4-ferrocenylaniline as a catalyst yields N-CNTs with higher nitrogen-doping levels compared with ferrocene in aniline solution [17]. Another seldom-explored approach that can also be useful in modulating the nitrogen content and species in N-CNTs is the use of halogens. Halogens, such as fluorine, are potential oxidizing agents that could induce defects in CNTs during the nucleation stage, this defect sites can easily accept nitrogen species resulting in higher nitrogen-doping levels. However, reports on the use of

halogens to modulate nitrogen-content in N-CNTs are limited.

In this study, 1,1′-ferrocenyldiacrylonitriles (Scheme 1) containing nitrogen-heteroatoms (*para*-CN), nitrogen- and chlorine-heteroatoms (*para*-Cl), and nitrogen- and fluorine-heteroatoms (*para*-$CF_3$) were synthesized and characterized. The X-ray crystallographic structure of the *para*-$CF_3$ catalyst is reported for the first time. The 1,1′-ferrocenyl-diacrylonitriles have been investigated as novel catalyst for the synthesis of N-CNTs, carbon nanofibres (CNFs) and carbon spheres (CS). The chlorine and fluorine heteroatoms were used to evaluate the effect of halogenated catalysts on nitrogen-doping and iron encapsulation into the cavity of N-CNTs. We also present the effect of chlorine and fluorine heteroatoms on the diameters of N-CNTs and the products distribution of the products. The effect of varying the carbon and nitrogen source has been evaluated by using either acetonitrile or pyridine as the carbon and nitrogen source.

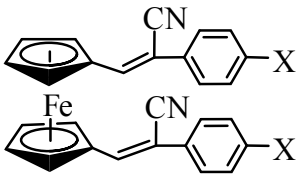


X=CN [*para*-CN catalyst]
X=$CF_3$ [*para*-$CF_3$ catalyst]
X=Cl [*para*-Cl catalyst]

Scheme 1: Structure of 1,1′-ferrocenyldiacrylonitriles used as catalysts.

## 2. Experimental

### 2.1 Materials and characterization

All chemicals and solvents used were of analytical grade and were used as received. Aluminium-backed silica gel 60 $F_{254}$ plates were used to carry out thin layer chromatography in solvents of varying polarity. Purification of products by column chromatography was accomplished by using silica gel 60, 0.063-0.2 mm. The melting points of various compounds were determined either by using a Bibby Stuart Scientific model SMP3 apparatus or by use of a Shimadzu Differential Scanning Calorimeter (DSC 60) apparatus. Infrared spectroscopy was conducted on a Perkin Elmer Universal 100 FTIR spectrometer equipped with an ATR accessory. The $^{1}$H- and $^{13}$C-NMR spectra were recorded on a 400 MHz Bruker Ultrashield spectrometer at RT. For NMR spectroscopy analysis, samples were dissolved in deuterated chloroform and values were obtained relative to tetramethylsilane. Mass spectra

of various compounds were obtained from a mass spectrometry (MS) with an electrospray ionization (ESI).

For synthesis of N-CNTs, acetonitrile 99.9% and pyridine 99.8% were purchased from LiChroSolv, Germany. N-CNTs were synthesized in a quartz tube (inner diameter 27 mm, length 850 mm) placed in a muffle furnace (Elite Thermal Systems Limited Model No. TSH12/50/610). The carrier gas used during synthesis of N-CNTs was 10% hydrogen in argon (v/v) purchased from Airflex Industrial Gases, South Africa. The rate of injection was controlled by a syringe pump (model no. NE-300, New Era Pump Systems Inc.). Images of N-CNTs were taken by use of a transmission electron microscope (TEM) (JEOL JEM 1010). The graphitic natures of N-CNTs were determined with Raman spectrometer (DeltaNu Advantage 532™). The thermo-stability of N-CNTs was studied by using a TA Instrument Q Series™ Thermal Analyzer DSC/TGA (Q600). Infrared spectra of N-CNTs embedded into KBr pellets ware recorded on a Perkin Elmer Spectrum RX1 FTIR spectrometer. Elemental analysis of N-CNTs was performed on a LECO CHNS-932 elemental analyzer, standardized with acetanilide.

## 2.2 General procedure for synthesis of 1,1′-ferrocenyldiacrylonitrile

The general procedure for the synthesis and characterization of 1,1′-ferrocenyl-diacrylonitriles is displayed in Scheme 2 and has been previously reported [18]. In brief, 1,1′-ferrocenedicarboxaldehyde and substituted phenylacetonitriles (2.2 eq.) were mixed in a Pyrex tube fitted with a ground glass joint. The compounds were thoroughly ground in the open air with a glass rod in the presence of 1-2 drops of piperidine to form a melt. The melt was first dried in open air, followed by drying under a vacuum line. The dry products were purified by means of silica gel chromatography. Formation of the products was determined by use of IR or NMR spectroscopy ($^{1}$H- and $^{13}$C-NMR). In the solid-state IR spectra, the formation of the products was characterized by the disappearance of the sharp carbonyl absorption band at approximately 1650 $cm^{-1}$ and the appearance of a strong nitrile absorption band at approximately 2200 $cm^{-1}$. The $^{1}$H- and $^{13}$C-NMR spectra showed the disappearance of the carbonyl resonance (≈10 ppm) and the appearance of alkene resonance peaks (≈7.4 ppm). Pure compounds were further analysed by melting point determination, mass spectrometry, microanalysis and X-ray diffraction.

### 2.2.1 1,1′-Ferrocenyldi[-2(4-cyanophenyl)acrylonitrile] (*para*-CN catalyst)

The general procedure for the synthesis of this catalyst is described in Section 2.2 and involves the use of 1,1′-ferrocenyldicarboxaldehyde (145.0 mg, 0.60 mmol) and 4-cyanophenylacetonitrile (188.0 mg, 1.32 mmol). Upon grinding, a deep maroon paste was formed which was dried to obtain a maroon solid. Reaction completion was monitored by use of preparative TLC plates with a solvent system of hexane/diethyl ether (1:1), and the product was then purified by means of column chromatography with a solvent system of hexane/diethyl ether (1:1) to obtain the product as a dark maroon crystals (219.0 mg, 74%) and 37.0 mg of the recovered starting 1,1′-ferrocenedicarboxaldehyde. d.p. *ca*. 325 °C; IR ($cm^{-1}$) 3182, 2926, 2852, 2213, 1608, 1587, 1510, 1452, 1417, 1371, 1319, 1251, 1180, 1035, 996, 918, 830, 819, 542, 501, 486, 456, 425; $^{1}$H-NMR spectra ($CDCl_3$) 7.55 (4H, d, *J* 8.4 Hz, ArH), 7.47 (4H, d, *J* 8.5 Hz, ArH), 7.34 (2H, s, CH), 5.08 (4H, s, $C_5H_4$), 4.65 (4H, s, $C_5H_4$); $^{13}$C-NMR spectra ($CDCl_3$) 132.7, 125.3, 77.2, 73.7, 72.2; HR-MS ($C_{30}H_{18}FeN_4$) ES: [M + $H^+$] *m/z* calc. 491.0959, found 491.0969.

### 2.2.2 1,1′-Ferrocenyldi[-2(4-chlorophenyl)acrylonitrile] (*para*-Cl catalyst)

The general procedure for synthesis of this catalyst is described in Section 2.2 and involves the use of 1,1′-ferrocenyldicarboxaldehyde (145.0 mg, 0.60 mmol) and 4-chlorophenylacetonitrile (200.0 mg, 1.32 mmol). Upon grinding the two substances in the presence of a drop of piperidine (0.05 ml), the solid mixture transformed into a brown paste, which eventually turned into a red solid. The reaction completion was monitored by using preparative TLC plates with a solvent system of hexane/dichloromethane (1:1). The red paste was dried, then purified by means of column chromatography in hexane and dichloromethane (1:1) solution to obtain the product as a red solid and 87.0 mg of the recovered starting 1,1′-ferrocenedicarboxaldehyde. Characterization of the red solid gave the *para*-Cl catalysts (153.0 mg, 52%) m.p. 238 °C; IR ($cm^{-1}$) 3087, 3050, 2209, 1898, 1649, 1598, 1493, 1456, 1411, 1374, 1329, 1305, 1251, 1186, 1094, 1037, 997, 917, 827, 815, 774, 745, 540, 499, 489, 437, 396; $^{1}$H-NMR spectra ($CDCl_3$) 7.22 (4H, s, ArH), 7.18 (4H, s, ArH), 7.15 (2H, s, CH), 5.06 (4H, s, $C_5H_4$), 4.56 (4H, s, $C_5H_4$); $^{13}$C-NMR spectra ($CDCl_3$) 140.1, 129.1, 126.0, 79.3, 72.7, 71.5; HR-MS ($C_{28}H_{18}Cl_2FeN_2$) ES: $[M]^+$ *m/z* calc. 508.0196, found 508.0199.

### 2.2.3 1,1′-Ferrocenyldi[-2(4-{trifluoromethyl}phenyl)acrylonitrile] (*para*-$CF_3$ catalyst)

The general procedure for synthesis of this catalyst is described in Section 2.2 and involves the use of 1,1′-ferrocenyldicarboxaldehyde (145.0 mg, 0.60 mmol) and 4-

(trifluoromethyl)phenylacetonitrile (244.0 mg, 1.32 mmol). Upon grinding a deep red paste was formed, which was dried to obtain a red solid. The reaction completion was monitored by use of preparative TLC plates with a solvent system of hexane/diethyl ether (1:1) and the product was then purified by means of column chromatography with a solvent system of hexane/diethyl ether (1:1) to obtain red crystals as the product (268.0 mg, 78%) and 31.0 mg of the recovered starting 1,1′-ferrocenedicarboxaldehyde. m.p. 252 °C; IR ($cm^{-1}$) 3059, 2924, 2216, 1617, 1593, 1456, 1421, 1324, 1255, 1157, 1111, 1070, 1000, 925, 824, 729, 667, 642, 621, 584, 477, 421; $^{1}$H-NMR spectra ($CDCl_3$) 7.40 (8H, q, *J* 5 Hz, ArH), 7.31 (2H, s, CH), 5.12 (4H, s, $C_5H_4$), 4.62 (4H, s, $C_5H_4$); $^{13}$C-NMR spectra ($CDCl_3$) 141.4, 125.9, 124.8, 107.3, 79.1, 77.2, 73.1, 72.9; HR-MS ($C_{30}H_{18}F_6FeN_2$) ES: $[M]^+$ *m/z* calc. 576.0724, found 576.0717.

### 2.2.3.1 X-ray crystallography analysis of the *para*-$CF_3$ catalyst

Crystal evaluation and data collection for the *para*-$CF_3$ catalyst was performed on a Bruker Smart *APEXII* diffractometer with Mo Kα radiation (λ = 0.71073 Å) and a diffractometer to crystal distance of 4.00 cm. The initial cell matrix was obtained from three series of scans at different starting angles. Each series consisted of 12 frames collected at intervals of 0.5° in a 6° range with the exposure time of about 10 seconds per frame. The reflections were successfully indexed by an automated indexing routine built in the *APEXII* program suite [19]. Data collection method involved ω scans of width 0.5°. Data reduction was carried out by means of the program *SAINT+* and *XPREP* [19] while, the structure was solved by direct methods by using *SHELXS* [20] program(s). The structures obtained were refined by using the *SHELXL* [20]. *WinGX* [21] and *ORTEP3* [22] were used to prepare molecular graphics and material for publication [20]. The crystal data and structure refinement information for the *para*-$CF_3$ catalyst are summarized in Table 1.

Table 1. Crystal data and structure refinement for the *para*-$CF_3$ catalyst.

| | |
|---|---|
| Empirical formula | $C_{30}\ H_{18}\ F_6\ Fe\ N_2$ |
| Formula weight | 576.31 |
| Temperature (K) | 293(2) |
| Wavelength (Å) | 0.71073 |
| Crystal system | Triclinic |
| Space group | *P*-1 |
| Unit cell dimensions (Å/°) | |
| a, $\alpha$ | 7.3569(3), 78.379(2) |
| b, $\beta$ | 11.7726(4), 87.424(2) |
| c, $\gamma$ | 14.2107(5), 86.612(2) |
| V ($Å^3$) | 1202.76(8) |
| Z | 2 |
| σ ($mg/m^3$) | 1.591 |
| μ ($mm^{-1}$) | 0.697 |
| F(000) | 584 |
| Crystal size ($mm^3$) | 0.450 x 0.090 x 0.090 |
| $\theta$ range (°) | 1.768 to 28.320. |
| Index ranges | $-9 \le h \le 9$, $-15 \le k \le 15$, $-18 \le l \le 18$ |
| Reflections ions collected | 30000 |
| Independent reflections | 5944 [R(int) = 0.0326] |
| Completeness to $\theta$ | 99.6 % (25.242°) |
| Absorption correction | Semi-empirical from equivalents |
| Max. and min. transmission | 0.939 & 0.731 |
| Refinement | Full-matrix least-squares on $F^2$ |
| Data/restraints/parameters | 5944/0/352 |
| GOOF on $F^2$ | 1.220 |
| Final R indices [I>2sigma(I)] | R1 = 0.0707, *w*R2 = 0.1739 |
| R indices (all data) | R1 = 0.0715, *w*R2 = 0.1743 |
| Largest diff. peak and hole ($e.Å^{-3}$) | 1.933 &.972 |

### 2.3 Synthesis of N-CNTs

N-CNTs were synthesized by using a chemical vapour deposition (CVD) technique as outlined by Ombaka *et al*. [7] and Oosthuizen *et al*. [23]. In brief, three ferrocenyl-diacrylonitriles with substituted *para*-$CF_3$, -CN or -Cl (Scheme 1) were used as catalysts. Acetonitrile or pyridine was used as the main nitrogen and carbon source. A solution made by dissolving 0.25 g of the catalyst in 9.75 g of either acetonitrile or pyridine (i.e. 2.5 wt.% of catalyst) was made and used to synthesize N-CNTs.

The solution of synthesis precursors was injected at a flow rate of 0.8 mL $min^{-1}$ into a quartz tube placed in a muffle furnace. The synthesis precursors were carried through the quartz tube by a carrier gas (10% hydrogen in argon (v/v)), which was pumped at a rate of 100 mL $min^{-1}$ at 80 kPa. A reaction temperature of 850 °C was used for all experiments and, the furnace was set to maintain this temperature for 30 minutes during synthesis. Thereafter, upon completion of the reaction, the reactor was left to cool to room temperature and the products formed were collected from the hot zone of the quartz tube.

## 3. Results and discussion

### 3.1 Synthesis of *para*-CN, *para*-Cl and *para*-$CF_3$ catalysts

Grinding together 1,1′-ferrocenedicarboxaldehyde and the substituted phenylacetonitriles in the presence of a drop of piperidine yielded the *para*-CN, *para*-Cl and *para*-$CF_3$ substituted catalysts as depicted in Scheme 2 [18]. The reaction mixture readily turned into a melt or a gum upon grinding at ambient temperatures. The obtained melt or gum was dried under vacuum and IR and $^1$H-NMR spectroscopy were used to confirm the reaction completion. Formation of the 1,1′-ferrocenyldiacrylonitriles was marked by the disappearance of a sharp IR absorption band at ≈1650 $cm^{-1}$ (CHO) and the appearance of a strong nitrile absorption band at ≈2200 $cm^{-1}$. From the $^1$H-NMR spectra, the formation of 1,1′-ferrocenyldiacrylonitriles was marked by the disappearance of a aldehyde proton resonance peak (≈10 ppm) and the appearance of an ethylene proton resonance peak (≈7.4 ppm).

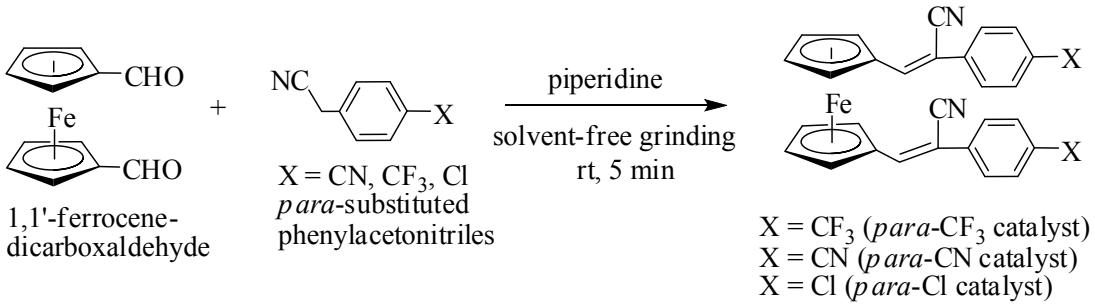


Scheme 2. Mechanochemical synthesis of 1,1′-ferrocenyldiacrylonitriles under solvent-free conditions.

### 3.1.1 Crystal structure of the *para*-$CF_3$ catalyst

Synthesis and characterization of the *para*-$CF_3$ catalyst was reported in our previous publication [18], however, the crystal structure of this catalyst has not been reported. The molecular structure and atom numbering scheme of the *para*-$CF_3$ catalyst is presented in Figure 1. Selected bond distances and angles of the *para*-$CF_3$ structure are summarized in Table 2. The crystal structure of the *para*-$CF_3$ catalyst contains a more bulky -$CF_3$ group on the *para*-position as opposed to the *para*-CN and -Cl groups in the previously reported catalysts [18].

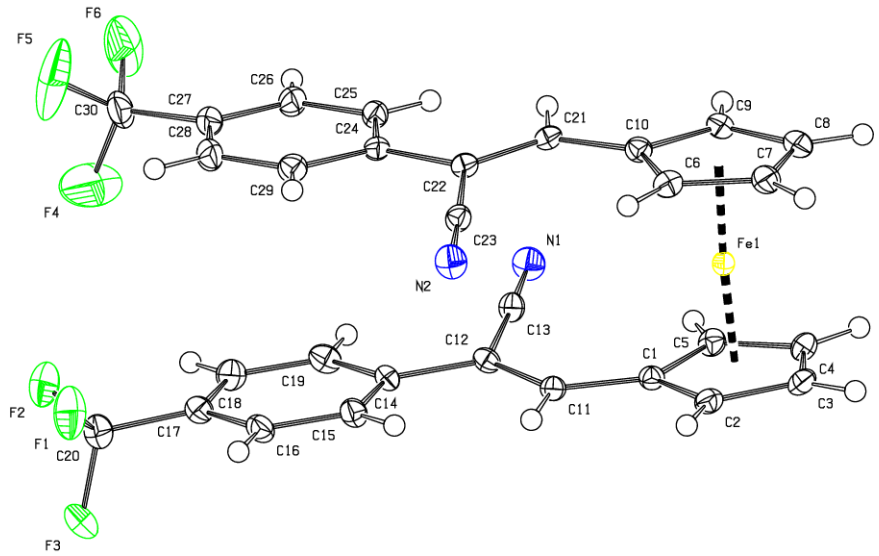


Figure 1: ORTEP diagram for the *para*-$CF_3$ catalyst along with the atom-numbering scheme. The displacement ellipsoids are drawn at 50% probability level.

The bulky -$CF_3$ group does not seem to affect the arrangement of the two *para*-(trifluoromethyl)phenylacrylonitrile moieties since the structure adopts a *cisoidal*

conformation which is observed in less bulky groups (*para* –CN and –Cl) that have been previously reported [18]. However, the two -$CF_3$ groups seem to influence the conformation around the $C_{11}$-$C_{13}$ and $C_{20}$-$C_{22}$ double bond in which the CN groups are observed to face opposite directions. The steric strain caused by the -$CF_3$ groups also tends to influence the cyclopentadienyl rings which are staggered by an angle of 17.9° from an ideal eclipsed geometry. The staggering angle in the para-CN and para-Cl were smaller (15.85° and 0.654° respectively) [18].

All Fe-C bond distances and angles are well within the expected ranges of similar ferrocenyl derivatives [18]. In the *para*-$CF_3$ catalyst, the cyanoethyl benzonitrile groups are staggered by an angle of 170.5(4)° while, in the *para*-CN and -Cl catalysts the cyanoethyl benzonitrile groups were staggered by 165.86(18)° and 156.3(4)° respectively [18]. As the *para*-substituent increases in size (*i.e.* Cl < CN < $CF_3$) the angle by which the cyanoethyl benzonitrile groups are staggered also increases. The increase in steric strain could be perpetuated by repulsive interactions between the two cyanoethyl benzonitrile groups resulting in a wider angle of staggering.

Table 2. Bond lengths [Å] and angles [°] for *para*-$CF_3$ catalyst.

| | | | |
|---|---|---|---|
| C-$C_{Cp}$ | 1.442(5) | C-$C_{Cp}$ | 1.444(5) |
| C=C | 1.355(5) | C=C | 1.354(5) |
| C-$C_{Ph}$ | 1.480(5) | C-$C_{Ph}$ | 1.483(5) |
| | | | |
| $C_{Cp}$-C=C | 130.4(3) | $C_{Cp}$-C=C | 130.2(3) |
| C=C-$C_{Ph}$ | 124.2(3) | C=C-$C_{Ph}$ | 124.3(3) |
| C=C-$C_N$ | 119.8(3) | C=C-$C_N$ | 119.7(3) |
| $C_{Ph}$-*C*-$C_N$ | 116.0(3) | $C_{Ph}$-*C*-$C_N$ | 116.0(3) |
| | | | |
| C=C-$C_{Ph}$-$C_{Ph}$ | 170.5(4) | C=C-$C_{Ph}$-$C_{Ph}$ | 171.3(4) |

### 3.2 Effect of the *para*-substituent and nitrogen source on SCNMs

In this section, the SCNMs synthesized by using the *para*-$CF_3$, -CN and -Cl catalysts are named SCNMs-F, SCNMs-CN and SCNMs-Cl respectively. In a similar manner, the N-CNTs obtained by use of *para*-$CF_3$, -CN and -Cl catalysts are named N-CNTs-F, N-CNTs-CN, and N-CNTs-Cl respectively.

### 3.2.1 Yield of SCNMs

The yields of products obtained from all three catalysts dissolved in pyridine and acetonitrile are summarized in Table 3. Amongst the three catalysts used, the *para*-$CF_3$ catalyst gave the highest yield with pyridine or acetonitrile solution. The enhanced yield obtained with the *para*-$CF_3$ catalyst could have been promoted by fluorine-heteroatoms. Fluorine may have restructured the iron catalysts to a more active phase of higher carbon solubility hence increasing the yield of SCNMs [24]. The *para*-Cl catalysts gave the lowest yield with pyridine and acetonitrile. The observed decrease in product yield possibly arises because the *para*-Cl catalyst is less efficient for the growth of SCNMs compared with the *para*-$CF_3$ and -CN catalysts [25]. The *para*-Cl moiety may have deactivated the catalysts by reacting with the catalysts active sites thus retarding SCNMs growth rate and decreasing the yield as inferred from the works of Pattinson *et al*. [26].

Table 3: Yield and product distribution of pristine SCNMs and amorphous carbon obtained by use of the three catalysts dissolved in pyridine or acetonitrile.

| Catalyst | pyridine | | | | acetonitrile | | | |
|---|---|---|---|---|---|---|---|---|
| | Yield (mg) | N-CNTs (%) | CS (%) | Amorphous carbon (%) | Yield (mg) | N-CNTs (%) | CNFs (%) | Amorphous carbon % |
| Para-$CF_3$ | 256 | 80 | 13 | 7 | 30 | 80 | - | 20 |
| Para-CN | 131 | 70 | 20 | 10 | 20 | 40 | 30 | 30 |
| Para-Cl | 100 | 30 | 50 | 20 | 15 | 55 | 20 | 25 |

A comparison of the total product yields obtained with either pyridine or acetonitrile shows that higher product yields were obtained with pyridine compared with acetonitrile. Pyridine has five carbon atoms in its structure while acetonitrile has two carbon atoms, thus pyridine supplies higher quantities of carbon than acetonitrile leading to greater yields of SCNMs [25]. Acetonitrile has more nitrogen atoms than pyridine increasing the nitrogen concentrations in the synthesis precursors this slows down SCNMs growth rates thus lowering the yields [24].

### 3.2.2 Morphology of SCNMs

Morphologies of synthesized SCNMs have been determined by use of TEM analysis. The TEM images of the SCNMs synthesized by use of all three catalysts in pyridine are

presented in Figure 2, while the images of those synthesized in acetonitrile are presented in Figure 3. The use of pyridine as a carbon/nitrogen source seems to yield N-CNTs as the main product (apart from the *para*-Cl catalyst) with CS as the minor product (Figure 2 and Table 3). When acetonitrile is used as a carbon/nitrogen source, N-CNTs are still produced as the major product but the minor product in this case is now CNFs (Figure 3 and Table 3).

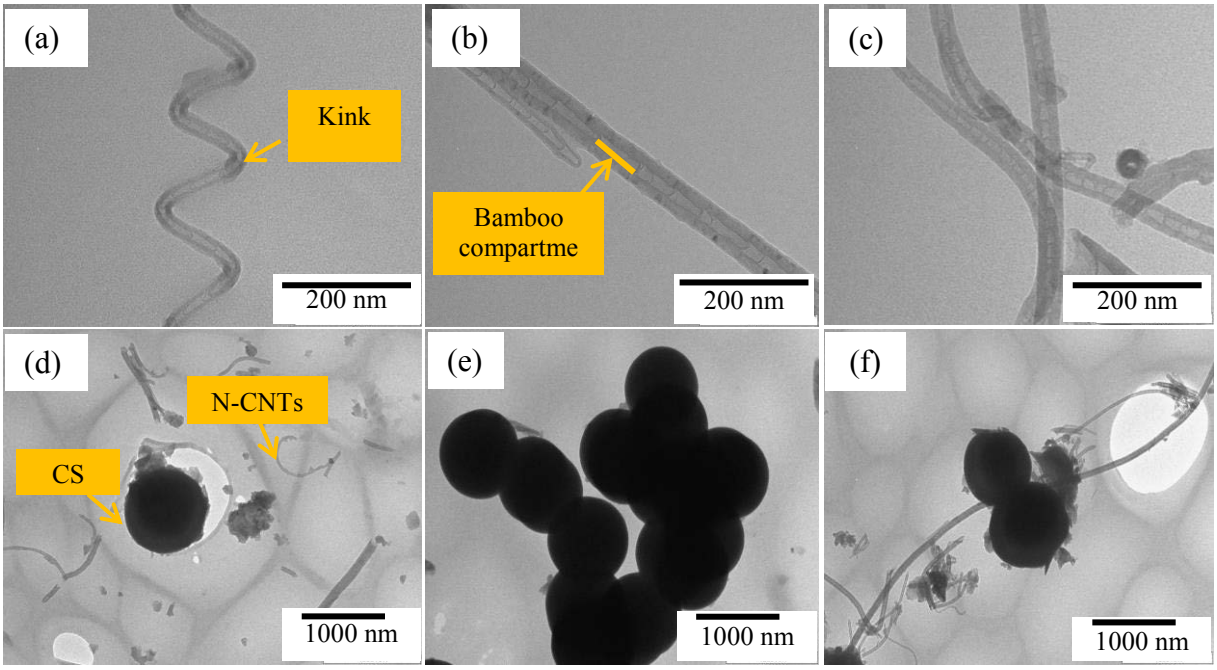


Figure 2: High magnification TEM images of pristine N-CNTs synthesized by use of (a) *para*-$CF_3$, (b) *para*-Cl and (c) *para*-CN catalysts, and low magnification TEM images of N-CNTs and CS synthesized by using (d) *para*-$CF_3$, (e) *para*-Cl and (f) *para*-CN catalysts in pyridine as the nitrogen source.

TEM images of all N-CNTs (Figures 2 and 3) exhibit bamboo compartments associated with nitrogen-doping [27]. N-CNTs synthesized by use of the *para*-$CF_3$ catalyst in pyridine are predominantly kinked (Figure 2a). Such kinks are usually accredited to defects induced by pentagonal and heptagonal structures which may have been caused by the etching effect of fluorine [25]. This could indicate that the use of *para*-$CF_3$ as a catalyst in pyridine achieves more nitrogen-doping on N-CNTs than we observe when we used either *para*-CN or -Cl as catalysts in pyridine.

The *para*-Cl catalyst yields the highest quantity of CS while the *para*-$CF_3$ catalyst gives the least amount of CS (Table 3). This can be attributed to the fact that fluorine, just like oxygen can act as an oxidising agent that ‗deans out' dangling carbon atoms, which prevalently form CS, and in the process reduces the formation of CS. On the contrary, the

*para*-Cl moiety seems to have poisoned the iron nanoparticle catalysts to favour formation of CS [28]. This observations contradict the report of Lv *et al*. [12] who observed good CNTs yield with chlorinated synthesis precursors.

The use of *para*-$CF_3$, and acetonitrile as a carbon/nitrogen source, yields N-CNTs as the only SCNMs, while using *para*-CN and *para*-Cl yields a mixture N-CNTs and CNFs (Table 3 and Figure 3). The *para*-Cl in acetonitrile gave higer percentages of N-CNTs than in pyridine (Table 3). The formation of CNFs can be correlated with the abundance of reactive hydrogen radicals emanating from the catalyst during synthesis [29]. The molecular hydrogen pumped through the reaction chamber reduces $Fe^{2+}$ species to $Fe^0$ that catalyses SCNM growth, but the reactive hydrogen radicals enhance CNF formation [30]. During synthesis, chlorine and fluorine heteroatoms present in the *para*-$CF_3$ and -Cl catalysts can react with such reactive hydrogen radicals, thereby reducing their abundance and promoting formation of N-CNTs.

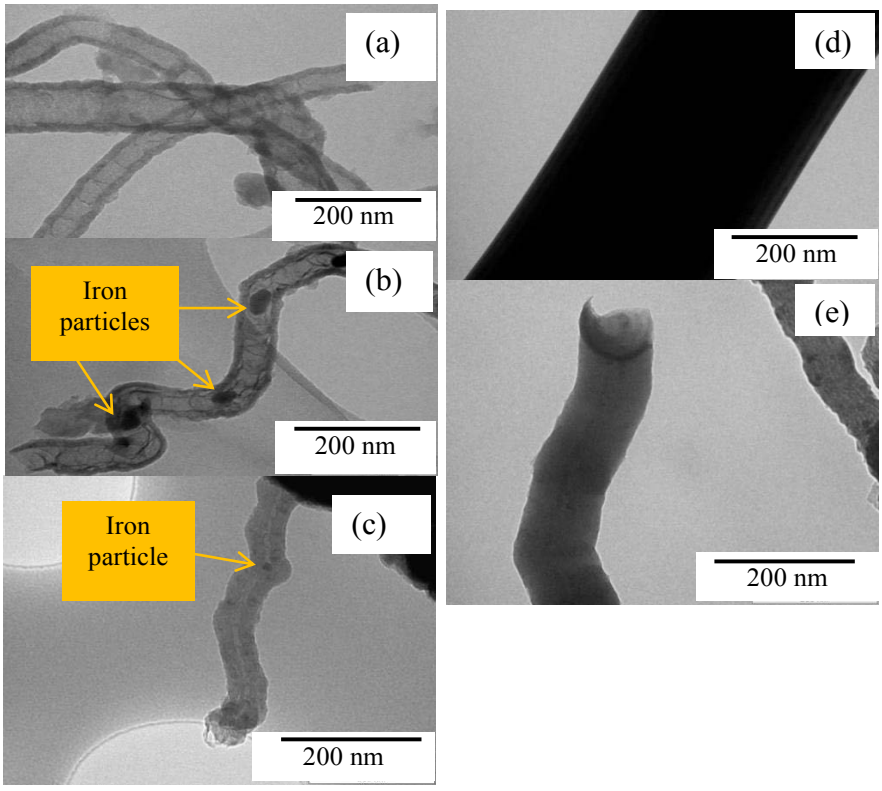


Figure 3: TEM images of pristine N-CNTs synthesized by using (a) *para*-CN, (b) *para*-$CF_3$ and (c) *para*-Cl catalyst in acetonitrile. TEM images of CNFs synthesized by use of (d) *para*-CN and (e) *para*-Cl catalyst in acetonitrile.

TEM images of N-CNTs synthesized by use of the *para*-$CF_3$ and -Cl catalysts in acetonitrile also depict encapsulated iron nanoparticles in the N-CNTs cavities (Figures 3b and c). N-CNTs obtained from the *para*-$CF_3$ catalyst show more iron encapsulation than those obtained from the *para*-Cl catalyst. Similar encapsulated iron nanoparticles are absent in the images of N-CNTs synthesized from the *para*-CN catalyst indicating that chlorine and fluorine heteroatoms have aided the formation of iron-encapsulated N-CNTs. In a similar manner, Lv *et al*. reported the synthesis of metal-filled CNTs by use of chlorine-substituted benzene [12] and ferrocene catalysts. Since no iron encapsulation was observed when pyridine was used as the nitrogen source, it is possible that the ratio of carbon:halogen influences the encapsulation of iron.

The outer and inner diameters (OD and ID respectively) of all N-CNTs (Figure 4) have been obtained from analysis of the TEM images. The diameters of N-CNTs obtained with pyridine are generally smaller than those obtained with acetonitrile as a nitrogen source. The OD and ID of N-CNTs synthesized using all three catalysts in pyridine showed no significant difference as opposed to those synthesized using the *para*-$CF_3$ and -Cl catalysts in acetonitrile which exhibited reduced OD and ID compared with the N-CNTs obtained from the *para*-CN catalyst.

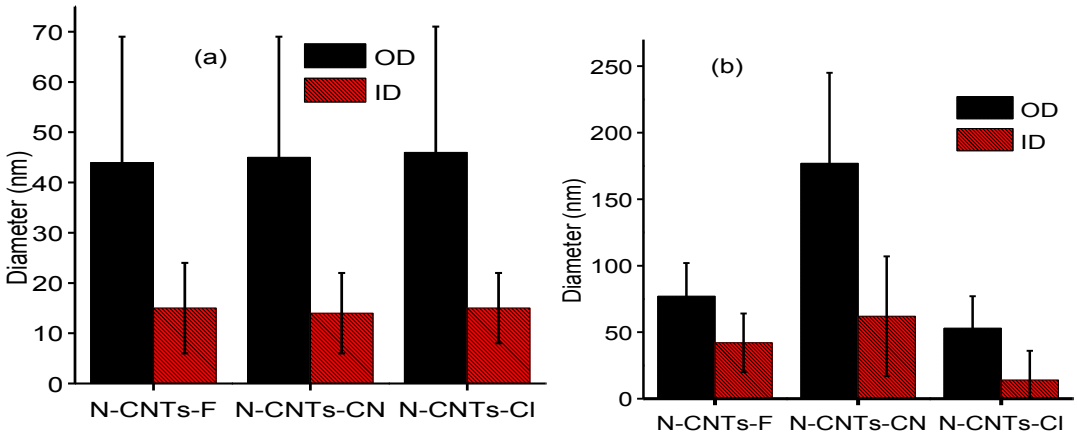


Figure 4: Outer diameter (OD) and inner diameter (ID) of pristine N-CNTs synthesized by using the *para*-$CF_3$, *para*-CN and *para*-Cl catalysts in (a) pyridine and (b) acetonitrile.

Pyridine was a better carbon source than acetonitrile because it gave higher yields of more pure SCNMs with all catalysts (Table 3). Hence, further characterization of SCNMs by use of Raman spectroscopy, TGA and FTIR were only conducted on the products obtained from pyridine.

### 3.2.3 Crystallinity of SCNMs

Raman spectroscopy was used to evaluate the crystallinity of SCNMs synthesized from all three catalysts in pyridine. The Raman spectra are presented in Figure 5a. From the Raman spectra, two first-order peaks, i.e. a disorder band (D-band) at 1376-1399 $cm^{-1}$ and a graphitic band (G-band) at 1569-1604 $cm^{-1}$ are observed [31]. The D-band is due to the breathing modes of disordered $sp^2$ carbons, while the G-band is caused by the stretching modes of $sp^2$ graphitic carbon networks [32]. An increase of disorder in the graphene structures results in a more intense D-band than the G-band, and *vice-versa* for a decrease in disorder. Thus, the Tuinstra-Koening relationship $I_D/I_G$ (integrated area of the D-band:integrated area of the G-band) has been applied to determine the crystalline nature of SCNMs [33, 34]. A lower $I_D/I_G$ ratio would imply that the samples analysed had a higher degree of crystallinity, while a higher $I_D/I_G$ ratio would imply the reverse.

SCNMs from the *para*-$CF_3$ catalyst (SCNMs-F) show the lowest value of $I_D/I_G$ while SCNMs from the *para*-Cl catalyst (SCNMs-Cl) have the highest $I_D/I_G$ value (Figure 5b). The higher $I_D/I_G$ value observed from SCNMs-Cl is indicative of the presence of more amorphous carbons in these samples as amorphous carbons are normally inherently disordered and thus give rise to a strong D-band intensity [35]. This observation further supports the greater quantity of amorphous carbon observed from TEM analysis of SCNMs-Cl (Table 3). Likewise, the lower $I_D/I_G$ value of SCNMs-F corresponds with the lower percentage of amorphous carbons in these samples as observed from the TEM analysis (Table 3). Generally, the $I_D/I_G$ ratio correlated directly with the quantity of amorphous carbon in the SCNMs.

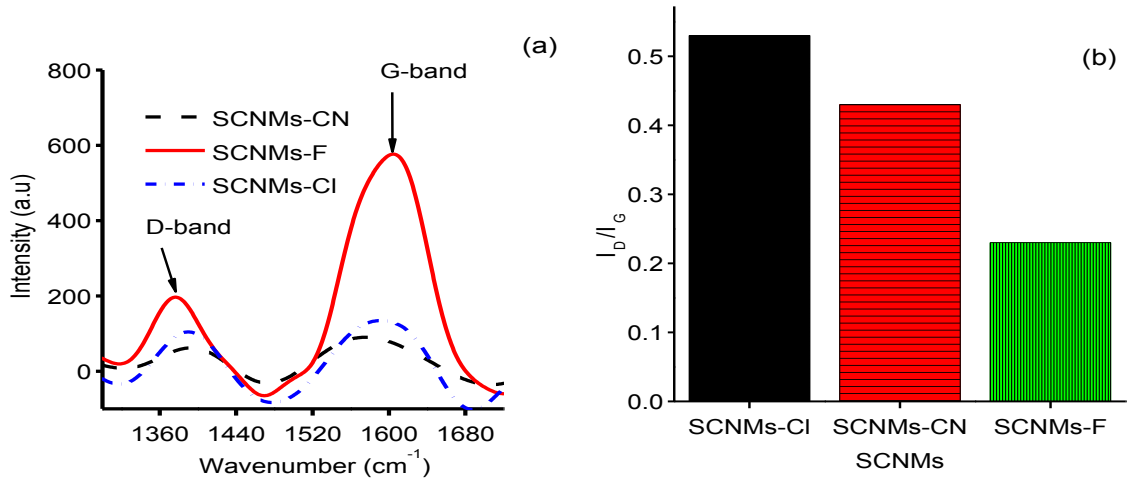


Figure 5: (a) Raman spectra and (b) $I_D/I_G$ ratio of pristine SCNMs synthesized by use of *para*-$CF_3$, *para*-CN and *para*-Cl catalysts in pyridine.

The G-band seems to shift from 1592 $cm^{-1}$ (SCNMs-Cl) to 1604 $cm^{-1}$ (SCNMs-F). This shift is attributed to the reduction of the in-plane correlation length in ordered graphene sheets [31]. Such a reduction can be perpetuated by nitrogen-doping of N-CNTs which can alter the correlation length in the graphene structures of N-CNTs. It is also important to note that the D- and G-bands of SCNMs-F exhibit a much greater intensity than those of other samples (Figure 5a). Similar observations were made from the Raman spectra of N-CNTs synthesized with 4 wt.% oxygen in acetonitrile [7]. Since fluorine neighbours oxygen in the periodic table, it is possible that fluorine just like oxygen can etch the walls of N-CNTs or aid the incorporation of a specific nitrogen species into the graphene structure of N-CNTs thus increasing the Raman intensity [36].

### 3.2.4 Thermal stability of SCNMs

TGA analyses were used to determine the thermal stability of SCNMs synthesized by use of all three catalysts in pyridine. The thermograms and derivative thermograms (DTG) are presented in Figure 6. From the thermograms (Figure 6a) it is evident that SCNMs-F are the least thermally stable while SCNMs-Cl and -CN exhibit a similar thermal stability. The lower decomposition temperature of SCNMs-F can be associated with the increased number of kinks observed from TEM images of these samples. These kinks are induced by defects in N-CNTs which result in a lowering of the decomposition temperature [37]. It is also possible that N-CNTs-F contain higher amounts of nitrogen compared with N-CNTs-Cl and N-CNTs-CN. Since nitrogen-doping introduces defects in N-CNTs, samples with higher nitrogen-doping levels are prone to be less thermally stable [37]. The observed lower thermal stability of SCNMs-F parallels the observation made from TGA analysis of N-CNTs synthesized by using 4 wt.% oxygen in acetonitrile [7]. Thus, it is likely that fluorine, just like oxygen, enhances nitrogen-doping into N-CNTs. Between 800-1000 °C, the residual weight on all curves increases due to oxidation of iron to iron oxide (Figure 6a).

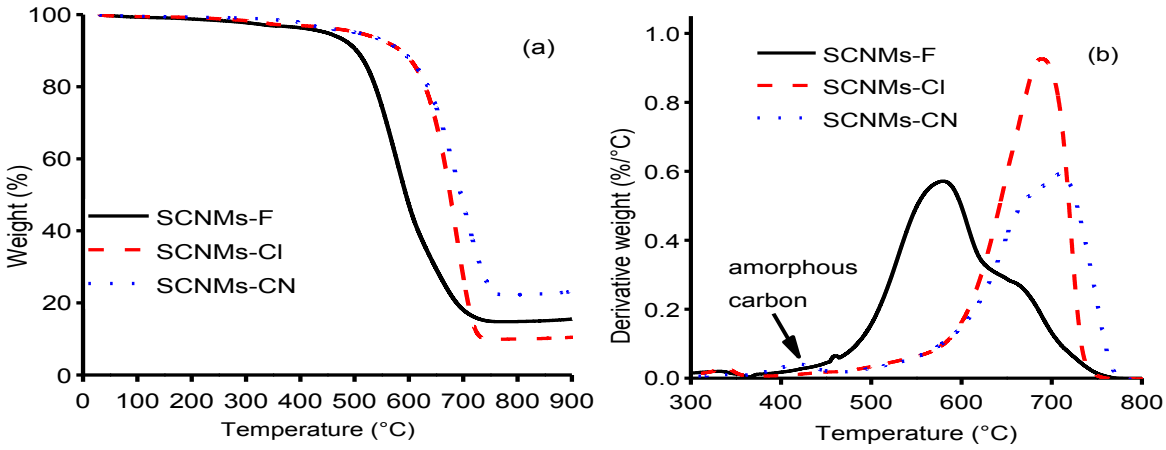


Figure 6: (a) Thermograms and (b) derivative thermograms (DTG) of pristine SCNMs synthesized by using *para*-$CF_3$, *para*-CN and *para*-Cl catalysts in pyridine.

The DTG of all SCNMs showed a minor peak (≈350-450 °C) and a broad major peak (≈500-800 °C). The minor peak is associated with amorphous carbon present in all samples as observed from TEM analysis. The major peak arises from the overlap of the decomposition peaks of N-CNTs and CS. The peak corresponding to SCNMs-F significantly differs from those for SCNMs-CN and SCNMs-Cl in terms of shape and position. This can be due to the incorporation of a specific nitrogen species in the N-CNTs-F, as mentioned earlier [36]. This nitrogen species may have increased the number of defect sites in N-CNTs-F leading to an overall decrease in thermal stability of N-CNTs-F [38]. A similar trend in DTG curves is also observed in the DTG of N-CNTs synthesized by use of 4 wt. % oxygen in acetonitrile [7]. Thus, it is possible that both oxygen and fluorine etch the walls of N-CNTS creating more defective N-CNTs which are thermally unstable or they both aid doping of a single nitrogen species into N-CNTs [7, 36]. The DTG curve for SCNMs-Cl is narrower and sharper than that of SCNMs-F and SCNMs-CN indicating that this sample is more homogeneous than the other two samples.

### 3.2.5 Surface chemistry of N-CNTs and CS

FTIR spectroscopy and elemental analysis were used to analyse the surface chemistry of the SCNMs synthesized by use of all three catalysts in pyridine (Figure 7). A broad band appearing at ≈3400 $cm^{-1}$ is observed in the spectra of all samples and is assigned to the stretching vibrations of -OH groups in water molecules adsorbed onto the SCNMs [39]. The transmittance peaks at ≈2950-2850 $cm^{-1}$ correspond with the stretching vibration of dangling $CH_2$ and $CH_3$ groups attached to the aromatic rings of graphene and amorphous carbons [40].

The stretching vibrations of $CO_2$ groups arising from the single beam FTIR spectrometer are observed at ≈2381 $cm^{-1}$ [41]. The stretching modes of the C=C bonds found in the aromatic rings of CNTs are observed at 1678 $cm^{-1}$, while the C-H vibration modes are observed at 788 and 699 $cm^{-1}$ [40].

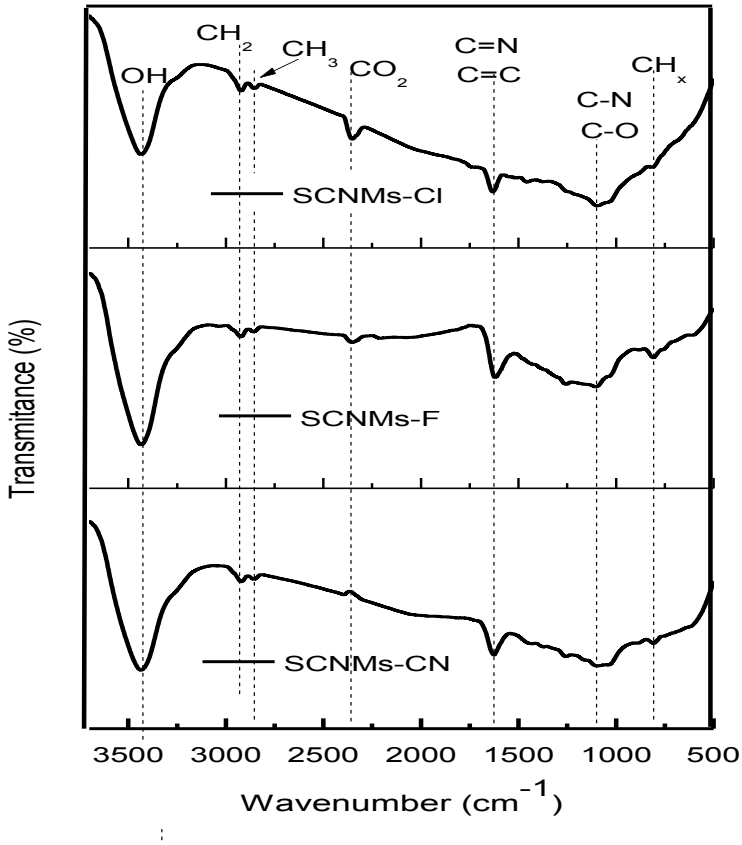


Figure 7: FTIR spectra of pristine SCNMs synthesized by using *para*-$CF_3$, *para*-CN and *para*-Cl catalysts in pyridine.

The stretching vibrations of C=N that have been reported to appear at ≈1567 $cm^{-1}$ [41-44] appear to have overlapped with the C=C stretching modes to form a broad peak between 1519-1713 $cm^{-1}$. This peak is most prominent and intense in SCNMs-F compared with SCNMs-Cl and SCNMs-CN. Therefore, it is possible that there is more nitrogen-doping in N-CNTs-F than in N-CNTs-Cl and N-CNTs-CN. This possibility is further supported by the kinked morphology observed from the TEM images of SCNMs-F and the lower thermal stability of these samples observed from TGA analysis. A comparison of the FTIR spectra of N-CNTs-F and N-CNTs synthesized by use of 4 wt.% oxygen [7], shows that for N-CNTs-F the C=N band shifted to a higher wavenumber. Thus, it is probable that N-CNTs-F contain a

large amount of a single nitrogen species that differs from that in the previously reported N-CNTs [7].

Elemental analysis of the SCNMs obtained with the three catalysts showed that 4.6-6.3 wt. % of nitrogen was present in all SCNMs (Figure 8). SCNMs-F and SCNMs-Cl exhibit almost similar levels of nitrogen-doping. SCNMs-CN showed the least amount of nitrogen doping despite having two extra nitrogen atoms on the structure of the *para*-CN catalyst, suggesting that the generated nitrogen species do not favour nitrogen-doping. Since, SCNMs-F and SCNMs-Cl have an almost similar nitrogen content, it is expected that their thermal decomposition temperature would be almost equal. However, this is not the case as SCNMs-F are less thermally stable than SCNMs-Cl (Figure 6). Therefore, it is possible that though both materials contain almost equal amounts of nitrogen, the nitrogen species present in these samples differs. This is supported by the increased kinked morphology observed in N-CNTs-F, the enlarged peak at 1519-1713 $cm^{-1}$ observed from FTIR spectra of N-CNTs-F, and the enhances Raman intensity of SCNMs-F. In general, both fluorine and chlorine enhances the nitrogen-doping of N-CNTs. It is possible that during synthesis, the halogens induce defects on the graphene layers of N-CNTs, the defects then aid further nitrogen-doping into N-CNTs.

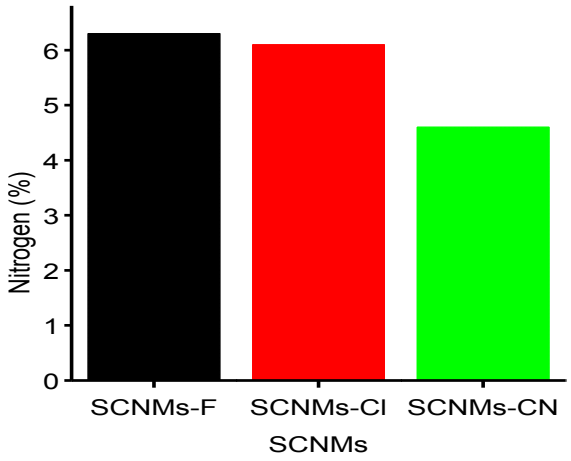


Figure 8: Nitrogen content in pristine SCNMs synthesized by use of *para*-$CF_3$, *para*-CN and *para*-Cl catalysts in pyridine.

## Conclusions

1,1′-Ferrocenyldiacrylonitriles were synthesized *via* a solvent-free approach and the X-ray crystallographic structure of 1,1′-ferrocenyldi[-2(4-{trifluoromethyl}phenyl)acrylonitrile] is reported for the first time. From the crystallographic studies, it is apparent that the X-ray

structures of the three catalysts are influenced by the size of the *para*-substituent.

N-CNTs were successfully synthesized by use of 1,1′-ferrocenyldiacrylonitriles as catalysts in either pyridine or acetonitrile as both the nitrogen and carbon source. The use of pyridine yielded N-CNTs as the major SCNM product and CS as the minor product. The use of acetonitrile gave N-CNTs as the major SCNM and CNFs as the minor product. The yields obtained with pyridine were generally higher that those obtained with acetonitrile.

Amongst the three catalyst used (i.e. *para*-$CF_3$, *para*-Cl and *para*-CN), the *para*-$CF_3$ catalyst was most efficient for the synthesis of high percentages of N-CNTs in pyridine and acetonitrile. The morphology, thermal stability and surface chemistry of N-CNTs synthesized by use of pyridine and the *para*-$CF_3$ catalyst significantly differed from the *para*-Cl or *para*-CN catalysts with pyridine as they were kinked and less thermally stable. This could imply that fluorine, just like oxygen, modulates the nitrogen content and species incorporated into N-CNTs.

The halogenated catalysts in acetonitrile promoted iron filling of N-CNTs and reduced the diameters of N-CNTs while decreasing the abundance of CNFs. On the other hand, no significant difference was observed in the tube diameters of N-CNTs obtained by use of pyridine and the three catalysts. This implied that the effect of halogens on tube diameters is dependent on the carbon:halogen ratio.

**Corresponding author**

*****Corresponding author. Telephone: +27-31 260 8256; Fax: +27-31 260 3091

*E-mail address*: nyamori@ukzn.ac.za (V. O. Nyamori)

**Acknowledgments**

This research was financed by the National Research Foundation (NRF) and University of KwaZulu-Natal (UKZN). Lucy M. Ombaka is grateful for the award of doctoral bursary from the UKZN, collage of Agriculture, Engineering and Science. We are grateful to Prof B. S. Martincigh for assisting in proofreading the manuscript and her critical comments of the manuscript. We are also grateful to Ms. T. A. Ntshele for assisting with purification of the catalysts.

## References

[1] L. M. Ombaka, P. Ndungu, V. O. Nyamori, Catal. Today 217 (2013) 65-75.

[2] H. Dai, Nanotube growth and characterization, in: M.S. Dresselhaus, G. Dresselhaus (Eds.), Carbon Nanotubes Synthesis, Structure, Properties and Applications, Springler-Verlag, Heidelberg, 2001, pp. 29–51.

[3] R. Yuge, K. Toyama, T. Ichihashi, T. Ohkawa, Y. Aoki, T. Manako, Appl. Surf. Sci. 258 (2012) 6958- 6962.

[4] J. J. Niu, J.N. Wang, Y. Jiang, L. F. Su, J. Ma, Microporous and Mesoporous Mater. 100 (2007) 1-5.

[5] G. Wang, Y. Ling, F. Qian, X. Yang, X.-X. Liu, Y. Li, J. of Power Sources 196 (2011) 5209-5214.

[6] M. I. Ionescu, Y. Zhang, R. Li, H. Abou-Rachid, X. Sun, Appl. Surf. Sci. 258 (2012) 4563-4568.

[7] L. M. Ombaka, P. G. Ndungu, V. O. Nyamori, J. Mater. Sci. 50 (2015) 1187-1200.

[8] P. Chen, F. Yang, A. Kostka, W. Xia, ACS Catal. 4 (2014) 1478-1486.

[9] B. Padya, D. Kalita, P. K. Jain, G. Padmanabham, M. Ravi, K. S. Bhat, J. Nanoelectron. Optoe. 8 (2013) 177-181.

[10] R. C. Che, L. M. Peng, X. F. Duan, Q. Chen, X. L. Liang, Adv. Mater. 16 (2004) 401-405.

[11] S. Liu, X. Tang, Y. Mastai, I. Felnerc, A. Gedanken, J. Mater. Chem. 10 (2000) 2502-2506.

[12] R. Lv, F. Kang, W. Wang, J. Wei, J. Gu, K. Wang, D. Wu, Carbon 45 (2007) 1433-1438.

[13] X. Gui, K. Wang, W. Wang, J. Wei, X. Zhang, R. Lv, Y. Jia, Q. Shu, F. Kang, D. Wu, Mater. Chem. Phys. 113 (2009) 634-637.

[14] V. O. Nyamori, S. D. Mhlanga, N. J. Coville, J. Organomet. Chem. 693 (2008) 2205-2222.

[15] E. N. Nxumalo, V. O. Nyamori, N. J. Coville, J. Organomet. Chem. 693 (2008) 2942-2948.

[16] E. N. Nxumalo, N. J. Coville, Materials 3 (2010) 2141-2171.

[17] E. N. Nxumalo, V. O. Nyamori, N. J. Coville, J. Organomet. Chem. 693 (2008) 2942-2948.

[18] L. M. Ombaka, P. G. Ndungu, B. Omondi, V. O. Nyamori, J. Coord. Chem. 67 (2014) 1905-1922.

[19] Bruker, APEX2, SAINT-Plus, XPREP and SADABS. Bruker AXS Inc., Madison, Wisconsin, USA. (2008).

[20] G. M. Sheldrick, Acta Cryst. A64 (2008) 112-122.

[21] L. J. Farrugia, J. Appl. Cryst. 32 (1999) 837-838.

[22] L. J. Farrugia, J. Appl. Cryst. 30 (1997) 565.

[23] R. S. Oosthuizen, V. O. Nyamori, Appl. Organomet. Chem. 26 (2012) 536-545.

[24] S. W. Pattinson, R. E. Diaz, N. A. Stelmashenko, A. H. Windle, C. Ducati, E. A. Stach, K. K. K. Koziol, Chem. Mater. 25 (2013) 2921-2923.

[25] A. Shaikjee, N. J. Coville, Carbon 50 (2012) 3376-3398.

[26] S. W. Pattinson, V. Ranganathan, H. K. Murakami, K. K. K. Koziol, A. H. Windle, ACS Nano 6 (2012) 7723-7730.

[27] L.Chen, K. Xia, L. Huang, L. Li, L. Pei, S. Fei, Int. J. Hydrogen Energy, 38 (2013) 3297-3303.

[28] A. Nieto-Màrquez, J. L. Valverde, M. A. Keane, Appl. Catal. A: General 352 (2009) 159-170.

[29] K. B. Teo, C. Singh, M. Chhowalla, W. I. Milne, Encyclopedia of nanoscience and nanotechnology 10 (2003) 1-22.

[30] L. Delzeit, I. McAninch, B. A. Cruden, D. Hash, B. Chen, J. Han, M. Meyyappan, J. Appl. Phys. 91 (2002) 6027-6033.

[31] A. C. Ferrari, J. Robertson, Philos. Trans. A Math Phys. Eng. Sci. 362 (2004) 2477-2512.

[32] H. Hiura, T. Ebbesen, K. Tanigaki, H. Takahashi, Chem. Phys. Lett. 202 (1993) 509-512.

[33] K. A. Wepasnick, B. A. Smith, J. L. Bitter, D. H. Fairbrother, Anal. Bioanal. Chem. 396 (2010) 1003-1014.

[34] Y. Liu, C. Pan, J. Wang, J. Mater. Sci. 39 (2004) 1091-1094.

[35] T. Sharifi, F. Nitze, H. R. Barzegar, C.-W. Tai, M. Mazurkiewicz, A. Malolepszy, L. Stobinski, T. Wågberg, Carbon 50 (2012) 3535-3541.

[36] L. M. Ombaka, P. G. Ndungu, V. O. Nyamori, RSC Adv. 5 (2015) 109-122.

[37] K. Chizari, A. Vena, L. Laurentius, U. Sundararaj, Carbon 68 (2014) 369-379.

[38] S. Santangelo, M. Lanza, C. Milone, J. Phys. Chem. C 117 (2013) 4815-4823.

[39] U.-J. Kim, C. A. Furtado, X. Liu, G. Chen, P. C. Eklund, J. Am. Chem. Soc. 127 (2005) 15437-15445.

[40] L. Vanyoreka, R. Meszarosa, S. Barany, Colloids and Surfaces A: Physicochem. Eng. Aspects 448 (2014) 140-146.

[41] A. Misra, P. K. Tyagi, M. K. Singh, D. S. Misra, Diamond Relat. Mater. 15 (2006) 385-388.

[42] T. Maiyalagan, B. Viswanathan, Mater. Chem. Phys. 93 (2005) 291-295.

[43] T. J. Bandosz (2009) Surface chemistry of carbon materials. In: Serp P, Fiueiredo JL (Eds.), Carbon materials fo catalysis. John Wiley & Sons, Inc. United States of America, pp 63.

[44] U. Ritter, N. G. Tsierkezos, Yu. I. Prylutskyy, L. Y. Matzui, V. O. Gubanov, M. M. Bilyi, M. O. Davydenko, J. Mater. Sci. 47 (2012) 2390-2395.

# CHAPTER FIVE

# TUNING THE NITROGEN CONTENT AND SURFACE PROPERTIES OF NITROGEN-DOPED CARBON NANOTUBES SYNTHESIZED USING A NITROGEN-CONTAINING FERROCENYL DERIVATIVE AND ETHYLBENZOATE

J Mater Sci
DOI 10.1007/s10853-014-8675-4

## Tuning the nitrogen content and surface properties of nitrogen-doped carbon nanotubes synthesized using a nitrogen-containing ferrocenyl derivative and ethylbenzoate

Lucy M. Ombaka · Patrick G. Ndungu · Vincent O. Nyamori

Received: 23 June 2014 / Accepted: 16 October 2014


**Abstract** Aligned nitrogen-doped carbon nanotubes (N-CNTs) containing 6.4–15.7 wt% of nitrogen were synthesized by pyrolysis of 3-ferrocenyl-2-(4-cyanophenyl)-acrylonitrile as the catalyst in either acetonitrile or a solution of acetonitrile and ethylbenzoate. For comparison, N-CNTs were synthesized by pyrolysis of 3-ferrocenyl-2-(4-cyanophenyl)acrylonitrile in toluene. The effect of oxygen and the carbon source used during synthesis was investigated. The use of 3-ferrocenyl-2-(4-cyanophenyl)acrylonitrile in acetonitrile as a nitrogen and carbon source selectively yielded mainly N-CNTs, while use of toluene as a carbon source yielded both N-CNTs and carbon spheres. Elemental analysis of the N-CNTs synthesized using both acetonitrile and ethylbenzoate (source of oxygen) indicated that addition of oxygen enhanced the nitrogen content of N-CNTs. This was further supported by results from Raman spectroscopy, and XRD revealed that the alignment of N-CNTs increased upon addition of oxygen. Electrical conductivity measurements of N-CNTs showed a negative relationship between the amount of oxygen in the starting materials and the conductivity of N-CNTs.

### Introduction

Doping of carbon nanotubes (CNTs) with nitrogen to form nitrogen-doped carbon nanotubes (N-CNTs) offers an appropriate channel for improving the electronic and physical properties of CNTs [1, 2]. Furthermore, the afore mentioned properties of N-CNTs can be improved by modulating their alignment and outer diameters (OD) [3].

## Supplementary Information

The supplementary information for Chapter five is indexed as Appendix 2 and is located at the end of the thesis.

# Tuning the nitrogen content and surface properties of nitrogen-doped carbon nanotubes synthesized using a nitrogen-containing ferrocenyl derivative and ethylbenzoate

**Lucy M. Ombaka[‡], Patrick G. Ndungu[#] and Vincent O. Nyamori[*]**

School of Chemistry and Physics, University of KwaZulu-Natal, Westville Campus, Private Bag X54001, Durban 4000, South Africa

## Abstract

Aligned nitrogen-doped carbon nanotubes (N-CNTs) containing 6.4-15.7 wt.% of nitrogen were synthesized by pyrolysis of 3-ferrocenyl-2-(4-cyanophenyl)acrylonitrile as the catalyst in either acetonitrile or a solution of acetonitrile and ethylbenzoate. For comparison, N-CNTs were synthesized by pyrolysis of 3-ferrocenyl-2-(4-cyanophenyl)acrylonitrile in toluene. The effect of oxygen and the carbon source used during synthesis was investigated.

The use of 3-ferrocenyl-2-(4-cyanophenyl)acrylonitrile in acetonitrile as a nitrogen and carbon source selectively yielded mainly N-CNTs, while use of toluene as a carbon source yielded both N-CNTs and carbon spheres. Elemental analysis of the N-CNTs synthesized by using both acetonitrile and ethylbenzoate (source of oxygen) indicated that addition of oxygen enhanced the nitrogen content of N-CNTs. This was further supported by results from Raman spectroscopy, X-ray diffraction (XRD), Fourier transform infrared spectroscopy and inverse gas chromatography surface energy analysis. The higher nitrogen-containing N-CNTs were less graphitic and showed a higher base constant ($K_b$) compared to N-CNTs synthesized without oxygen. Analysis of transmission electron microscopy images showed that the outer diameters of the N-CNTs decreased upon increasing the oxygen composition by mass in the synthesis precursors from 1-4 wt.% oxygen, the oxygen was derived from ethylbenzoate. In addition, the scanning electron microscopy and XRD revealed that, the alignment of N-CNTs increased upon addition of oxygen. Electrical conductivity measurements of N-CNTs showed a negative relationship between the amount of oxygen in the starting materials and the conductivity of N-CNTs.

Keywords: Nitrogen-doped carbon nanotube; Chemical vapour deposition; Surface properties; Ethylbenzoate; Acetonitrile

## 1. Introduction

Doping of carbon nanotubes (CNTs) with nitrogen to form nitrogen-doped carbon nanotubes (N-CNTs) offers an appropriate channel for improving the electronic and physical properties of CNTs [1, 2]. Furthermore, the aforementioned properties of N-CNTs can be improved by modulating their alignment and outer diameters (OD) [3]. Consequently, research is increasingly being focused on developing synthetic procedures that facilitate the control of the type of nitrogen species incorporated and nitrogen content, alignment and OD of N-CNTs during synthesis [4]. N-CNTs contain electron-rich nitrogen species such as pyridinic and pyridinic oxide [5] moieties, which enhance their electronic and physical properties. As a result, N-CNTs can be suitable for a wide range of applications and as components in electronic [6] and field emission devices [7]. N-CNTs can also be used as catalysts or as metal catalyst supports [8]. For instance, well aligned N-CNTs have shown good field emission properties [9], while increasing the amount of pyridinic nitrogen in N-CNTs enhances the catalytic activity of Pd supported on N-CNTs [10].

One useful approach in increasing the percentage of nitrogen-doping and the nitrogen species incorporated into the tubes is the use of high nitrogen-containing organic precursors, such as mixtures of imidazole and acetonitrile together with organometallic catalysts during synthesis of the N-CNTs [11]. In a similar manner, the level and type of nitrogen-doping can be increased by the use of nitrogen-containing organometallic compounds as catalysts together with nitrogen-containing carbon sources such as acetonitrile. For example, Nxumalo *et al*. [12] reported the use of nitrogen-containing ferrocenyl derivatives as catalysts, and as a source of carbon and nitrogen in the synthesis of N-CNTs. Another useful approach entails the incorporation of oxygen-containing compounds, such as alcohols and water, which act as oxidising agents during the synthesis of N-CNTs [4]. For instance, different ratios of alcohols and nitrogen-containing organic solvents have been used to control the nitrogen content and OD of N-CNTs [13].

Esters are volatile oxygen containing organic compounds, which are usually less toxic compared with alcohols such as methanol. Their application as a source of oxygen and in the modulation of N-CNTs remains unexploited. In this account, ethylbenzoate was used as the ester of choice because it contains a low ratio of O:C (2:9) making it a good source of low oxygen content. Additionally, ethylbenzoate is a non-polar solvent, which promotes the solubility of the ferrocenyl catalyst in ethylbenzoate. Hence, we report the use of different ratios of ethylbenzoate and acetonitrile to modulate the nitrogen content, OD, and alignment

of N-CNTs. Also we report for the first time the effect of increasing nitrogen-doping levels on the surface energy of N-CNTs. In addition, the chemical vapour deposition (CVD) method for the synthesis of N-CNTs by using 3-ferrocenyl-2-(4-cyanophenyl)acrylonitrile as a catalyst, and also as a carbon and nitrogen source, is reported for the first time.

## 2. Experimental

### 2.1 Materials

Ferrocenecarboxaldehyde 98%, 4-cyanophenylacetonitrile 97%, piperidine 99%, ethylbenzoate 99%, diethyl ether 99.8% and hexane 97% were purchased from Sigma Aldrich. Acetonitrile 99.9% and toluene 99.4% were purchased from LiChroSolv. All reagents and solvents were of analytical grade and were used as received from the suppliers. Aluminium-backed silica gel 60 $F_{254}$ plates purchased from Merck were used to carry out thin layer chromatography in solvents of varying polarity. Purification of 3-ferrocenyl-2-(4-cyanophenyl)acrylonitrile by column chromatography was accomplished by using Merck silica gel 60, 0.063-0.2 mm.

N-CNTs were synthesized in a quartz tube (inner diameter 27 mm, length 850 mm) placed in a muffle furnace (Elite Thermal Systems Limited Model No. TSH12/50/610). The carrier gas used during synthesis of N-CNTs was 10% hydrogen in argon (v/v) purchased from Airflex Industrial Gases. The rate of injection was controlled by a syringe pump (model no. NE-300, New Era Pump Systems Inc.).

### 2.2 Characterization

The catalyst, 3-ferrocenyl-2-(4-cyanophenyl)acrylonitrile was characterized by use of Fourier transform infrared (FTIR) spectrometer, nuclear magnetic resonance (NMR) spectrometry, mass spectrometry and determination of its melting point. The melting point was determined by using a Bibby Stuart Scientific model SMP3 apparatus. Infrared spectra were recorded on a PerkinElmer Universal ATR Spectrum 100 FTIR spectrometer. The $^{1}$H- and $^{13}$C-NMR spectra were recorded on a 400 MHz Bruker Ultrashield spectrometer at room temperature. A mass spectrum (MS) of the catalyst was obtained from a Waters Synapt G2-mass spectrometer using electrospray ionization (ESI).

Images of N-CNTs were taken by using transmission electron microscopy (TEM) (JEOL JEM 1010) and a scanning electron microscopy (SEM) (JEOL JSM 6100). A high resolution-TEM (JEOL 2100) was used to take higher magnification images of the N-CNTs.

X-ray diffraction (XRD) spectra were obtained from a Rigaku D/max RB X-ray diffractometer by using graphite monochromatized high-intensity Cu $K_\alpha$ radiation ($\lambda$ = 0.15406 nm). Elemental analysis was performed on a LECO CHNS-932 elemental analyzer, standardized with acetanilide. To determine the graphitic nature of the N-CNTs, a Raman spectrometer (DeltaNu Advantage 532™) was used. The thermo-stability of N-CNTs was determined by using a Q Series™ Thermal Analyzer DSC/TGA (Q600). The surface energy and acid-base properties were determined with an Inverse Gas Chromatography Surface Energy Analyzer (IGC-SEA) (SMS, Alperton, UK). Infrared spectra of N-CNTs embedded into KBr pellets ware recorded on a PerkinElmer FTIR spectrometer spectrum RX1. The I-V properties of N-CNTs were determined by using a four-point probe model connected to a digital micro voltmeter (DMV-001 Scientific Equipment ROORKEE), a low current source (LCS-02 Scientific Equipment ROORKEE) and a Proportional Integral Derivative (PID) controlled oven (PID 200).

### 2.3 Synthesis of 3-ferrocenyl-2-(4-cyanophenyl)acrylonitrile

The catalyst, 3-ferrocenyl-2-(4-cyanophenyl)acrylonitrile, was synthesized *via* a mechanochemical approach under solvent-free conditions following the procedure outlined by Imrie *et al*. [14] Ferrocenecarboxaldehyde (200.0 mg, 0.93 mmol) and 4-cyanophenylacetonitrile (132.0 mg, 0.93 mmol) were ground together in the presence of 2 drops of piperidine to yield a maroon paste. The paste was first dried in air, then under vacuum to obtain a maroon product. The maroon product was purified by means of column chromatography on silica gel with a solvent system of (1:1) hexane/diethyl ether to obtain 3-ferrocenyl-2-(4-cyanophenyl)acrylonitrile as dark red crystals. Yield (311.0 mg; yield of 98%); m. p. 139 ºC (lit [57] 140 ºC). IR ($cm^{-1}$) 3099, 3050, 2943, 2225, 2207, 1609, 1585, 1452, 1408, 1367, 1312, 1252, 1178, 1103, 1032, 998, 920, 833, 826, 543, 501, 487, 432; $^1$H-NMR (ppm) in $CDCl_3$: 7.68 (4H, s, ArH), 7.50 (1H, s, CH), 4.99 (2H, t, *J* 1.9, $C_5H_4$), 4.61 (2H, t, *J* 1.8, $C_5H_4$), 4.24 (5H, s, $C_5H_5$); $^{13}$C-NMR (ppm) in $CDCl_3$ 132.85, 125.45, 146.60, 139.12, 118.56, 118.34, 111.36, 104.52, 77.18, 72.56, 70.68, 70.10. MS ($C_{20}H_{14}FeN_2$) ES: $[M]^+$ *m/z* calcd 338.050638, found 338.0500 (Supplementary Information S1).

### 2.4 Synthesis of N-CNTs

N-CNTs were synthesized by use of a floating catalyst CVD method at 800, 850 and 900 °C. The CVD experimental set-up and procedure used is described in detail elsewhere [15, 16]. Briefly, a flow rate of 0.8 mL $min^{-1}$ was used to feed a solution of the precursors into a

quartz tube which was placed in the middle of a tube furnace. The solution was carried through the quartz tube by a carrier gas made-up of 10% hydrogen in argon (v/v) which was pumped through the system at a rate of 100 mL $min^{-1}$ at 80 kPa. The furnace was set to a reaction temperature of 800, 850 and 900 °C for 30 minutes, and the products were collected from the hot zone of the quartz tube upon completion of the reaction

The compound, 3-ferrocenyl-2-(4-cyanophenyl)acrylonitrile, was used as a catalyst while acetonitrile or toluene were used as a carbon source. In addition to being a carbon source, acetonitrile also acted as a nitrogen source. The solution used to synthesize N-CNTs was made by dissolving 0.25 g of the catalyst in 9.75 g of acetonitrile or toluene to make a total of 10 g of solution (i.e. 2.5 wt.% of catalyst).

In order to study the effect of oxygen during synthesis, acetonitrile was used as a carbon and nitrogen source at a synthesis temperature of 850 °C. To introduce varying amounts of oxygen into the synthesis precursors, 1, 2, 3 and 4 wt.% of oxygen was derived from ethylbenzoate using the formula:

$$\text{wt.\% oxygen} = \frac{\text{total weight of oxygen in } x \text{ g of ethylbenzoate}}{10 \text{ g}} \text{ x } 100$$

where $x$ g = 0.5, 1.0, 1.5 or 2.0 g of ethylbenzoate

Exactly 0.5, 1.0, 1.5 or 2.0 g of ethylbenzoate was added to 0.25 g of the catalyst and each solution was then prepared to a total mass of 10 g with acetonitrile. See Supplementary Information S2 for a summary of the oxygen and nitrogen percentages in acetonitrile solution. Prior to characterization, all N-CNTs were synthesized in triplicate and the products from the three runs pooled together.

### 2.5 Electrical conductivity measurements

For I-V measurements of pristine N-CNTs, thin films of the N-CNTs were prepared based on modification of a previously reported vacuum filtration method [17]. In brief, 30 mg of N-CNTs were suspended in 10 mL of ethanol and sonicated for 30 minutes to form a homogeneous mixture. The mixture was vacuum filtered through Whatman filter paper. The filter paper containing the N-CNTs was then dried in an oven at 100 °C to evaporate excess ethanol and adsorbed water. The resulting film of supported N-CNTs was stored in a sealed container for further conductivity analysis. The thickness of the film was measured by using a micrometre screw gauge. To determine the exact N-CNT film thickness, the thickness of the filter paper was subtracted from the thickness of the filter paper together with N-CNTs

layer. As a control measure, I-V measurements were performed on the filter paper alone and this showed no conductivity.

## 3. Results and discussion

### 3.1 Synthesis of 3-ferrocenyl-2-(4-cyanophenyl)acrylonitrile

Mechanochemical grinding of ferrocenecarboxaldehyde and 4-cyanophenylacetonitrile in the presence of a catalytic amount of piperidine yielded 3-ferrocenyl-2-(4-cyanophenyl)-acrylonitrile and water as a by-product (Scheme 1).

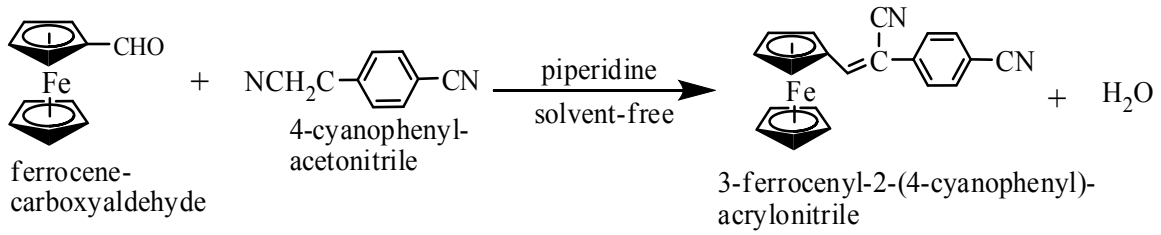


**Scheme 1**: Synthesis of 3-ferrocenyl-2-(4-cyanophenyl)acrylonitrile

Upon grinding the reactants for 2 minutes, a melt was formed which turned into a solid after 5 minutes. Formation of the product was monitored by the use of thin layer chromatography, FTIR and NMR spectroscopy. Formation of the product was characterized by the disappearance of a sharp carbonyl absorption band (≈1650 $cm^{-1}$) and the appearance of a strong nitrile absorption band (≈2207 $cm^{-1}$) in the solid-state FTIR spectra. From the $^{1}$H-NMR spectra, formation of the product was marked by the disappearance of a carbonyl proton resonance peak (≈10 ppm) and the appearance of an ethylene proton resonance peak (≈7.5 ppm). This was further verified by use of $^{13}$C-NMR spectra, in which the strong carbonyl carbon resonance peak (≈190 ppm) disappeared, and MS confirmed that the compound was prepared.

### 3.2 Effect of acetonitrile or toluene as carbon source on selectivity towards N-CNTs

The compound, 3-ferrocenyl-2-(4-cyanophenyl)acrylonitrile ($[M]^{+}$ *m/z* 338.0500), was used as a catalyst to synthesize N-CNTs in either acetonitrile or toluene. To acquire accurate information on the effect of carbon source, only pristine N-CNTs were studied. A higher product yield was obtained with toluene than with acetonitrile. Synthesis conducted by the use of acetonitrile selectively yielded mainly N-CNTs (Table 1, Fig. 1a and 2a) and a small percentage of amorphous carbon while toluene yielded a mixture of N-CNTs and carbon

spheres (CS) (Fig. 1b and 2b). From the TEM images of N-CNTs synthesized in acetonitrile or toluene, bamboo and cup-shaped compartments (see Fig. 2) associated with nitrogen-doping were evident [18].

The selectivity towards formation of N-CNTs when acetonitrile is used can be explained by considering the decomposition products of toluene and acetonitrile as well as the carbon shell formation mechanism [19]. According to this mechanism, formation of N-CNTs or CS is controlled by two competing processes, i.e. the catalyst forward rate ($V_s$) and the carbon shell growth rate ($V_p$). When $V_p$ is greater than $V_s$ the formation of N-CNT is favoured, while when $V_p$ is almost equal to or less than $V_s$ a mixture of N-CNTs and CS is formed [20].

**Table 1** Product distribution of pristine N-CNTs and carbon spheres obtained by using either acetonitrile or toluene as the carbon source and 3-ferrocenyl-2-(4-cyanophenyl)acrylonitrile as the catalyst

| *Exp. | *$T_{max}$ (°C) | Carbon source | Product yield (mg) | N-CNTs % | Carbon spheres % | Amorphous carbon + $FeO_x$ % |
|---|---|---|---|---|---|---|
| 1 (a) | 900 | toluene | 449.9 | 10 | 85 | 5 |
| (b) | 900 | acetonitrile | 209.6 | 87 | - | 13 |
| 2 (a) | 850 | toluene | 242.8 | 50 | 40 | 10 |
| (b) | 850 | acetonitrile | 140.1 | 95 | - | 5 |
| 3 (a) | 800 | toluene | 210.0 | 5 | 5 | 90 |
| (b) | 800 | acetonitrile | 112.6 | 90 | - | 10 |

*Exp: Experiment; *$T_{max}$: Maximum synthesis temperature

Acetonitrile decomposes to form hydrogen cyanide and methane in the gas phase as the first generation products [21]. These carbon species are light hydrocarbons that have been reported to be efficient sources of carbon material [22] resulting in $V_p$ being higher than $V_s$ which favours formation of N-CNTs. On the contrary, toluene decomposes to form benzyl and phenyl radicals by losing atomic hydrogen and methyl respectively [23]. The atomic hydrogen generated creates a hydrogen-rich surface on the catalyst that does not favour carbon growth. This results in $V_p$ being equal to or less than $V_s$ leading to formation of CS and N-CNTs. Additionally, the benzyl and phenyl radicals could act as nucleation sites to grow icosahedral shells which can roll-up to form carbon spheres [22].

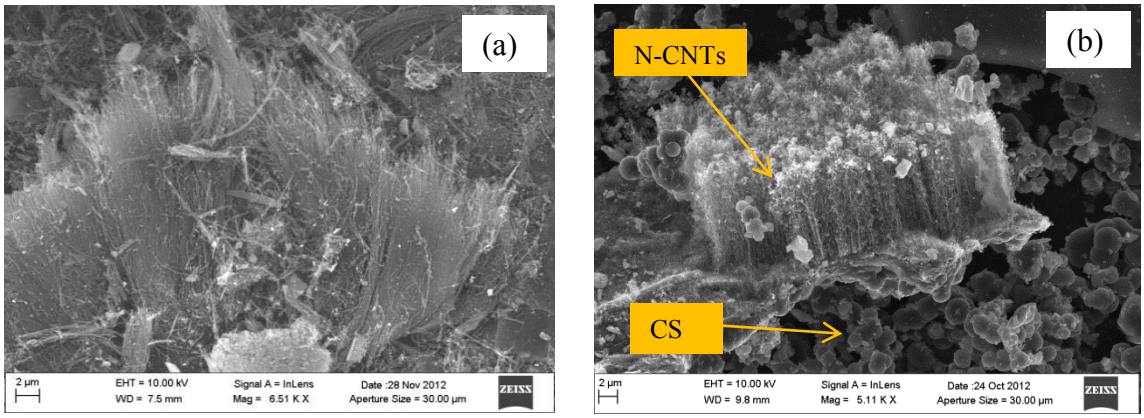


**Fig. 1** SEM images of pristine N-CNTs synthesized at 850 °C by using (a) acetonitrile and (b) toluene and 3-ferrocenyl-2-(4-cyanophenyl)acrylonitrile as the catalyst. Note that CS are only present in Fig.1b

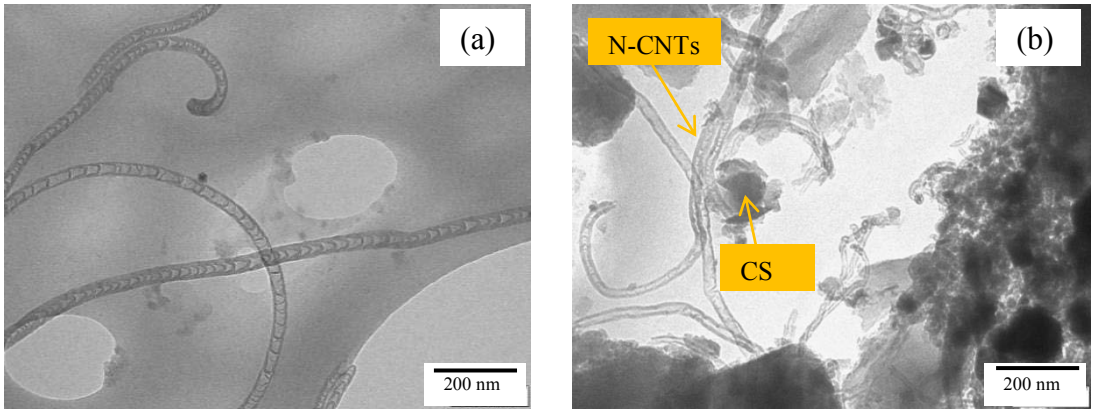


**Fig. 2** TEM images of pristine N-CNTs synthesized at 850 °C by using (a) acetonitrile and (b) toluene and 3-ferrocenyl-2-(4-cyanophenyl)acrylonitrile as the catalyst

At 850 °C when either acetonitrile or toluene was used, the highest percentage of N-CNTs was obtained (Table 1, entries 2a and 2b). Also the use of toluene at a higher synthesis temperature (900 °C) yielded more carbon spheres than N-CNTs, while at a lower temperature (800 °C) mainly amorphous carbons were obtained (Table 1, entries 1a and 3a). Since acetonitrile was more selective than toluene at 850 °C, it was used to investigate the effect of oxygen during synthesis of N-CNTs at this temperature.

### 3.3 Effect of oxygen on the synthesized N-CNTs

#### 3.3.1 Effect of oxygen on the yield of N-CNTs

Increasing the oxygen wt.% in the starting materials resulted in a decrease of the product yield (see Supplementary Information S3). Oxygen could be added up to 4 wt.% while maintaining an effective growth of N-CNTs. Addition of 5 wt.% oxygen resulted in

formation of more amorphous carbons than N-CNTs while addition of 6 wt.% oxygen resulted in no product formation. This was expected, considering that, at high temperatures, oxygen reacts with carbon present in the reaction chamber to form $CO_x$ species, which exit the chamber as exhaust gases. Hence, as the oxygen percentage was increased, more carbon was converted to $CO_x$ species reducing the carbon supply needed for N-CNT growth and resulting in a lower yield. As the oxygen percentage increased, the catalyst particle size also increased due to formation of larger $Fe_3C$ particles (see Section 3.3.4). The larger $Fe_3C$ particles may be poor catalysts for the initiation stage of N-CNT growth leading to lower N-CNT yields.

### 3.3.2 Effect of oxygen on nitrogen content of N-CNTs

The use of 3-ferrocenyl-2-(4-cyanophenyl)acrylonitrile in a solution of ethylbenzoate and acetonitrile at 850 °C yielded N-CNTs with bamboo compartments as evidenced from the TEM images (Fig. 3).

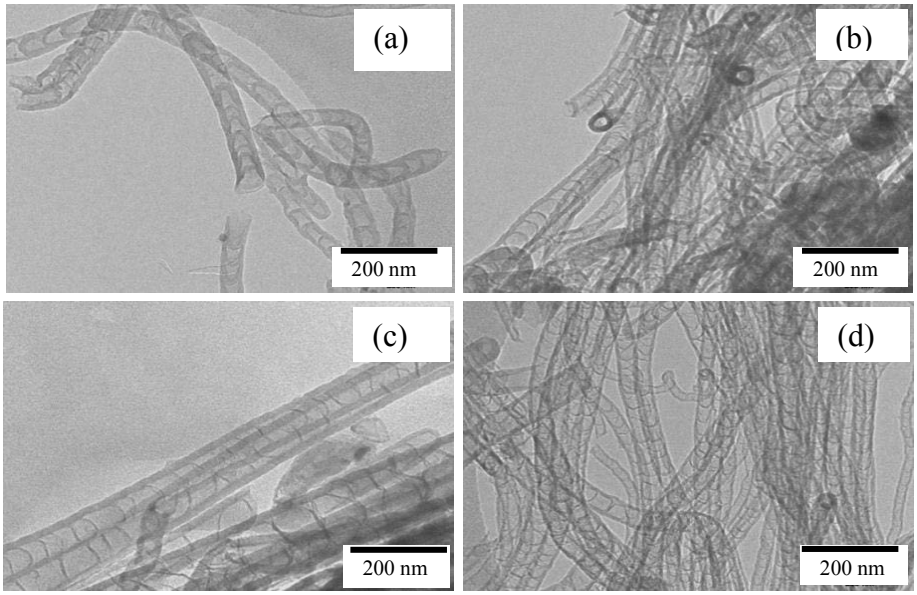


**Fig. 3** TEM images of pristine N-CNTs synthesized at 850 °C by using (a) only acetonitrile, (b) 1 wt.% oxygen in acetonitrile, (c) 2 wt.% oxygen in acetonitrile, (d) 3 wt.% oxygen in acetonitrile. The oxygen was derived from ethylbenzoate and the catalyst used was 3-ferrocenyl-2-(4-cyanophenyl)acrylonitrile

From elemental analysis, the use of only acetonitrile yielded N-CNTs containing 6.4 wt.% of nitrogen. The nitrogen-doping levels increased from 6.4 wt.% to 15.7 wt.% upon addition of 1 wt.% of oxygen to acetonitrile (Fig. 4 (a). A further increase in the oxygen content (2-4

wt.%) did not result in an additional increment of the nitrogen-doping level. Conventionally, the level of nitrogen-doping is expected to decrease with a decrease in the amount of nitrogen present in the precursors [24]. However, introduction of 1 wt.% oxygen resulted in an increase in nitrogen-doping as the weight % of nitrogen in the precursors decreased. Oxygen is not doped into the tubes but can enhance the incorporation of pyridinic oxide species. The analysis shows that a low oxygen concentration (1 wt.%) enhances nitrogen-doping of N-CNTs while higher concentrations of oxygen (2-4 wt.%) do not favour it. In a similar manner, Bepete *et al.*[4] and Liu *et al.* [25] observed an increase in nitrogen-doping level in N-CNTs upon introduction of low oxygen concentrations by using alcohols and water respectively. A possible explanation is that, at low oxygen concentration (1 wt.%), a favourable oxidative atmosphere which reduces the concentration of reactive hydrogen species is formed. The reduction of hydrogen species promotes a conducive environment for faster chemisorption of nitrogen species into CNTs [26]. In contrast, higher oxygen concentrations (2-4 wt.%) create a highly oxidative atmosphere that reacts with nitrogen species forming stable nitrogen dioxide and hence, reducing the amount of nitrogen chemisorbed into N-CNTs. Except for N-CNTs synthesized with 2 wt.% oxygen, the average length of the compartments of all other N-CNTs reduced with increase in nitrogen-doping levels (cf Figs. 4a and b). This indicated that higher nitrogen-doping levels promoted a faster rate of closure of the compartments resulting in shorter compartments [27].

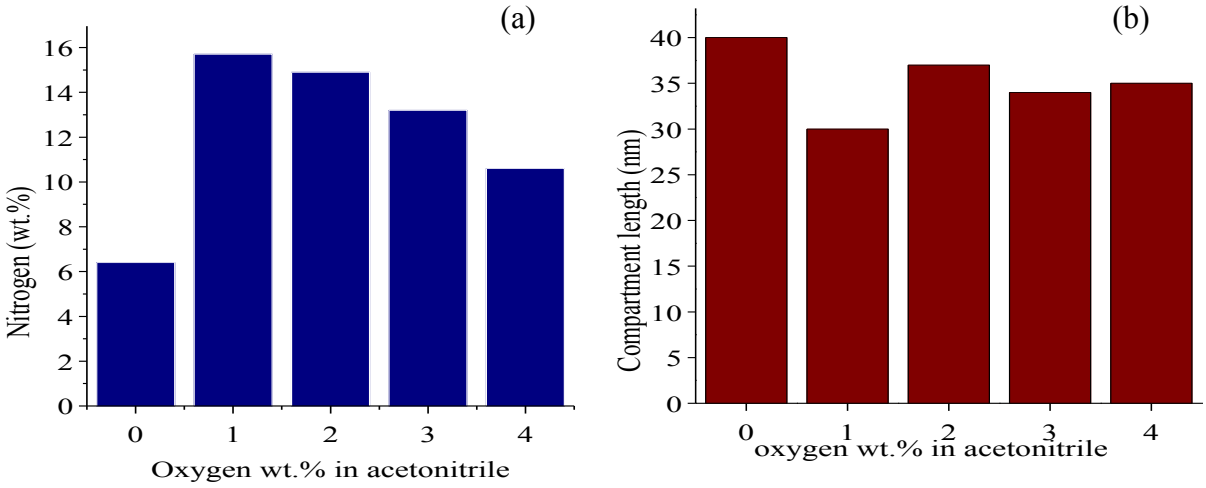


**Fig. 4** (a) Nitrogen content and (b) compartment length of pristine N-CNTs synthesized by using different wt.% of oxygen derived from ethylbenzoate in acetonitrile at 850 °C

### 3.3.3 Effect of oxygen on the morphology of N-CNTs

The OD of N-CNTs can be modulated by varying the levels of nitrogen-doping in N-CNTs. For example, Koós *et al*. reported a decrease in the OD of N-CNTs as a result of increased nitrogen-doping of CNTs [24]. This is because nitrogen species are predominant on the tube edges leading to closure of the tubes and making it unfavourable for further graphitic layering [27]. N-CNTs synthesized by using 0-4 wt.% oxygen in acetonitrile showed an average OD of 42-60 nm (Table 2).

The largest average OD was 60 nm from N-CNTs synthesized in acetonitrile only, while the smallest average OD was 42 nm from N-CNTs synthesized in the presence of 4 wt.% of oxygen. In general, addition of 1-4 wt.% of oxygen to acetonitrile resulted in a decrease of the OD. Since the nitrogen-doping levels directly correlate with OD, it is possible that the decrease in tube OD was due to an increase in nitrogen-doping (Fig.4). This observation parallels those reported by Liu *et al*. who observed a constant decrease of tube OD with increase of nitrogen-doping in N-CNTs [11]. However, at higher oxygen concentrations (2-4 wt.% oxygen), a further decrease in the OD of N-CNTs can be associated with etching of the outer walls. The etching effect on N-CNTs caused by high oxygen concentrations was observed from HR-TEM image analysis (Fig. 5).

**Table 2** Effect of oxygen on the morphology of pristine N-CNTs synthesized by using acetonitrile and ethylbenzoate at 850 °C and 3-ferrocenyl-2-(4-cyanophenyl)acrylonitrile as the catalyst

| wt.% Oxygen | *Ave. OD±SD (nm) | *Ave. ID±SD (nm) | *Ave. wall thickness±SD (nm) | N-CNTs % | Amorphous carbon, + $FeO_x$ % |
|---|---|---|---|---|---|
| 0 | 60±40 | 22±19 | 14±5 | 95 | 5 |
| 1 | 55±23 | 35±20 | 7±6 | 90 | 10 |
| 2 | 47±24 | 32±21 | 5±3 | 85 | 15 |
| 3 | 46±22 | 36±16 | 4±3 | 78 | 22 |
| 4 | 42±20 | 39±17 | 4±3 | 65 | 35 |

Ave.: average; OD: outer diameter; ID: inner diameter; SD: standard deviation,

*experimentally measured values

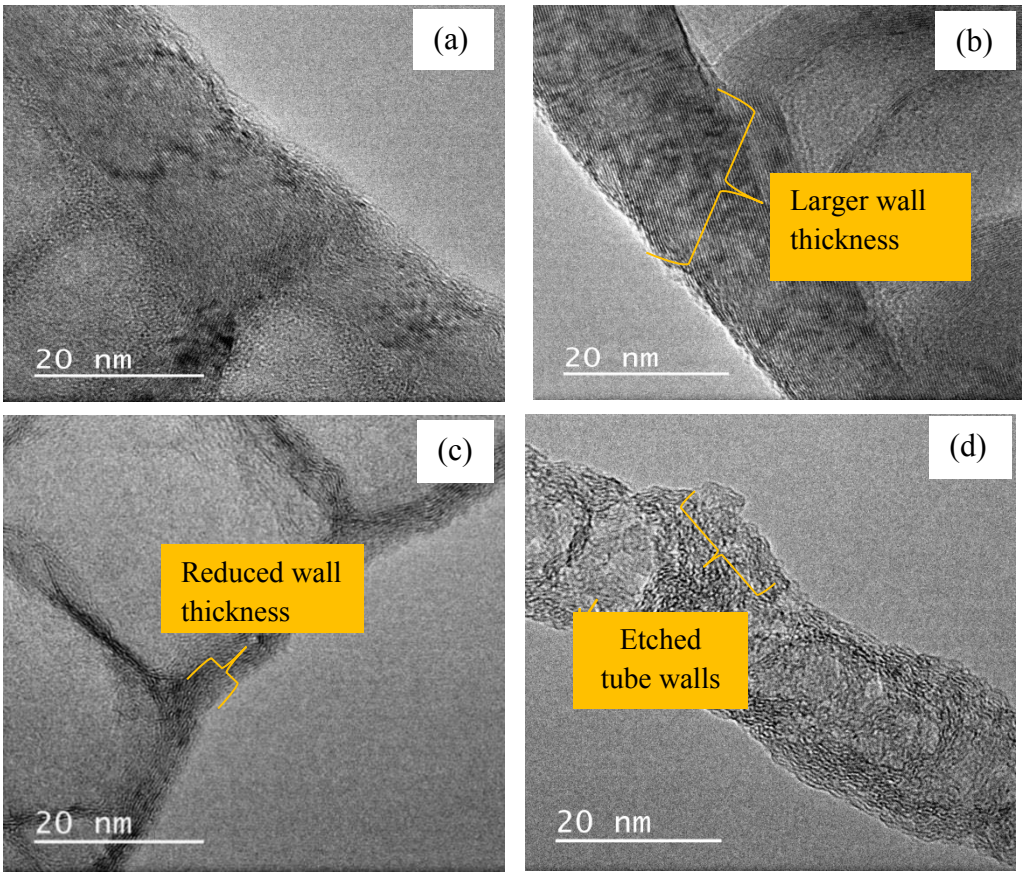


**Fig. 5** HR-TEM images of pristine N-CNTs synthesized at 850 °C by using (a) only acetonitrile, (b) 1 wt.% oxygen, (c) 3 wt.% oxygen and (d) 4 wt.% oxygen in acetonitrile and 3-ferrocenyl-2-(4-cyanophenyl)acrylonitrile as the catalyst

Images of N-CNTs synthesized in higher oxygen contents (3-4 wt.% oxygen) showed evidence of partially formed tubes, serrated tube walls and reduced wall thickness (Fig. 5). This could imply that at a higher oxygen concentration, a highly oxidative atmosphere forms in the reaction chamber. The highly oxidative atmosphere etches the outer walls of the N-CNTs leading to formation of thinner tube walls. Another possible explanation is that, oxygen forms a stable oxidized ring around the outer walls of N-CNTs. The stable oxidized ring hinders further deposition of carbon layers onto the outer walls of N-CNTs thus resulting a in smaller OD [26]. In general, the wall thickness reduced as increasing amounts of oxygen were added to acetonitrile. The inner diameters of N-CNTs were observed to increase with increase in oxygen percentage. This increase in inner diameter can be attributed to an increase in the catalyst size (Fig. 6) as the oxygen percentage increased. As the catalyst size increases, its diameter also increases resulting in an increase in the size of the inner cavity of

N-CNTs [28]. Ci *et al*. [29] who observed an increase in inner diameters of CNTs with increasing iron catalyst size made similar observations.

### 3.3.4 Effect of oxygen on crystallinity and graphene interlayer spacing

XRD characterization of CNTs gives useful information on structural strain, impurities, OD and distribution of chirality in CNTs [30]. The intensity and width of the $C_{002}$ reflection of graphene can be associated with various microstructural parameters of N-CNTs, namely: the number of graphene layers, variations of the interlayer spacing, lattice distortions, tube OD, tube alignment and crystallinity of the graphene layers [31]. The XRD patterns of N-CNTs are similar to that of graphite and comprise of a graphite-like peak ($C_{002\ l}$) associated with the interlayer spacing of graphene and a family of ($C_{h,k,0}$) peaks caused by the honeycomb lattice of a single graphene sheet [30].

The diffractograms of N-CNTs synthesized by using 0-4 wt.% oxygen in acetonitrile are shown in Fig. 6. For all diffractograms, the peak at $2\theta = 26.4°$ showed a strong intensity and it was indexed as the $C_{(002)}$ reflection of graphite [31]. The $C_{(002)}$ peak of N-CNTs synthesized by using acetonitrile alone was sharper and narrower compared with the $C_{(002)}$ peaks of N-CNTs synthesized in the presence of oxygen. Additionally, the full widths at half maxima (FWHM) of the $C_{(002)}$ peaks increased linearly with increase in oxygen content in the precursors (Table 3).

Broadening of the FWHM of the $C_{(002)}$ peak can either be due to a decrease in crystallinity caused by an increase in the nitrogen-doping levels, or a decrease in OD of the N-CNTs. An increase in nitrogen-doping increases the structural strain by increasing the surface defects on the regular graphite layers of the CNTs leading to broadening of the FWHM [32]. Hence, N-CNTs synthesized in the presence of acetonitrile alone, which had a smaller FWHM were considered more crystalline than those synthesized in the presence of oxygen [33].

Likewise, broadening of the $C_{(002)}$ peak can be induced by an increase in structural strain resulting from changes in the interlayer spacing (d-spacing). The d-spacing of the synthesized N-CNTs was ≈0.34 nm (Table 3) which is comparable to those documented in previous reports [34, 35]. From XRD analysis, the value of the calculated d-spacing was observed to increase with a decrease in the tube OD and wall thickness caused by the addition of oxygen. Previous studies have shown that as the tube OD decreases, the number of walls reduces and the curvature of the tube walls increases resulting in increased strain in the nanotubes [35]. The increase in strain brings about columbic repulsions between like charges on the walls resulting in an increased d-spacing and FWHM. On the contrary, as the

tube OD increase, the wall curvature decreases leading to a decrease of strain in the nanotubes. This results in an increased interaction between the walls leading to a decrease of the d-spacing. Hence, the increase in d-spacing and FWHM resulting from a decrease in tube OD and wall thickness was consistent with observations in literature [35]. The intensity of the $C_{(002)}$ peak showed a correlation with the alignment of N-CNTs which is discussed in Section 3.3.7.

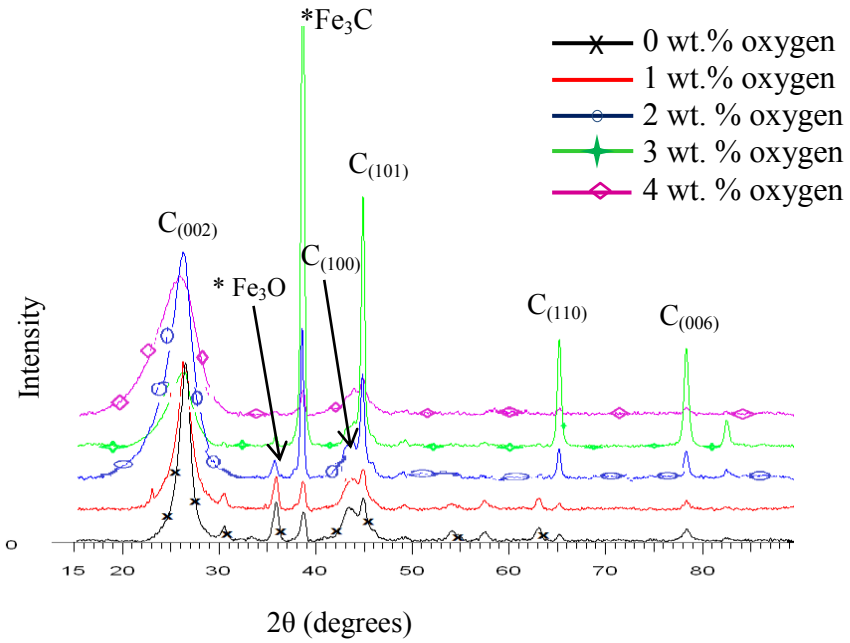


**Fig. 6** XRD diffractograms of pristine N-CNTs synthesized by using 0-4 wt.% oxygen in acetonitrile at 850 °C using 3-ferrocenyl-2-(4-cyanophenyl)acrylonitrile as the catalyst. The residual iron carbide from the catalyst is symbolised by an asterisk (*)

A peak at ≈38.6° with an interlayer spacing of ≈0.23 nm was observed in all the diffractograms and it was indexed as the $Fe_3C$ reflection [36]. The presence of $Fe_3C$ peak could imply that $Fe_3C$ was the predominant catalytic phase during N-CNTs growth as suggested by Wirth *et al*. [37] From the diffractograms, addition of 1-3 wt.% of oxygen did not hamper the formation of $Fe_3C$, but instead promoted it as the peak intensity increased when 1-3 wt.% of oxygen was used. This increment in residual iron carbide was also evidenced from the thermogravimetric curves of N-CNTs (Fig. 8) which showed an increase in the residual weight when 1 to 3 wt.% of oxygen was used. However, addition of 4 wt.% oxygen resulted in a sharp decrease in the intensity of the $Fe_3C$ peak and the residual weight of N-CNTs. This could imply that addition of 4 wt.% oxygen retarded the formation of $Fe_3C$. Furthermore, as the $Fe_3C$ reflection intensity increased, the $C_{(002)}$ intensity was

observed to decrease monotonically. This could imply that the crystallinity of $Fe_3C$ influenced the intensity of $C_{(002)}$ peak.

**Table 3** X-ray structural parameters of pristine N-CNTs synthesized by using 0-4% oxygen in acetonitrile at 850 °C and 3-ferrocenyl-2-(4-cyanophenyl)acrylonitrile as the catalyst

| wt.% Oxygen | *FWHM of $C_{(002)}$ peak (°) | Intensity of $C_{(002)}$ peak | Interlayer spacing of $C_{(002)}$ peak (nm) | Intensity of $Fe_3C$ peak | Interlayer spacing of $Fe_3C$ (nm) |
|---|---|---|---|---|---|
| 0 | 1.258 | 8113 | 0.3369 | 3810 | 0.2328 |
| 1 | 1.519 | 6425 | 0.3386 | 3833 | 0.2330 |
| 2 | 1.847 | 4921 | 0.3407 | 6577 | 0.2335 |
| 3 | 2.794 | 3135 | 0.3464 | 23260 | 0.2332 |
| 4 | 4.296 | 6053 | 0.3506 | 923 | 0.2331 |

*FWHM: full width at half maximum

### 3.3.5 Effect of oxygen on the graphitic nature of N-CNTs

The graphitic nature of the N-CNTs was determined by using Raman spectroscopy. The Raman spectra of all synthesized N-CNTs showed two first order peaks, i.e. a disorder band (D-band) at 1345-1367 $cm^{-1}$and a graphitic band (G-band) at 1553-1601 $cm^{-1}$ (Fig. 7a). The D-band corresponds to the $A_{1g}$ breathing modes of disordered carbon networks, while the G-band corresponds to splitting of the $E_{2g}$ stretching modes of graphitic carbon networks [38]. The ratio of the integrated area of the D-band to that of the G-band ($I_D/I_G$) was used to determine the level of disorder in N-CNTs [39, 40].

Doping of CNTs with nitrogen introduces disorder in the regular graphite layers of CNTs, hence an increase in the nitrogen-doping of CNTs results in an enhanced D-band leading to a higher $I_D/I_G$ ratio [41]. The $I_D/I_G$ ratios of the N-CNTs increased when 1 wt.% oxygen was used, however, upon addition of 2-4 wt.% oxygen the $I_D/I_G$ ratio decreased but retained a value higher than that of N-CNTs synthesized without oxygen (Fig. 7b). The higher $I_D/I_G$ ratio of N-CNTs synthesized in the presence of oxygen indicates that addition of oxygen increased nitrogen-doping which in turn increased the structural defects in N-CNTs [42]. This increase in structural defects can be attributed to an increased disturbance of perfect hexagonal structure and layering of the graphene sheets due to introduction of pentagons or

heptagons [41]. The observations made from Raman spectroscopy were in good agreement with the nitrogen-content derived from elemental analysis of the synthesized N-CNTs (cf. Fig. 7b and 4).

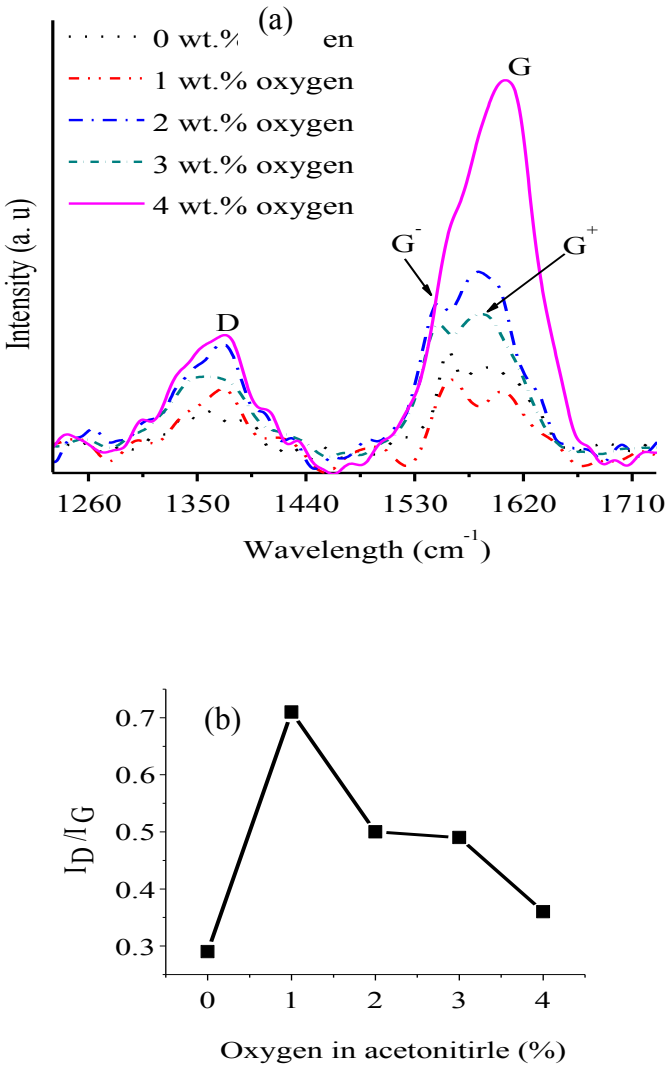


**Fig. 7** (a) Raman spectra and (b) $I_D/I_G$ ratios of pristine N-CNTs synthesized by using 0-4 wt.% of oxygen in acetonitrile at 850 °C and 3-ferrocenyl-2-(4-cyanophenyl)acrylonitrile as the catalyst

From the Raman spectra, the G-bands of all N-CNTs were spilt into two peaks at ≈1553 and ≈1601 $cm^{-1}$ associated with the $G^-$ and $G^+$ modes respectively. The $G^-$ mode arises from atomic displacement along the circumferential direction and it is indicative of the presence of metallic CNTs [43]. The $G^+$ mode arises from atomic displacement along the tube axis and it is related to the chirality of N-CNTs [44]. As the amount of oxygen in acetonitrile increased

from 0-4 wt. %, the $G^-$ peak diminished while the $G^+$ peak intensified. Diminishing of the $G^-$ peak indicated that increasing the amount of oxygen decreased the abundance of metallic N-CNTs [43]. While the increase in intensity of the $G^+$ peak can be attributed to an increase in the comprehensive strain of the C-C bonds or C-C-C angles in the graphene structures of N-CNTs [45]. The increase in strain was caused by an increase of the curvature of N-CNTs as the OD of the tubes decreased; which is in agreement with our XRD analysis

The G-band of N-CNTs synthesized with 4 wt.% oxygen was mainly composed of the $G^+$ peak and a very weak $G^-$ peak appearing as a peak shoulder. This resulted in a more symmetrical G-band, showing an exceptionally high intensity relative to the D-band (Fig. 7a). The high G-band intensity could be indicative of a single peak component arising from N-CNTs with a homogenous low OD and a single chirality. CNTs with small OD (≤ 10 nm) have been reported to exhibit a strong G-band intensity compared with the D-band intensity [35]. Also, the Raman spectra of N-CNTs synthesized with 4 wt.% oxygen showed peaks at 296.5 and 310.6 $cm^{-1}$ (see Supplementary Information S4). These peaks can be attributed to the radial breathing mode (RBM) of the thin walled (2-3 nm) tubes present in this sample (Table 2). These observations are analogous to those made from the Raman spectra of single-walled CNTs (SWCNTs), which exhibit a RBM and a very strong G-band compared to the D-band [30]. Since N-CNTs synthesized using 0-3% oxygen did not exhibit the RBM, diameter estimations were not estimated from the RBM.

### 3.3.6 Effect of oxygen on the thermal stability of N-CNTs

Thermal stability of N-CNTs was investigated by the use of TGA analysis. The thermograms and derivative thermograms (DTG) are shown in Fig. 8. From the thermograms and DTG, it can be deduced that N-CNTs synthesized with oxygen in acetonitrile exhibit a lower initial decomposition temperature (≈420 °C) compared with N-CNTs synthesized in acetonitrile only (≈510 °C). The thermal stability of N-CNTs was also observed to decrease as the amount of oxygen in acetonitrile increased (Fig. 8a). This decrease in thermal stability can be attributed to an increase in defects introduced by the nitrogen-doping level. Such defects can act as hot spots in the sample, which, initiate decomposition at lower temperatures, and thus result in a lower thermal stability of N-CNTs [46].

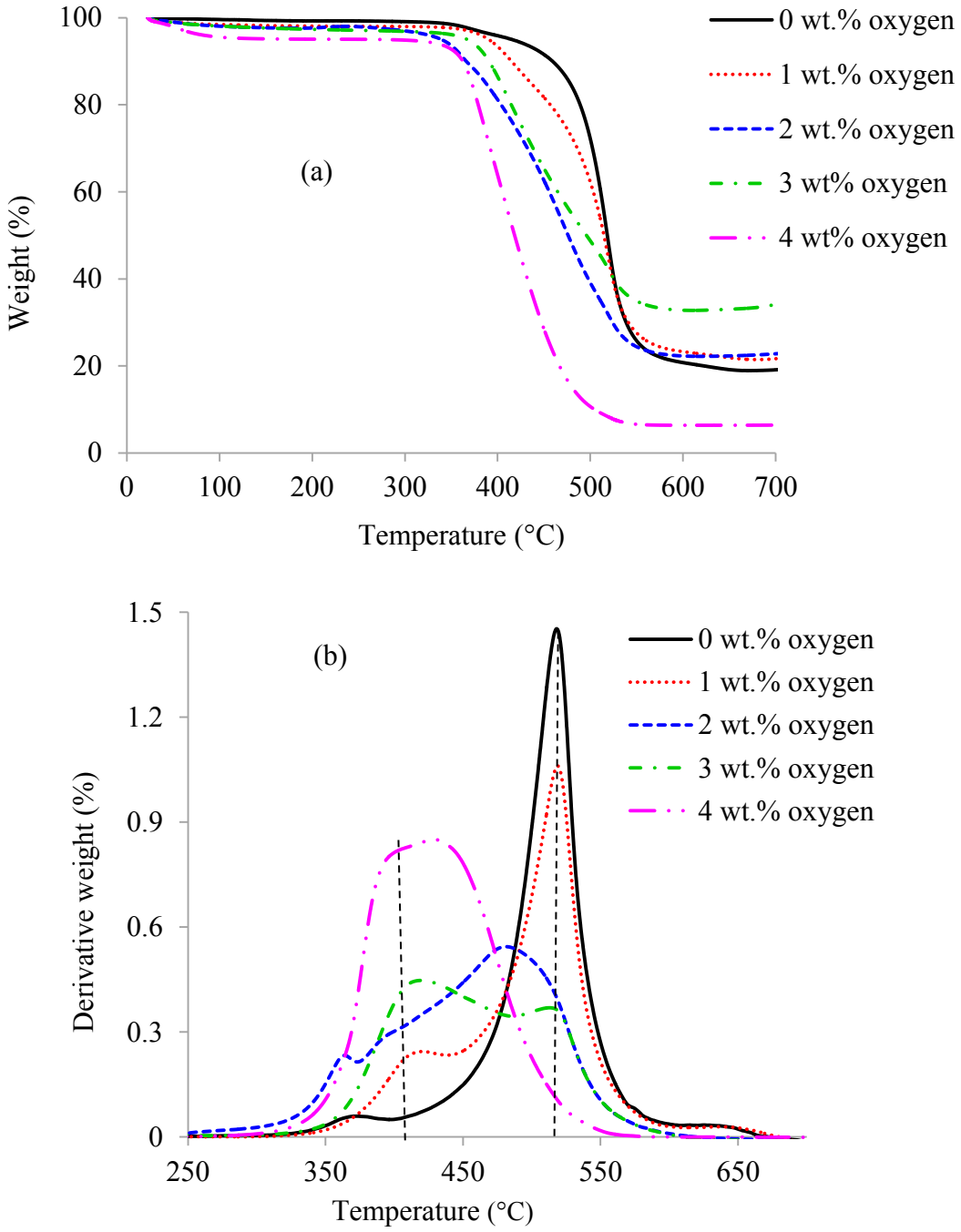


**Fig. 8** (a) Thermograms and (b) derivative thermograms of pristine N-CNTs synthesized by using 0-4 wt.% of oxygen in acetonitrile at 850 °C and 3-ferrocenyl-2-(4-cyanophenyl)acrylonitrile as the catalyst

Addition of oxygen also led to an increase in the amount of amorphous carbon (Table 2) which are less thermally stable and hence posses a lower initial decomposition temperature. The DTG of N-CNTs synthesized with 1-4 wt.% oxygen in acetonitrile revealed the appearance of peaks (marked by a dashed line) at ≈420 °C upon introduction of oxygen.

These peaks are ascribed to the presence of amorphous carbons. The derivative weight of these peaks was observed to increase as the amount of oxygen incorporated into acetonitrile increased. In contrast, the derivative weight of the peaks at ≈510 °C (marked with a continuous line) which are associated with N-CNTs, was observed to decrease with a decrease in oxygen content. This could imply that as the oxygen percentage is increased the amount of amorphous carbons increases leading to an overall decrease in thermal stability of N-CNTs [47]. Similar observations were made from TEM analysis summarised in Table 2 whereby, the distribution of amorphous carbon increased with the increase of oxygen content. The trend of decreasing thermostability from TGA analysis concurred with the increase in FWHM observed from XRD analysis.

### 3.3.7 Effect of oxygen on alignment of N-CNTs

The alignment of N-CNTs was determined from the SEM images and analysis of wide-angle XRD diffraction patterns. For each sample, at least twenty SEM images of N-CNTs were analysed and the representative images shown in Fig. 9. From the SEM images, N-CNTs synthesized by using acetonitrile mainly showed a tangled morphology, while N-CNTs synthesized by using 1-4 wt.% of oxygen in acetonitrile mainly showed an aligned morphology. For example, vertically aligned N-CNTs with open tube-ends were observed from the SEM images of N-CNTs grown from 3 wt.% of oxygen (Fig. 9c).

The degree of alignment of N-CNTs was also determined by evaluating the intensity of the $C_{(002)}$ peak of the N-CNTs from the XRD diffraction patterns. Cao *et al*. reported that aligned CNTs show a higher intensity of the $C_{(002)}$ peak compared to that of disordered CNTs [48]. From our results, the $C_{(002)}$ peak intensities of N-CNTs synthesized by using 0 to 3 wt.% of oxygen were seen to decrease, with an increase in oxygen content (Fig. 6 and Table 3). This could imply that the degree of N-CNT alignment increased with an increase of oxygen content from 0 to 3 wt.%. Thus, the trend of the variation in the alignment of the N-CNTs observed from the XRD analysis supported the trend observed from the SEM images. Since oxygen possesses a ‗deaning effect' on as-grown CNTs [49], it is possible that incorporation of a low oxygen content brings about etching of the outer walls of CNTs resulting in the formation of more aligned N-CNTs.

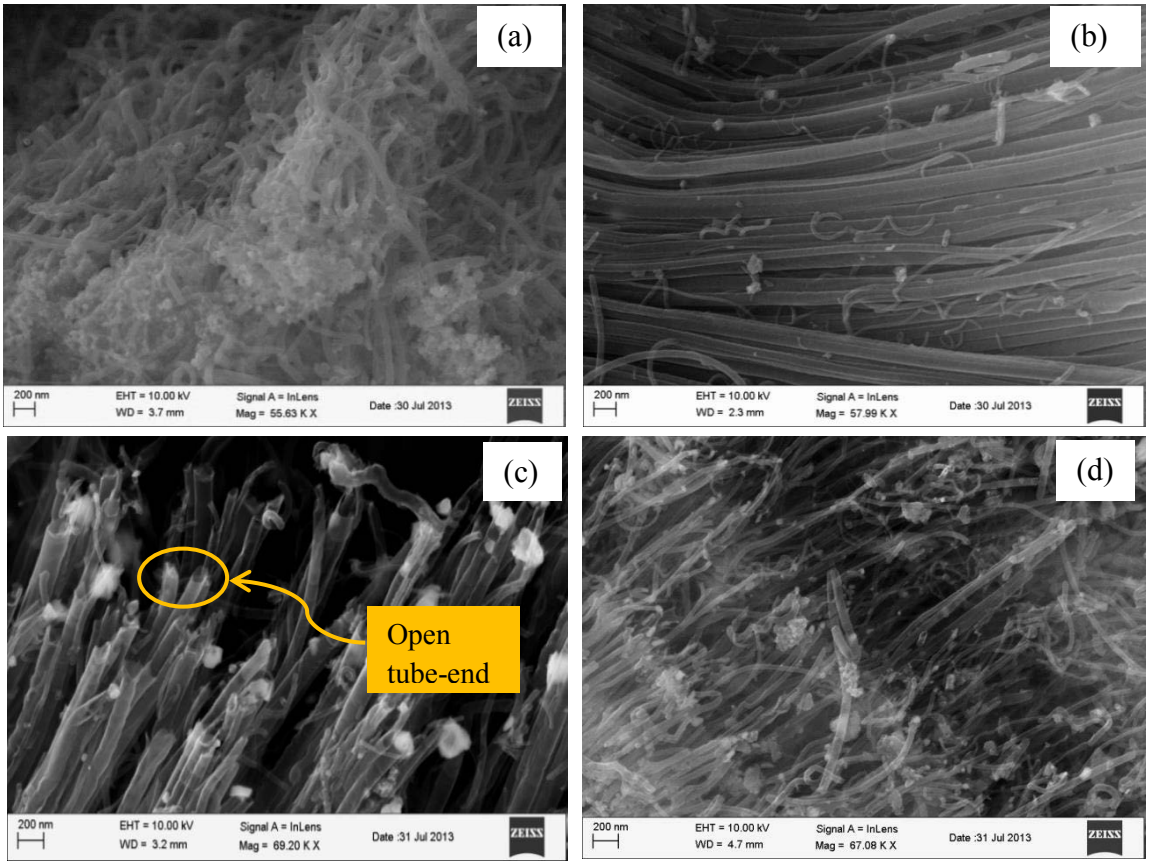


**Fig. 9** SEM images of pristine N-CNTs synthesized using (a) only acetonitrile, (b) 1 wt.% oxygen, (c) 3 wt.% oxygen and (d) 4 wt.% oxygen in acetonitrile at 850 °C and 3-ferrocenyl-2-(4-cyanophenyl)acrylonitrile as the catalyst. Note the difference in alignment of N-CNTs in Fig. 9a and 9b

### 3.3.8 Effect of oxygen on the surface chemistry of N-CNTs

The surface chemistry of N-CNTs was investigated by means of inverse gas chromatography (IGC)-surface energy analysis and FTIR spectroscopy. From the IGC analysis, addition of oxygen to acetonitrile modified the surface energy and acid-base properties of the N-CNTs (Table 4). The dispersive surface energy ($\gamma s^D$) of N-CNTs was determined by using the Doris and Gray method [50]. N-CNTs synthesized in the presence of oxygen showed an appreciably high $\gamma s^D$ (>70 $mJm^{-2}$) which was higher than the $\gamma s^D$ of N-CNTs synthesized with acetonitrile only (Table 4). The increased $\gamma s^D$ of N-CNTs synthesized by using oxygen was attributed to an increase in: surface defects on the graphene layers, nitrogen-containing functional groups with high $\gamma s^D$ and open tube ends [51]. Similar observations were also made from elemental analysis and Raman spectroscopy.

**Table 4** Surface energy and surface chemistry of selected pristine N-CNTs synthesized at 850 °C using 3-ferrocenyl-2-(4-cyanophenyl)acrylonitrile as the catalyst

| wt.% Oxygen | Nitrogen (wt. %) | Surface energy ($ys^D$) $mJm^{-2}$ | $K_a$ | $K_b$ | $K_a/K_b$ |
|---|---|---|---|---|---|
| 0 | 6.4 | 34 | 0.0500 | 0.3888 | 0.1286 |
| 1 | 15.7 | 112 | 0.1121 | 0.7183 | 0.1560 |
| 2 | 14.9 | 78 | 0.0818 | 0.6432 | 0.1272 |

The surface acid-base properties of N-CNTs were evaluated by using dichloromethane, acetonitrile and ethyl acetate as the polar probes. To compare the surface basicity of different N-CNTs the Lewis base constant $K_b$ was used [52]. The basic constant ($K_b$) of N-CNTs synthesized in the presence of oxygen was higher than that of N-CNTs synthesized with acetonitrile only (Table 4). This suggests that the surface of N-CNTs synthesized in the presence of oxygen contained more basic functionalities than that of N-CNTs synthesized in acetonitrile only [5].

The FTIR spectra of N-CNTs synthesized using 0-4 wt.% oxygen in acetonitrile is presented in Fig. 10. A broad band at 3427 $cm^{-1}$ was observed in all spectra and it was consistent with the –OH stretching vibration of hydrogen bonded adsorbed water, alcohols or carboxylic acids [45]. Since the band at 1723 $cm^{-1}$ attributed to the C=O group was weak, the broad peak at 3427 $cm^{-1}$ was ascribed to adsorbed water molecules. The peaks at 2949 and 2871 $cm^{-1}$ were designated as the stretching vibration of $CH_2$ and $CH_3$ groups [53]. The peak at 2381 $cm^{-1}$ was designated as the stretching vibrations of $CO_2$ groups originating from the FTIR spectrometer [54]. The aromatic stretching modes of the C=C present in the graphene structure of CNTs were observed at 1678 $cm^{-1}$, while the C-H vibration modes were assigned to the peaks at 788 and 699 $cm^{-1}$ [53]. The presence of N-CNTs was evidenced by the existence of peaks at 1567, 1389 and 1110 $cm^{-1}$ assigned to stretching vibrations of C=N, C-$NH_3$ and C-N functional groups respectively [2, 54-56].

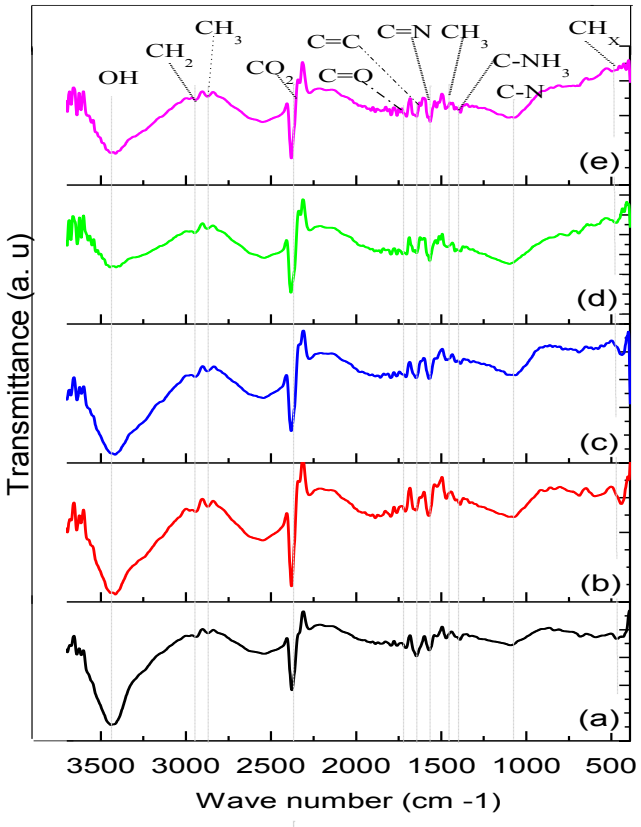


**Fig. 10** FTIR spectra of pristine N-CNTs synthesized by using (a) only acetonitrile, (b) 1 wt.% oxygen, (c) 2 wt.% oxygen, (d) 3 wt.% oxygen and (e) 4 wt.% oxygen in acetonitrile at 850 °C and 3-ferrocenyl-2-(4-cyanophenyl)acrylonitrile as the catalyst

Doping of CNTs with nitrogen results in substitution of an $sp^2$ carbon with nitrogen to form C=N or C-N bonds showing IR activity [54]. The intensity of the peak at 1567 $cm^{-1}$ assigned to the C=N group was observed to increase when 1-4 wt.% oxygen in acetonitrile was used to synthesize N-CNTs. For N-CNTs synthesized without oxygen, the intensity of the C=N band at 1567 $cm^{-1}$ was smaller than that of the C=C band at 1678 $cm^{-1}$. On the contrary, for N-CNTs synthesized by using 1-4 wt.% oxygen the intensity of the C=N band at 1567 $cm^{-1}$ was larger than that of the C=C band at 1678 $cm^{-1}$. This increase in intensity of the C=N peak at 1567 $cm^{-1}$ can be related to an increase in nitrogen-doping level, which was also observed from elemental analysis. The increase in density of C=N functional groups observed from the FTIR spectra, could be related to an increase of basic functional groups such as pyridinic or pyridinic oxide species as observed from the IGC analysis. Such N-CNTs can be used as metal-free catalysts or as metal catalyst supports [8].

### 3.3.9 Effect of oxygen on the conductivity of N-CNTs

The conductivity of all N-CNTs was determined by the use of a four-point probe within a temperature range of 296 to 383 K. To calculate the conductivity ($\sigma$) in S $m^{-1}$ the following equation was used:

$$\text{conductivity } (\sigma) = \frac{1}{[\rho]} \text{ and } \rho = \frac{\pi h}{\ln 2}\left[\frac{\Delta v}{I}\right]$$

where $\rho$ is the resistivity, $h$ is the film thickness, $\Delta V$ is the change in voltage and $I$ is the measured current.

For all N-CNTs, a buckypaper (compact film) was obtained by pressurizing the N-CNTs to a similar film thickness. The electrical properties of buckypapers are dependent on the inter-tube interactions between individual N-CNTs, nanotube junctions, length of the N-CNTs, purity, type, and preparation techniques [57]. High inter-tube interactions improve the overall electrical properties of N-CNTs by minimizing the internal resistance [58]. To improve the inter-tube interactions of the intermingled N-CNTs, a high pressure was used during formation of the buckypaper.

The conductivity of all N-CNTs increased with increase in temperature implying that the samples exhibited semiconducting properties (Fig. 11).

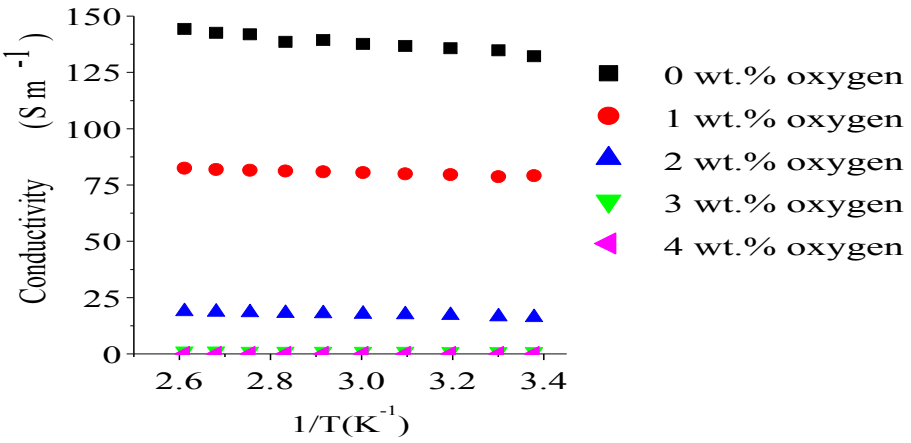


**Fig. 11** Conductivity of pristine N-CNTs synthesized at 850 °C by using 0-4 wt.% oxygen in acetonitrile and 3-ferrocenyl-2-(4-cyanophenyl)acrylonitrile as the catalyst

Increasing the amount of oxygen in acetonitrile from 0-4 wt.% resulted in a decrease of conductivity. This decrease in conductivity was directly related to the decrease of N-CNTs OD and N-CNTs junctions resulting from addition of 0-4 wt.% oxygen. As the OD and junctions of N-CNTs decreased, the mean free path of charge carriers also decreased therefore decreasing the conductivity of N-CNTs [59]. Additionally, as the OD decreases the columbic repulsion between graphene layers of N-CNTs increases (see Section 3.3.4.). The increased columbic repulsion can induce polarization effects, which may block transmission of electrons by increasing the resistance in N-CNTs and in turn reducing the current flow in N-CNTs. Ibrahim *et al*. [5], who reported a decrease in conductivity as the tube OD decreased and the nitrogen doping levels increased, made similar observations.

## 4. Conclusions

We have reported the successful synthesis of N-CNTs by using 3-ferrocenyl-2-(4-cyanophenyl)acrylonitrile as a novel catalyst. The use of acetonitrile as a carbon source selectively formed only N-CNTs while, the use of toluene as a carbon source yielded a mixture of N-CNTs and carbon spheres. Selectivity towards N-CNT formation was accredited to the decomposition products of acetonitrile when used as a carbon source. The results obtained demonstrate that nitrogen-containing organometallic compounds are versatile catalysts for synthesis of N-CNTs because they act as catalysts and as a nitrogen source. We have also demonstrated a simple approach of tuning the nitrogen content, surface energy, surface basicity, alignment, and conductivity of N-CNTs by adding a low concentration of oxygen derived from an ester, namely, ethylbenzoate. The bulk electronic and physical properties of N-CNTs were strongly influenced by the OD of N-CNTs that was modulated by adding oxygen to acetonitrile. Low oxygen concentrations were favourable for the growth of well-aligned N-CNTs containing higher levels of nitrogen. However, there is a need to conduct further studies to determine the mechanism by which low oxygen concentrations influence the physicochemical properties of N-CNTs.

## Acknowledgments

The National Research Foundation (NRF) and University of KwaZulu-Natal (UKZN) financed this research. We are grateful to Prof B. S. Martincigh, Dr. N. Nombona and Dr. R. S. Mwakubambanya, for assisting in proof-reading the manuscript and their critical comments of the manuscript.

## Supplementary material

Supplementary Material Available: Tables detailing mole ratios used during synthesis and data obtained from yields of products. A figure obtained from Raman spectroscopy.

## References


1. Ionescu MI, Zhang Y, Li R, Abou-Rachid H, Sun X (2012) Nitrogen-doping effects on the growth, structure and electrical performance of carbon nanotubes obtained by spray pyrolysis method. Appl Surf Sci 258:4563
2. Ritter U, Tsierkezos NG, Prylutskyy YI, Matzui LY, Gubanov VO, Bilyi MM, Davydenko MO (2012) Structure–electrical resistivity relationship of N-doped multi-walled carbon nanotubes. J Mater Sci 47:2390
3. Liu H, Zhang Y, Li R, Sun X, Abou-Rachid H (2011) Effects of bimetallic catalysts on synthesis of nitrogen-doped carbon nanotubes as nanoscale energetic materials. Particuology 9:465
4. Bepete G, Tetana ZN, Lindner S, Rümmeli MH, Chiguvare Z, Coville NJ (2013) The use of aliphatic alcohol chain length to control the nitrogen type and content in nitrogen doped carbon nanotubes. Carbon 52:316
5. Ibrahim EMM, Vyacheslav OK, Leonhardt A, Hampel S, Oswald S, Rümmeli MH, Büchner B (2010) Synthesis, characterization, and electrical properties of nitrogen-doped single-walled carbon nanotubes with different nitrogen content. Diamond Relat Mater 19:1199
6. Jana D, Sun C-L, Chen L-C, Chen K-H (2013) Effect of chemical doping of boron and nitrogen on the electronic, optical, and electrochemical properties of carbon nanotubes. Prog Mater Sci 58:565
7. Lai Y-H, Lian H-B, Lee K-Y (2009) Field emission of vertically aligned carbon nanotubes with various content of nitrogen. Diamond Relat Mater 18:544
8. Ombaka LM, Ndungu P, Nyamori VO (2013) Usage of carbon nanotubes as platinum and nickel catalyst support in dehydrogenation reactions. Catal Today 217:65
9. Padya B, Kalita D, Jain PK, Padmanabham G, Ravi M, Bhat KS (2013) Nitrogen incorporated highly aligned carbon nanotube arrays thin film grown from single feedstock for field emission. J Nanoelectron Optoe 8:177

10. Chizari K, Janowska I, Houllé M, Florea I, Ersen O, Romero T, Bernhardt P, Ledoux MJ, Pham-Huu C (2010) Tuning of nitrogen-doped carbon nanotubes as catalyst support for liquid-phase reaction. Appl Catal A: General 380:72
11. Liu J, Zhang Y, Ionescu MI, Li R, Sun X (2011) Nitrogen-doped carbon nanotubes with tunable structure and high yield produced by ultrasonic spray pyrolysis. Appl Surf Sci 257:7837
12. Nxumalo EN, Chabalala VP, Nyamori VO, Witcomb MJ, Coville NJ (2010) Influence of methylimidazole isomers on ferrocene-catalysed nitrogen doped carbon nanotube synthesis. J Organomet Chem 695:1451
13. Thurakitseree T, Kramberger C, Zhao P, Aikawa S, Harish S, Chiashi S, Einarsson E, Maruyama S (2012) Diameter-controlled and nitrogen-doped vertically aligned single-walled carbon nanotubes. Carbon 50:2635
14. Imrie C, Kleyi P, Nyamori VO, Gerber TIA, Levendis DC, Look J (2007) Further solvent-free reactions of ferrocenylaldehydes: synthesis of 1,10-ferrocenyldiimines and ferrocenylacrylonitriles. J Organomet Chem 692:3443
15. Oosthuizen RS, Nyamori VO (2012) Heteroatom-containing ferrocene derivatives as catalysts for MWCNTs and other shaped carbon nanomaterials. Appl Organomet Chem 26:536
16. Nyamori VO, Nxumalo EN, Coville NJ (2009) The effect of arylferrocene ring substituents on the synthesis of multi-walled carbon nanotubes. J Organomet Chem 694:2222
17. Trancik JE, Barton SC, Hone J (2008) Transparent and catalytic carbon nanotube films. J Nano Lett 8:982
18. Chen L, Xia K, Huang L, Li L, Pei L, Fei S (2013) Facile synthesis and hydrogen storage application of nitrogen-doped carbon nanotubes with bamboolike structure. Int J Hydrogen Energy 38:3297
19. Kovalevski VV, Safronov AN (1998) Pyrolysis of hollow carbons on melted catalyst. Carbon 36:963
20. Zhang C, Lv M, Wang X, Li J, Yang X, Yang J, Hu H (2013) Controllable synthesis and formation mechanism of carbon micro/nano-structural materials. Chem Phys Lett 586:121
21. Lifshitz A, Tamburu C (1999) Thermal decomposition of acetonitrile. Kinetic modeling. Int J Chem Kinet 30:341

22. Shaikjee A, Coville NJ (2012) The role of the hydrocarbon source on the growth of carbon materials. Carbon 50:3376
23. Derudi M, Polino D, Cavallotti C (2011) Toluene and benzyl decomposition mechanisms: elementary reactions and kinetic simulations. Phys Chem Chem Phys 13:21308
24. Koós AA, Dowling M, Jurkschat K, Crossley A, Grobert N (2009) Effect of the experimental parameters on the structure of nitrogen-doped carbon nanotubes produced by aerosol chemical vapor deposition. Carbon 47:30
25. Liu S, Zhang Y, Lin Y, Zhao Z, Li Q (2014) Tailoring the structure and nitrogen content of nitrogen-doped carbon nanotubes by water-assisted growth. Carbon 69:247
26. Rümmeli MH, Borowiak-Palen E, Gemming T, Pichler T, Knupfer M, Kalbác M, Dunsch L, Jost O, Silva SRP, Pompe W, Buchner B (2005) Novel catalysts, room temperature, and the importance of oxygen for the synthesis of single-walled carbon nanotubes. Nano lett 5:1209
27. Sumpter BG, Meunier V, Romo-Herrera JM, Cruz-Silva E, Cullen DA, Terrones H, Smith DJ, Terrones M (2007) Nitrogen-mediated carbon nanotube growth: diameter reduction, metallicity, bundle dispersability, and bamboo-like structure formation. ACS Nano 1:369
28. Jourdain V, Bichara C (2013) Current understanding of the growth of carbon nanotubes in catalytic chemical vapour deposition. Carbon 58:2
29. Ci L, Vajtai R, Ajayan PM (2007) Vertically aligned large-diameter double-walled carbon nanotube arrays having ultralow density. J Phys Chem C 111:9077
30. Belin T, Epron F (2005) Characterization Methods of carbon nanotubes: a review. Mater Sci Eng B 119:105
31. Lambin P, Loiseau A, Culot C, Biro L (2002) Structure of carbon nanotubes probed by local and global probes. Carbon 40:1635
32. Chiang YC, Lin W-H, Chang Y-C (2011) The influence of treatment duration on multi-walled carbon nanotubes functionalized by $H_2SO_4/HNO_3$ oxidation. Appl Surf Sci 257:2401
33. Khani H, Moradi O (2013) Influence of surface oxidation on the morphological and crystallographic structure of multi-walled carbon nanotubes *via* different oxidants. J Nanostructure Chem 3:73
34. Paradise M, Goswami T (2007) Carbon nanotubes–production and industrial applications. Mater Des 28:1477

35. Singh DK, Iyer PK, Giri PK (2010) Diameter dependence of interwall separation and strain in multiwalled carbon nanotubes probed by X-ray diffraction and Raman scattering studies. Diamond Relat Mater 19:1281
36. Emmenegger C, Bonard J-M, Mauron P, Sudan P, Lepora A, Grobety B, Züttel A, Schlapbach L (2003) Synthesis of carbon nanotubes over Fe catalyst on aluminium and suggested growth mechanism. Carbon 41:539
37. Wirth CT, Bayer BC, Gamalski AD, Esconjauregui S, Weatherup RS, Ducati C, Baehtz C, Robertson J, Hofmann S (2012) The phase of iron catalyst nanoparticles during carbon nanotube growth. Chem Mater 24:4633
38. Hiura H, Ebbesen T, Tanigaki K, Takahashi H (1993) Raman studies of carbon nanotubes. Chem Phys Lett 202:509
39. Wepasnick KA, Smith BA, Bitter JL, Fairbrother DH (2010) Chemical and structural characterization of carbon nanotube surfaces. Anal Bioanal Chem 396:1003
40. Liu Y, Pan C, Wang J (2004) Raman spectra of carbon nanotubes and nanofibers prepared by ethanol flames. J Mater Sci 39:1091
41. Sharifi T, Nitze F, Barzegar HR, Tai C-W, Mazurkiewicz M, Malolepszy A, Stobinski L, Wågberg T (2012) Nitrogen doped multi walled carbon nanotubes produced by CVD-correlating XPS and Raman spectroscopy for the study of nitrogen inclusion. Carbon 50:3535
42. Hussain S, Amade R, Jover E, Bertran E (2013) Nitrogen plasma functionalization of carbon nanotubes for supercapacitor applications. J Mater Sci 48:7620
43. Jorio A, Pimenta MA, Filho AGS, Saito R, Dresselhaus G, Dresselhaus MS (2003) Characterizing carbon nanotube samples with resonance Raman scattering. New J Phys 5:139.131
44. Saito R, Jorio A, Hafner JH, Lieber CM, Hunter M, McClure T, Dresselhaus G, Dresselhaus MS (2001) Chirality-dependent G-band Raman intensity of carbon nanotubes. Phys Rev B 64:085312
45. Kim U-J, Furtado CA, Liu X, Chen G, Eklund PC (2005) Raman and IR spectroscopy of chemically processed single-walled carbon nanotubes. J Am Chem Soc 127:15437
46. Chizari K, Vena A, Laurentius L, Sundararaj U (2014) The effect of temperature on the morphology and chemical surface properties of nitrogen-doped carbon nanotubes. Carbon 68:369
47. Santangelo S, Lanza M, Milone C (2013) Evaluation of the overall crystalline quality of amorphous carbon containing multiwalled nanotubes. J Phys Chem C 117:4815

48. Cao A, Xu C, Liang J, Wu D, Wei B (2001) X-ray diffraction characterization on the alignment degree of carbon nanotubes. Chem Phys Lett 344:13
49. Zhang G, Mann D, Zhang L, Javey A, Li Y, enilmez EY, Wang Q, McVittie JP, Nishi Y, Gibbons J, Dai H (2005) Ultra-high-yield growth of vertical single-walled carbon nanotubes: hidden roles of hydrogen and oxygen. PNAS 102:16141
50. Dorris GM, Gray DG (1980) Adsorption of normal-alkanes at zero surface coverage on cellulose paper and wood fibers. J Colloid & Interface Sci 77:353
51. Menzel R, Lee A, Bismarck A, Shaffer MSP (2009) Inverse gas chromatography of as-received and modified carbon nanotubes. Langmuir 25:8340
52. Khoo J, Burnett D, Menzel R, MSP Shaffer (2012) Surface energetic heterogeneity of carbon-based nanomaterials. www.TheSorptionSolution.com. Accesed 21 June 2012
53. Vanyoreka L, Meszarosa R, Barany S (2014) Surface and electrosurface characterization of surface-oxidized multi-walled N-doped carbon nanotubes. Colloids and Surfaces A: Physicochem Eng Aspects 448:140
54. Misra A, Tyagi PK, Singh MK, Misra DS (2006) FTIR studies of nitrogen doped carbon nanotubes. Diamond Relat Mater 15:385
55. Maiyalagan T, Viswanathan B (2005) Template synthesis and characterization of well-aligned nitrogen containing carbon nanotubes. Mater Chem Phys 93:291
56. Bandosz TJ (2009) Surface chemistry of carbon materials. In: Serp P, Fiueiredo JL (Eds.), Carbon materials fo catalysis. John Wiley & Sons, Inc. United States of America, pp 63
57. Jianwei Z, Dazhi J, Hua-Xin P (2014) A pressurized filtration technique for fabricating carbon nanotube buckypaper: Structure, mechanical and conductive properties. Microporous Mesoporous Mater 184:127
58. Jianwei Z, Dazhi J, Hua-Xin P, Faxiang Q (2013) Enhanced mechanical and electrical properties of carbon nanotube buckypaper by in situ cross-linking. Carbon 63:125
59. Latil S, Roche S, Mayou D, Charlier J-C (2004) Mesoscopic transport in chemically doped carbon nanotubes. Phys Rev Lett 92:256805

# CHAPTER SIX

# PYRROLIC NITROGEN-DOPED CARBON NANOTUBES: PHYSICOCHEMICAL PROPERTIES, INTERACTIONS WITH Pd AND THEIR ROLE IN THE SELECTIVE HYDROGENATION OF NITROBENZOPHENONE

RSC Advances

PAPER

View Article Online
View Journal | View Issue

CrossMark click for updates

Cite this: *RSC Adv.*, 2015, 5, 109

## Pyrrolic nitrogen-doped carbon nanotubes: physicochemical properties, interactions with Pd and their role in the selective hydrogenation of nitrobenzophenone†

Lucy M. Ombaka, Patrick G. Ndungu and Vincent O. Nyamori*

Nitrogen-doped carbon nanotubes (N-CNTs) containing 63%, 73% and 80% pyrrolic-N were synthesized and used to evaluate the influence of pyrrolic nitrogen on the physicochemical properties and catalytic activity of Pd supported on N-CNTs (Pd/N-CNTs). Micrographs of Pd/N-CNTs showed that Pd was located along the defect sites of N-CNTs indicating strong Pd-support interactions. X-ray photoelectron spectroscopy revealed that the abundance of $Pd^0$ decreased while that of $Pd^{2+}$ increased as the quantity of pyrrolic nitrogen increased. The $Pd^{2+}$ species were formed as Pd–N coordination complexes, which stabilized $Pd^{2+}$ nanoparticles. Selective hydrogenation of nitrobenzophenone to aminobenzophenone or *p*-benzylaniline was used to evaluate the catalytic performance of catalysts. Pd/N-CNTs exhibited a higher selectivity towards aminobenzophenone than Pd on carbon nanotubes and Pd on activated carbon. The enhanced selectivity towards nitro-reduction alone, observed with Pd/N-CNTs was attributed to the promoting effect of pyrrolic-N. Hence, Pd/N-CNTs are promising catalysts for the selective reduction of nitro arenes.

Received 16th October 2014
Accepted 24th November 2014

DOI: 10.1039/c4ra12523a

www.rsc.org/advances

## Chapter layout

The supplementary information for this section is indexed as appendix 3 located in the DVD attached at the end of the thesis.

**Pyrrolic nitrogen-doped carbon nanotubes: Physicochemical properties, interactions with Pd and their role in the selective hydrogenation of nitrobenzophenone**

Lucy M. Ombaka, Patrick G. Ndungu and Vincent O. Nyamori*
School of Chemistry and Physics, University of KwaZulu-Natal, Westville Campus, Private Bag X54001, Durban, 4000, South Africa

*Corresponding author. Telephone: +27-31 260 8256; Fax: +27-31 260 3091
*E-mail address*: nyamori@ukzn.ac.za (V. O. Nyamori)

## Abstract

Nitrogen-doped carbon nanotubes (N-CNTs) containing 63%, 73% and 80% pyrrolic-N were synthesized and used to evaluate the influence of pyrrolic nitrogen on the physicochemical properties and catalytic activity of Pd supported on N-CNTs (Pd/N-CNTs). Micrographs of Pd/N-CNTs showed that Pd was located along the defect sites of N-CNTs indicating strong Pd-support interactions. X-ray photoelectron spectroscopy revealed that the abundance of $Pd^0$ decreased while that of $Pd^{2+}$ increased as the quantity of pyrrolic nitrogen increased. The $Pd^{2+}$ species were formed as Pd-N coordination complexes, which stabilized $Pd^{2+}$ nanoparticles. Selective hydrogenation of nitrobenzophenone to aminobenzophenone or *p*-benzylaniline was used to evaluate the catalytic performance of catalysts. Pd/N-CNTs exhibited a higher selectivity towards aminobenzophenone than Pd on carbon nanotubes and Pd on activated carbon. The enhanced selectivity towards nitro-reduction alone, observed with Pd/N-CNTs was attributed to the promoting effect of pyrrolic-N. Hence, Pd/N-CNTs are promising catalysts for the selective reduction of nitro arenes.

## 1. Introduction

Graphene and carbon nanotubes (CNTs) are carbonaceous materials exhibiting unique properties, which make them attractive materials for use as metal catalyst supports.[1, 2] These properties include, high mechanical strength,[3, 4] good chemical stability,[3, 5] high surface area,[6, 7] notable electronic interactions with metal catalysts such as Pt and Ru[8, 9] and a mesoporous structure[10] which facilitates favourable reactant-product mass transport.[11] Due to these unique properties, CNTs and graphene are classified together with other smart carbonaceous supports such as graphene oxides and graphyne, which show novel properties as catalyst supports.[12-14]

When used as metal catalyst supports, CNTs show good mechanical and chemical stability,[3] metal dispersion,[15] higher substrate conversion, and an improved regio- and stereoselectivity[16] compared with traditional supports. This in turn has economic benefits since yields are generally increased and by-products or waste is reduced thus upholding green chemistry principles. Nonetheless, activated carbon (AC) is still a common carbonaceous material used as a catalyst support in the synthesis of industrial chemicals owing to its high surface area. However, AC suffers drawbacks such as faster deactivation rates,[17] poor metal-support electronic interactions, lower thermal and mechanical stability, metal catalyst agglomeration and leaching.[18] Thus, CNTs, which exhibit better support properties, are potentially the next generation of preferred carbonaceous supports.

Recent reports indicate that CNTs exhibit superior catalytic activity in industrial applications such as hydrogenation[19] and dehydrogenation[2] reactions. To improve the activity of CNTs, heteroatom-containing functional groups can be introduced onto the surface of CNTs. Heteroatoms such as nitrogen, oxygen, phosphorous, sulphur and boron can be used to modify the surface chemistry of CNTs.[2] Incorporation of nitrogen functionalities into the graphene layers of CNTs to form nitrogen-doped CNTs (N-CNTs) improves their utility in catalytic reactions.[20] For example, the presence of basic functional groups such as pyrrolic and pyridinic nitrogen in N-CNTs can enhance the chemical[2] and electronic properties of N-CNTs.[21] The improved chemical and electrical properties of N-CNTs result in activation of the metal catalyst[22] and enhancement of the binding energy between N-CNTs and metal catalysts.[23] Doping of CNTs with nitrogen also improves the physical properties of CNTs by introducing surface defects into the graphene structure of N-CNTs. Such surface defects promote N-CNT surface wetting resulting in increased catalytic activity.[24]

Depending on the procedure used to synthesize N-CNTs, various nitrogen species such as pyridine-like, pyridine-N-oxide, pyrrole-like, carbonitrile, graphitic/quaternary nitrogen and lactams can be present in N-CNTs (Fig. 1). The different nitrogen species influence the catalytic activity of N-CNTs in diverse ways. For instance, pyridinic nitrogens were reported to enhance the catalytic activity of Pd supported on N-CNTs.[25] However, the selective doping of N-CNTs with a single nitrogen species to facilitate structure-activity relationship studies remains under-researched.

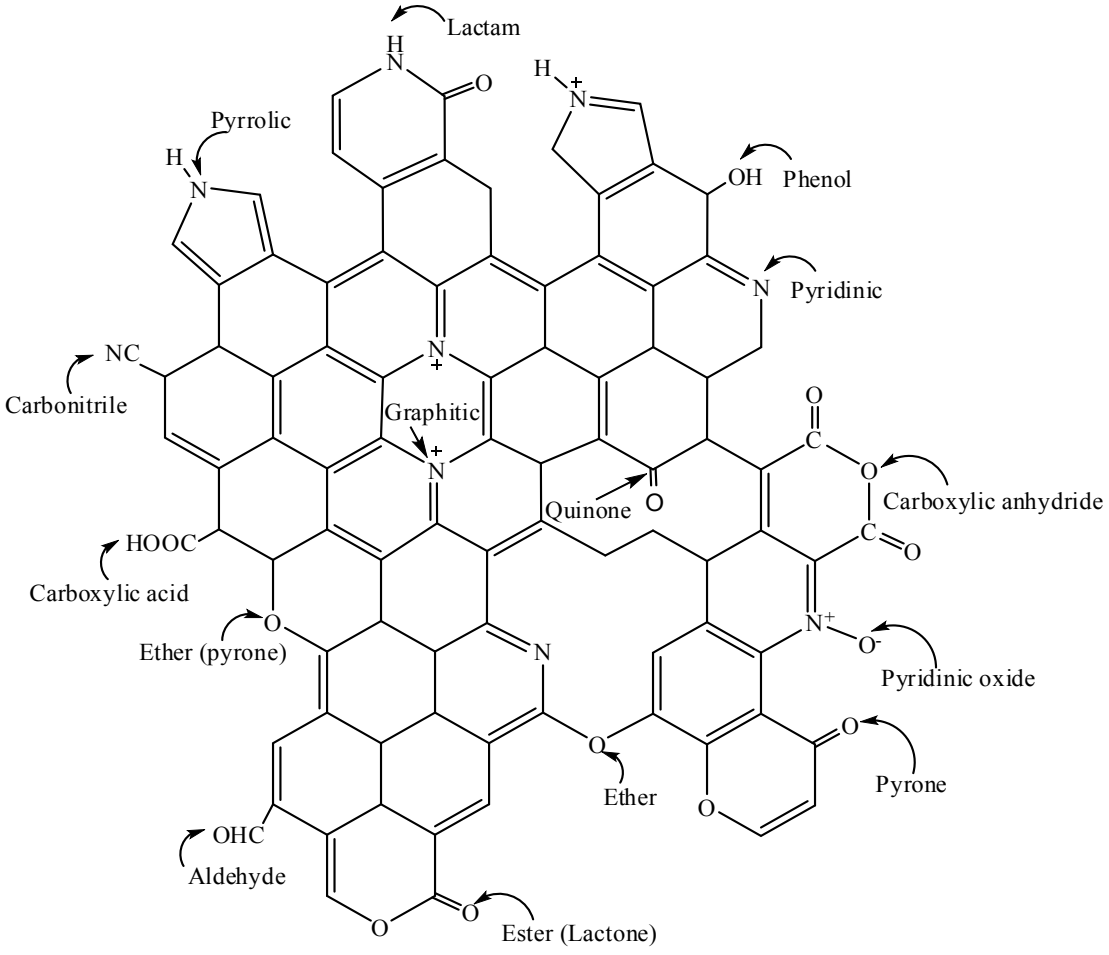


**Fig. 1** Graphical representation of possible nitrogen and oxygen functional groups present in N-CNTs.

Oxygen functional groups can be added to the surface of N-CNTs *via in-situ* or *ex-situ* treatment of N-CNTs with oxygen containing organic or inorganic compounds.[2] Oxygen functional groups such as carboxyl, carbonyl, lactone and quinone (Fig. 1) enhance the wettability of N-CNTs, further improving the catalytic performance of N-CNTs. The oxygen functional groups also act as anchoring sites for well dispersed metal nanoparticles supported

on N-CNTs. Thus, compared with CNTs, oxygen-functionalized N-CNTs exhibit enhanced metal nanoparticle properties such as better stability, smaller particle size, better dispersion and activation, which results in higher catalytic activity and selectivity.[2] As a result, oxygen-functionalised N-CNTs are potentially smart materials for application as catalysts or as metal catalyst supports used in catalytic reactions.

The catalytic activity of CNTs in hydrogenation reactions has been considerably studied.[19] However, limited studies report the catalytic activity of N-CNTs in general, and more specifically pyrrolic containing N-CNTs in the selective hydrogenation of nitro-arenes. Selective hydrogenation of nitro-arenes to amino-arenes is of immense industrial importance as amino-arenes are used in pharmaceuticals and in the production of fine chemicals. Aminobenzophenone is an example of an amino-arene which is industrially important as it is used as an intermediate in the synthesis of Schiff bases,[26] and in nonlinear optical materials generating blue lasers.[27, 28] *p*-Benzylaniline is another amino-arene that has the potential to be used as an intermediate for the synthesis of other Schiff bases. In this study, the selective hydrogenation of nitrobenzophenone (NBP) to aminobenzophenone was chosen as a model reaction. This is because NBP contains two reducible functional groups ($NO_2$ and CO), which allows for the evaluation of catalysts‘ selectivity towards reduction of the nitro group alone.

Ferrocene is commonly used as a catalyst in the CVD synthesis of N-CNTs.[29] To modulate the level of nitrogen-doping and the nitrogen species incorporated into N-CNTs, nitrogen-containing ferrocenyl derivatives can be used as catalysts instead of ferrocene.[30] In this study, the effect of using 3-ferrocenyl-2-(4-cyanophenyl)acrylonitrile as a catalyst for the introduction of nitrogen species into N-CNTs was evaluated. We report the selective synthesis of pyrrolic N-CNTs and their physicochemical properties. The influence of pyrrolic nitrogen on the chemical properties of Pd nanoparticles supported on the pyrrolic N-CNTs is also reported. Additionally, we investigated the role of pyrrole-like nitrogen in the selective hydrogenation of nitrobenzophenone to aminobenzophenone over Pd supported on N-CNTs. For comparison purposes, the catalytic activity of Pd supported on CNTs and also on AC was evaluated under similar reactions.

## 2. Experimental

### 2.1 Materials and instrumentation

The reagents 4-nitrobenzophenone (99%), 4-aminobenzophenone (97%) and diethyl ether (99.8%) were purchased from Sigma Aldrich, Germany. Palladium acetylacetonate {$Pd(acac)_2$} (synthesis grade) was purchased from Merck, Germany. Pd on activated carbon (5 wt. %) was purchased from Sigma-Aldrich, Germany. Toluene (99.4%) was purchased from LiChroSolv, Germany. All reagents and solvents were of analytical grade and used as received from the suppliers. Pd was loaded onto N-CNTs and CNTs in a cylindrical stainless steel reaction chamber (140 mm x 10 mm) sealed at one end with a Swagelok® fitting nut. To monitor the partial pressure used during synthesis of the catalyst, a Thyracont VD84/1 Pirani vacuum gauge was used. Hydrogenation of 4-nitrobenzophenone was conducted in a Parr® Instrument Co. 4848 reactor. The catalyst was separated from the reactants by first filtering the mixture through Whatman ashless, No. 42 filter paper purchased from Sigma-Aldrich Germany, followed by filtration through a PVDF 0.45 μm (GVS) membrane syringe filters purchased from Lasec, SA.

### 2.2 Synthesis of N-CNTs and CNTs

N-CNTs were synthesized by use of a chemical vapour deposition (CVD) method similar to that reported by Oosthuizen *et al*.[31] and Koch *et al*.[32] Briefly, the compound 3-ferrocenyl-2-(4-cyanophenyl)-acrylonitrile that we previously synthesized and characterized (Supplementary Information S1), was used as a catalyst, and it was synthesized following the protocol outlined by Imrie *et al*.[33] and Ombaka *et al*.[34] Acetonitrile was used as a carbon and nitrogen source, while ethylbenzoate was used as a source of oxygen. The solution used to synthesize N-CNTs was prepared by dissolving 0.25 g of the catalyst in 9.75 g of acetonitrile to make a total of 10 g of solution (i.e. 2.5 wt. % of catalyst). To introduce 1 wt. % and 2 wt. % of oxygen into the synthesis precursors, 0.5 and 1.0 g of ethylbenzoate was added to 0.25 g of the catalyst respectively. Each solution was then prepared to a total mass of 10 g with acetonitrile. The solution of precursors was injected into a quartz tube (placed inside a tube furnace) at a flow rate of 0.8 mL $min^{-1}$ with a syringe pump. The injected precursors were carried through the quartz tube by a carrier gas made-up of 10% hydrogen in argon (v/v) which was pumped through the system at a rate of 100 mL $min^{-1}$ and a pressure of 80 kPa. The furnace was set to a reaction temperature of 850 °C for 30 minutes.

CNTs were also synthesized by a CVD method as previously detailed by Oosthuizen *et al*.[31] For synthesis of CNTs, ferrocene was used as the catalyst while toluene was used as the carbon source. The solution used to synthesize CNTs was made by dissolving 0.25 g of ferrocene in 9.75 g of toluene to make 10 g of solution. The CNTs were synthesized at a temperature of 850 °C for 30 minutes by use of similar synthesis conditions as those outlined for N-CNTs.

The N-CNTs and CNTs were collected from the hot zone of the quartz tube upon completion of the reaction. All products were purified by first calcining the samples at 300 °C for 3 hours, followed by ultasonication of the samples in 6 M nitric acid for 40 minutes at room temperature. The sonicated mixture was then refluxed at 100 °C for 24 hours at a constant stirring rate of 300 rpm. After refluxing, the acid was neutralized with 3 M NaOH and the mixture sonicated for 40 minutes. Afterwards, the N-CNTs or CNTs were separated from the mixture *via* filtration and washed with deionized water until a neutral pH was obtained.

### 2.3 Synthesis of catalysts

Synthesis of the catalysts was achieved by loading Pd onto acid treated N-CNTs and CNTs to yield Pd/N-CNTs and Pd/CNTs respectively. Loading of 5 wt. % Pd onto each support was achieved *via* a metal organic-CVD (MOCVD) method as outlined by Suttisawat *et al*.[35] In detail, 0.072 g of $Pd(acac)_2$ was mixed with 0.475 g of acid treated N-CNTs or CNTs and ground thoroughly by using a pestle and mortar. The resulting mixture was placed inside a stainless steel MOCVD reactor and the reactor components sealed. The sealed MOCVD reactor was connected to a vacuum pump maintained at a partial pressure of 2.2 x $10^{-2}$ mbar for 45 minutes. After evacuating the MOCVD reactor for 45 minutes, it was placed in the middle of a muffle furnace operated at 120 °C for 30 minutes. This was followed by increasing the temperature to 300 °C at a rate of 2 °C $min^{-1}$ and thereafter maintaining it at 300 °C for 45 minutes. The system was then allowed to cool to ambient temperature while still under vacuum. Upon completion of the reaction, the formed catalysts were removed from the reactor by scraping with a spatula, and then characterized as outlined in Section 2.5.

### 2.4 Catalytic tests

Hydrogenation of nitrobenzophenone to aminobenzophenone was conducted in a closed vessel reactor by using a mole ratio of 1: 66 (Pd: nitrobenzophenone). For all catalytic tests, 180.0 mg of the catalyst was put into a Parr reactor stainless steel vessel and mixed with

1250 mg of 4-nitrobenzophenone and 100 mL of dry toluene. The reactor vessel and its contents was sealed and then stirred continuously under hydrogen gas at the desired reaction conditions. A control experiment without any catalyst was performed under similar conditions. To monitor the reaction progress, aliquots of 1 mL of the reactant mixture were collected from the reaction vessel at intervals of 2 hours, quenched with 4 mL of toluene, filtered as described in Section 2.1 and then analysed off-line by GC-FID or GC-MS. Upon completion of the reaction, the solution in the reaction vessel was cooled to ambient temperature, filtered as described in Section 2.1 and the filtrate kept in a sealed container for further analysis. The used catalyst was obtained as a filtration residue, washed with 100 mL of diethylether, dried at 100 °C overnight in an oven, and then kept in a sealed container for X-ray diffraction analysis. The conversion of 4-nitrobenzophenone (NBP) and selectivity to 4-aminobenzophenone (ABP) was calculated by using equations A and B, respectively.

$$\text{Conversion of NBP} = \frac{\text{Initial [NBP]} - \text{measured [NBP]}}{\text{Initial [NBP]}} \qquad \text{equation (A)}$$

$$\text{Selectivity to ABP} = \frac{\text{Measured [ABP]}}{\text{Measured [ABP]} + \text{Measured [other products]}} \qquad \text{equation (B)}$$

where, initial [NBP] is the initial concentration of NBP measured in mg $L^{-1}$ before starting the reaction, measured [NBP], [ABP] and [other products] are the concentrations of NBP, ABP and other products measured in mg $L^{-1}$ at various time intervals as obtained from GC analysis.

## 2.5 Characterization

Images of N-CNTs, CNTs and all catalysts were taken by using transmission electron microscopy (TEM) (JEOL JEM 1010) and scanning electron microscopy (SEM) (JEOL JSM 6100). A high resolution-TEM (JEOL 2100) was used to take higher magnification images. The thermal stability of N-CNTs and CNTs was determined by using a Q Series™ Thermal Analyzer DSC/TGA (Q600). X-ray photoelectron spectroscopy (XPS) analysis was performed with a KRATOS AXIS Ultra DLD equipped with Al Kα (1486 eV) X-rays, an X-ray Power of 20 W and a beam diameter of 100 μm. Fourier transform infrared (FTIR) spectra of supports and catalysts embedded into KBr pellets were recorded on a Perkin Elmer spectrum RX1 FTIR spectrometer. Temperature programmed reduction (TPR) analysis was conducted in 5% $H_2$ in argon by using a Micromeritics Autochem II Chemisorption Analyzer

(2920). The graphitic nature of N-CNTs and CNTs was determined by use of a Raman spectrometer (DeltaNu Advantage 532™). XRD spectra were obtained from a Bruker D8 Advance X-ray diffractometer equipped with a graphite monochromatized high-intensity Cu $K_\alpha$ radiation ($\lambda$ = 0.15406 nm). The Pd-loading content was determined by inductively coupled plasma-optical emission spectroscopy (ICP-OES) (Perkin Elmer Optima 5300 DV). Details for ICP-OES analysis are provided in the Supplementary Information S1. The surface area and nitrogen adsorption-desorption isotherms of the catalysts were determined by using a Micromeritics Tristar II surface area and porosity analyser. The hydrogenation products were characterized by using GC-FID (Shimadzu 2010 gas chromatograph) and GC-MS (Shimadzu GCMS-QP2010 SE gas chromatograph-mass spectrometer). The conditions under which the GC-FID and GC-MS analysis were performed are provided in Supplementary Information S1.

## 3. Results and discussion

### 3.1 Characterization of N-CNTs and CNTs

#### 3.1.1 Morphology of N-CNTs and CNTs

The N-CNTs synthesized by using 0, 1 and 2 wt. % oxygen in acetonitrile were coded as N-CNTs-0, N-CNTs-1 and N-CNTs-2 respectively (Fig. 2). The images of N-CNTs (Fig. 2B and c) showed the presence of bamboo compartments associated with nitrogen-doping of CNTs.[36] Similar bamboo compartments were absent in the image of CNTs synthesized from ferrocene and toluene (Fig. 2A). From the TEM images, some pristine CNTs exhibited a straight morphology (Fig. 2A), while some N-CNTs exhibited a kinked morphology consisting of curved and bent N-CNTs (Fig. 2B and C). The observed kinked morphology is caused by introduction of pentagonal and heptagonal structures into the graphene layers of N-CNTs.[37] Such pentagonal and heptagonal structures can be induced by pyrrolic and pyridinic nitrogen-doping of N-CNTs. Images of N-CNTs synthesized using oxygen showed an increased density of kinked N-CNTs, which is indicative of an increase in pyrrolic-N incorporation into N-CNTs as discussed later in Section 3.2.

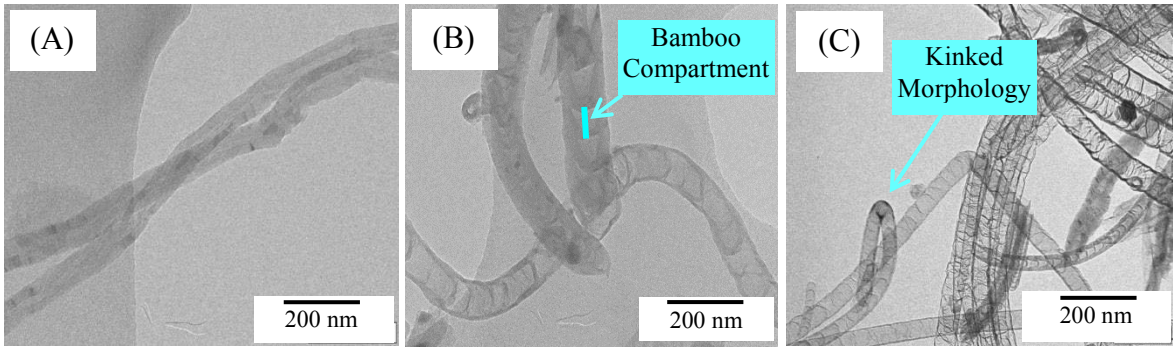


**Fig. 2** TEM images of (A) CNTs, (B) N-CNTs-0 and (C) N-CNTs-2.

All N-CNTs exhibited a reduced outer diameter (OD) compared with those of CNTs (Fig. 3). The reduced OD can be explained by the fact that, nitrogen species dominate tube edges impeding further formation of graphitic layers and resulting in closure of the tube.[36] The OD of N-CNTs-1 and N-CNTs-2 were observed to be smaller than that of N-CNTs-0. Since N-CNTs-1 and N-CNTs-2 were synthesized using 1 and 2 wt. % oxygen, the further reduction of their OD can be ascribed to the etching effect of oxygen resulting in thinner tube walls and smaller OD.

All N-CNTs exhibited larger inner diameters (ID) compared with those of CNTs (Fig. 3). This can be attributed to the formation of larger iron catalyst nanoparticles (NPs) in N-CNTs compared to those formed in CNTs during synthesis. It is possible that, the heteroatom-containing ferrocenyl derivative used to synthesize N-CNTs predominantly forms larger iron catalyst NPs compared to those formed by ferrocene which was used to synthesize CNTs.[38] Another possible explanation is that the presence of nitrogen and oxygen heteroatoms during synthesis facilities formation of larger iron catalyst NPs.[39] The presence of bigger catalyst NPs in N-CNTs can be related to the increase in residual iron content (CNTs < N-CNTs-0 < N-CNTs-1 < N-CNTs-2) evidenced from the (thermal gravimetric analysis) TGA thermograms of as-synthesized samples (Fig. 4A). The bigger catalyst particles could have favoured formation of larger inner diameters.

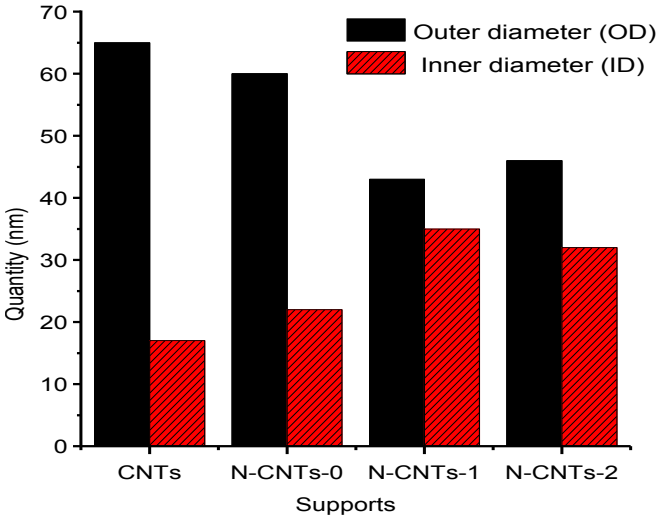


**Fig. 3** Outer diameter and inner diameter of N-CNTs and CNTs; for each sample at least 80 tubes were measured.

### 3.1.2 Thermal stability of N-CNTs and CNTs

The thermal stability and purity of N-CNTs and CNTs were determined by the use of TGA. Fig. 4 represents the thermograms and derivative thermograms (DTG) of as-synthesized and purified N-CNTs and CNTs. From the thermograms and DTG, both the as-synthesized and purified CNTs were more thermally stable than N-CNTs. The decreased thermostability of N-CNTs can be credited to the presence of defects induced by nitrogen-doping, which reduces the crystallinity of N-CNTs. Likewise, Raman analysis revealed that the crystallinity of N-CNTs was lower than that of CNTs (Supplementary Information S1). The decreased crystallinity observed with N-CNTs was associated with an increase in defect sites induced by nitrogen-doping. Such defects perpetuate decomposition at lower temperatures resulting in a lower thermal stability of the whole sample.[40]

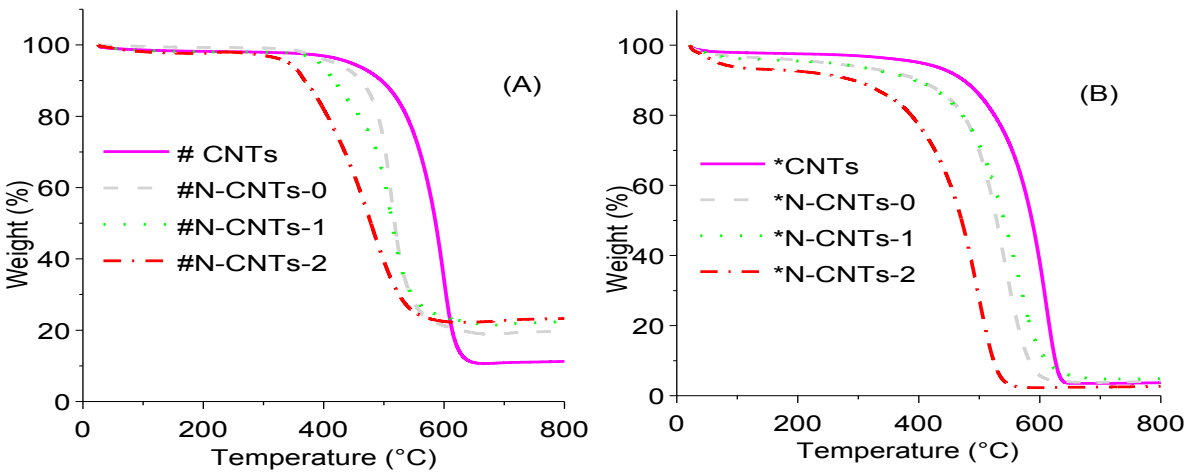

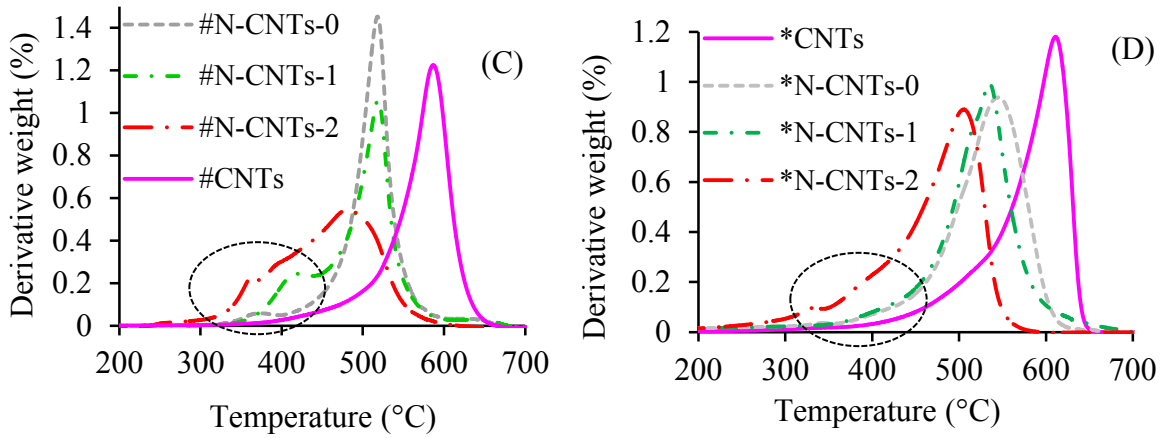


**Fig. 4.** Thermograms of (A) as-synthesized and (B) purified CNTs and N-CNTs; derivative thermograms of (C) as-synthesized and (D) purified CNTs and N-CNTs. The symbols hash (#) and asterisk (*) denote the as-synthesized and purified samples respectively.

All purified N-CNTs were less thermally stable than CNTs implying that the purification procedure did not severely remove the nitrogen present in N-CNTs. The thermal stability of purified N-CNTs decreased in the order N-CNTs-2 > N-CNTs-1 > N-CNTs-0. This decrease in thermal stability was attributed to an increase in pyrrole-like nitrogen. Purification of N-CNTs and CNTs reduced the iron content in all samples to similar quantities (Fig. 4B). A significant reduction of the peak associated with amorphous carbons and FeO residue at *ca.* 400 °C, marked by a dotted circle was achieved after sample purification (cf. Fig. 4C and D).

## 3.2 Characterization of catalysts

### 3.2.1 Surface chemistry

The surface of the Pd/N-CNTs and Pd/CNTs was analysed by the use of XPS and FTIR spectroscopy. From the XPS analysis, the total nitrogen percentage of N-CNTs-0, N-CNTs-1 and N-CNTs-2 was 4.4%, 3.5% and 2.5% respectively. The decrease of nitrogen content in the N-CNTs synthesized by using 1 and 2 wt. % of oxygen was related to the reduction in the quantity of nitrogen in the precursors used to synthesize these samples (Supplementary Information S2). A similar observation has been reported wherein the nitrogen percentage in N-CNTs reduced as the amount of nitrogen in the synthesis precursor was reduced.[41]

The N 1s spectra of all N-CNTs showed a broad peak between 399-405 eV resulting from an overlap of different peaks (Fig. 5A). Deconvolution of the broad N 1s peak gave three peaks at 398.5-398.4, 400.3-400.6 and 404.1-404.7 eV (Supplementary Information S3). The

peak at 398.4-398.5 eV was attributed to pyridinic and carbonitrile nitrogen species and it was coded N1.[42, 43] The peak at 400.3-400.6 eV was accredited to pyrrole nitrogen species and it was coded N2.[43-45] While the peak at 404.1-404.7 eV was attributed to nitrogen molecules adsorbed or encapsulated within the N-CNTs, it was coded N3.[46]

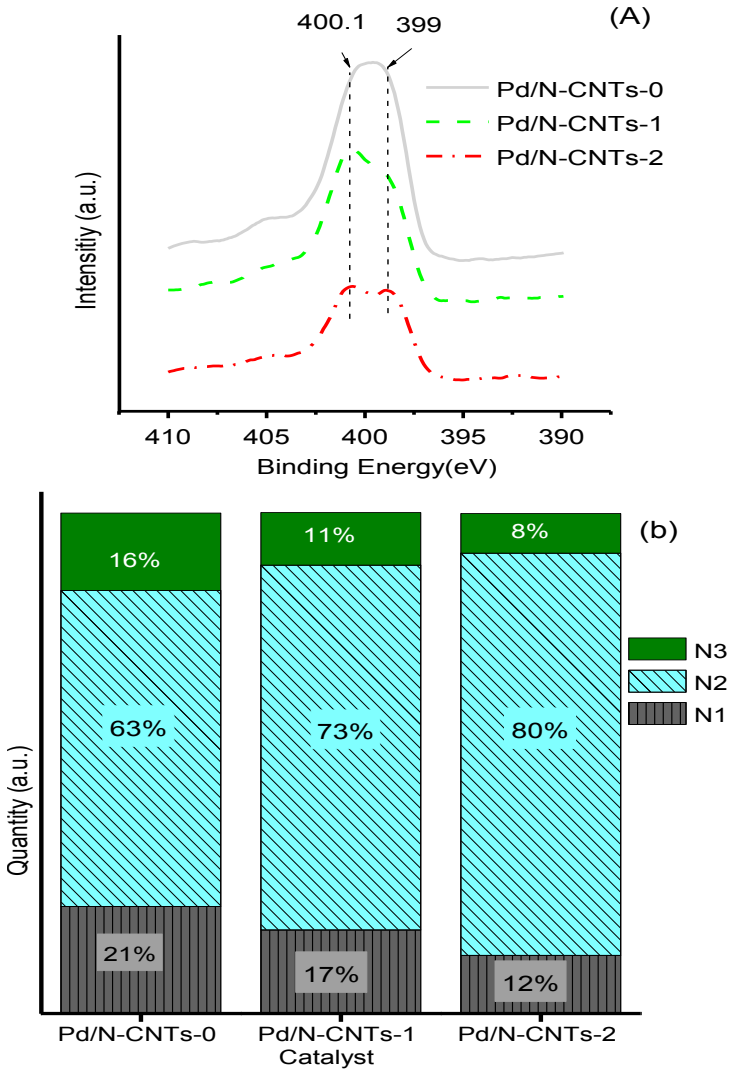


**Fig. 5** (A) N 1s XPS spectra of N-CNTs synthesized by using 0-2 wt. % oxygen in acetonitrile, and (B) variations in the nitrogen species (%) present in N-CNTs synthesized by using 0-2 wt % oxygen, see Supporting Information S3 for further details of N species (%). Where, the total nitrogen content in N-CNTs-0, N-CNTs-1 and N-CNTs-2 is 4.4%, 3.5% and 2.5% respectively.

Increasing the amount of oxygen from 0-2 wt. % during the synthesis of N-CNTs, resulted in an increase in the amount of N2 and a decrease in the amount of N1 and N3 (Fig. 5B). This could imply that the presence of oxygen favoured formation of N2 at the expense of N1 and N3. The decrease in N3 can be due to formation of N-O molecules *via* the reaction

between oxygen and nitrogen molecules on the iron catalyst surface. The $NO_x$ molecules exit the reaction chamber as exhaust gases. On the other hand, the decrease in N1 was accredited to an additional reaction induced by the presence of oxygen that favoured formation of N2. The possibility of an additional reaction initiated by oxygen was deduced from evaluating the C 1s and O 1s spectra of N-CNTs and CNTs.

Deconvolution of the C 1s spectra of N-CNTs and CNTs gave two common carbon species (C1 and C2) in all N-CNTs and CNTs. A third carbon species (C3) was only present in N-CNTs-1 and N-CNTs-2, while the fourth carbon species (C4) was only present in CNTs and N-CNTs-0 (Table 1 and Supplementary Information S3). The lowest energy peak obtained was at 284.4-284.7 eV (C1); this was assigned to graphitic carbon.[42, 47] A second peak was obtained at 285.5-285.9 eV (C2); this peak was assigned to C-N and C-O species.[48, 49] The third peak was obtained at 287.3-287.7 eV (C3); this was attributed to carbonyls in quinone, lactones and carboxyl groups.[49, 50] The fourth peak was obtained at 288.2-288.8 eV (C4); this was ascribed to carbonyls in carboxyl groups.[49, 50] Resonance shake-up satellite peaks caused by $\pi$- $\pi$ transitions in the aromatic rings were observed at 291.1-291.6 eV.[50]

**Table 1** Summary of C 1s XPS spectra of Pd/N-CNTs and Pd/CNTs.

| Sample | C at. % | | | | O at. % |
|---|---|---|---|---|---|
| | C1 | C2 | C3 | C4 | O Total |
| Pd/N-CNTs-0 | 52.7 | 33.8 | - | 8.9 | 10.4 |
| Pd/N-CNTs-1 | 45.9 | 28.6 | 21.7 | - | 8.3 |
| Pd/N-CNTs-2 | 42.4 | 27.3 | 23.5 | - | 13.5 |
| Pd/CNTs | 57.4 | 25.1 | - | 10.0 | 6.6 |

All N-CNTs exhibited lower quantities of C1 (graphitic carbon) compared with CNTs implying that, nitrogen-doping reduced the graphitic nature of CNTs. Additionally, the amount of graphitic carbon in N-CNTs further reduced as the percentage of pyrrolic groups increased (cf. Table 1 and Fig. 5B). Since the quantity of graphitic carbon in N-CNTs did not show a positive correlation with the total nitrogen content, the decrease in graphitic carbon was ascribed to formation of more pyrrole groups. An increase in pyrrolic groups enhanced the disorder in the N-CNTs, accounting for the reduced thermal stability of N-CNTs-1 and N-CNTs-2 observed from the thermograms and DTG of these samples. Similarly, the decrease in graphitic carbon resulted in decreased crystallinity of the N-CNTs as observed from Raman analysis[51] (Supplementary Information S1).

Based on the C 1s and O 1s spectra of N-CNTs, we propose that during the synthesis of N-CNTs-1 and N-CNTs-2 lactones are formed[52] as explained in the Supplementary Information S4. The formed lactones react with ammonia obtained from the reaction of hydrogen and acetonitrile[53] to form lactams. The lactams are then converted to pyrrole groups by the removal of a -CO group (Scheme 1).[44] As more oxygen is added into the synthesis precursor, more lactones are formed resulting in an increased formation of pyrrole groups at the expense of pyridinic and carbonitrile groups. Hence, lactones provide an additional route to that already present in N-CNTs-0, by which pyrrole groups are formed, thus, increasing selectivity towards pyrrole formation.

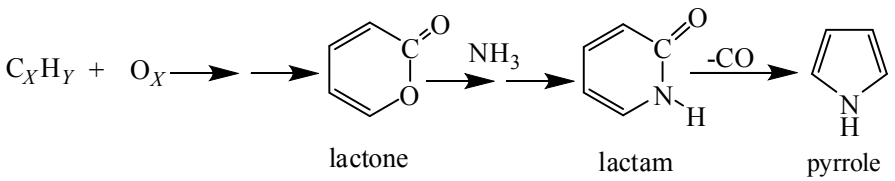


**Scheme 1.** Plausible synthetic route for pyrrole formation.

Further identification of the functional groups present in Pd/N-CNTs and Pd/CNTs was accomplished by the use of FTIR spectrometry. From the FTIR spectra of all samples, a clear distinction was observed between the functional groups present in N-CNTs and CNTs (Fig. 6). At ≈2373 $cm^{-1}$ a peak caused by $CO_2$ stretching vibrations was observed.[54, 55]

Another important peak was that at 1466 $cm^{-1}$ assigned to C=N in pyridinic groups.[55, 56] The intensity of this peak was quite weak in all Pd/N-CNTs but completely absent in Pd/CNTs. The transmittance peak of C=C in the graphene layers of CNTs was observed at 1653 $cm^{-1}$,[57, 58] while the peak assigned to C-N groups was observed at ≈1570 $cm^{-1}$.[55, 59] In Pd/CNTs, the peaks attributed to C-N and carbonitrile groups were absent but they were clearly visible in Pd/N-CNTs. The absence of these peaks indicated that no nitrogen-doping was present in Pd/CNTs as also observed from XPS analysis (Supplementary Information S3). It was interesting to note that for N-CNTs-0 the C=C and C-N peaks exhibited almost the same intensity while in N-CNTs-1 and N-CNTs-2 the intensity of the C=C peak was significantly lower than that of C-N. This was related to the presence of more pyrrole groups in N-CNTs-1 and N-CNTs-2 compared with N-CNTs-0.

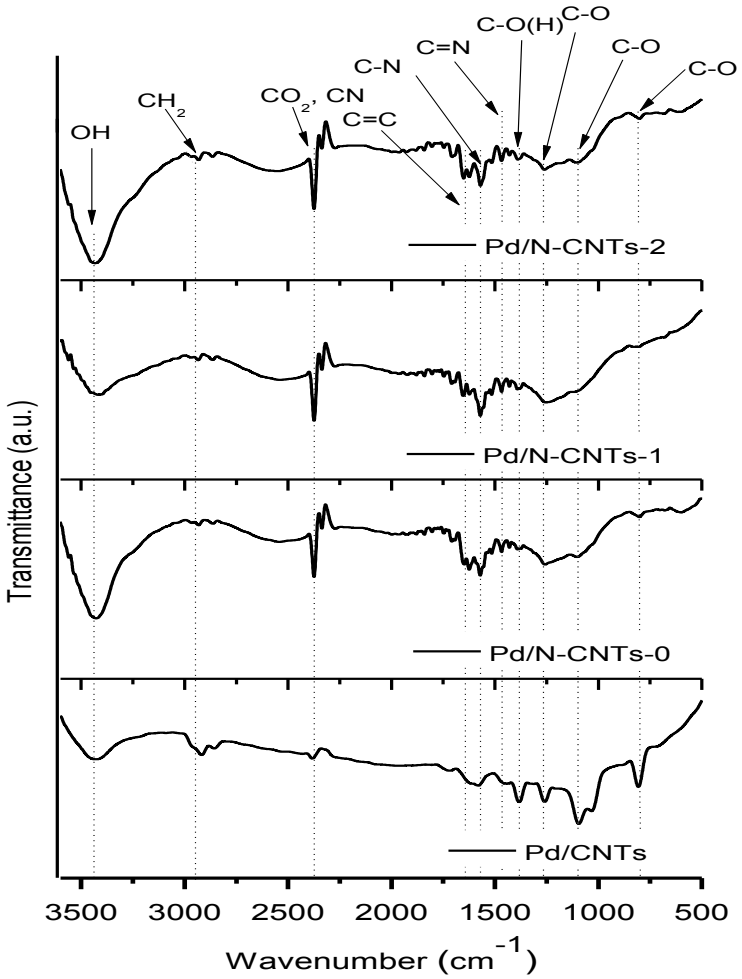


**Fig. 6** FTIR spectra of Pd/CNTs and Pd/N-CNTs.

The peak at 3420 $cm^{-1}$, attributed to hydrogen bonded –OH groups due to moisture and alcohols,[60, 61] was present in all samples. Peaks at 1393 and 1258 $cm^{-1}$ allotted to stretching of the C-O and C=C in the tubes[61] were stronger in Pd/CNTs than in Pd/N-CNTs. While the peaks at 1089 and 790 $cm^{-1}$, assigned to C-O vibrations and stretching modes,[57, 58] were only present in Pd/CNTs. The carbonyl peak appearing at 1706 $cm^{-1}$ was very weak in Pd/CNTs but slightly stronger in Pd/N-CNTs.[57, 58] This could imply that the hydrogen bonded –OH groups in Pd/CNTs were mainly from phenol groups and adsorbed water, while the –OH groups in Pd/N-CNTs are mainly due to carboxylic groups and adsorbed water. The peak at 2937 $cm^{-1}$, assigned to $CH_2$ groups, was present in all samples.[55, 57]

### 3.2.2 Textural properties

The surface area and pore size of CNTs and all N-CNTs increased after acid treatment (Supplementary Information S4). This implied that the acid treatment effectively de-bundled the tubes and opened their closed ends. The textural properties of Pd/N-CNTs and Pd/CNTs are presented in Table 2. Doping of CNTs with 4.4 at. % nitrogen containing 63% pyrrolic groups increased the surface area of Pd/CNTs from 52 to 55 $m^2g^{-1}$. The surface area of Pd/N-CNTs further increased to 89 $m^2g^{-1}$ as the nitrogen-content dropped to 3.5 at. % and the percentage of pyrrolic groups increased to 73%. A further drop in the nitrogen content to 2.5 at. % accompanied by an increase in the pyrrole content to 80% decreased the surface area of Pd/N-CNTs from 89 to 38 $m^2g^{-1}$. Thus, no clear relationship was observed between surface area and the nitrogen-doping levels as Pd/CNTs had a higher surface area than Pd/N-CNTs-2. Hence, the cause of surface area variation remained unclear.

**Table 2** Textural properties of Pd/CNTs and Pd/N-CNTs.

| Catalyst | at. % N | Pyrrole composition (%) | Surface area of catalyst ($m^2g^{-1}$) | Pore size distribution (nm) |
|---|---|---|---|---|
| Pd/CNTs | 0 | 0 | 52 | 4.1 |
| Pd/N-CNTs-0 | 4.4 | 63 | 55 | 4.5 |
| Pd/N-CNTs-1 | 3.5 | 73 | 89 | 4.1 |
| Pd/N-CNTs -2 | 2.5 | 80 | 38 | 4.1 |

All supports were classified as type IV mesoporous materials, exhibiting a hysteresis loop between 0.5-1.0 $P/P_0$ (Fig. 7, Supplementary Information S4).[62] Pd/CNTs and Pd/N-CNTs-0 showed a hysteresis loop between 0.7-1.0 $P/P_0$ which appeared very similar to a $H_1$ type hysteresis loop.[63] Such a hysteresis loop is intrinsic in independent regular cylindrical and spherical shaped pores.[64] In addition, Pd/N-CNTs-0 showed a more open hysteresis loop than Pd/CNTs (Supplementary Information S4), indicating that the pore size of CNTs increased upon doping with nitrogen (Table 2). The increase in pore size observed with Pd/N-CNTs-0 was associated with the increase in ID and the presence of compartments as observed from TEM analysis of N-CNTs (Fig. 3).

Pd/N-CNTs-1 and Pd/N-CNTs-2 showed an almost horizontal hysteresis loop between 0.5-0.9 $P/P_0$ that is associated with a $H_3$ type hysteresis loop.[63] The $H_3$ type hysteresis loop could be due to disordered pores forming the network of a porous matrix,[65] or large pores

formed by the bamboo compartments of N-CNTs. The disordered pores could be due to extensive structural disorder dominated with pyrrole groups, which are five membered rings that distort the graphene structure of CNTs. Alternatively, the disordered pores could result from oxygen etching some of the formed regular shaped pores, making them irregularly shaped.

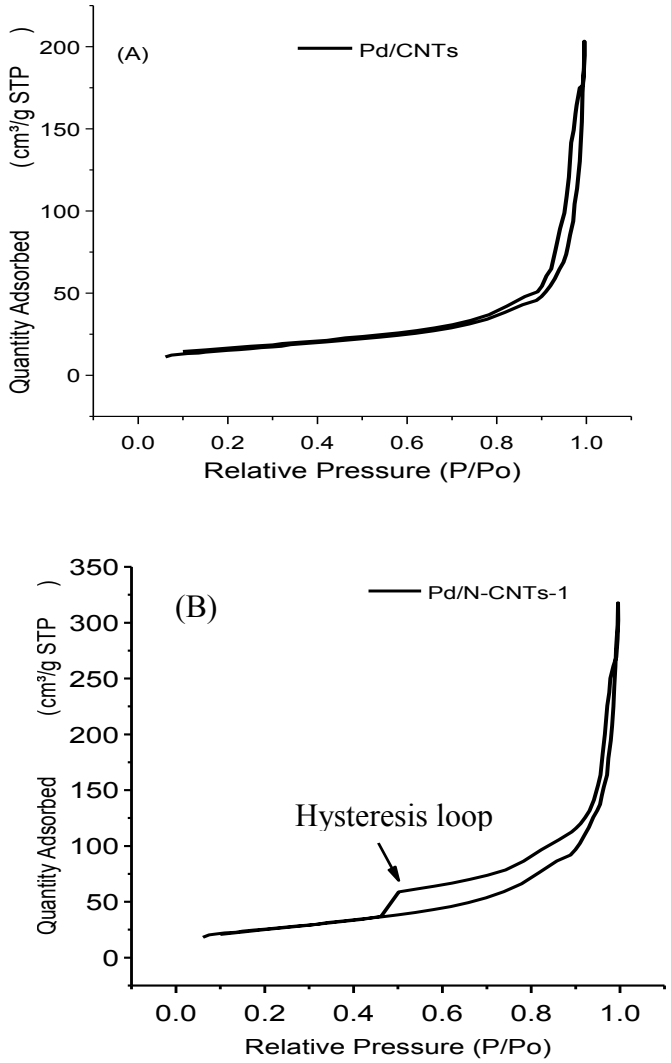


**Fig. 7** Representative $N_2$ adsorption–desorption isotherms of (A) Pd/CNTs and (B) Pd/N-CNTs.

### 3.2.3 Interactions of pyrrole N-CNTs with Pd nanoparticles

The influence of pyrrolic nitrogen on the interactions between N-CNTs and Pd NPs was inferred from XPS, FTIR, TPR, TEM and XRD analysis. The Pd 3d XPS spectra of Pd/N-CNTs and Pd/CNTs exhibited four overlapping peaks (Fig. 8). Deconvolution of these peaks (Supplementary Information S3) revealed the presence of $Pd^0$ and $Pd^{2+}$ species as summarized in Table 3.

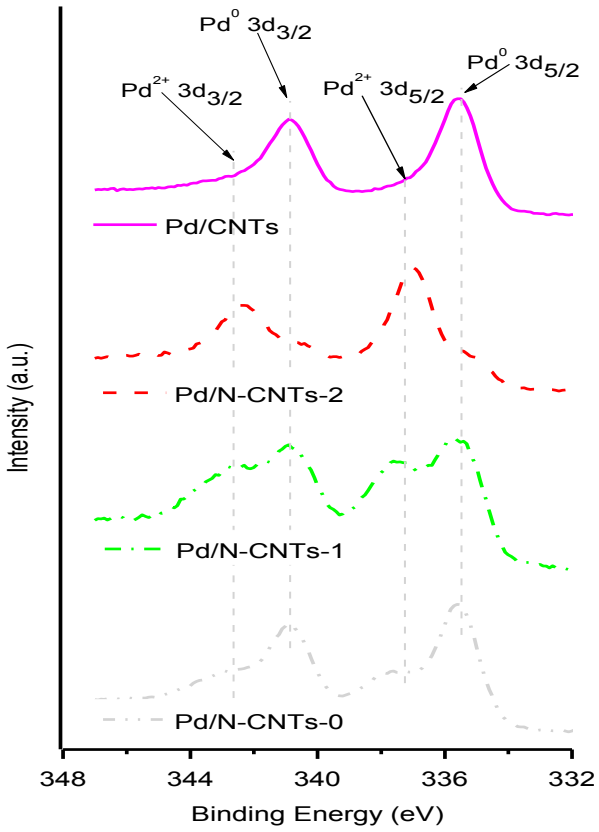


**Fig. 8.** Pd 3d XPS spectra of Pd/CNTs and Pd/N-CNTs synthesized by using 0-2% oxygen in acetonitrile.

Table 3 Pd species and atomic % of Pd in N-CNTs and CNTs.

| | Pd $3d_{5/2}$ | | | | Pd $3d_{3/2}$ | | | |
|---|---|---|---|---|---|---|---|---|
| | $Pd^0$ | | $Pd^{2+}$ | | $Pd^0$ | | $Pd^{2+}$ | |
| Sample | BE (eV) | at% | BE (eV) | at% | BE (eV) | at% | BE (eV) | at% |
| Pd/N-CNTs-0 | 335.6 | 36.5 | 337.7 | 20.5 | 340.8 | 24.8 | 342.8 | 18.1 |
| Pd/N-CNTs-1 | 335.4 | 20.0 | 337.3 | 34.1 | 340.8 | 23.1 | 342.8 | 22.7 |
| Pd/NCNTs-2 | 335.2 | 8.16 | 337.0 | 45.2 | 340.3 | 11.3 | 342.4 | 29.3 |
| Pd/CNTs | 335.6 | 44.11 | 337.5 | 11.5 | 340.9 | 33.74 | 342.9 | 10.62 |

As shown in Table 3 the binding energies at *ca*. 335.6 and 340.8 eV were assigned to $Pd^0$ species[47] while, those at *ca*. 337.7 and 342.8 eV were assigned to $Pd^{2+}$ species.[66-69] The $Pd^{2+}$ species in Pd/CNTs could be PdO formed *via* an oxidation reaction between $Pd^0$ and the surface oxygen groups in CNTs. However, the $Pd^{2+}$ species in N-CNTs were not entirely from PdO as no linear correlation was observed between the oxygen percentage and the percentage of $Pd^{2+}$ (cf. Table 1 and 3). It was noted that as the amount of pyrrolic nitrogen

increased from 0 (in CNTs) to 80% (in N-CNTs-2), the quantity of $Pd^0$ reduced while that of $Pd^{2+}$ increased (Table 3 and Fig. 8) and, the binding enegy of $Pd^0$ and $Pd^{2+}$ shifted to lower values. This indicated that as the percentage of pyrrolic nitrogen increased, $Pd^0$ species derived from $Pd(acac)_2$ were progressively being bonded to the pyrrolic nitrogen to form Pd-N complexes. This interaction could occur during synthesis of the catalyst following the reaction depicted in Scheme 2. Such a reaction could be due to the interaction of $Pd^0$ with neighbouring pyrrolic cations.[66, 70] The covalently bonded $Pd^{2+}$ could be stable, preventing further reduction of $Pd^{2+}$ to $Pd^0$ during synthesis.

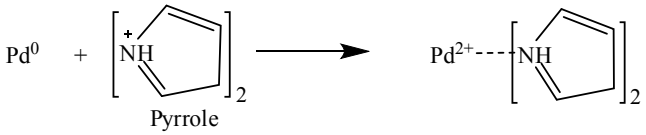


**Scheme 2.** Possible interactions between pyrrolic nitrogens and Pd nanoparticles.

To probe further, the existence of an interaction between Pd NPs and N-CNTs, the FTIR spectrum of N-CNTs-2 was compared with that of Pd/N-CNTs-2 (Fig. 9A). In N-CNTs-2 the peak assigned to C-N groups appeared at *ca*. 1567 $cm^{-1}$, while in Pd/N-CNTs-2 this peak appears at around 1552 $cm^{-1}$.[59] The shift of the C-N peak to lower wavenumbers in the presence of Pd NPs is indicative of interactions between pyrrolic nitrogen and Pd NPs.[70, 71]

The interaction between Pd NPs and the surface of different supports was also studied by using TPR and the profiles obtained are presented in Fig. 9B. From the TPR profiles, a broad peak was observed between 60-150 °C; this peak was associated with reduction of $Pd^{2+}$ species, possibly in PdO.[72] The $Pd^{2+}$ reduction peak was observed to gradually broaden towards higher temperatures as the quantity of pyrrolic groups increased in N-CNTs-0 and N-CNTs-2. This shift towards higher temperatures is indicative of formation of stronger metal-support interactions as the number of pyrrolic nitrogen groups increased. However, the $Pd^{2+}$ reduction peak of Pd/N-CNTs-1 occurred at a lower temperature than expected.

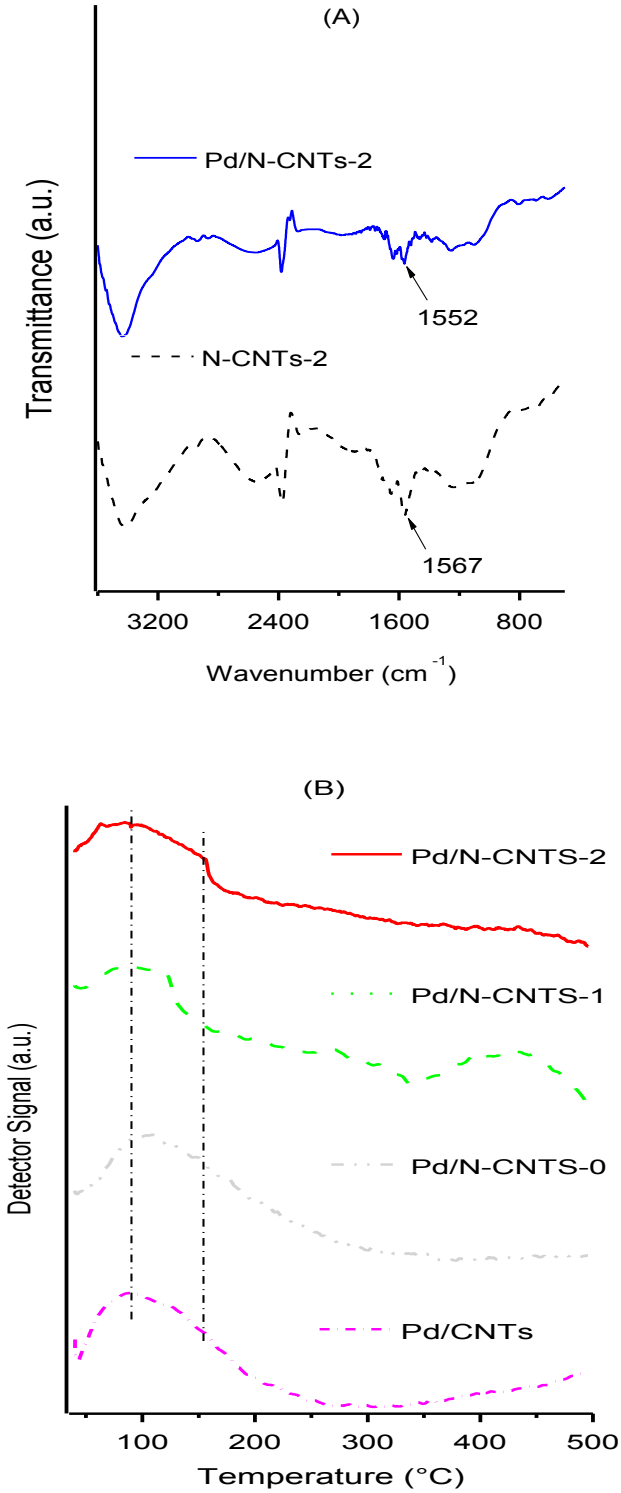


**Fig. 9** (A) FTIR spectra of N-CNTs-2 and Pd/N-CNTs-2, and (B) TPR profiles of Pd/CNTs and Pd/N-CNTs.

TPR profiles showed that the intensity of the $Pd^{2+}$ reduction peak did not increase in a manner similar to that observed from the Pd 3d XPS spectra (Fig. 8). This implied that the

increased quantity of $Pd^{2+}$ observed from the Pd 3d XPS spectra was not entirely due to the formation of more PdO. This observation further supported our hypothesis that the increase in $Pd^{2+}$ species in Pd/N-CNTs was due to interactions between Pd NPs and pyrrolic nitrogen groups. A weak desorption peak was observed at *ca*. 50 °C in the TPR profile of Pd/CNTs alone. This peak was ascribed to decomposition of Pd-$\beta$-hydride[73] and its absence in all the other profiles implied that no Pd-$\beta$-hydride was formed when Pd NPs were supported on N-CNTs.

The TEM images of Pd/CNTs and Pd/N-CNTs are presented in Fig. 10. Pd NPs supported on N-CNTs-0, N-CNTs-1 and N-CNTs-2 exhibited a more even particle dispersion compared with Pd NPs supported on CNTs (cf. Fig. 10A, 10B, 10C and 10D). Pd NPs were randomly distributed on CNTs, while on N-CNTs-1 and N-CNTs-2 Pd NPs were typically located along the compartmental layers. These defect sites consist of pentagons and heptagons induced by nitrogen-doping.[36] This indicated that electronic charges are localized on the pentagons and heptagons, which enhance electronic interactions between Pd NPs and defect sites, leading to well dispersed Pd NPs.[74, 75]

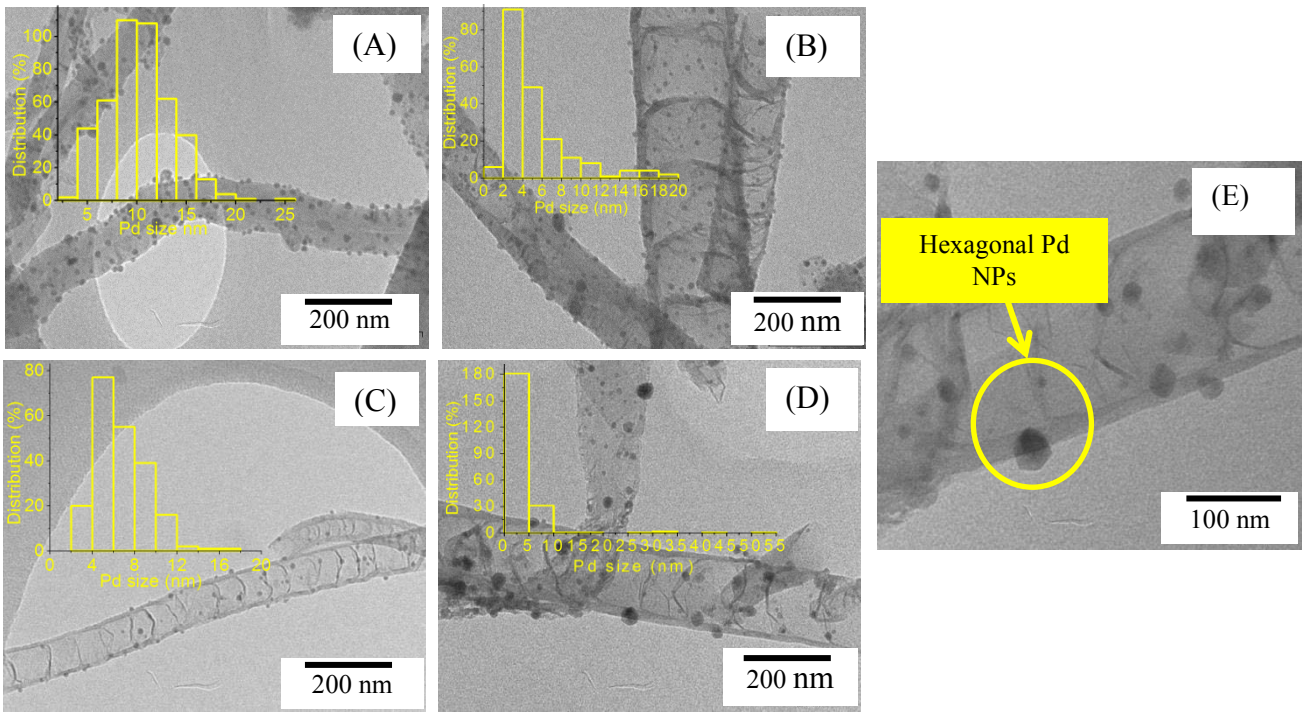


**Fig. 10** TEM images of (A) Pd/CNTs, (B) Pd/N-CNTs-0, (C) Pd/N-CNTs-1, (D) Pd/N-CNTs-2 and (E) a higher magnification image of Pd/N-CNTs-2. Inset histograms in images a, b, c and d are the corresponding Pd NPs size distributions.

Interestingly, some hexagonal Pd NPs were only observed in Pd/N-CNTs-2 as shown in Fig. 10E which is a higher magnification of Fig. 10D. This could imply that the high composition of pyrrolic nitrogen (80%) provided a sufficient quantity of molecules that acted as surface capping agents, also facilitated formation of hexagonal Pd NPs.

Representative images of supported Pd NPs analysed by TEM at a higher magnification are shown in Fig. 11. From the TEM images, Pd NPs supported on N-CNTs-0 (Fig. 11A) appeared spherical while Pd NPs supported on N-CNTs-2 (Fig. 11B) appeared hexagonal. The hexagonal Pd NPs similar to those observed in the lower magnification images of Pd/N-CNTs-2 (Fig. 10E).

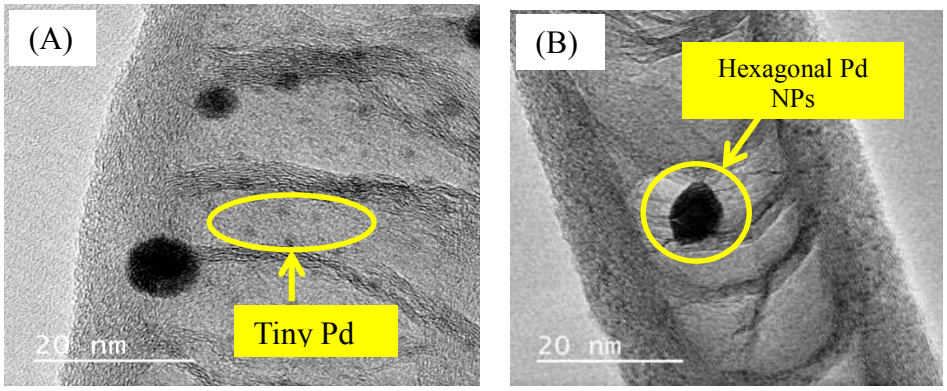


**Fig. 11** TEM images of (A) Pd/CNTs-0 and (B) Pd/N-CNTs-2,

High magnification images of Pd/N-CNTs-0 showed the presence of tiny Pd NPs forming nanoclusters and larger Pd NPs (Fig. 11A). Such tiny particles were mainly present in Pd/N-CNTs-0 containing the highest level of nitrogen-doping. Consequently, formation of nanoclusters was ascribed to greater nitrogen-doping levels and the presence of more pyridinic/carbonitrile groups. Generally, higher nitrogen-doping levels favoured the formation of tiny Pd NPs, while higher levels of pyrrolic nitrogen favoured formation of hexagonal Pd NPs.

The XRD diffractograms of various catalysts are presented in Fig. 12 where 5% Pd/AC was used as an external standard. The peak at 26.4° was indexed as the $C_{(002)}$ reflection of the hexagonal graphite in CNTs and N-CNTs. The peaks at 40° and 45° present in Pd/AC, Pd/CNTs and all Pd/N-CNTs were indexed as the Pd (111) and Pd (200) reflections of $Pd^{0}$.[76] Pd/CNTs showed an extra peak at 67° that was indexed as the Pd (220) reflection. All catalysts had similar Pd loading levels as obtained from ICP-OES analysis (Table 4). Therefore, the absence of the Pd (220) reflection in Pd/N-CNTs was related to differences in

Pd NP sizes. A further evaluation of the Pd NP sizes was performed by using the Pd (111) diffraction peak and TEM image analysis.

The Pd NP sizes were estimated from the Pd (111) diffraction peak, by applying the Debye-Scherrer equation given by:

$$D = \frac{0.89\lambda}{\beta cos\theta}$$

where $D$ is the crystal size of Pd NPs, $\lambda$ = 0.154 nm which is the wavelength of the X-rays, $\theta$ is the diffraction angle of the Pd (111) reflection and $\beta$ is the full width at half maximum of the Pd (111) reflection.

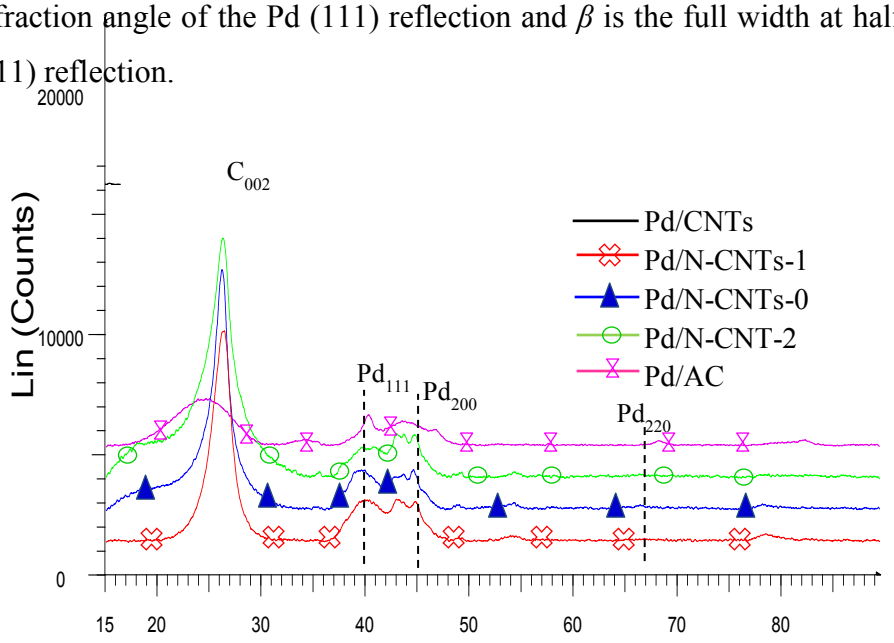


**Fig. 12** XRD diffractograms of Pd/CNTs, Pd/N-CNTs and Pd/AC.

In addition, the particle size of supported Pd NPs was determined by measuring the size of at least 200 Pd NPs from the TEM images (Fig. 10). Both the TEM and XRD analyses of Pd NP sizes showed a comparable trend in the particle size variation (Table 4). Based on the XRD analysis, Pd NPs supported on CNTs exhibited larger particle sizes than Pd NPs supported on N-CNTs. Pd NPs supported on N-CNTs-0 showed the smallest particle size. The Pd NP sizes decreased as the total percentage nitrogen in N-CNTs increased. This indicated that increasing nitrogen-doping levels in N-CNTs introduced more functional groups which adequately anchored the Pd NPs. The well-anchored Pd NPs were less prone to NP sintering and agglomeration during the cooling stages of catalyst synthesis resulting in smaller particle sizes.[2]

**Table 4** Summary of Pd wt. %, Pd NP size and X-ray structural parameters of catalysts.

| Catalyst | Pd loading wt. % (ICP-OES) | Ave. Pd NP size (nm) TEM | Ave. Pd NP diameter (nm) XRD | 2θ of $Pd_{(111)}$ peak (°) | FWHM of $Pd_{(111)}$ peak (°) | Inter layer spacing (Å) |
|---|---|---|---|---|---|---|
| Pd/CNTs | 4.9 | 8 | 4.5 | 39.429 | 1.867 | 2.28347 |
| Pd/N-CNTs-0 | 4.5 | 5 | 3.8 | 39.938 | 2.254 | 2.25554 |
| Pd/N-CNTs -1 | 5.0 | 7 | 4.0 | 39.924 | 2.11 | 2.25631 |
| Pd/N-CNTs-2 | 4.9 | 5 | 4.1 | 39.892 | 2.085 | 2.25807 |
| Pd/AC | 5.0[$] | 12 | 10.7 | 40.278 | 0.793 | 2.23728 |

NP: Nanoparticle, [$]As determined by the manufacturer, Ave: Average, FWHM: Full width at half maximum

### 3.3 Catalytic activity tests

The catalytic activity of Pd/N-CNTs, Pd/CNTs, N-CNTs-2 and Pd/AC was evaluated with the aim of determining the influence of pyrrolic nitrogen on the selective nitro-reduction of NBP. Since NBP has three reducible groups *viz.* $NO_2$, CHO and C=C, selectivity towards ABP was more vital than the conversion of NBP because this selectivity is an indication of the catalysts‘ efficiency in the formation of substituted anilines. Fig. 13 and Table 5 presents the catalytic activity of these catalysts. All Pd/N-CNTs showed a greater conversion of NBP than Pd/CNTs after 24 hours of the reaction. This indicated that doping of CNTs with nitrogen enhanced the activity of Pd NPs (Fig. 13A).

Pd/N-CNTs-1 and Pd/N-CNTs-2 with a smaller at. % N content were more active than Pd/N-CNTs-0 which had the highest at. % N. Since Pd/N-CNTs-1 and Pd/N-CNTs-2 had a higher pyrrolic N content than Pd/N-CNTs-0, it is plausible that pyrrolic nitrogen enhances activity. The pyrrolic nitrogen groups could have promoted Pd-support interactions by forming Pd-N coordination complexes.[77] Such complexes can alter the electronic and structural properties of Pd NPs as explained in Section 3.2.3 resulting in improved activities.[76] The improved activity of Pd/N-CNTs could also be due to the stronger metal-support interactions as observed from TPR analysis. Such strong metal-support interactions can enhance Pd NP dispersion, reduce Pd NP agglomeration and sintering during reactions, resulting in a higher activity.[25]

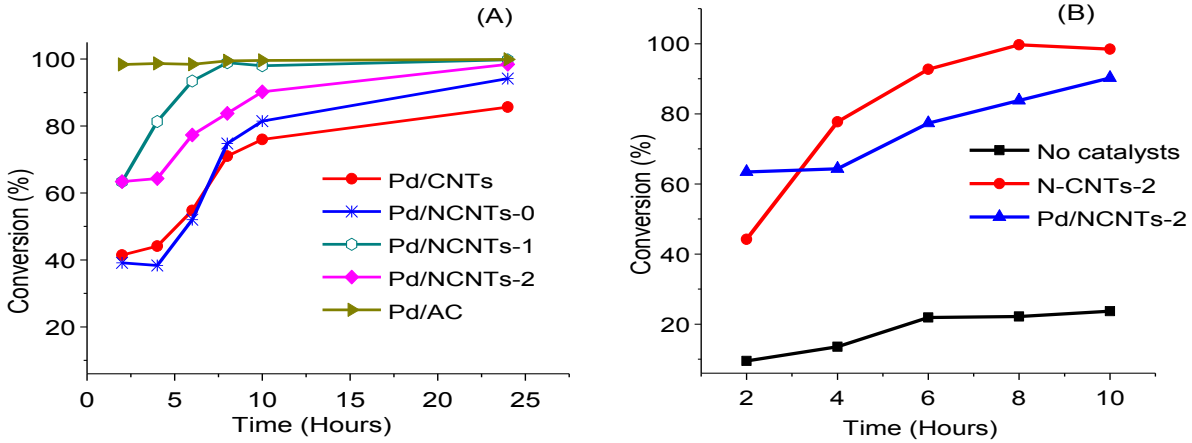


**Fig. 13** (A) Conversion of NBP over Pd/N-CNTs, Pd/CNTs, Pd/AC and (B) conversion of NBP over Pd/N-CNTs-2 and N-CNTs-2.

Pd/N-CNTs-2 with the highest percentage of pyrrolic nitrogen and the lowest surface area showed an activity higher than that of Pd/N-CNT-0 and Pd/CNTs, but slightly lower than that of Pd/N-CNTs-1. To further probe the cause of the enhanced activity over Pd/N-CNTs-2, the activity of purified N-CNTs-2 was evaluated. N-CNTs-2 exhibited a higher activity than Pd/N-CNTs-2 (Fig. 13A). This indicated that pyrrolic-containing N-CNTs are good catalysts for the hydrogenation of NBP and, Pd plays a minor role in the catalytic activity of Pd/N-CNTs. A possible explanation for the lower activity observed with Pd/N-CNTs-2 is that some of the pyrrolic groups were bound to Pd NPs, thus reducing the quantity of pyrrolic groups available for NBP conversion. This implied that the pyrrolic groups in N-CNTs-2 largely promoted the catalytic activity of Pd/N-CNTs-2. Thus, the enhanced activity of Pd/N-CNTs-2 despite having a low surface area, could be due to the promotin effect of pyrroclic groups. The availabiliy of more pyrrolic groups also resulted in more disorder in Pd/N-CNTs-2 compared with other catalysts as evidenced form the XPS and TGA analysis. Such a high content of disorded sites are related to nitrogen-induced defects which can lower the work function of materials resulting in increased catalyst activity.[78] Pd/AC showed the highest activity, and this was attributed to its high surface area of 890 $m^2g^{-1}$ (Supplementary Information S5). No correlation was observed between Pd NP size and catalytic activity.

Hydrogenation of NBP over Pd/CNTs, Pd/N-CNTs-1 and Pd/N-CNTs-2 yielded only ABP, while hydrogenation of NBP over Pd/N-CNTs-0 and Pd/AC yielded ABP and *p*-benzylaniline (Scheme 3). Although, Pd/AC showed the highest conversion of NBP, its selectivity to either ABP or *p*-benzylaniline was poor compared to that of Pd/CNTs and Pd/N-CNTs. Up to 10 hours of reaction, all Pd/N-CNTs showed greater selectivity towards ABP than Pd/CNTs (Fig. 14A and Table 5). Thereafter selectivity over Pd/N-CNTs-2

increased, and that of Pd/N-CNTs-1 and Pd/CNTs were almost constant while that of Pd/N-CNTs-0 sharply dropped. Pd/AC showed the lowest selectivity to ABP throughout the whole reaction period. Given that Pd/-N-CNTs-1 and Pd/N-CNTs-2 showed a greater selectivty than Pd/CNTs, we deduced that nitrogen-doping of CNTs enhanced the selective reduction of the nitro group to an amine group.[79] As the amount of pyrrolic nitrogen increased, selectivity towards ABP also increased for Pd/N-CNTs-1 and Pd/N-CNTs-2, while no correlation was observed between the selectivities and the total N%. This implied that selectivity was influenced more by the presence of pyrrolic nitrogen than the total N%. Other studies have shown that the species of nitrogen and not just the nitrogen content in N-CNTs play a significant role in influencing the catalytic properties of N-CNTs as as metal catalyst supports.[80]

N-CNTs-2 showed a much lower selectivity towards ABP compared with Pd/N-CNTs-2 (Fig. 14B), impying that Pd NPs were responsible for the selectivty observed with Pd/N-CNTs-2. Therefore, the enhanced selectivity over Pd/N-CNTs was majorly attributed to the presence of Pd-N complexes. Such complexes minimise Pd NP sintering and agglomeration during the reaction thus, increasing Pd NPs stability and dispersion.[76] The increased stability and dispersion of Pd NPs could increase the hydrogen chemisorption capacity of Pd NPs hence increasing the selectivity. The presence of more disordered pores in N-CNTs could also facilitate a faster mass transfer of ABP from the catalyst surface back into the solution.[2] This could prevent a further reduction of ABP to *p*-benzylaniline resulting in an increased selectivity. Corma *et al*. compared the selective nitro-reduction of nitrobenzaldehyde to aminobenzaldehyde over supported Au and Pd.[81] Their findings showed a lower selectivity over Pd compared with Au. Hence, the enhanced selectivity towards ABP observed with Pd/NCNTs can be due to the promoting effect of N-CNTs supports.

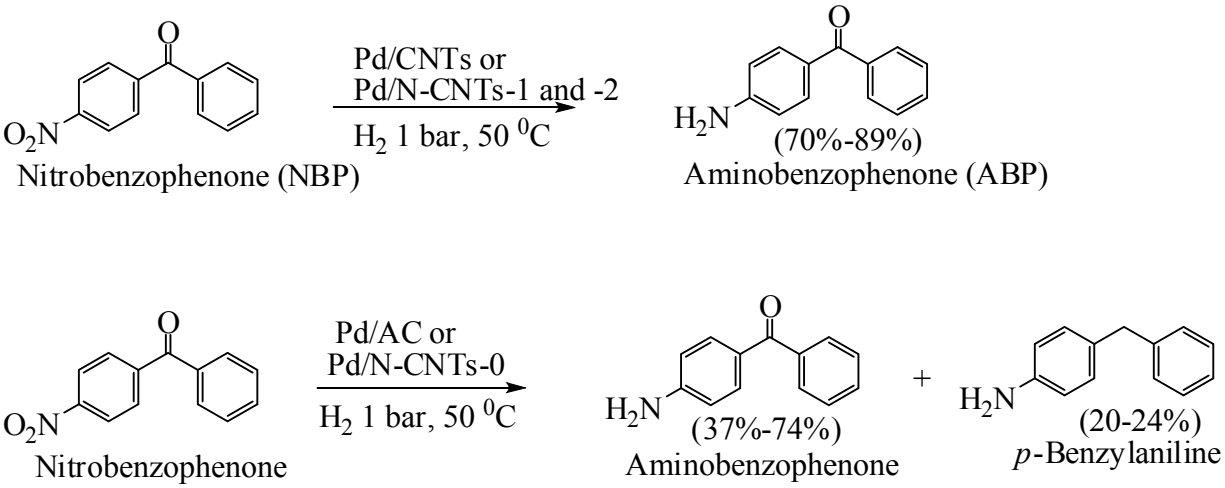


**Scheme 3.** Hydrogenation of NBP over various catalysts.

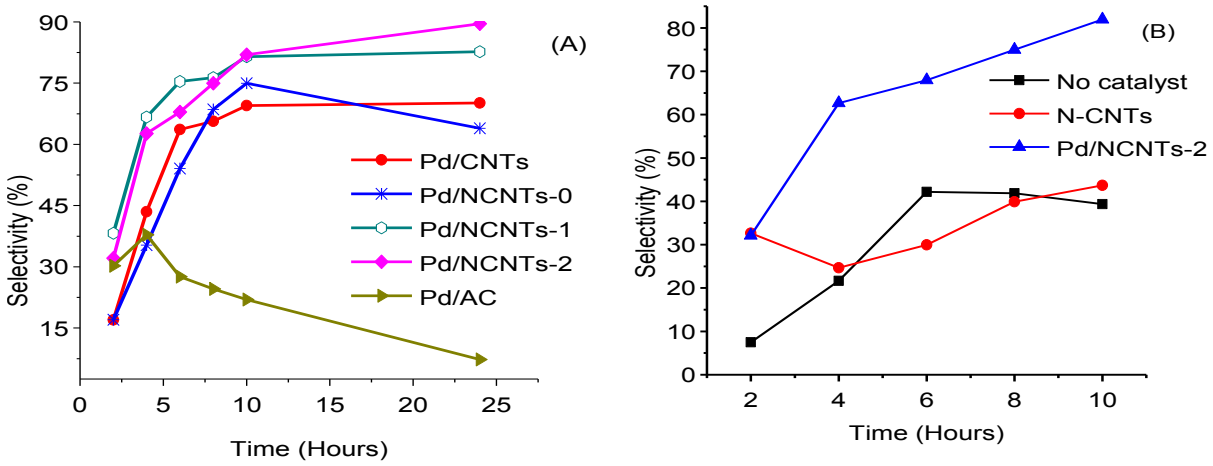


**Fig. 14** (A) Selectivity towards ABP over Pd/N-CNTs, Pd/CNTs, Pd/AC and (B) selectivity towards ABP over Pd/N-CNTs-2 and N-CNTs-2.

Selectivity over Pd/N-CNTs-0 dropped after 10 hours implying that Pd/N-CNTs-0 possess a different catalytic pathway compared with Pd/CNTs, Pd/N-CNTs-1 and Pd/N-CNTs-2. The different catalytic pathway in Pd/N-CNTs-0 was accredited to the existence of tiny Pd NPs forming nanoclusters. A similar drop in selectivity was observed over Pd/AC which also had tiny Pd NPs in the form of clusters (Supplementary Information S6). Such Pd nanoclusters may possess a different reaction mechanism from the larger Pd NPs.[82] This different reaction mechanism could have favoured the further reduction of ABP to *p*-benzylaniline accounting for the drop in selectivity (Supplementary Information S6 and Table 5).

**Table 5** Summary of the catalytic performance of catalysts after 24 hours of the reaction.

| Catalyst | Conversion of NBP (%) | Selectivity to ABP (%) | Selectivity to *p*-benzylaniline (%) | *Other products |
|---|---|---|---|---|
| Pd/CNTs | 85 | 70 | - | morpholine-4-carbal, 2-phenylethanol |
| Pd/N-CNTs-0 | 93 | 63 | 6.3 | morpholine-4-carbal |
| Pd/N-CNTs-1 | 100 | 83 | - | morpholine-4-carbal |
| Pd/N-CNTs -2 | 98 | 89 | - | morpholine-4-carbal |
| Pd/AC | 100 | 24 | 24 | benzophenone |

*Other hydrogenation products detected from the GC-MS

Since all catalysts had a similar quantity of residual iron catalyst (Fig. 4B) the possibility of the residual iron catalyst influencing the observed catalytic trend was ruled out. From the TEM analysis no iron particles were observed on the surface of the supports. This implied that the residual iron was encapsulated inside the CNTs and N-CNTs and hence not available for surface catalysis.

Pd/N-CNTs-2, which showed the highest selectivity after 24 hours, was used to evaluate the effect of pressure on the catalytic activity and selectivity. It was observed that as the pressure increased the catalytic activity and selectivity over Pd/N-CNTs-2 was reduced (Supplementary Information S7). Thus, the optimum pressure for the hydrogenation of NBP was 1 bar.

### 3.4 Stability of Pd NPs after hydrogenation reactions

The stability of Pd NPs on N-CNTs-0, N-CNTs-1 and N-CNTs-2 after use was analysed by XRD. From the XRD diffractograms, the Pd NP size of used catalysts was determined in a similar manner to that outlined in Section 3.2.3. Used Pd/CNTs was not analysed because it strongly adhered to the filter paper resulting in a low catalyst recovery, which was insufficient for XRD analysis. Table 6 shows the average diameters of the Pd NPs before and after reaction. The size of the Pd NPs in N-CNTs-0 and N-CNTs-1 increased after the reaction while in N-CNTs-2 the size of the Pd NPs did not change. This implied that Pd sintering and agglomeration may have occurred only in Pd/N-CNTs-0 and Pd/N-CNTs-1. Thus, the Pd NPs in N-CNTs-2 were considered very stable; owing to the formation of more

Pd-N complexes in Pd/N-CNTs-2 than in Pd/N-CNTs-0 and Pd/N-CNTs-1. In a similar manner, Chen *et al*. showed that pyridinic nitrogen can complex with $Ru^{3+}$ as a ligand to form stable $Ru^{3+}$ particles, which were resilient to metal sintering and agglomeration.[20]

**Table 6** Average Pd NP sizes of various catalysts before and after a single reaction.

| Catalyst | [#]Ave. Pd NP diameter (nm) | [$]Ave. Pd NP diameter (nm) |
|---|---|---|
| Pd/N-CNTs-0 | 3.8 | 5.0 |
| Pd/N-CNTs-1 | 4.0 | 5.8 |
| Pd/N-CNTs-2 | 4.1 | 4.1 |

Ave: average, NP: nanoparticle, [#]before hydrogenation reaction, [$]after hydrogenation reaction

The diffractograms of the used catalysts showed an increase in the intensity of the Pd (111) reflection compared with those of the fresh catalyst (Supplementary Information S8). This increase in the Pd (111) reflection indicated that more $Pd^0$ was formed *via* the hydrogen reduction of $Pd^{2+}$ during the reaction.

## 4. Conclusions

Pyrrolic N-CNTs containing 2.5-4.4 at. % of nitrogen were successfully synthesized by means of CVD method. Selectivity towards formation of pyrrolic nitrogen was promoted by the incorporation of oxygen derived from ethylbenzoate during synthesis of the N-CNTs. Increasing the amounts of pyrrolic groups in N-CNTs significantly altered the physicochemical properties of N-CNTs such as thermal stability, textural properties and surface wetness. Also, an increase in the pyrrolic percentage improved the interactions between Pd and N-CNTs resulting in better dispersion and more stable Pd NPs. The improved dispersion and stability of Pd NPs was associated with a strong interaction between the pyrrolic nitrogen and Pd NPs. The catalytic activity and selectivity of Pd/N-CNTs in the hydrogenation of NBP was dependent on the percentage of pyrrolic nitrogen and not on the total nitrogen content. Pd/N-CNTs showed an enhanced selectivity compared with Pd/CNTs and Pd/AC. Thus, Pd supported on pyrrolic N-CNTs is a promising catalyst for the selective reduction of NBP and other industrially important nitro arenes such as nitrobenzene derivatives.

## Acknowledgements

The authors wish to thank the University of KwaZulu-Natal and the National Research Foundation (NRF) for financial support. We are grateful to Professor Bice Martincigh and Dr. R. S. Mwakubambanya for their insightful suggestions during the manuscript development and their assistance with proof-reading.

## References

1. Y. Tang, Z. Yang, X. Dai, D. Ma and Z. Fu, *J. Phys. Chem. C*, 2013, **117**, 5258-5268.
2. L. M. Ombaka, P. Ndungu and V. O. Nyamori, *Catal. Today*, 2013, **217**, 65-75.
3. H. Dai, *Nanotube growth and characterization, in: M. S. Dresselhaus, G. Dresselhaus (Eds.), Carbon Nanotubes Synthesis, Structure, Properties and Applications, Springler-Verlag, Heidelberg*, 2001, pp. 29-51.
4. A. Politano, A. R. Marino, D. Campi, D. Farías, R. Miranda and G. Chiarello, *Carbon*, 2012, **50**, 4903-4910.
5. J. S. Qi, J. Y. Huang, J. Feng, D. N. Shi and J. Li, *ACS Nano*, 2011, **5**, 3475-3482.
6. A. Loiseau, X. Blasé, J.-C. Charlier, P. Gadelle, C. Journet, C. Laurent and A. Peigney, *Synthesis methods and growth mechanism, in: A. Loiseau, P. Launois, P. Petit, S. Roche, J.-P. Salvetat (Eds.), Understanding Carbon Nanotubes, Springer-Heidelberg,*, Springer, 2006, pp. 49-122.
7. C. Wang, L. Zhang, Z. Guo, J. Xu, H. Wang, K. Zhai and X. Zhuo, *Microchim. Acta*, 2010, **169**, 1-6.
8. J. Wang, G. Yin, Y. Shao, Z. Wang and Y. Gao, *J. Phys. Chem.*, 2008, **112**, 5784-5789.
9. A. Politano and G. Chiarello, *Nanoscale*, 2013, **5**, 8215-8220.
10. J.-S. Lee, S.-I. Kim, J.-C. Yoon and J.-H. Jang, *ACS Nano*, 2013, **7**, 6047-6055.
11. J. J. Niu, J. N. Wang, Y. Jiang, L. F. Su and J. Ma, *Microporous Mesoporous Mater*, 2007, **100**, 1-5.
12. K. S. Novoselov, A. K. Geim, S. V. Morozov, D. Jiang, Y. Zhang, S. V. Dubonos, I. V. Grigorieva and A. A. Firsov, *Science*, 2004, **306**, 666-669.
13. K. P. Loh, Q. Bao, G. Eda and M. Chhowalla, *Nat. Chem*, 2010, **2**, 1015-1024.
14. D. Malko, C. Neiss, F. Viñes and A. Görling, *Phys. Rev. Lett.*, 2012, **108**, 086804-086807.
15. Y. Wang, N. Shah, F. E. Huggins and G. P. Huffman, *Energy Fuels*, 2006, **20**, 2612-2615.

16. J.-H. Olivier, F. Camerel, R. Ziessel, P. Retailleau, J. Amadou and C. Pham-Huu, *New J. Chem.*, 2008, **32**, 920-924.
17. M. P. Lázaro, E. García-Bordeje, D. Sebastián, M. J. Lázaro and R. Moliner, *Catal. Today*, 2008, **138**, 203-209.
18. S. Domínguez-Domínguez, Á. Berenguer-Murcia, B. K. Pradhan, Á. Linares-Solano and D. Cazorla-Amorós., *J. Phys. Chem. C*, 2008, **112**, 3827-3834.
19. R. S. Oosthuizen and V. O. Nyamori, *Platinum Met. Rev.*, 2011, **55**, 154-169.
20. J J. L. Chen, Z. H. Zhu, S. B. Wang, Q. Ma, V. Rudolph and G. Q. Lu, *Chem. Eng. J.*, 2010, **156**, 404-410.
21. E. M. M. Ibrahim, O. K. Vyacheslav, A. Leonhardt, S. Hampel, S. Oswald, M. H. Rümmeli and B. Büchner, *Diamond Relat. Mater.*, 2010, **19**, 1199-1206.
22. F. R. García-García, J. Àlvarez-Rodríguez, I. Rodríguez-Ramos and A. Guerrero-Ruiz, *Carbon*, 2010, **48**, 267-276.
23. W. An and C. H. Turner, *J. Phys. Chem. C*, 2009, **113**, 7069-7078.
24. C. Yonghai, Y. Hao, T. Jun, P. Feng, W. Hongjuan, L. Jing, Z. Wenxu and W. Ning-Bew, *Carbon*, 2013, **57**, 433-442.
25. K. Chizari, I. Janowska, M. Houllé, I. Florea, O. Ersen, T. Romero, P. Bernhardt, M. J. Ledoux and C. Pham-Huu, *Appl. Catal. A: General*, 2010, **380**, 72-80.
26. A. S. Saghiyan, L. A. Stepanyan, L. L. Manasyan, A. V. Geolchanyan, S. M. Djamgaryan, H. R. Ajvazyan, H. A. Panosyan, V. I. Maleev and T. F. Saveleva, *Tetrahedron Lett.*, 2010, **21**, 2638-2645.
27. A. K. Bhowmik, S. Tan, A. C. Ahyi, J. A. Dharmadhikari, A. K. Dharmadhikari and D. Mathur, *Opt. Commun.*, 2007, **280**, 472-476.
28. Z. Li, B. Wu, G. Su and G. Huang, *Appl. Phys. Lett.*, 1997, **70**, 562-564.
29. E. N. Nxumalo and N. J. Coville, *Materials*, 2010, **3**, 2141-2171.
30. E. N. Nxumalo, V. O. Nyamori and N. J. Coville, *J. Organomet. Chem.*, 2008, **693**, 2942-2948.
31. R. S. Oosthuizen and V. O. Nyamori, *Appl. Organomet. Chem.*, 2012, **26**, 536-545.
32. R. J. Koch, M. Weser, W. Zhao, F. Viñes, K. Gotterbarm, S. M. Kozlov, O. Höfert, M. Ostler, C. Papp, J. Gebhardt, H. P. Steinrück, A. Görling and Th. Seyller, *Phys. Rev. B*, 2012, **86**, 075401-075406.
33. C. Imrie, P. Kleyi, V. O. Nyamori, T. I. A. Gerber, D. C. Levendis and J. Look, *J. Organomet. Chem.*, 2007, **692**, 3443-3453.

34. L. M. Ombaka, P. G. Ndungu, B. Omondi and V. O. Nyamori, *J. Coord. Chem.*, 2014, **67**, 1905-1922.
35. Y. Suttisawat, P. Rangsunvigit, B. Kitiyanan, M. Williams, P. Ndungu, M. V. Lototskyy, A. Nechaev, V. Linkov and S. Kulprathipanja, *Int. J. Hydrogen Energy*, 2009, **34**, 6669-6675.
36. B. G. Sumpter, V. Meunier, J. M. Romo-Herrera, E. Cruz-Silva, D. A. Cullen, H. Terrones, D. J. Smith and M. Terrones, *ACS Nano*, 2007, **1**, 369-375.
37. L. Lizhao, L. Feng and Z. Jijun, *Nano Res.*, 2014, **7**, 626-657.
38. K. Chizari and U. Sundararaj, *Mater. Lett.*, 2014, **116**, 289-292.
39. S. Liu, Y. Zhang, Y. Lin, Z. Zhao and Q. Li, *Carbon*, 2014, **69**, 247-254.
40. K. Chizari, A. Vena, L. Laurentius and U. Sundararaj, *Carbon*, 2014, **68**, 369-379.
41. A. A. Koós, M. Dowling, K. Jurkschat, A. Crossley and N. Grobert, *Carbon*, 2009, **47**, 30-37.
42. Z. Luo, S. Lim, Z. Tian, J. Shang, L. Lai, B. MacDonald, C. Fu, Z. Shen, T. Yu and J. Lin, *J. Mater. Chem.*, 2011, **21**, 8038-8044.
43. E. T. Kang, K. G. Neoh, S. H. Khor, K. L. Tan and B. T. G. Tan, *Polymer*, 1990, **31**, 202-207.
44. S. Kundu, W. Xia, W. Busser, M. Becker, D. A. Schmidt, M. Havenith and M. Muhler, *Phys. Chem. Chem. Phys.*, 2010, **12**, 4351-4359.
45. S. Wang, F. Wang and X. Ge, *Synth. Met.*, 1986, **16**, 99-104.
46. Y. Cao, H. Yu, J. Tan, F. Peng, H. Wang, J. Li, W. Zheng and N.-B. Wong, *Carbon*, 2013, **57**, 433-442.
47. C. J. Powell, *J. Electron Spectrosc. Relat. Phenom.*, 2012, **185**, 1-3.
48. S. C. Ray, A. Saha, N. R. Jana and R. Sarkar, *J. Phys. Chem. C*, 2009, **113**, 18546-18551.
49. D. Briggs and G. Beamson, *Anal. Chem.*, 1992, **64**, 1729-1736.
50. S. Kundu, Y. Wang, W. Xia and M. Muhler, *J. Phys. Chem. C*, 2008, **112**, 16869-16878.
51. S. Z. Mortazavi, P. Parvin, A. Reyhani, R. Malekfar and M. Soghra, *RSC Adv.*, 2013, **3**, 1397–1409.
52. G. Beamson, D. T. Clark, N. W. Hayes, D. S.-L. Law, *Surf. Sci. Spectra*, 1994, **3**, 357-365.
53. H. Li, Y. Wu, H. Luo, M. Wang and Y. Xu, *J. Catal.*, 2003, **214**, 15-25.

54. A. Misra, P. K. Tyagi, M. K. Singh and D. S. Misra, *Diamond Relat. Mater.*, 2006, **15**, 385-388.
55. G. Lazar and I. Lazar, *J. Non-Cryst. Solids*, 2003, **331**, 70-78.
56. T. Barzetti, E. Selli, D. Moscotti and L. Forni, *J. Chem. Soc., Faraday Trans.*, 1996, **92**, 1401-1407.
57. L. Vanyoreka, R. Meszarosa and S. Barany, *Colloids and Surfaces A: Physicochem. Eng. Aspects*, 2014, **448**, 140-146.
58. P. E. Fanning and M. A. Vannice, *Carbon*, 1993, **31**, 721-730.
59. T. J. Bandosz, *Carbon materials fo catalysis*, John Wiley & Sons, Inc., United States of America, 2009, pp. 63-66.
60. U.-J Kim, C. A. Furtado, X. Liu, G. Chen and P. C. Eklund, *J. Am. Chem. Soc.*, 2005, **127**, 15437-15445.
61. M. Aydin, *Vib. Spectrosc*, 2013, **65**, 84-93.
62. Z. Lei, D. Bai and X. S. Zhao, *Microporous Mesoporous Mater.*, 2012, **147**, 86-93.
63. K. S. W. Sing, D. H. Everett, R. A. W. Haul, L. Moscou, R. A. Pierotti, J. Rouquerol and T. Siemieniewska, *Pure & Appl. Chem.*, 1985, **57**, 603-619.
64. C. J. Rasmussen, A. Vishnyakov, M. Thommes, B. M. Smarsly, F. Kleitz and A. V. Neimark, *Langmuir*, 2010, **26**, 10147-10157.
65. H.-J. Woo and P. A. Monson, *Phys. Rev. E*, 2003, **67**, 041207-041224.
66. J. Y. Kim, K. Park, S. Y. Bae, G. C. Kim, S. Lee and H. C. Choi, *J. Mater. Chem.*, 2011, **21**, 5999-6005.
67. X.-F. Guo, D.-Y. Jang, H.-G. Jang and G.-J. Kim, *Catal. Today*, 2012, **186**, 109-114.
68. S. Santra, P. Ranjan, P. Bera, P. Ghosh and S. K. Mandal, *RSC Adv.*, 2012, **2**, 7523-7533.
69. T. H. Fleisch and G. J. Mains, *J. Phys. Chem.*, 1986, **90**, 5317-5320.
70. I. Rivas, J. Badano, C. Lederhos, D. Liprandi, E. Cagnola and C. V. M. Quiroga, *Quim. Nova*, 2011, **34**, 87-90.
71. M. Baghayeri, H. Veisi, H. Veisi, B. Maleki, H. Karimi-Malehd and H. Beitollahi, *RSC Adv.*, 2014, **4**, 49595-49604.
72. O. S. G. P. Soares, J. J. M. Órfão and M. F. R. Pereira, *Ind. Eng. Chem. Res.*, 2010, **49**, 7183-7192.
73. M. Gurratha, T. Kuretzky, H. P. Boehm, L. B. Okhlopkova, A. S. Lisitsyn and V. A. Likholobov, *Carbon*, 2000, **38**, 1241-1255.
74. A. Staykov, Y. Ooishi and T. Ishihara, *J. Phys. Chem. C*, 2014, **118**, 8907-8916.

75. L. Bardotti, F. Tournus, R. Delagrange, J. M. Benoit, O. Pierre-Louis and V. Dupuis, *Appl. Surf. Sci.*, 2014, **301**, 564-567.
76. P. Chen, L. M. Chew, A. Kostka, M. Muhlera and W. Xia, *Catal. Sci. Technol*, 2013, **3**, 1964-1971.
77. D. He, C. Zeng, C. Xu, N. Cheng, H. Li, S. Mu and M. Pan, *Langmuir*, 2011, **27**, 5582-5588.
78. Q. B. Wen, L. Qiao, W. T. Zheng, Y. Zeng, C. Q. Qu, S. S. Yu and Q. Jiang, *Physica E*, 2008, **40**, 890-893.
79. P. Chen, F. Yang, A. Kostka and W. Xia, *ACS Catal.*, 2014, **4**, 1478-1486.
80. W. Ouyang, D. Zeng, X. Yu, F. Xie, W. Zhang, J. Chen, J. Yan, F. Xie, L. Wange, H. Meng and D.Yuan, *Int. J. Hydrogen Energy*, 2014, **39**, 15996-16005.
81. A. Corma and P. Serna, *Science*, 2006, **313**, 332-334.
82. C. Torres, C. Campos, J. L. G. Fierro, M. Oportus and P. Reyes, *Catal. Lett.*, 2013, **143**, 763-771.

# CHAPTER SEVEN

# CHEMOSELECTIVE HYDROGENATION OF NITROBENZOPHENONE OVER Pd-SUPPORTED ON NITROGEN-DOPED CARBON NANOTUBES

Lucy M. Ombaka, Patrick G. Ndungu and Vincent O. Nyamori*
School of Chemistry and Physics, University of KwaZulu-Natal, Westville Campus, Private Bag X54001, Durban, 4000, South Africa

## Abstract

Nitrogen-doped carbon nanotubes (N-CNTs) with varying surface areas were synthesized *via* a chemical vapour deposition technique by use of ferrocene and a ferrocenyl derivative as catalysts. The N-CNTs were functionalized by means of acid treatment and used as Pd nanoparticle supports (Pd/N-CNTs). Both N-CNTs and Pd/N-CNTs were characterised by the use of transmission electron microscopy (TEM), Raman spectroscopy, thermogravimetric analysis and nitrogen adsorption-desorption isotherms. Selective reduction of nitrobenzophenone to aminobenzophenone was used as a model reaction to test the effect of surface area of the Pd catalyst on selectivity towards aminobenzophenone. Pd/N-CNTs having a higher Pd surface area showed an enhanced selectivity towards aminobenzophenone and a higher nitrobenzophenone conversion. The effect of temperature and solvent on the selectivity towards aminobenzophenone over Pd/N-CNTs was also determined. Increasing the reaction temperature favoured the selective reduction of the nitro-group. It was also evidenced that an aprotic solvent showed a more enhanced selectivity than a protic solvent towards aminobenzophenone. Furthermore, a recycling test was performed on one of the catalyst. The recycling test showed that the catalyst could be recycled while still maintaining a reasonable catalytic conversion of upto 84%.

Key words: Hydrogenation, nitrogen-doped carbon nanotubes, Pd, nitrobenzophenone, aminobenzophenone, solvent-effect.

*Corresponding author. Telephone: +27-31 260 8256; Fax: +27-31 260 3091
*E-mail address*: nyamori@ukzn.ac.za (V. O. Nyamori)

## 1. Introduction

The selective hydrogenation of substituted nitro-arenes is frequently employed to synthesize anilines, which are applied in various fields such as in the synthesis of pesticides [1], dyes and drugs [2]. In certain instances, the substituted nitro-arenes contain other functional groups, for instance, carbonyl, C=C or halogens, which are also labile to hydrogenation. The selective nitro-hydrogenation of such nitro-arenes is challenging, as it requires a catalyst that will specifically reduce the nitro-group alone. Another task encountered in the chemoselective reduction of nitro-arenes to anilines is the presence of competing reactions, such as condensation reactions and the deep hydrogenation of nitro-arenes to cyclic amines [3].

Different strategies can be utilized to overcome the aforementioned difficulties experienced during hydrogenation of nitro-arenes. The functional groups on the catalyst surface can be manipulated to enhance the adsorption of the nitro-groups to the catalyst. However, the adsorption strength should not be too strong as to derail the desorption of the aniline from the catalyst surface [3]. The dispersion and mesoporosity of the catalyst is another important aspect because increasing the dispersion increases the surface area of catalytically active sites which could enhance selectivity [4]. Other reaction parameters, such as pressure and temperature, also play a vital role in the design of a highly selective catalytic system [5]. The solvent used during a nitro-reduction reaction also affects selectivity towards anilines. This is because the solubility of hydrogen differs in varying solvents with volatile non-polar solvents showing better hydrogen solubility [5]. The homogenous suspension of the heterogeneous catalyst in solvents applied during hydrogenation also influences selectivity [5]. Solvents exhibiting good catalyst dispersion are likely to show a better selectivity.

Several supported metal catalysts have been used for the hydrogenation of nitro-arenes, however, supported Pd is the most versatile catalyst for nitro-reduction [6]. Pd supported on carbon nanotubes (CNTs) is an example of a supported Pd catalyst known to show excellent selectivity towards nitro-reduction [3, 6]. Despite the superior physicochemical properties of nitrogen-doped carbon nanotubes (N-CNTs) over CNTs [7], few accounts report on the selective nitro-reduction over Pd supported on N-CNTs. In our previous report, we presented data on the influence of pyrrollic-nitrogen species on the selective hydrogenation of nitrobenzophenone to aminobenzophenone [8]. In this account, the catalyst that exhibited the highest selectivity towards aminobenzophenone in the previous report was studied and

evaluated further. This was accomplished by comparing the selectivity of the previously reported catalyst (Pd/N-CNTs-2) which has a surface area of 38 $m^2g^{-1}$, to that of Pd/N-CNTs with a surface area of 123 $m^2g^{-1}$. In addition, the effect of temperature and solvent on the selectivity towards aminobenzophenone is also evaluated. The recyclability of the catalyst is also analyszed.

## 2. Experimental

### 2.1 Materials and instrumentation

The reagents 4-nitrobenzophenone (99%), 4-aminobenzophenone (97%) and diethyl ether (99.8%) were purchased from Sigma Aldrich. Palladium acetylacetonate {$Pd(acac)_2$} of synthesis grade was purchased from Merck, Germany. Toluene (99.4%) and 2-propanol (99%) were purchased from LiChroSolv. All reagents and solvents were pure analytical grade and were used as received from the suppliers. Pd was loaded onto N-CNTs in a cylindrical stainless steel reaction chamber (140 mm x 10 mm) sealed at one end with a Swagelok® face seal fitting [8]. To monitor the partial pressure used during synthesis of the catalyst a Thyracont VD84/1 Pirani vacuum gauge was used. Hydrogenation of 4-nitrobenzophenone was conducted in a Parr® Instrument Co. 4848 reactor. The catalyst was separated from the reactants by first filtering the mixture through Whatman ashless, No. 42 filter paper purchased from Sigma-Aldrich Germany, followed by filtration through a PVDF 0.45 μm (GVS) membrane syringe filter, SA.

### 2.2 Synthesis of N-CNTs

N-CNTs were synthesized by use of a chemical vapour deposition (CVD) method as detailed by Ombaka *et al.* [8]. Two types of N-CNTs were synthesized, one was obtained by using 3-ferrocenyl-2-(4-cyanophenyl)acrylonitrile as a catalyst (N-CNTs-2), the other was obtained by use of ferrocene as a catalyst (N-CNTs-Fe). Both N-CNTs were synthesized following the protocol outlined by Ombaka *et al*. [9]. Acetonitrile was used as a carbon and nitrogen source, while ethylbenzoate was used as a source of oxygen. The solution used to synthesize N-CNTs-2 was prepared by adding 1.0 g of ethylbenzoate to 0.25 g of 3-ferrocenyl-2-(4-cyanophenyl)acrylonitrile and then preparing the solution to a total mass of 10 g with acetonitrile. For synthesis of N-CNTs-Fe, ferrocene was used as a catalyst while acetonitrile was used as a carbon source. The solution used to synthesize N-CNTs-Fe was

made by dissolving of 0.25 g of ferrocene in 9.75 g of acetonitrile only to make 10 g of solution.

A flow rate of 0.8 mL $min^{-1}$ was used to feed each solution of the precursors into a quartz tube, which was placed in the middle of a tube furnace. The solution was carried through the quartz tube by a carrier gas made-up of 10% hydrogen in argon (v/v) which was pumped through the system at a rate of 100 mL $min^{-1}$ at 80 kPa. The furnace was set to a reaction temperature of 850 °C for 30 minutes. The products were collected from the hot zone of the quartz tube upon completion of the reaction. The residual catalyst was removed from the N-CNTs *via* acid treatment with 6 M nitric acid at 100 °C for 24 hours as described previously publication [8].

### 2.3 Synthesis of catalysts

Synthesis of the catalysts was achieved by loading Pd onto acid treated N-CNTs-2 and N-CNTs-Fe to yield Pd/N-CNTs-2 and Pd/N-CNTs-Fe respectively as previously described [8]. Loading of 5 wt.% Pd onto each support was achieved *via* a solvent-free metal organic-CVD (MOCVD) method as outlined by Suttisawat *et al*. [10]. The MOCVD approach employs a ‗greener' solvent-free technique which utilizers fewer reaction steps compared with solution methods and eliminates the use of templates or surfactants during synthesis. In detail, 0.072 g of palladium acetylacetonate {Pd $(acac)_2$} was mixed with 0.475 g of acid treated N-CNTs and ground thoroughly by use of a pestle and mortar. The resulting mixture was placed inside a stainless steel MOCVD reactor and the reactor components sealed. The sealed MOCVD reactor was connected to a vacuum pump maintained at a partial pressure of 2.2-2.8 x $10^{-2}$ mbar for 45 minutes. After evacuating the MOCVD reactor for 45 minutes, it was placed in the middle of a muffle furnace operated at 120 °C for 30 minutes. This was followed by increasing the temperature to 300 °C at a rate of 2 °C $min^{-1}$ and thereafter maintaining it at 300 °C for 45 minutes. The system was then allowed to cool to ambient temperature while still under vacuum. Upon completion of the reaction, the formed catalysts were removed from the reactor by scraping with a spatula.

### 2.4 Catalytic tests

Hydrogenation of nitrobenzophenone to aminobenzophenone was conducted in a closed vessel reactor by use of a mole ratio of 1:66 (Pd:nitrobenzophenone). For all catalytic tests, 180.0 mg of the catalyst was put into a stainless steel Parr reactor vessel and mixed with 1250 mg of 4-nitrobenzophenone and 100 mL of dry toluene or 2-propanol. The reactor

vessel and its contents was sealed and then stirred continuously under hydrogen gas at the desired reaction conditions. To monitor the reaction progress, aliquots of 1 mL of the reactants were collected from the reaction vessel at intervals of 2 hours and analysed with an off-line GC-FID. Upon completion of the reaction, the solution in the reaction vessel was cooled to ambient temperature, filtered through a MN 615 filter paper and then through a 0.45 μm PVDF syringe filter and the filtrate kept in a sealed container for further analysis. To conduct recycling tests, the recovered catalyst was obtained as a filtration residue. The used catalyst was washed with 100 mL of diethyl ether and ethanol and then dried at 100 °C over 10% hydrogen in argon (v/v) for 2 hours. The conversion of 4-nitrobenzophenone (NBP) and selectivity to 4-aminobenzophenone (ABP) was calculated by the use of equations 1 and 2, respectively.

$$\text{Conversion of NBP} = \frac{\text{Initial [NBP]} - \text{measured [NBP]}}{\text{Initial [NBP]}} \qquad \text{equation (1)}$$

$$\text{Selectivity to ABP} = \frac{\text{Measured [ABP]}}{\text{Measured [ABP]} + \text{Measured [other products]}} \qquad \text{equation (2)}$$

where, initial [NBP] is the initial concentration of NBP measured in mg $L^{-1}$ before starting the reaction, measured [NBP], [ABP] and [other products] are the concentrations of NBP, ABP and other products measured in mg $L^{-1}$ at various time intervals as obtained from GC analysis.

## 2.5 Characterization

Images of N-CNTs and all catalysts were taken by using transmission electron microscopy (TEM) (JEOL JEM 1010). The thermostability of N-CNTs was determined by using a TA instrument Q Series™ Thermal Analyser DSC/TGA (Q600). The graphitic nature of the N-CNTs was determined by Raman spectroscopy (DeltaNu Advantage 532™). The Pd-loading content was determined by inductively coupled plasma-optical emission spectroscopy (ICP-OES) (Perkin Elmer Optima 5300 DV). The surface area and nitrogen adsorption-desorption isotherms of the catalysts were determined with a Micromeritics Tristar II surface area, porosity analyser and ASAP 2020C V2.01 H. The hydrogenation products were characterized by means of GC-FID (Shimadzu 2010 gas chromatograph) and GC-MS (Shimadzu GCMS-QP2010 SE).

## 3. Results and discussion

### 3.1 Characterization of N-CNTs and Pd/N-CNTs

The N-CNTs synthesized by use of 2 wt.% oxygen were coded as N-CNTs-2 while those synthesized from ferrocene catalyst were coded N-CNTs-Fe. Subsequently, Pd loaded onto N-CNTs-2 was named Pd/N-CNTs-2 while Pd supported on N-CNTs-Fe was named Pd/N-CNTs-Fe. The TEM images of purified N-CNTs-Fe and N-CNTs-2 are presented in Figures 1a and b respectively. These images depict the presence of bamboo compartments that are consistent with nitrogen-doped carbon nanotubes [11]. The outer and inner diameters of N-CNTs-Fe were larger than that of N-CNTs-2. The smaller tube diameter of N-CNTs-2 is due to the etching effect of oxygen used to synthesize N-CNTs-2 [12].

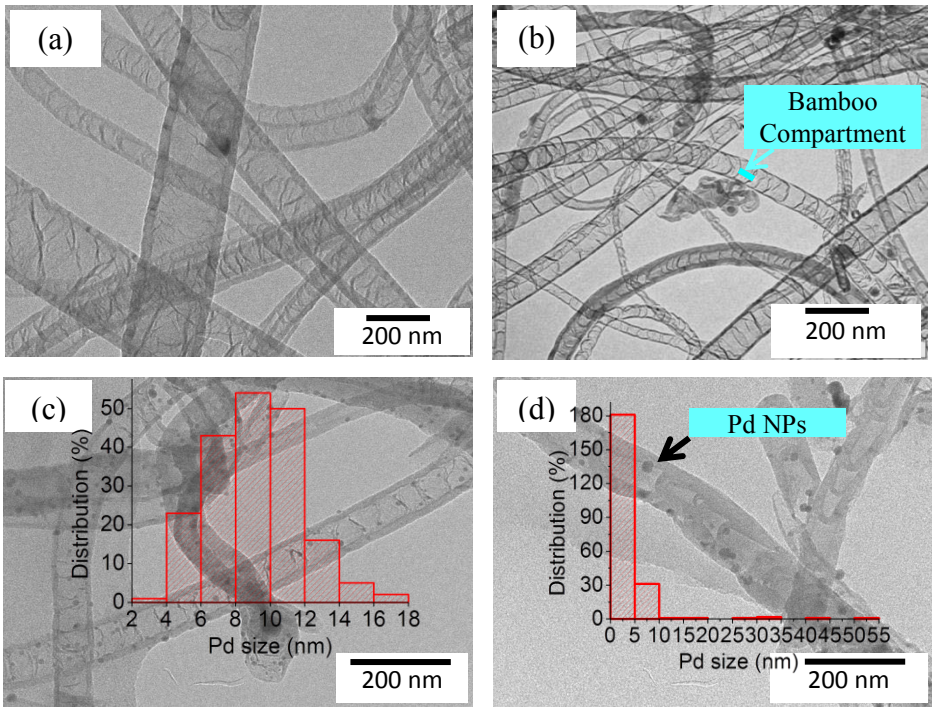


Figure 1: TEM images of (a) N-CNTs-Fe (outer diameter 111 ± 81; inner diameter 81 ± 66), (b) N-CNTs-2 (outer diameter 47 ± 24; inner diameter 32 ± 21), (c) Pd/N-CNTs-Fe and (d) Pd/N-CNTs-2.

TEM images of Pd/N-CNTs-Fe and Pd/N-CNTs-2 are shown in Figures 1c and d respectively. From these Figures Pd nanoparticles (NPs) were observed, and the presence of Pd was further verified by ICP-OES analysis (Table 1). To determine the Pd NP size, at least 200 particles from TEM images were measured. Pd NPs in Pd/N-CNTs-Fe have larger diameters than those in Pd/N-CNTs-2 (Figure 1 and Table 1). The smaller particle size in

Pd/N-CNTs-2 can be attributed to the presence of pyrrolic-nitrogen in N-CNTs-2 which aided nucleation of lesser-sized particles [8]. A more detailed characteriztion of N-CNTs-2 and Pd/N-CNTs-2 was reported in our previous publication [8].

Raman specroscopy was used to further characterize the purified N-CNTs. The Raman spectra of N-CNTs consist of three prominent peaks namely; a disorder band (D-band) at ≈1350 $cm^{-1}$, a graphitic band (G-band) at ≈1550 $cm^{-1}$ and an overtone mode of the D-band (G′-band) at ≈2650 [12,13]. Both the D- and G-band consist of an overlap of several peaks that can be used to characterize the extent of disorder in N-CNTs [14]. The G′-band is sensitive to changes in the electronic structure of N-CNTs that can be instigated by an increase in nitrogen-doping levels or the incoporation of a particular nitrogen species [15]. Increasing the amount of nitrogen-doping in N-CNTs has been reported to decrease the intensity of the G′-band [15]. The Raman spectra of N-CNTs-2 did not exhibit a G′-band (Figure 2a), while the spectra of N-CNTs-Fe (Figure 2b) showed a G′-band. This implies that N-CNTs-2 either have a higher nitrogen-doping level than N-CNTs-Fe or the nitrogen species in N-CNTs-2 differs from that in N-CNTs-Fe, and thus alters its electronic properties.

Both the D- and G-bands were present in the Raman spectra of N-CNTs-2 and N-CNTs-Fe (Figure 2). Deconvolution of the D-band by use of a Lorenzian fitting gave three distinct peaks in N-CNTs-2 and one peak for the N-CNTs-Fe. Multiple peaks in the D-band are indicative of an increse in the distrurbance of the regular graphene layers of N-CNTs caused by defects originating from nitrogen-doping [16].

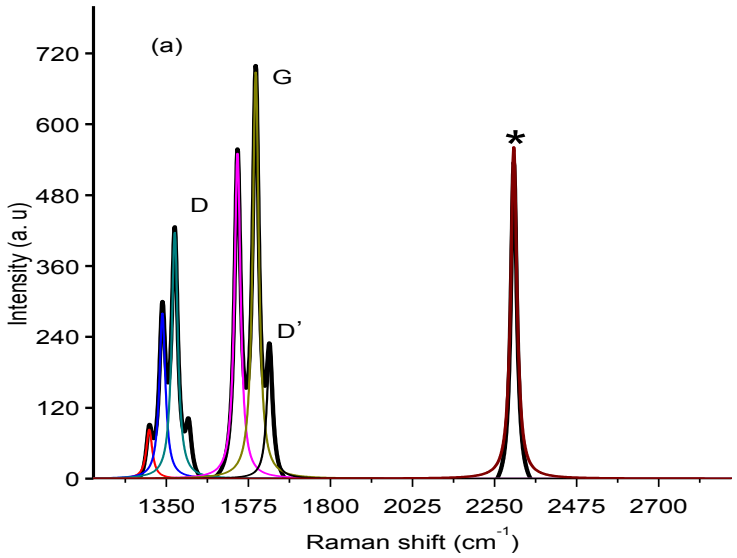

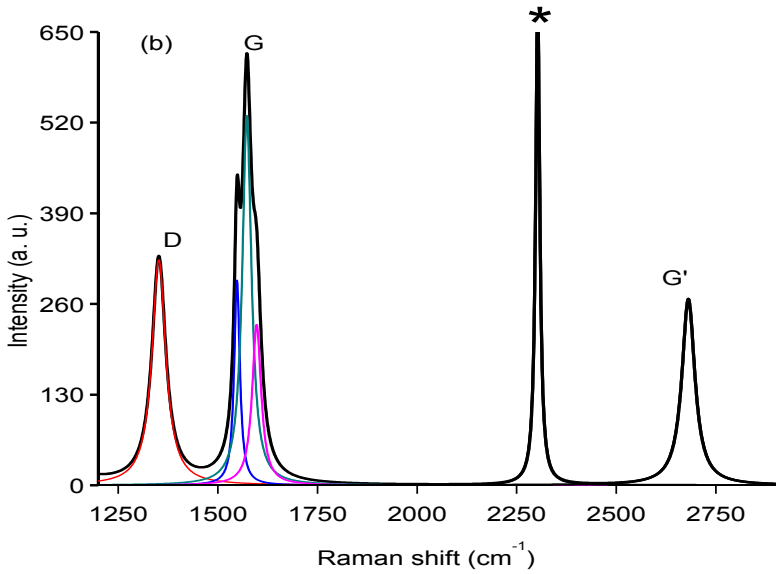


Figure 2: Raman spectra of (a) N-CNTs-2, (b) N-CNTs-Fe and *$N_2$ gas

Deconvolution of the G-band with a Lorenzian fitting program gave three distinct peaks in the G-band of N-CNTs-2 and N-CNTs-Fe. Although the number of deconvoluted peaks in the G-band was similar for both samples, the position of the deconvoluted peaks differed as the peaks of N-CNTs-2 were shifted to higher wavelengths than those of N-CNTs-Fe. More precisely, a peak at ≈1633 $cm^{-1}$ (D′-band) was only observed in the spectrum of N-CNTs-2. The D′-band is reported to be brought about by distortions of the regular graphene sheets in N-CNTs resulting in irregular $d_{002}$ spacing [14]. Hence, the presence of this D′-band in N-CNTs-2 alone implied that the graphene layers in this sample were highly disordered owing to synthesis in the presence of oxygen. This observed increase in disorder was attributed to the presence of pyrrolic-nitrogen in N-CNTs-2 [8]. A peak at ≈2300 $cm^{-1}$ associated with the Raman mode of $N_2$ gas trapped in the cavity of N-CNTs and, also found in the sorrounding atmosphere was observed [8].

The ratio of the intergrated area of the D-band:G-band ($I_D/I_G$) was used to determine the overal cyrstallinity of the two samples [17]. A larger $I_D/I_G$ ratio implies that the sample is less crystalline. A ratio of 0.54 was obtained for N-CNTs-2 while N-CNTs-Fe gave a ratio of 0.52. The two ratios were close, but the ratio of N-CNTs-2 was slightly higher than that of N-CNTs-Fe. Thus, the higher $I_D/I_G$ ratio in N-CNTs-2 coupled with the presence of multiple peaks in the D-band, the presence of a D′-band and the absence of the G′-band in this sample indicates that the N-CNTs-2 sample is less crystalline than N-CNTs-Fe. This lower level of

crystallinity in N-CNTs-2 can be attributed to the presence of pyrrolic-nitrogen species [8] or a higher nitrogen-doping level in N-CNTs-2 than in N-CNTs-Fe.

TGA was used to determine the thermostability of N-CNT-2 and N-CNTs-Fe. N-CNTs-2 were less thermally stable compared with N-CNTs-Fe (Figure 3). The lower thermostability of N-CNTs-2 is accedited to the presence of more defects which iniciate the decomposition of these sample at lower temperatures [8]. Such defects can be due to pyrrolic-nitrogen species that are present mainly in N-CNTs-2 [8] or a higher nitrogen-doping level in N-CNTs-2 than in N-CNTs-Fe. The lower thermostability of N-CNTs-2 further supports the higher level of disorder exhibited from Raman spectroscopic analysis of this sample.

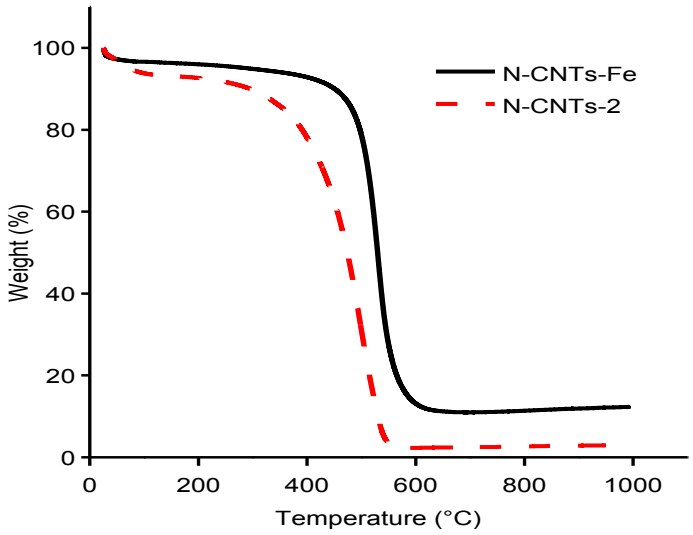


Figure 3: Thermograms of purified N-CNTs-2 and N-CNTs-Fe.

A close analysis of the thermograms also shows that N-CNT-Fe had 12% of residual iron while, N-CNTs-2 had 3% of residual iron. The higher iron content in N-CNTs-Fe was attributed to the use of ferrocene as a catalyst to synthesize N-CNTs-Fe. Ferrocene may have favoured formation of more residual iron in N-CNTs-Fe compared with the ferrocenyl derivative used to synthesize N-CNTs-2. Iron particles were not observed on the TEM images of NCNTs-Fe, thus, it is plausible that the residual iron particles would not be accessible to the hydrogenation substrates and hence would not influence the catalytic performance of N-CNTs-Fe [18].

The textural properties of Pd/N-CNTs-2 and Pd/N-CNT-Fe were analyzed by use of $N_2$ adsorption–desorption and chemisorption studies. Pd/N-CNT-Fe showed a much higher surface area than Pd/N-CNTs-2 (Table 1). Both Pd/N-CNTs-Fe and Pd/N-CNTs-2 had pore sizes larger than 2 nm and were classified as type IV mesoporous materials (Table 1).

Additionally, both catalysts showed a hysteresis loop between 0.5-0.9 $P/P_0$ (Figure 4) consistent with type IV mesoporous materials [19].

Table 1: Physical properties of Pd/N-CNTs-Fe and Pd/N-CNTs-2.

| Catalyst | surface area of Pd/N-CNTs ($m^2g^{-1}$) | surface area of Pd ($m^2g^{-1}$) | Pore size distribution (nm) | Pd loading wt.% from ICP-OES | Ave. Pd NP size (nm) from TEM |
|---|---|---|---|---|---|
| Pd/N-CNTs-Fe | 123 | 4.83 | 4.5 | 4.8 | 9.0 |
| Pd/N-CNTs-2 | 38 | 3.72 | 4.1 | 4.9 | 4.5 |

The quantity of adsorbed $N_2$ was higher in Pd/N-CNTs-Fe compared with that in Pd/N-CNTs-2 (Figure 4). From TEM analysis Pd/N-CNTs-Fe appeared more de-bundled and less aligned than Pd/N-CNTs-2. Since there was no significant difference between the pore size of Pd/N-CNTs-2 and Pd/N-CNTs-Fe (Table-1); the higher quantity of adsorbed $N_2$ in Pd/N-CNTs-Fe was attributted to its higher surface area [4]. The metallic surface area of Pd was higher in Pd/N-CNTs-Fe than in Pd/N-CNTs-2 (Table 1). This indicated that the higher surface area of N-CNTs-Fe facilitated a better dispersion of Pd NPs resulting in a greater Pd surface area.

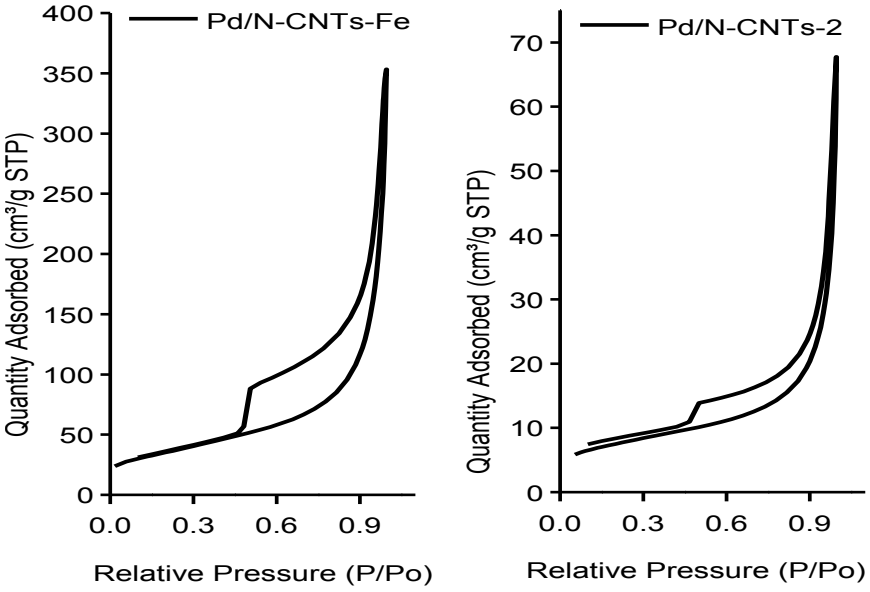


Figure 4: $N_2$ adsorption–desorption isotherms of Pd/N-CNTs-Fe and Pd/N-CNTs-2.

## 3.2 Catalytic tests

### 3.2.1 Dependence of catalytic performance on surface area

To determine the effect of surface area on NBP conversion, Pd/N-CNTs-Fe and Pd/N-CNTs-2, which are significantly different in their Pd NP surface area but similar in other physicochemical aspects were used. The conversion over Pd/N-CNTs-2 reached completion after six hours, while that of Pd/N-CNTs-Fe seemed not to attain completion even after ten hours of the reaction (Figure 5). Hence, the catalytic activity of Pd/N-CNTs-Fe was higher than that of Pd/N-CNTs-2. This indicated that when the surface area of the support is high, then the active sites are spread over a large area thereby improving Pd catalyst surface area which in turn favours higher conversion rates [3].

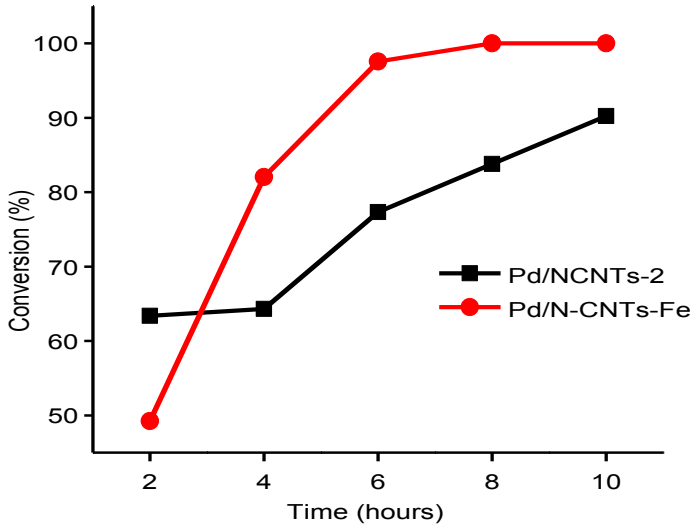


Figure 5: Conversion of NBP over Pd/N-CNTs-2 and Pd/N-CNTs-Fe

To further probe the dependace of catalytic activity on the catalyst surface area, the rate constants of the reactions were evaluated. The converion of NBP followed a pseudo-first order kinetics as depicted in Figure 6 [20]. Based on this kinetic order, the rate constant was determined to be 0.99 $hour^{-1}$ for the reaction over Pd/N-CNTs-Fe and 0.21 $hour^{-1}$ for Pd/N-CNTs-2. The Pd/N-CNTs-Fe showed a greater rate constant for NBP reduction than Pd/N-CNTs-2. Similar observations were made in our previous report [8], where Pd supported on activated carbon which had a higher surface area than Pd/N-CNTs-2 showed a better NBP conversion. Thus the rate of NBP conversion is dependent on the surface area of the Pd

catalyst. This indicates that more catalytically active sites are present in Pd catalysts on supports having higher surface areas than those with lower surface areas.

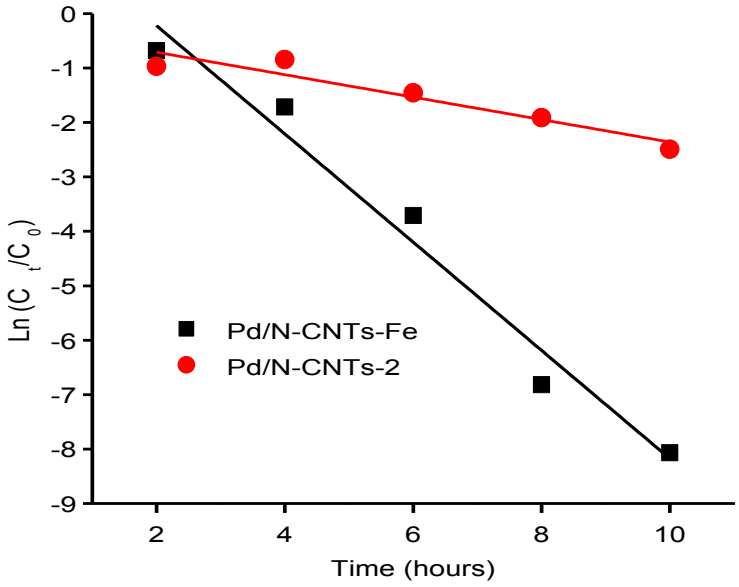


Figure 6: Kinetic plots for the hydrogenation of NBP.

The selectivity towards ABP over Pd/N-CNTs-2 and Pd/N-CNTs-Fe was also followed with time. Figure 7 represents the selectivity curves for the two catalysts. Both catalysts gave ABP as the main hydrogenation product (Scheme 1). The selectivity of both catalysts was almost equal for the first four hours of the reaction. After four hours, the selectivity over Pd/N-CNTs-Fe rapidly increased relative to that of Pd/N-CNTs-2. Thus, it was evident that for N-CNTs, a higher Pd NP surface area promoted a higher selectivity towards ABP. Contrary to these observations, Pd on activated carbon showed a lower selectivity towards ABP than Pd/N-CNTs-2 despite the higher support surface area obtained with the former catalyst [8]. Hence, although the surface area of the support indirectly influences selectivity; the type of Pd support seems to have a more pronounced effect on selectivity, with N-CNTs showing a superior selectivity than activated carbon. This implies that the interactions between Pd, N-CNTs and nitro-arenes favour nitro-reduction [7, 18].

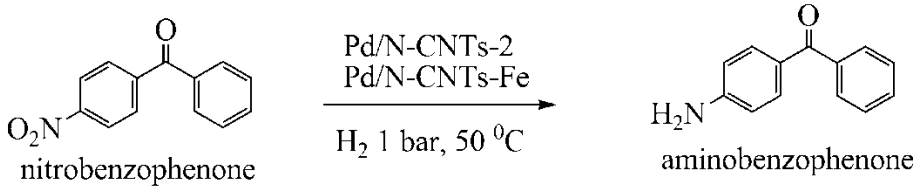


Scheme 1. Hydrogenation of NBP over Pd/N-CNTs-2 and Pd/N-CNTs-Fe catalysts.

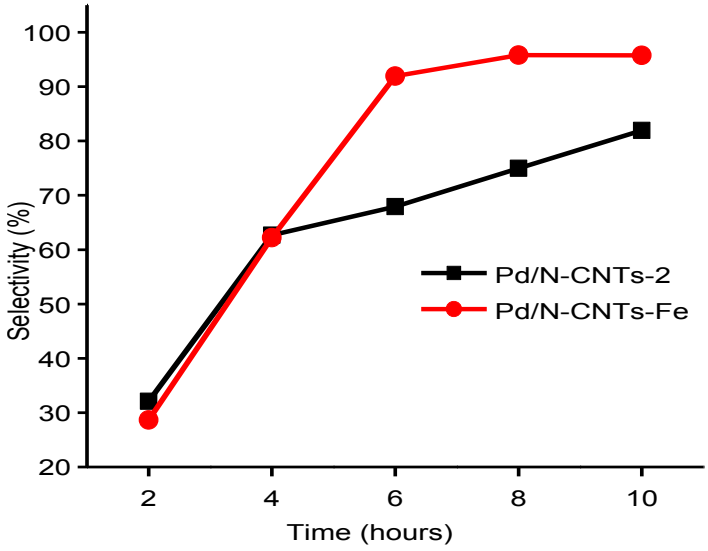


Figure 7: Selectivity to ABP over Pd/N-CNTs-2 and Pd/N-CNTs-Fe.

### 3.2.2 Effect of temperature on the catalytic perfomance

To evaluate the effect of temperature, Pd/N-CNTs-2 which was previously reported as the best performing catalyst was used [8]. The reactions were carried out in toluene and at four different temperatures (25, 50, 75 and 100 °C) while the pressure was maintained at 14 bar. In general, the conversion of NBP increased with an increase in temperature (Figure 8). However, after 4 hours of reaction time, a drop in the conversion of NBP is observed with the reaction temperatures of 25 and 50 °C. This drop in activity is associated with fluctuations in reactor temperatures causing experimental errors (Figure 8). At a temperature of 100 °C a complete conversion of NBP was attained within two hours of the reaction.

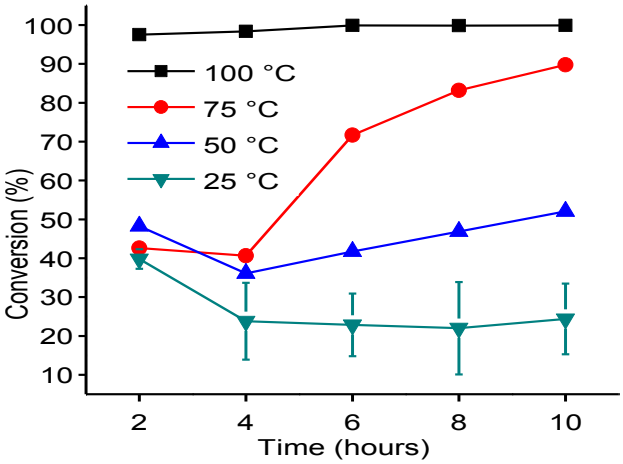


Figure 8: Conversion of NBP over Pd/N-CNTs-2 at a constant pressure of 14 bar and different reaction temperatures.

Similarly, the selectivity towards ABP increased with an increase in temperature (Figure 9). Based on the observed increase in catalytic activity and selectivity with increase in temperature, it was evident that increasing the temperature enhanced the reaction rate [21]. The increase in reaction rate could be due to increased mass transfer rates, increased hydrogen quantities in the solution and NBP solubility or a decrease in activation energy.

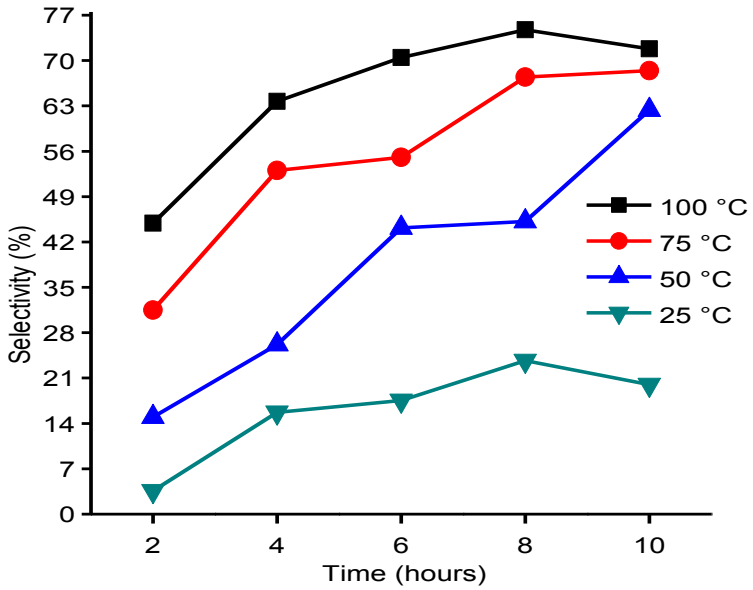


Figure 9: Selectivity towards ABP over Pd/N-CNTs-2 at a constant pressure of 14 bar and different reaction temperatures.

### 3.2.3 Effect of solvent on the catalytic performance of Pd/N-CNTs-2

The effect of solvent was evaluated by comparing the catalytic performance of Pd/N-CNTs-2 in a protic solvent (2-propanol) and an aprotic solvent (toluene). A temperature of 50 °C and pressure of 1 bar was used to allow for the comparison of the catalytic performance with those reported earlier [8]. NBP conversion was higher in 2-propanol than in toluene (Figure 10). This indicates that the concentration of hydrogen was higher in 2-propanol than in toluene [22]. Since 2-propanol acts as a proton donor, it is possible that protons originating from molecular hydrogen and 2-propanol both participated in the hydrogenation reaction resulting in an increased conversion. Also, the surface of Pd/N-CNTs-2 contained hydroxy groups [8] which facilitates a better catalyst dispersion in 2-propanol than in toluene resulting in an enhanced conversion.

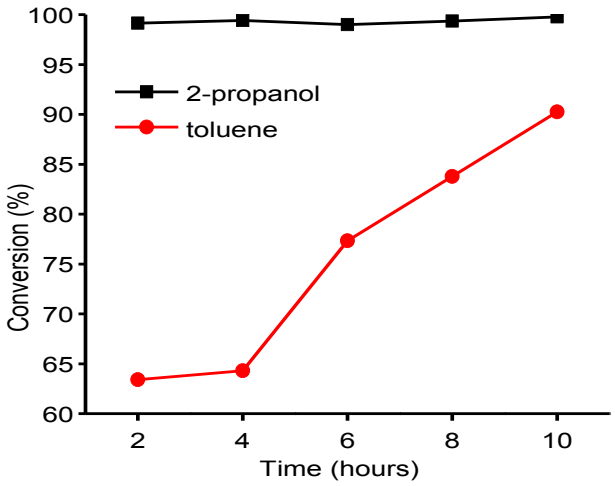


Figure 10: Conversion of NBP over Pd/N-CNTs-2 in toluene and 2-propanol.

There was no significant difference in selectivity for the first four hours. Contrary to the conversion trend, after four hours of the reaction, the selectivity in toluene increased more rapidly than the selectivity in 2-propanol (Figure 11). The reduced selectivity in 2-propanol can be attibuted to the presence of competing side-reactions. This competing reactions may have been perpetuated by the higher proton concentration in 2-propanol than in toluene.

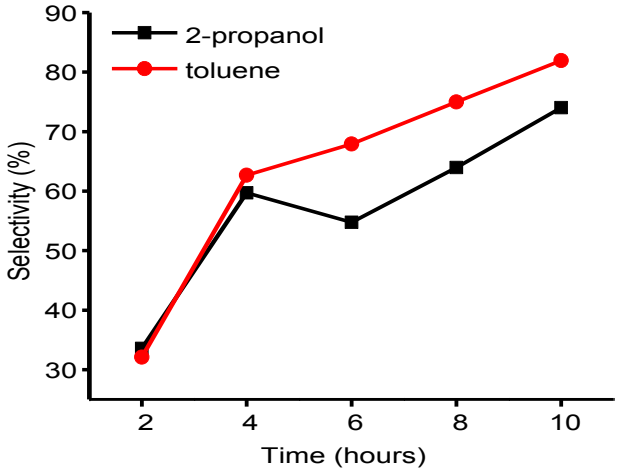


Figure 11: Selectivity towards ABP over Pd/N-CNTs-2 in toluene and 2-propanol at 50 °C and 1 bar.

### 3.2.4 Recyling test for Pd/N-CNTs-2

To evaluate the recyclability of Pd/N-CNTs-2, the used catalyst was recyled once owing to its low recovery caused by adhesion of the catalyst to the filter paper. Toluene which gave a higher selectivity than 2-propanol was used for the recycling test. Prior to recycling, the catalyst was separated from the toluene solution by filtration, washed with diethyl ether and ethanol, then dried overnight at 120 °C. Equal amounts of the fresh and recycled catalyst is compared for NBP conversion and selectivity towards ABP as presented in Figures 12 and 13 respectively.

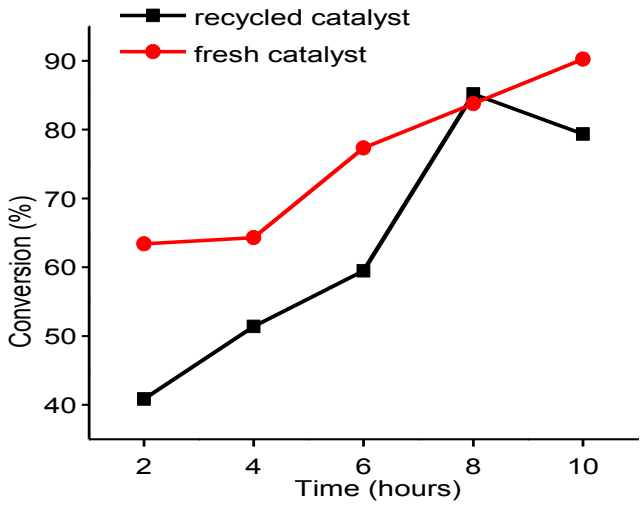


Figure 12: Conversion of NBP over equal amounts of fresh and recycled Pd/N-CNTs-2 in toluene at 50 °C and 1 bar.

The conversion and selectivity towards ABP over the recycled catalyst were moderately high but lower than that of the fresh catalyst (Figures 12 and 13). A drop in the activity of the recycled catalyst was noticed after eight hours of the reaction, this drop was attributed to experimental errors arising from temperature flactuations in the reactor. A previously conducted analysis of the Pd NPs in the recyled Pd/N-CNTs-2 had shown that the recycled Pd NPs were more metallic and had maintained their initial particle size [8]. Hence, the overal drop in catalytic activity and selectivity of the used catalyst compared with the fresh catalyst was not caused by deactivation or agglometation of the Pd NPs but due to the support. Since N-CNTs-2 were also catalyticaly active [8], it is possible that after the first cycle of the hydrogenation reaction, the acidic by-products bind to the active sites. This results in a reduction in the quantity of active nitrogen species in the N-CNTs which in turn lowers the activity and selectivity of Pd/N-CNTs.

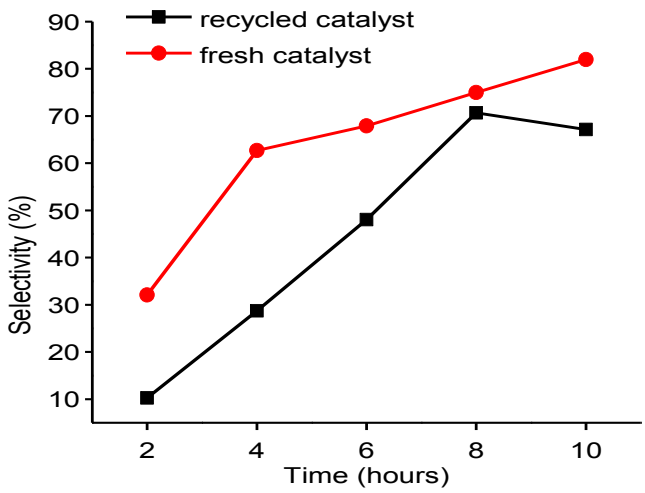


Figure 13: Selectivity towards ABP over equal amounts of fresh and recycled Pd/N-CNTs-2 in toluene at 50 °C and 1 bar.

## Conclusions

N-CNTs were succesfully synthesized by use of ferrocene and 3-ferrocenyl-2-(4-cyanophenyl)acrylonitrile as catalysts. N-CNTs obtained with ferrocene had a higher surface area, were less disordered but less thermaly stable than those synthesized from 3-ferrocenyl-2-(4-cyanophenyl)acrylonitrile. The chemoselective nitro-reduction of NBP to ABP over Pd/N-CNTs was achieved in a closed reactor. The surface area of the catalysts played a significant role in the selective nitro-reduction of ABP. A higher Pd nanoparticle surface area enhanced the selectivity towards aminobenzophenone. Increasing the reaction

temperature enhanced both NBP conversion and ABP formation. The selectivity towards ABP was enhanced by the use of an aprotic solvent. The recycling test indicated that Pd/N-CNTs-2 could be recycled once while still maintaining a reasonable catalytic activity. Thus, the findings of this study reveal the role of surface area, temperature and solvent in increasing the selectivity towards anilines.

**Acknowledgements**

The authors wish to thank the University of KwaZulu-Natal and the National Research Foundation (NRF) for financial support. Lucy M. Ombaka is grateful for the award of doctoral bursary from the UKZN, College of Agriculture, Engineering, and Science. We are grateful to Professor Bice Martincigh and Dr. R. S. Mwakubambanya for their insightful suggestions during the manuscript development and their assistance with proofreading.

## References

[1] A. Corma, H. Garcia, Chem. Soc. Rev. 37 (2008) 2096-2126.

[2] H.-U. Blaser, H. Steiner, M. Studer, Chemcatchem 1 (2009) 210-221.

[3] P. Tomkins, E. Gebauer-Henke, W. Leitner, T.E. Mueller, ACS Catal. In press (2014).

[4] L.M. Ombaka, P. Ndungu, V.O. Nyamori, Catal. Today 217 (2013) 65-75.

[5] F. Figueras, B. Coq, J. Mol. Catal. A: Chem. 173 (2001) 223-230.

[6] R.S. Oosthuizen, V.O. Nyamori, Platinum Metals Rev. 55 (2011) 154-169.

[7] P. Chen, L.M. Chew, A. Kostka, M. Muhlera, W. Xia, Catal. Sci. Technol 3 (2013) 1964-1971.

[8] L.M. Ombaka, P.G. Ndungu, V.O. Nyamori, RSC Adv.5 (2015) 109-122.

[9] L.M. Ombaka, P.G. Ndungu, B. Omondi, V.O. Nyamori, J. Coord. Chem. 67 (2014) 1905-1922.

[10] Y. Suttisawat, P. Rangsunvigit, B. Kitiyanan, M. Williams, P. Ndungu, M.V. Lototskyy, A. Nechaev, V. Linkov, S. Kulprathipanja, Int. J. Hydrogen Energy 34 (2009) 6669-6675.

[11] B.G. Sumpter, V. Meunier, J.M. Romo-Herrera, E. Cruz-Silva, D.A. Cullen, H. Terrones, D.J. Smith, M. Terrones, ACS Nano 1 (2007) 369-375.

[12] L.M. Ombaka, P.G. Ndungu, V.O. Nyamori, J. Mater. Sci. 50 (2015) 1187-1200.

[13] G. Keru, P.G. Ndungu, V.O. Nyamori, J. Nano. Mat. 2013 (2013) 1-7.

[14] L.G. Bulusheva, A.V. Okotrub, I.A. Kinloch, I.P. Asanov, A.G. Kurenya, A.G. Kudashov, X. Chen, H. Song, Phys. Stat. Sol. (B) 245 (2008) 1971-1974.

[15] K. Chizari, A. Vena, L. Laurentius, U. Sundararaj, Carbon 68 (2014) 369-379.

[16] T. Sharifi, F. Nitze, H.R. Barzegar, C.-W. Tai, M. Mazurkiewicz, A. Malolepszy, L. Stobinski, T.Wågberg, Carbon 50 (2012) 3535-3541.

[17] K.A. Wepasnick, B.A. Smith, J.L. Bitter, D.H. Fairbrother, Anal. Bioanal. Chem. 396 (2010) 1003-1014.

[18] P. Chen, F. Yang, A. Kostka, W. Xia, ACS Catal. 4 (2014) 1478-1486.

[19] Z. Lei, D. Bai, X.S. Zhao, Microporous Mesoporous Mater. 147 (2012) 86-93.

[20] X. Gu, W. Qi, X. Xu, Z. Sun, L. Zhang, W. Liu, X. Pan, D. Su, Nanoscale 6 (2014) 6609-6616.

[21] X.-F. Guo, D.-Y. Jang, H.-G. Jang, G.-J. Kim, Catal. Today 186 (2012) 109-114.

[22] A. Jourdant, E. González-Zamora, J. Zhu, J. Org. Chem. 67 (2002) 3163-3164.

# CHAPTER EIGHT

# CONCLUSIONS AND FUTURE WORK

## Project summary

The aims of this study were to utilise green chemistry principles in the synthesis of novel and known halogen- and nitrogen-containing ferrocenyl derivatives and to characterize the compounds by means of various techniques including single crystal X-ray crystallography. The ferrocenyl derivatives were applied as catalysts in the synthesis nitrogen-doped carbon nanotubes (N-CNTs). In addition, this study aimed at utilizing different solvents, oxygen- and halogen-heteroatoms to control the physicochemical properties of synthesized N-CNTs. The N-CNTs were used as Pd catalyst supports (Pd/N-CNTs) applied in the selective hydrogenation of nitrobenzophenone to aminobenzophenone. Issues such as the effect of nitrogen-doping, nitrogen-species, surface area, solvent, temperature and pressure on the catalytic performance of Pd/N-CNTs were investigated.

## Conclusions

Eight novel 1,1′-ferrocenyldiacrylonitriles were synthesized by the use of a solvent-free mechanochemical approach. The compounds were synthesized within short reaction times (3-5 minutes), giving high product yields of up to 78% and producing water as the only by-product. This simplified the purification procedure employed during synthesis. Based on the solvent-less reaction, short reaction times, high yields, and benign by-product (water) obtained from the synthesis of these compounds; the applied solvent-free method upheld some of the principles of green chemistry.

Studies on the effect of the *para*-substituent indicated that the electronegativity of the *para*-substituent can be used to control the yield, spectroscopic and electrochemical properties of 1,1′-ferrocenyldiacrylonitriles. Stronger electron-withdrawing groups at the *para*-position of phenyl acetonitrile gave higher yields of ferrocenyldiacrylonitriles while the relatively weaker electron-withdrawing groups gave lower yields. Also, selectivity towards ferrocenyldiacrylonitrile formation was favoured by the presence of a strong electron-withdrawing group on the *para*-substituent of the phenyl rings. The UV absorption wavelengths of ferrocenyldiacrylonitriles were red-shifted by the presence of strong electron-withdrawing groups at the *para*-position of the compounds. From cyclic

voltammetry analysis, the presence of strong electron-withdrawing groups at the *para*-position of ferrocenyldiacrylonitriles increased the positive shift in the redox potential of the ferrocenyl moiety.

Attaching a strong electron-withdrawing group at the *para*-position of the ferrocenyl-diacrylonitriles allowed the optoelectronic properties of the ferrocenyldiacrylonitriles to be tuned. In addition, the donor–acceptor electronic interactions and electron transfer processes were enhanced when two $\pi$-acceptor ligands were attached to one ferrocenyl moiety. On the contrary, attaching two ferrocenyl moieties to a single $\pi$-acceptor reduced the electron transfer process. Hence, the redox behaviour of ferrocenyldiacrylonitrles was switched from reversible to irreversible by altering the number of $\pi$-acceptor groups attached to the ferrocenyl moiety. Therefore, these compounds are potentially useful for application in nonlinear optical devices, biosensors, and in molecular switch devices. From the single crystal X-ray analysis, the structures of five compounds were obtained. The X-ray crystallographic analysis showed the different preferred solid state conformations of the ferrocenyl moiety in mono- and di-substituted ferrocenyldiacrylonitriles.

Amongst the eight novel ferrocenyldiacrylonitriles that were synthesized, three compounds (i.e. 1,1′-ferrocenyldi[-2(4-cyanophenyl)acrylonitrile], 1,1′-ferrocenyldi[-2(4-{trifluoromethyl}phenyl)acrylonitrile] and 1,1′-ferrocenyldi[-2(4-chlorophenyl)acrylonitrile]) were used as new catalysts to synthesize N-CNTs. The choice of these compounds as catalysts was because these compounds were obtained in relatively higher yields than the other compounds and they only differed in their *para*-substituent (i.e. *para*-$CF_3$, *para*-Cl and *para*-CN). Hence, this allowed for the evaluation of the effect of the *para*-substituent and halogens during synthesis of N-CNTs.

N-CNTs were successfully synthesized by using these three 1,1′-ferrocenyldi-acrylonitriles as novel catalysts either in pyridine or acetonitrile as the nitrogen and carbon source. All 1,1′-ferrocenyldiacrylonitriles in pyridine gave only N-CNTs and CS, while in acetonitrile; the catalysts gave N-CNTs and CNFs as the only SCNMs. Thus, N-CNTs were obtained from both solvents. The yields and purity of N-CNTs obtained with pyridine were generally higher that those obtained with acetonitrile. Therefore, pyridine is deemed as a better carbon and nitrogen source when using 1,1′-ferrocenyldiacrylonitriles as catalysts to synthesize N-CNTs.

The *para*-$CF_3$ catalyst was the most efficient for the synthesis of high percentages of N-CNTs in pyridine and acetonitrile. The N-CNTs obtained by using *para*-$CF_3$ in pyridine significantly differed in terms of morphology, thermal stability and surface chemistry

compared with the *para*-Cl or *para*-CN derived N-CNTs. This implied that the fluorine atom modulates the nitrogen content and type of nitrogen species incorporated into N-CNTs. Thus, the results suggest that the use of fluorinated ferrocenyl derivatives can control the nitrogen-doping of N-CNTs. The halogenated catalysts in acetonitrile promote filling of the N-CNT cavity with iron and reduce the diameter of N-CNT while decreasing the abundance of CNFs.

N-CNTs were also successfully synthesized by use of 3-ferrocenyl-2-(4-cyanophenyl)-acrylonitrile as a new catalyst and acetonitrile as the carbon and nitrogen source. This demonstrated that nitrogen-containing organometallic compounds are versatile catalysts for synthesis of N-CNTs because they act as catalysts and as a nitrogen source. The effect of acetonitrile and toluene as carbon sources in the synthesis of N-CNTs was investigated. From the results, we deduced that acetonitrile, as a carbon source was selective towards formation of N-CNTs only, while the use of toluene as a carbon source yielded a mixture of N-CNTs and CS. Selectivity towards N-CNT formation was accredited to the decomposition products of acetonitrile when used as a carbon source.

The use of oxygen as an oxidant to control the physicochemical properties of N-CNTs *in situ* was evaluated. By using ethyl benzoate as a source of low quantities of oxygen, a simple new procedure of tuning the nitrogen content, surface energy, surface basicity, alignment and conductivity of N-CNTs was developed. Low oxygen concentrations were favourable for the growth of well-aligned N-CNTs containing higher levels of nitrogen and with a narrower diameter distribution. The bulk electronic and physical properties of N-CNTs were strongly influenced by the nitrogen species in N-CNTs and the outer diameter of N-CNTs.

The N-CNTs synthesized by use of 0-2 wt. % oxygen were purified, then loaded with 5% Pd NPs, and analysed by means of XPS and other techniques. From the XPS analysis, use of 3-ferrocenyl-2-(4-cyanophenyl)acrylonitrile as a catalyst together with acetonitrile yielded N-CNTs containing 4.4 at. % nitrogen. Three nitrogen species, *viz*. pyridinic, pyrrolic and molecular nitrogen, were present in the N-CNTs. Of the three nitrogen species, pyrrolic nitrogen was the most abundant. Addition of oxygen derived from ethyl benzoate into the synthesis precursors increased the selectivity towards formation of pyrrolic nitrogen. However, increasing further quantities of ethyl benzoate in the synthesis precursors was accompanied by a reduction of nitrogen quantities in the synthesis precursors. This resulted in a decrease of the nitrogen atomic percentage in N-CNTs.

Increasing the amounts of pyrrolic groups in N-CNTs significantly altered the physicochemical properties of N-CNTs such as thermal stability, textural properties and

surface wetness. An increase in the pyrrolic-nitrogen percentage also improved the interactions between Pd and N-CNTs resulting in better dispersion and more stable Pd NPs. The catalytic activity and selectivity of Pd/N-CNTs in the hydrogenation of nitrobenzophenone were found to be dependent on the percentage of pyrrolic nitrogen and not on the total nitrogen content.

Pd/N-CNTs showed an enhanced selectivity compared with Pd/CNTs and Pd/AC resulting in higher product yield, higher atom economy and a reduction of by-products. The nitrogen species in Pd/N-CNTs were successfully used to control the catalytic activity and selectivity of the Pd/N-CNTs catalyst. Hence, amongst the tested catalysts, Pd/N-CNTs were the most efficient and perceived to be green catalysts.

The effect of temperature, pressure, and protic and aprotic solvent on the catalytic activity of Pd/N-CNTs was evaluated. It was evident that increasing the reaction temperature increases the catalytic activity and selectivity while increasing the pressure reduces activity and selectivity. The protic solvent gave a higher activity but with lower selectivity than the aprotic solvent. In addition, a recycling test was performed on Pd/N-CNTs-2. Recycled Pd/N-CNTs-2 showed a good activity and selectivity; however, its performance was lower than that of the fresh catalyst. In general, Pd supported on pyrrolic N-CNTs is a promising catalyst for the sustainable hydrogenation of nitro-arenes to substituted anilines such as aminobenzophenone and other industrially important anilines.

As a whole, this study reports the solvent-free synthesis of novel mono- and bi-metallic ferrocenyl derivatives whose heteroatoms tune the physicochemical properties of N-CNTs. It is evident that oxygen, fluorine and chlorine can be used to increase nitrogen doping in N-CNTs, with oxygen facilitating the incorporation of pyrrolic-nitrogen species. In addition, fluorine and chlorine can be used to aid the encapsulation of iron nanoparticles into the cavity of N-CNTs. Pyrrolic-nitrogen species enhance the catalytic performance of Pd/N-CNTs. Thus, the synthesis of Pd/N-CNTs with nitrogen species that control the catalytic performance of the catalyst is achieved.

## Future work

1. Although the solvent-free method used to synthesize the ferrocenyl derivatives was green, the product purification process utilized organic solvents such as dichloromethane that are considered harmful to the environment. Hence, in future, greener solvents such as supercritical carbon dioxide can be explored during

purification of similar compounds.

2. The successful synthesis of a ferrocenyl derivative containing two metal centres opens the avenue for using a solvent-free approach to synthesize other bimetallic compounds containing similar or different metal centres.
3. Since ferrocenyldiacrylonitriles had a low solubility in acetonitrile, the solid-state pyrolysis of ferrocenyldiacrylonitrile catalysts, in a CVD set-up can be explored for the synthesis of N-CNTs.
4. Following the effective use of oxygen to tune the physicochemical properties of N-CNTs, further studies can be conducted to determine the mechanism by which low oxygen concentrations influence the physicochemical properties of N-CNTs. The possibility of selectively incorporating pyrrolic nitrogen into N-CNTs while maintaining similar total nitrogen at. % can be explored. It will also be interesting and useful to determine whether selectivity towards other nitrogen species (e.g. pyridinic nitrogen) in N-CNTs can be achieved by use of oxygen and ferrocene as a catalyst.
5. Since the increase in pyrrolic nitrogen in N-CNTs resulted in formation of more $Pd^{2+}$ species, Pd should be loaded onto N-CNTs in the presence of a reducing agent such as hydrogen. The possibility of scaling-up the synthesis of pyrrolic containing Pd/N-CNTs and the commercialization of this catalyst can be explored.
6. Pd/N-CNTs showed good catalytic performance for the hydrogenation of nitrobenzophenone. Therefore, the catalytic activity of Pd/N-CNTs containing pyrrolic nitrogen can be investigated in other hydrogenation reactions such as reduction of unsaturated carbon-carbon bonds. Further recycling tests can be performed on Pd/N-CNTs and Pd/CNTs. Apart from Pd/N-CNTs catalysts, N-CNTs can also be investigated as supports for other metal catalysts and applied in other catalytic reactions.

## APPENDICES AVAILABLE IN DVD

## APPENDIX 1: Supporting Information for Chapter Three

***1,1'-Ferrocenyldi[-2(4-cyanophenyl)acrylonitrile](Compound 2)***

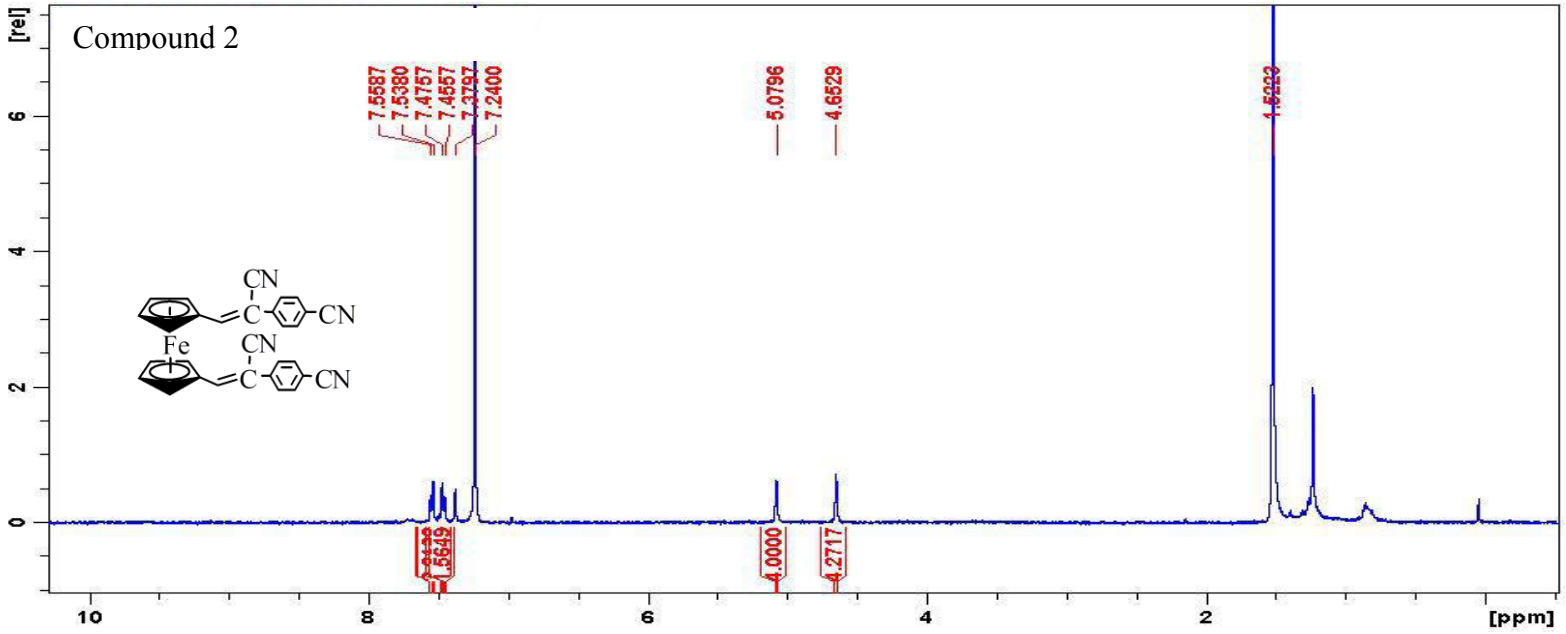


**Figure 1: proton NMR for compound 2**

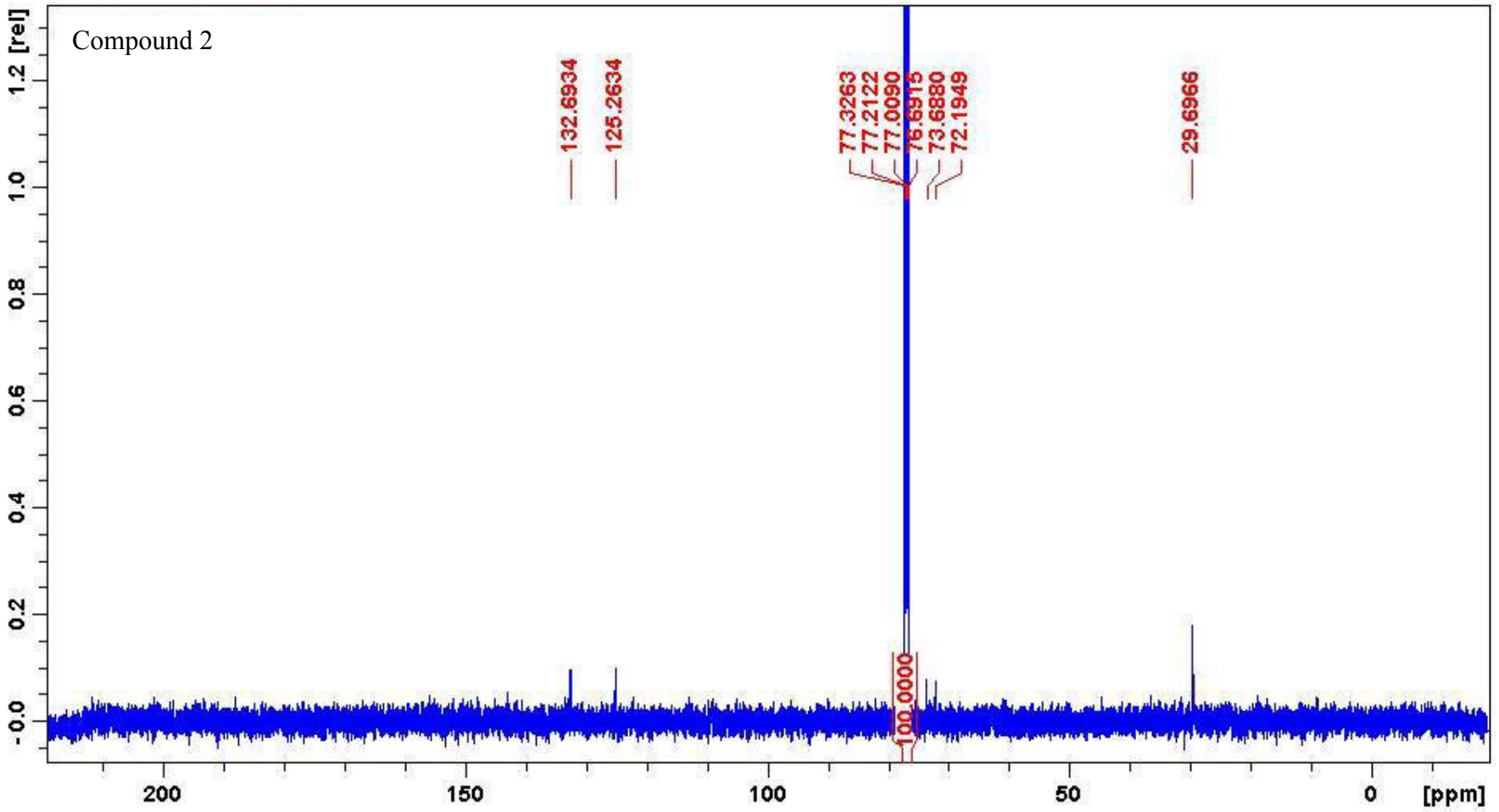


**Figure 2: $^{13}$Carbon for compound 2**

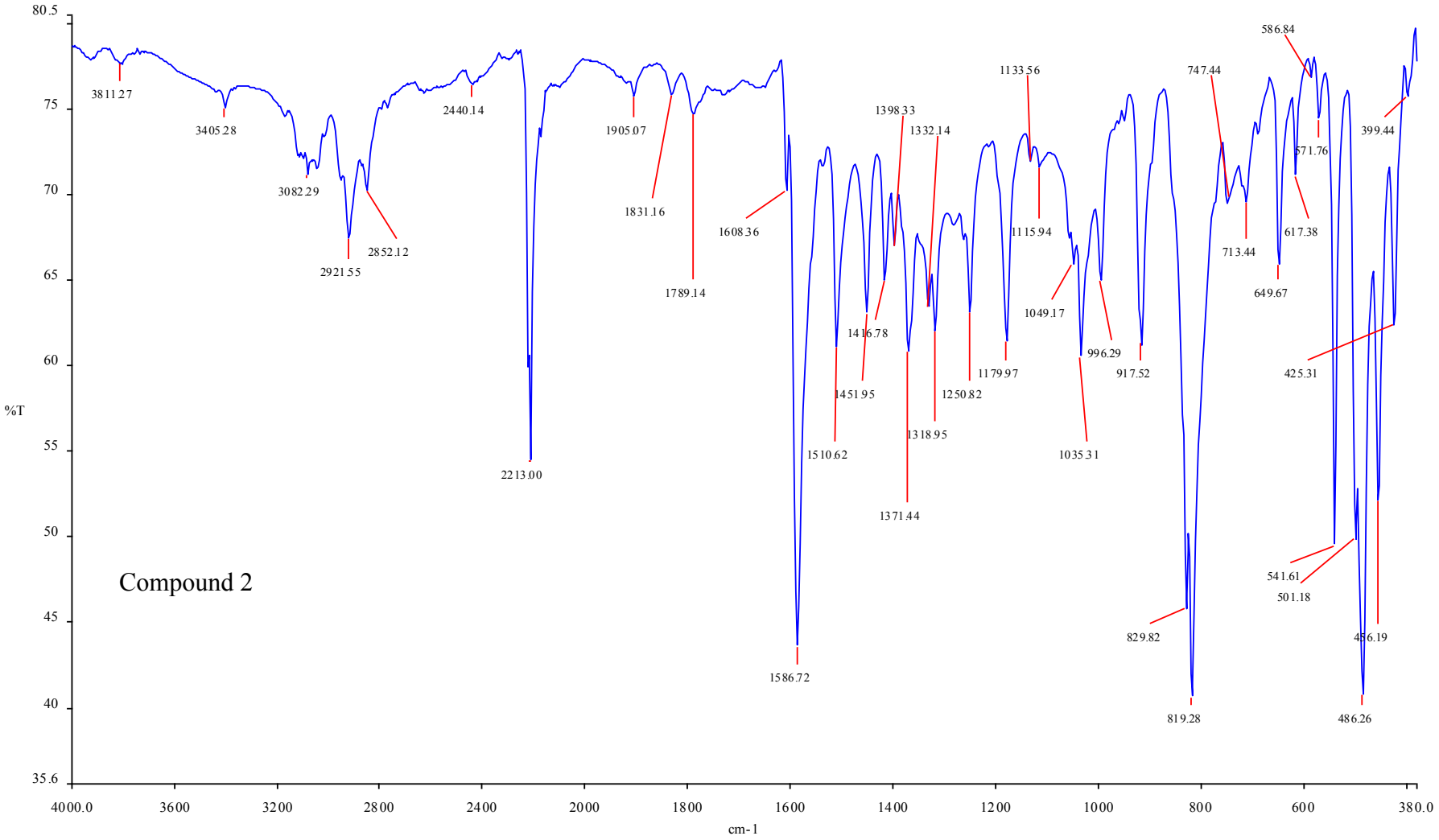


**Figure 3: FT-IR-spectra for compound 2**

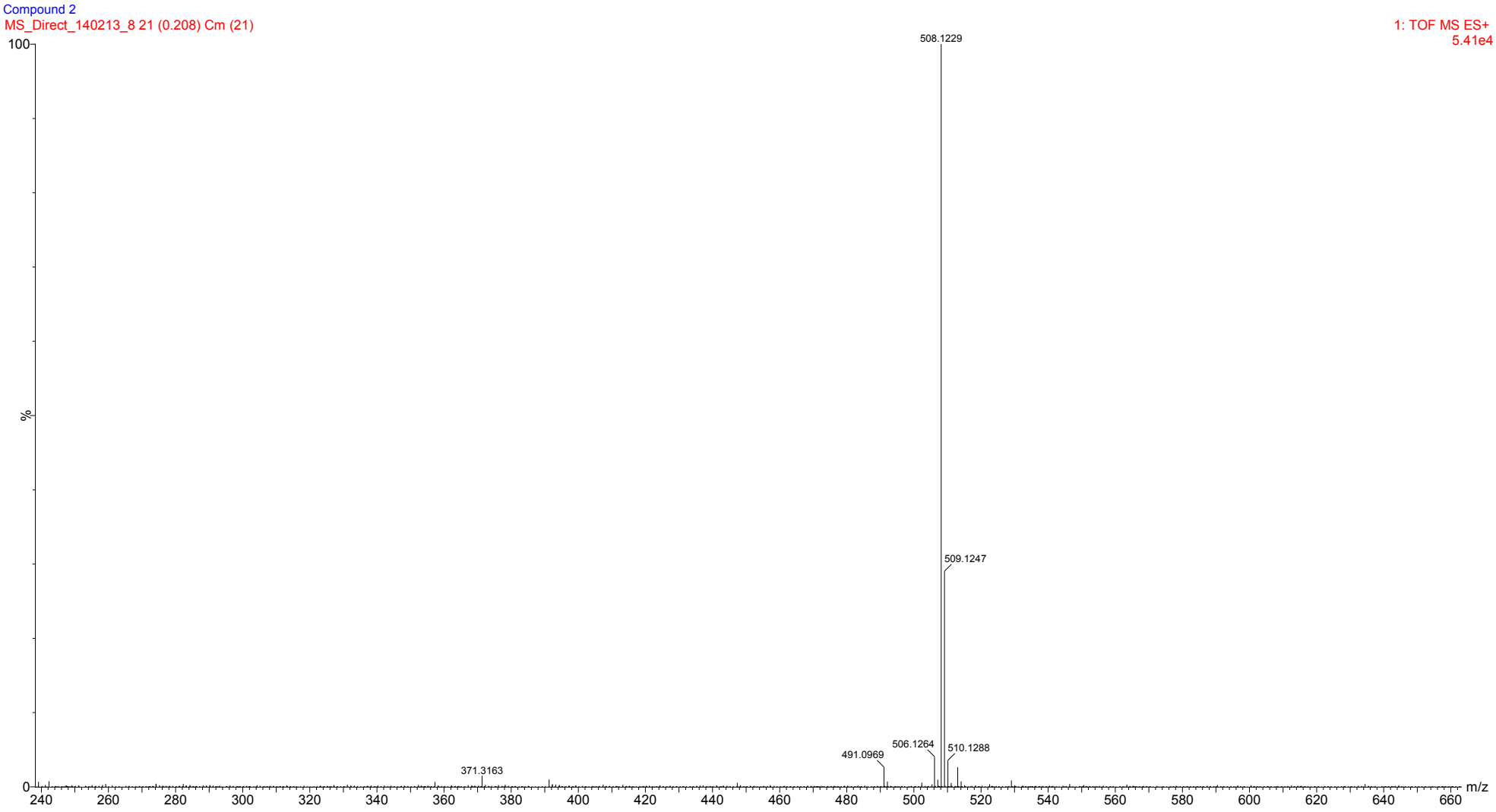


**Figure 4: HR-MS for compound 2**

*1,1'-Ferrocenyldi[-2(4-{trifluoromethyl}phenyl)acrylonitrile] (Compound 3)*

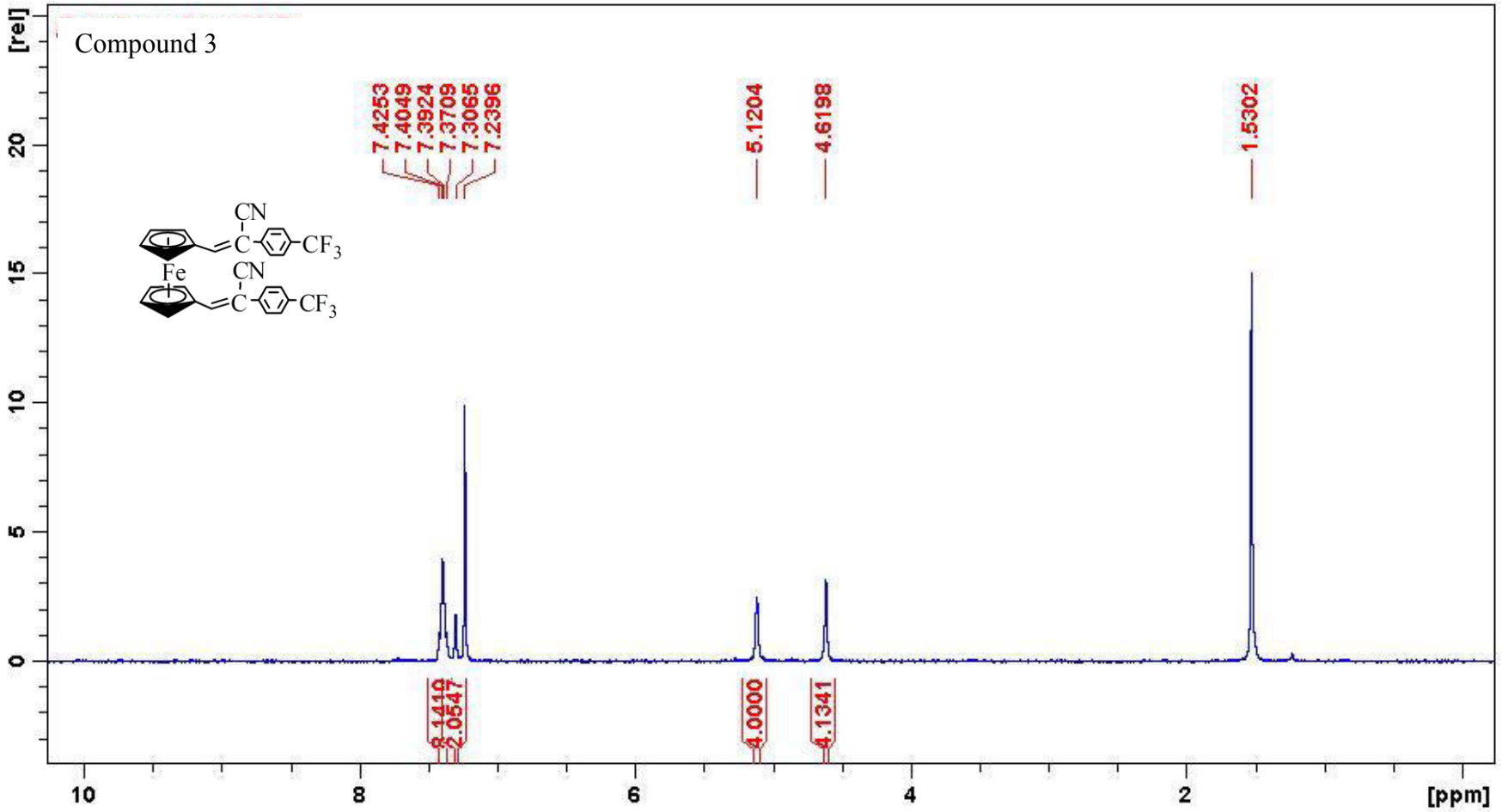


**Figure 5: proton NMR for compound 3**

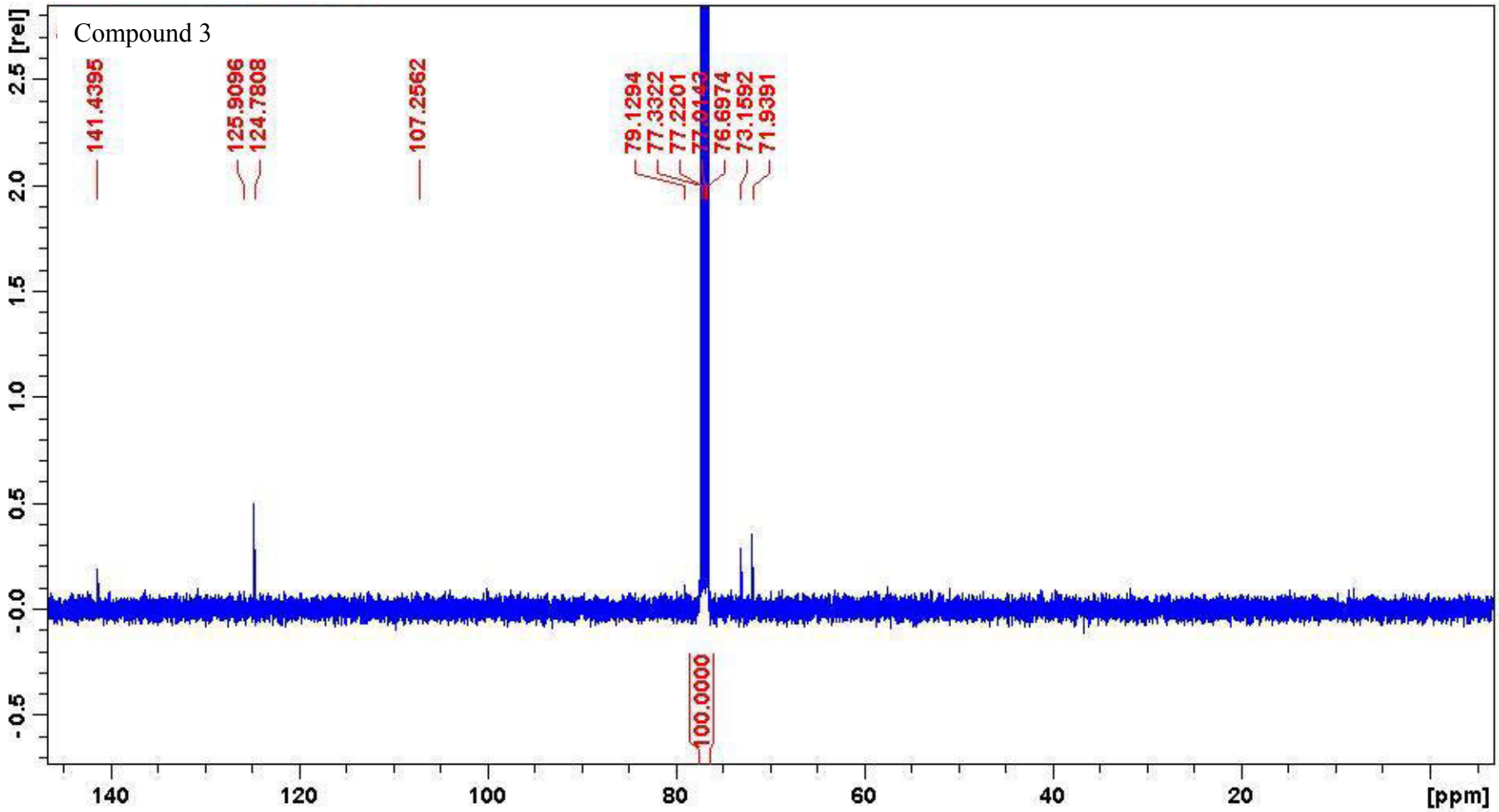


**Figure 6: $^{13}$Carbon NMR for compound 3**

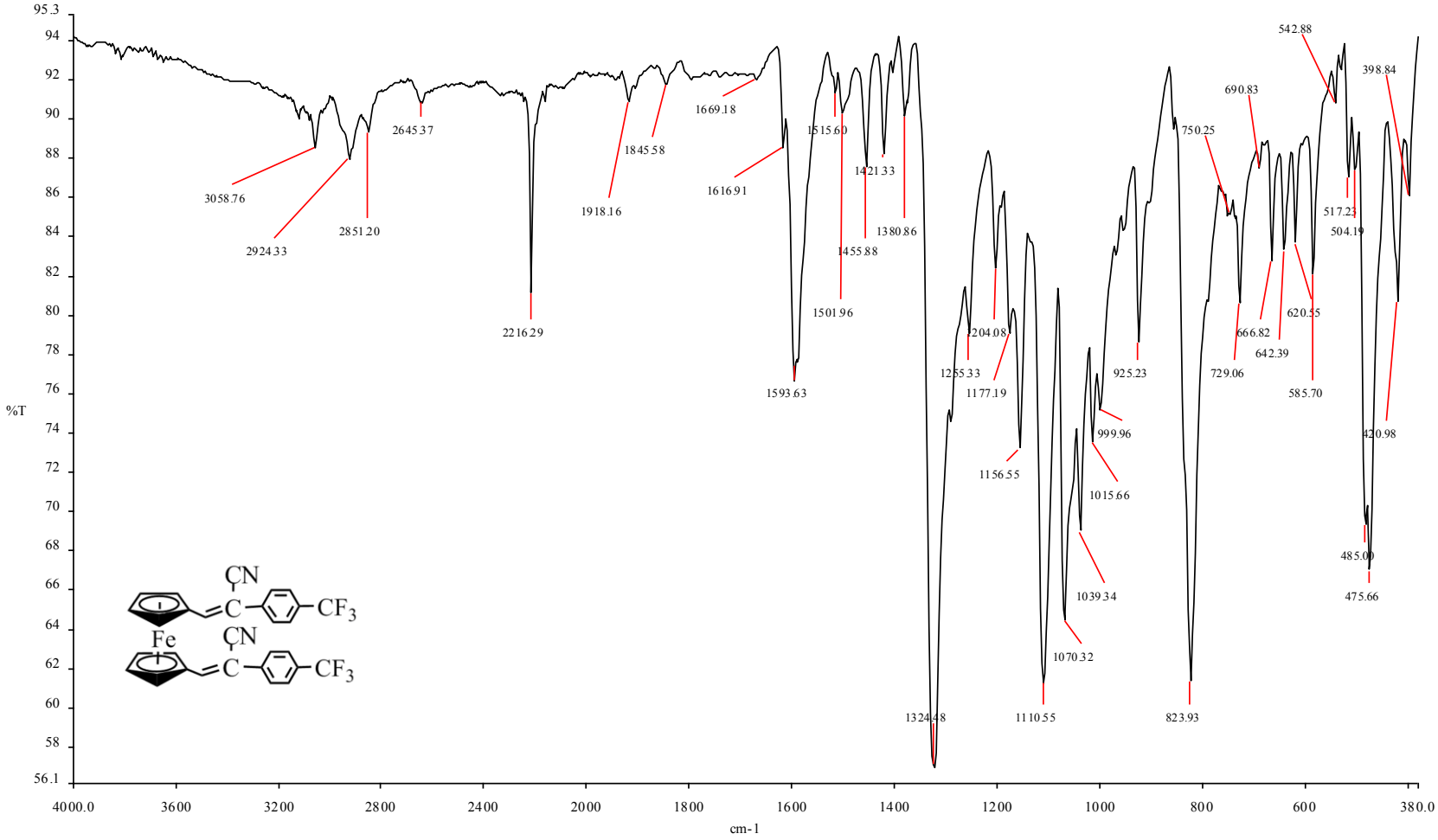


**Figure 7: FT-IR spectra for compound 3**

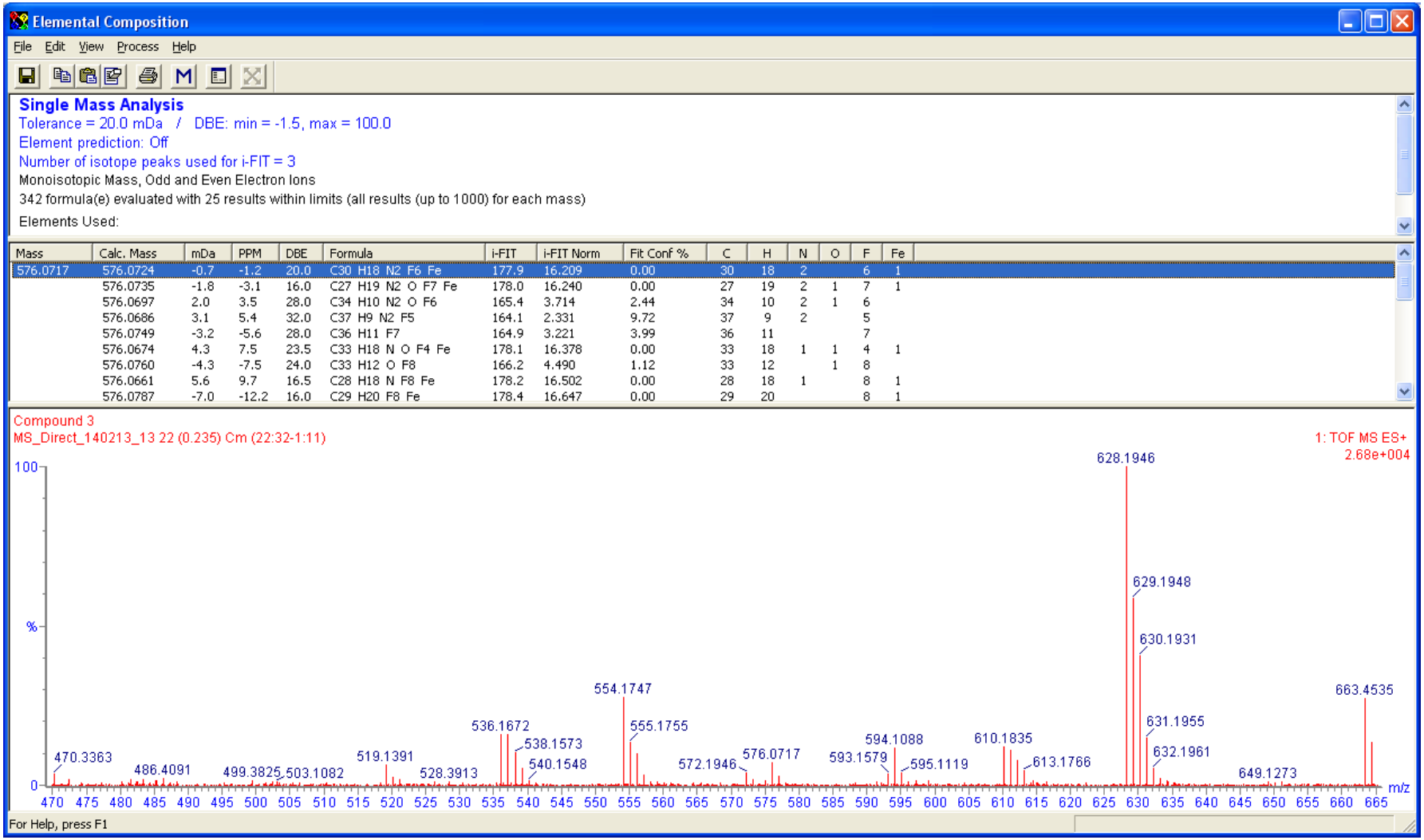


**Figure 8: HR-MS for compound 2**

*1,1'-Ferrocenyldi[-2(4-chlorophenyl)acrylonitrile] (compound 4)*

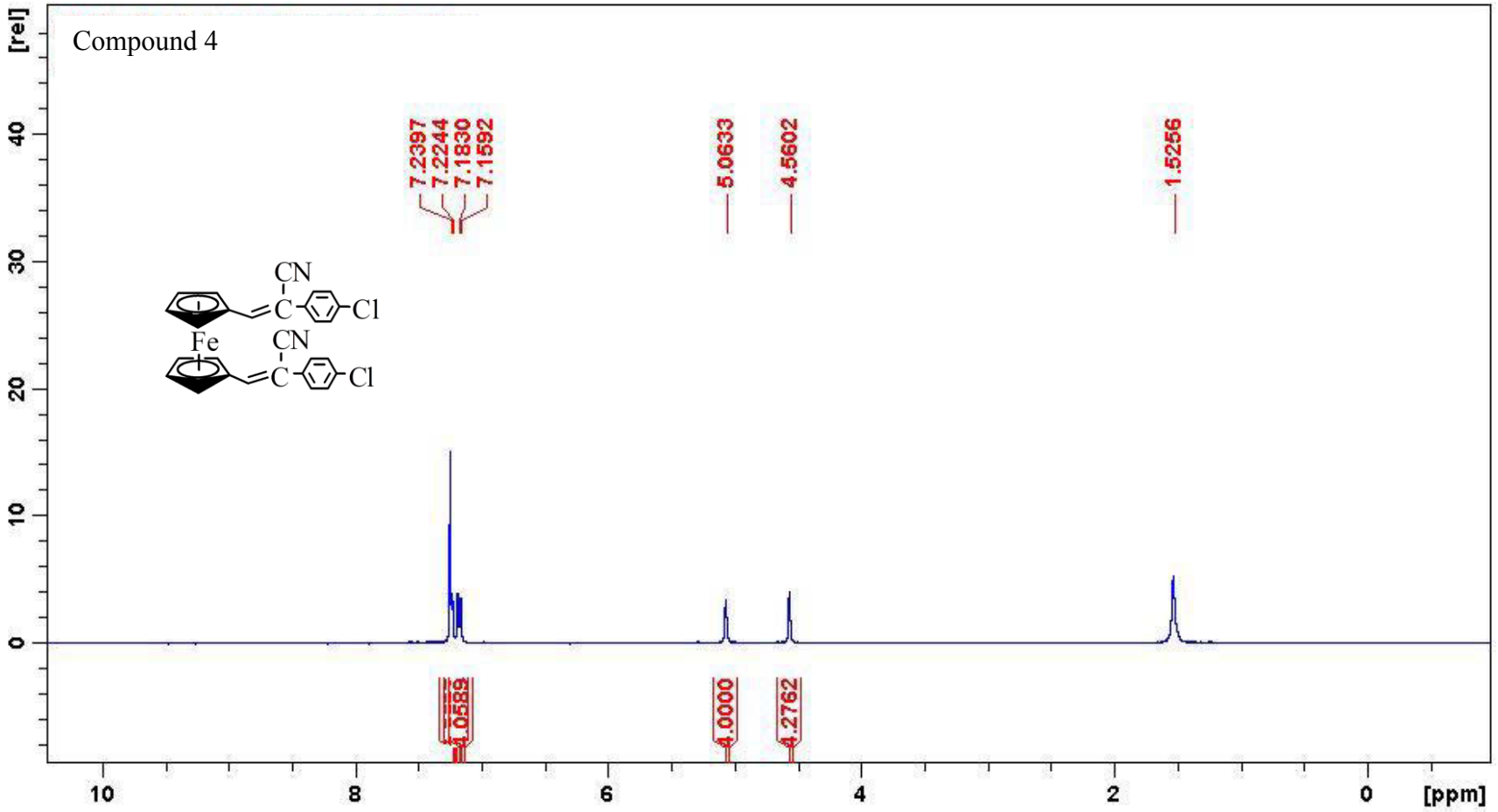


**Figure 9: proton NMR for compound 4**

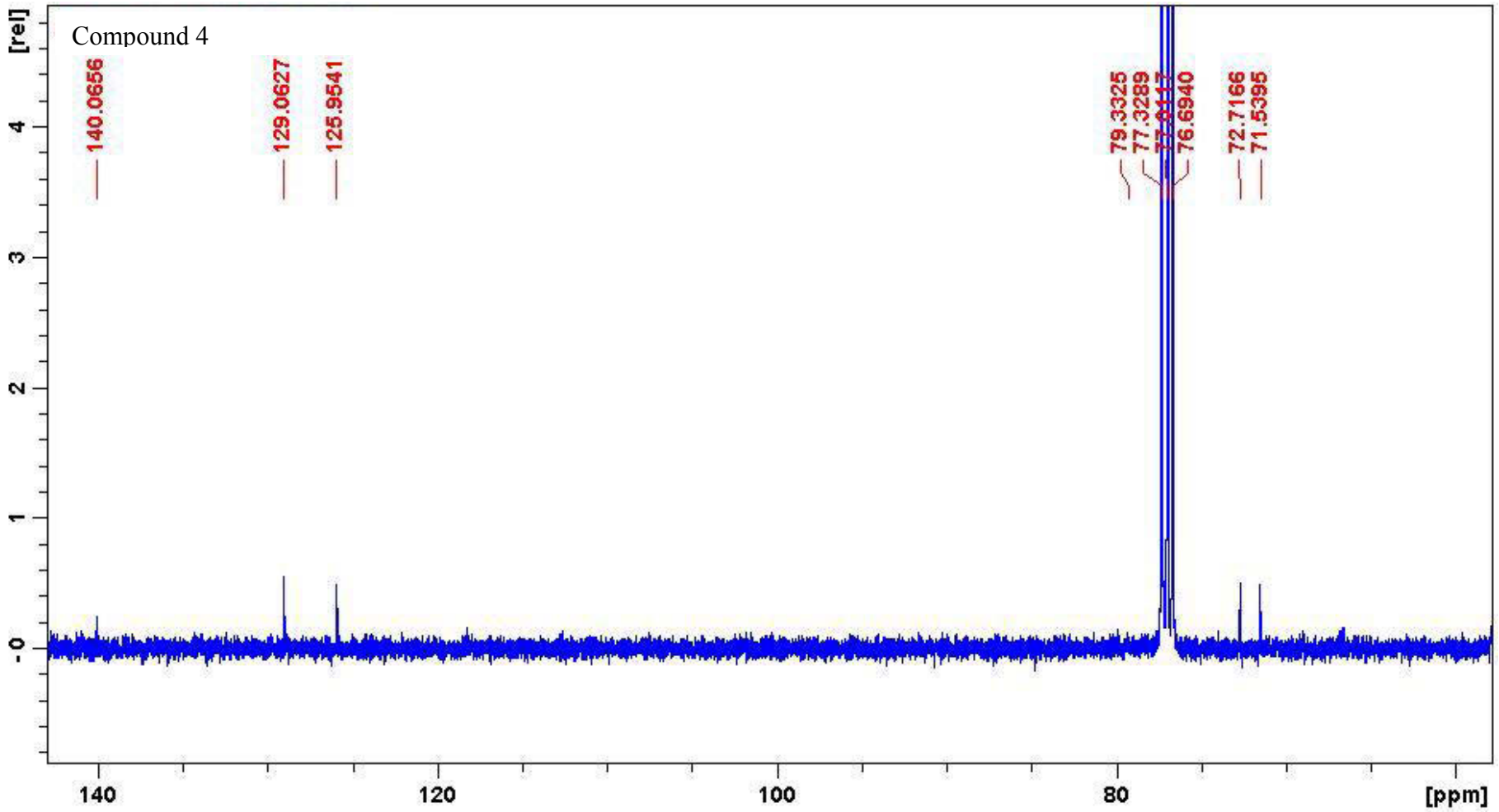


**Figure 10: $^{13}$Carbon for compound 4**

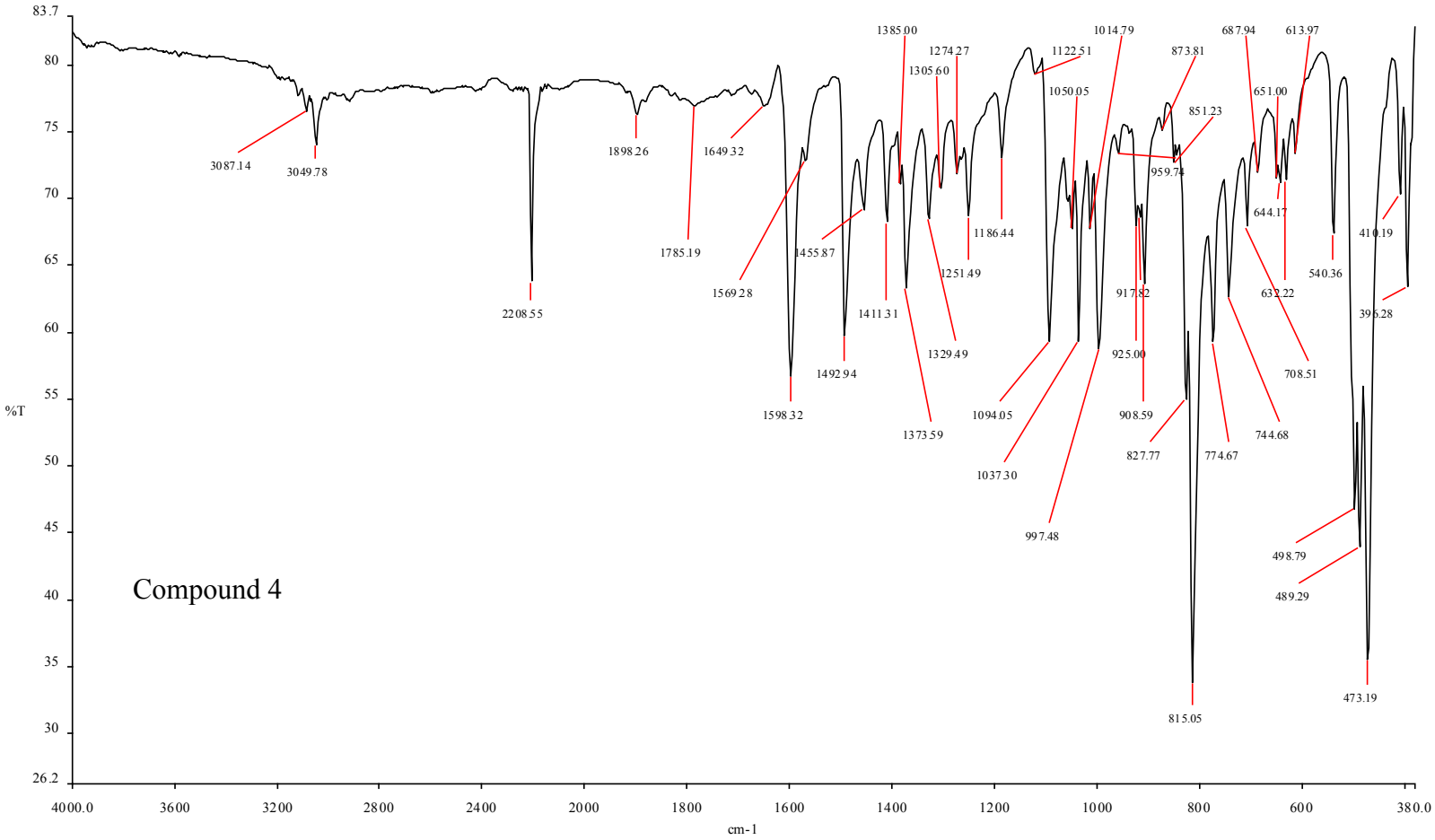


**Figure 11: FT-IR spectra for compound 4**

## Elemental Composition Report



### Single Mass Analysis

Tolerance = 5.0 PPM / DBE: min = -1.5, max = 100.0
Element prediction: Off
Number of isotope peaks used for i-FIT = 3

Monoisotopic Mass, Odd and Even Electron Ions
13 formula(e) evaluated with 1 results within limits (up to 50 best isotopic matches for each mass)
Elements Used:
C: 25-30 H: 15-20 N: 0-5 Cl: 1-2 Fe: 0-2

Compound 1B 31 (0.512) Cm (1:31)
TOF MS ES+

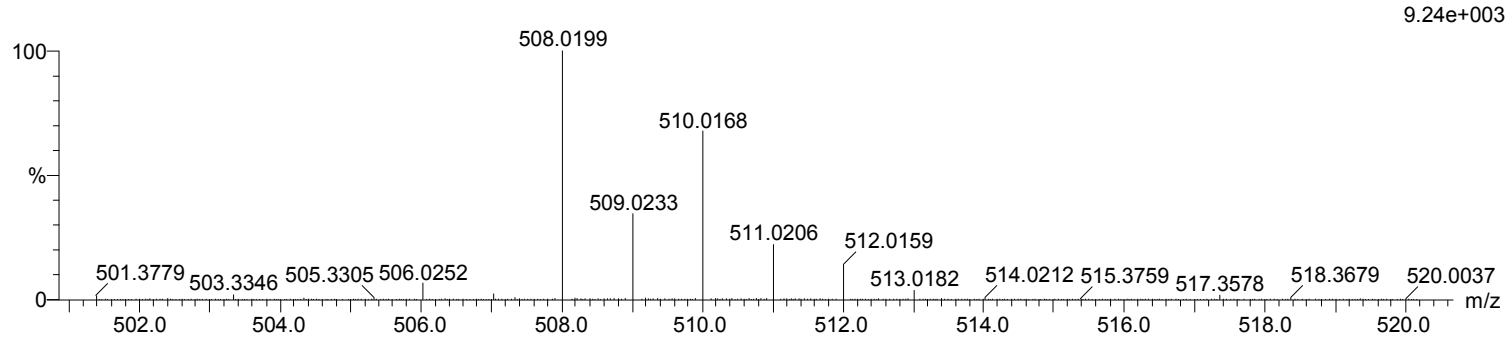


| | | | | | | | |
|---|---|---|---|---|---|---|---|
| Minimum: | | | | -1.5 | | | |
| Maximum: | | 5.0 | 5.0 | 100.0 | | | |
| Mass | Calc. Mass | mDa | PPM | DBE | i-FIT | i-FIT (Norm) | Formula |
| 508.0199 | 508.0196 | 0.3 | 0.6 | 20.0 | 312.9 | 0.0 | C28 H18 N2 Cl2 Fe |

**Figure 12: HR-MS for compound 4**

***Ferrocenyl-carboxl-2(4-chlorophenyl)acrylonitrile (compound 5)***

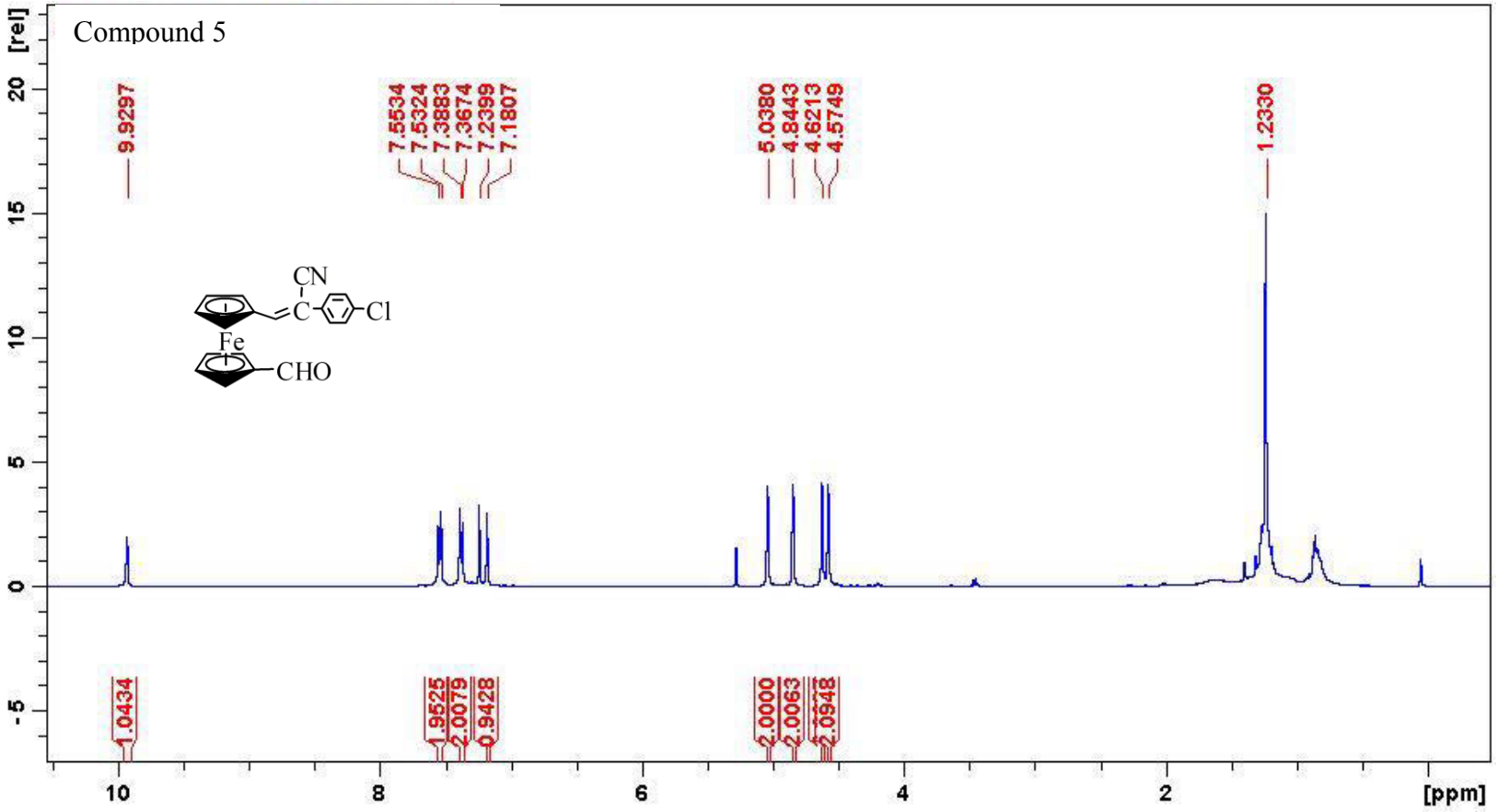


**Figure 13: proton NMR for compound 5**

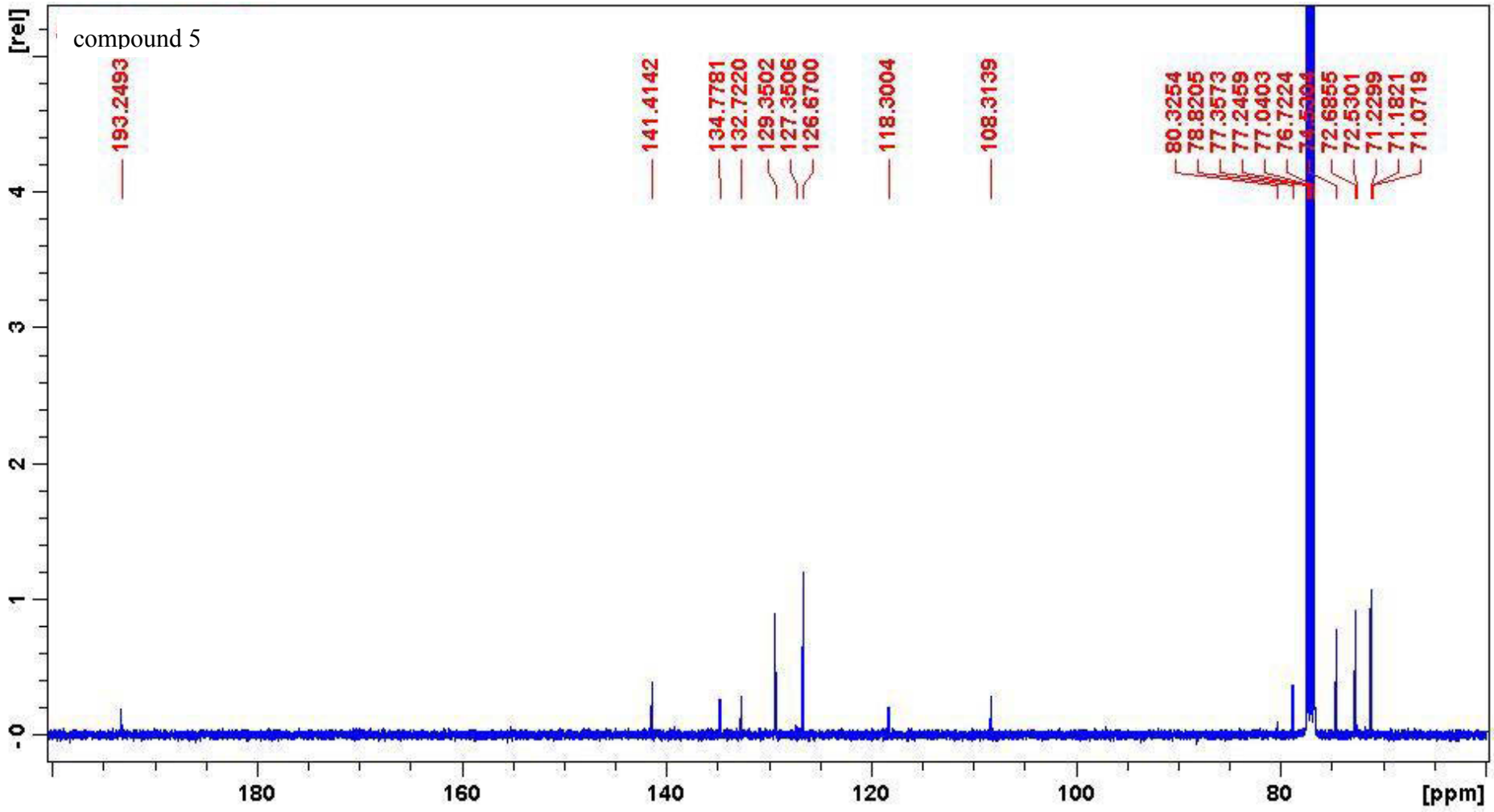


**Figure 14: $^{13}$Carbon for compound 5**

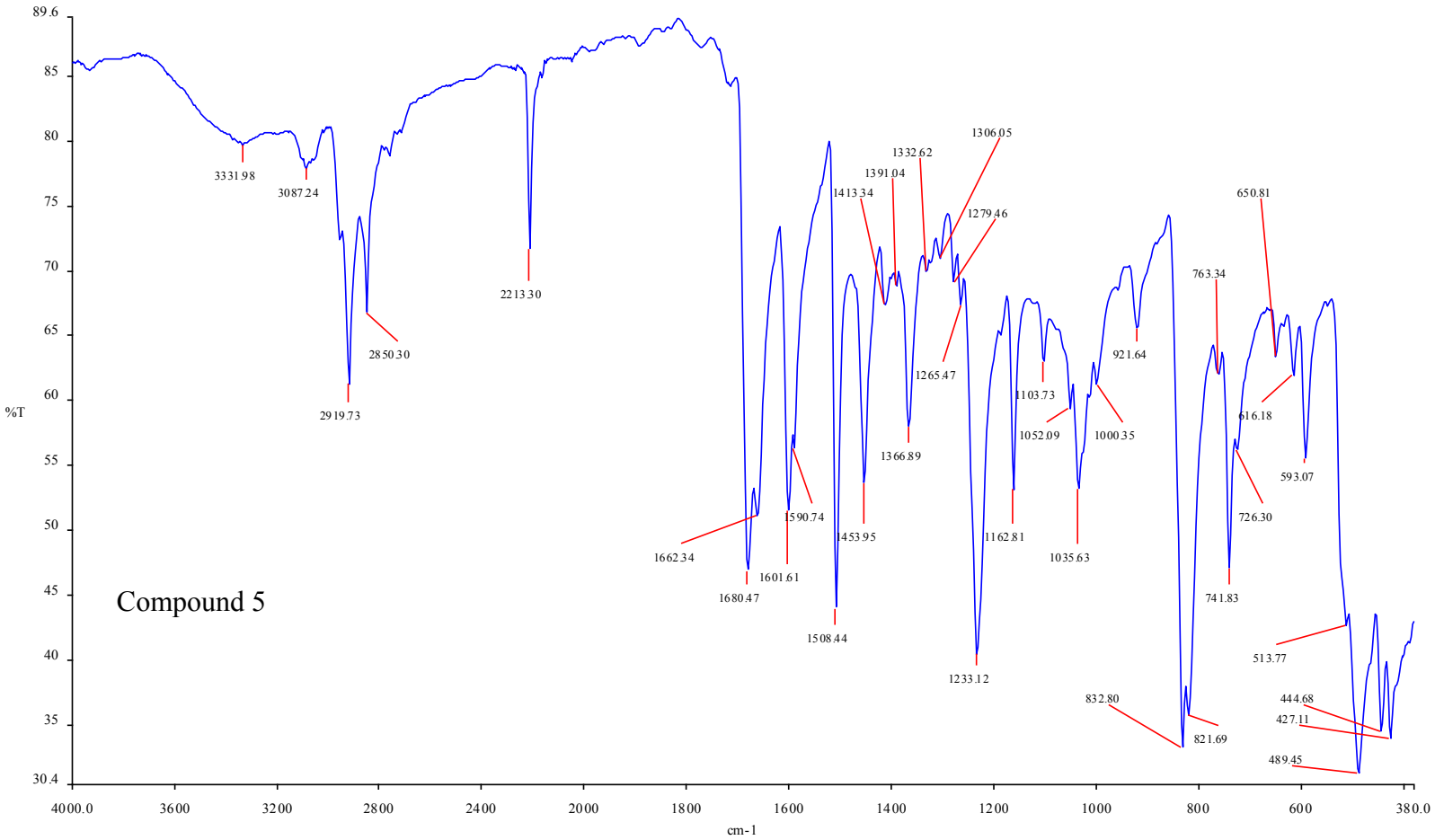


**Figure 15: FT-IR spectrum for compound 5**

## Elemental Composition Report



### Single Mass Analysis

Tolerance = 5.0 PPM / DBE: min = -1.5, max = 50.0
Element prediction: Off
Number of isotope peaks used for i-FIT = 3

Monoisotopic Mass, Even Electron Ions
82 formula(e) evaluated with 1 results within limits (up to 50 best isotopic matches for each mass)
Elements Used:
C: 20-25 H: 10-15 N: 0-5 O: 0-5 Cl: 1-1 Fe: 0-2

1B(2) 2 (0.017) Cm (1:31)
TOF MS AP+

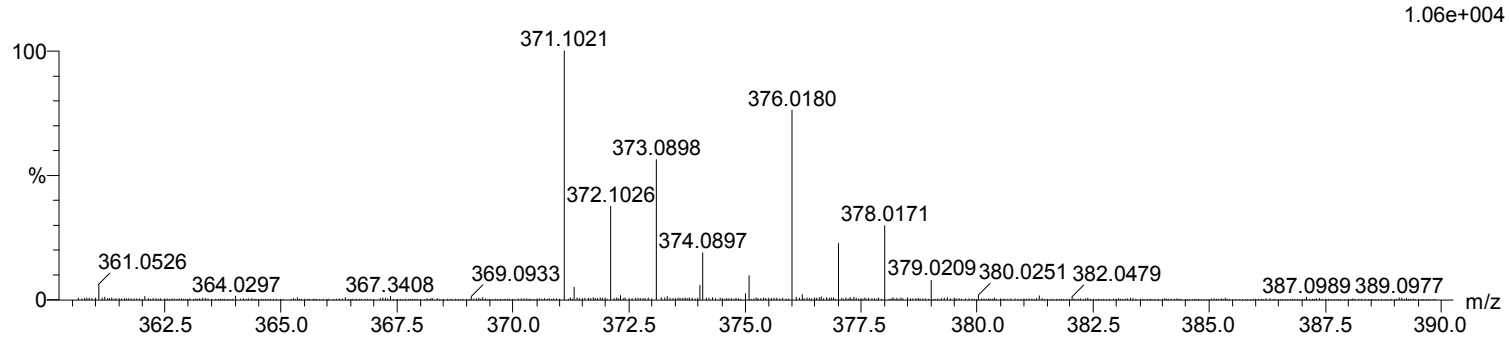


| | | | | | | | |
|---|---|---|---|---|---|---|---|
| Minimum: | | | | -1.5 | | | |
| Maximum: | | 5.0 | 5.0 | 50.0 | | | |
| Mass | Calc. Mass | mDa | PPM | DBE | i-FIT | i-FIT (Norm) | Formula |
| 376.0180 | 376.0192 | -1.2 | -3.2 | 13.5 | 421.7 | 0.0 | C20 H15 N O Cl Fe |

**Figure 16: HR-MS for compound 5**

*1,1'-Ferrocenyldi[-2(4-fluorophenyl)acrylonitrile] (compound 6)*

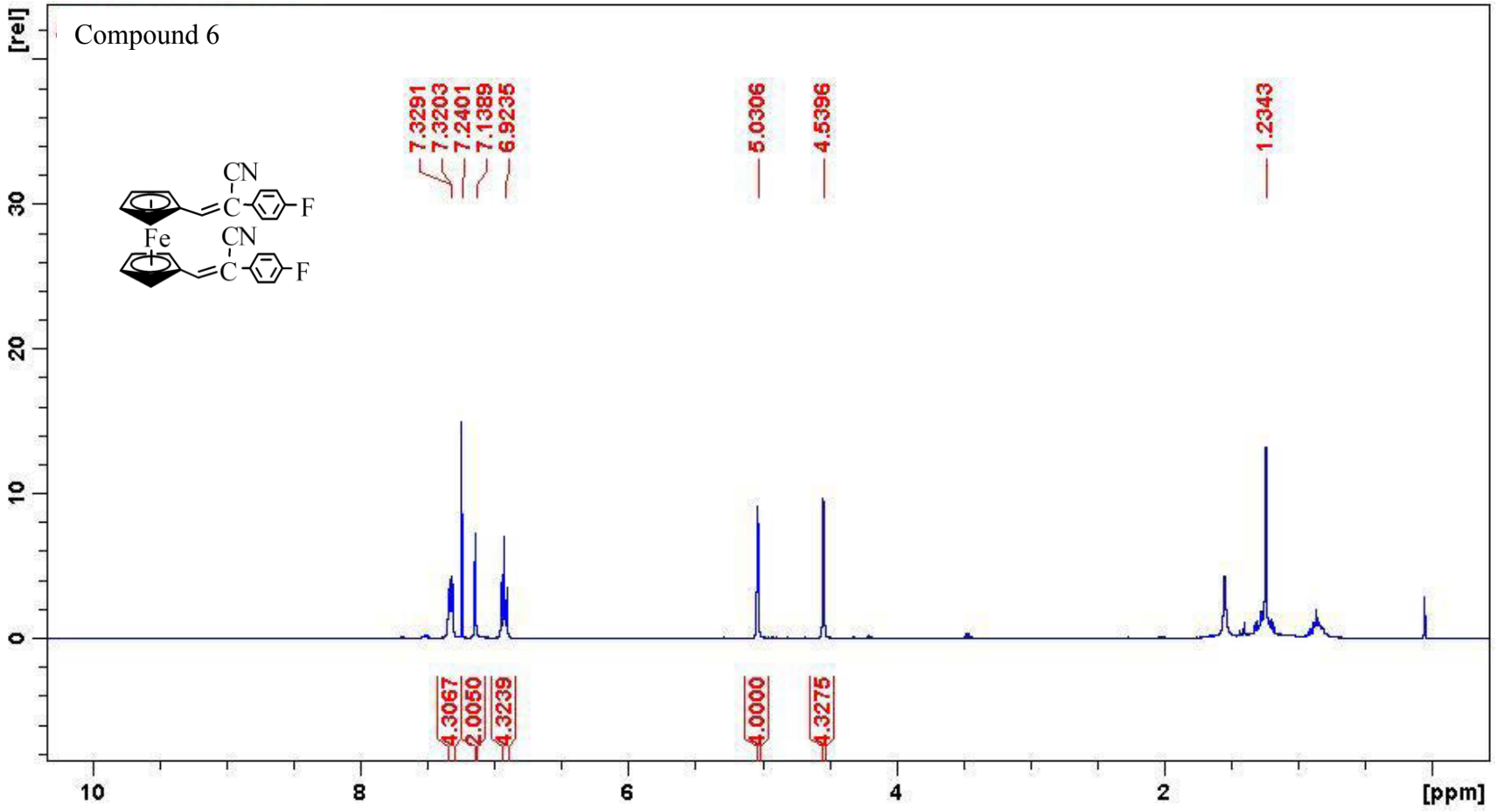


**Figure 17: proton NMR for compound 6**

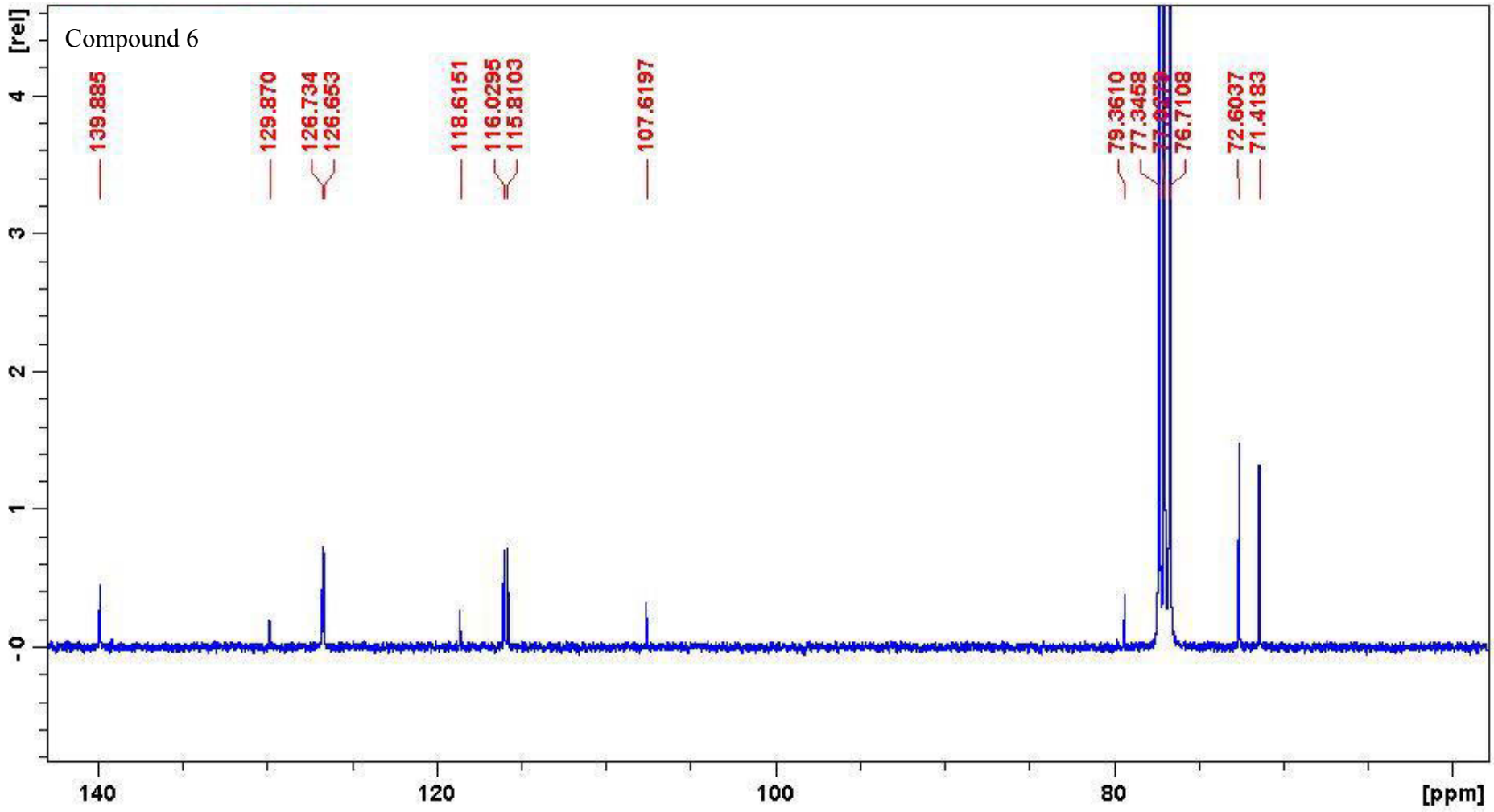


**Figure 18: $^{13}$Carbon for compound 6**

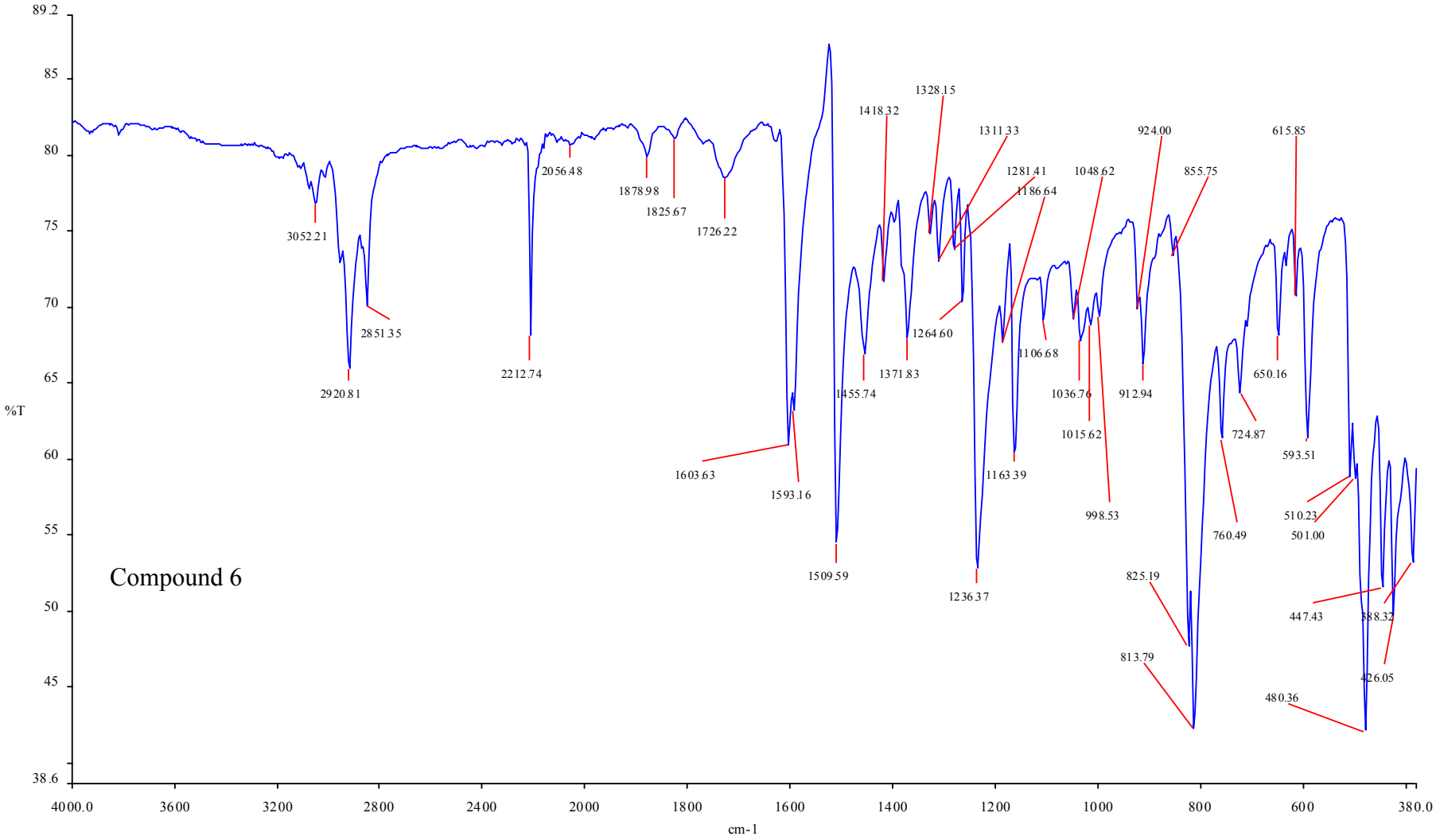


**Figure 19: FT-IR spectrum for compound 6**

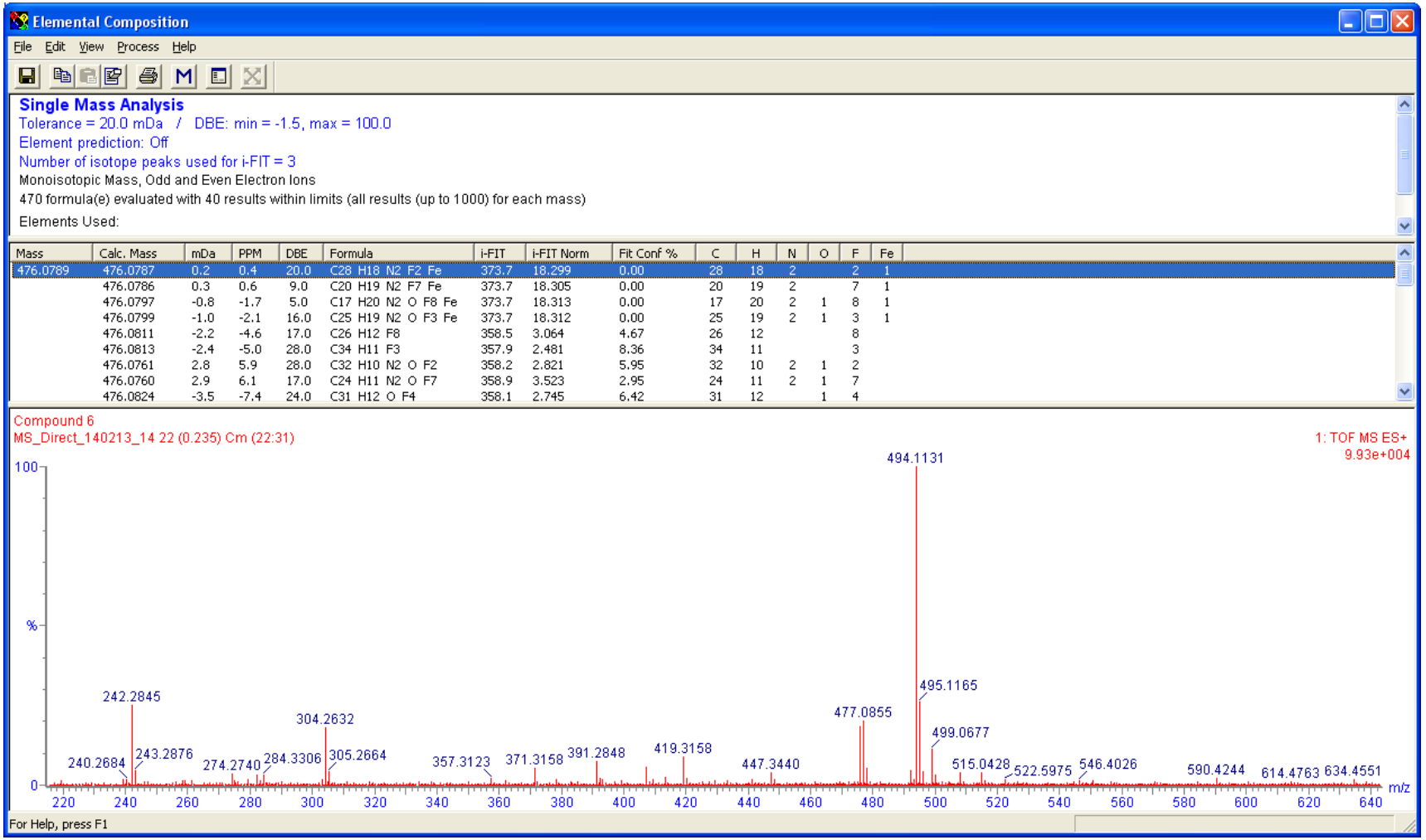


**Figure 20: HR-MS for compound 6**

***Ferrocenyl-carboxl-2(4-fluorophenyl)acrylonitrile (compound 7)***

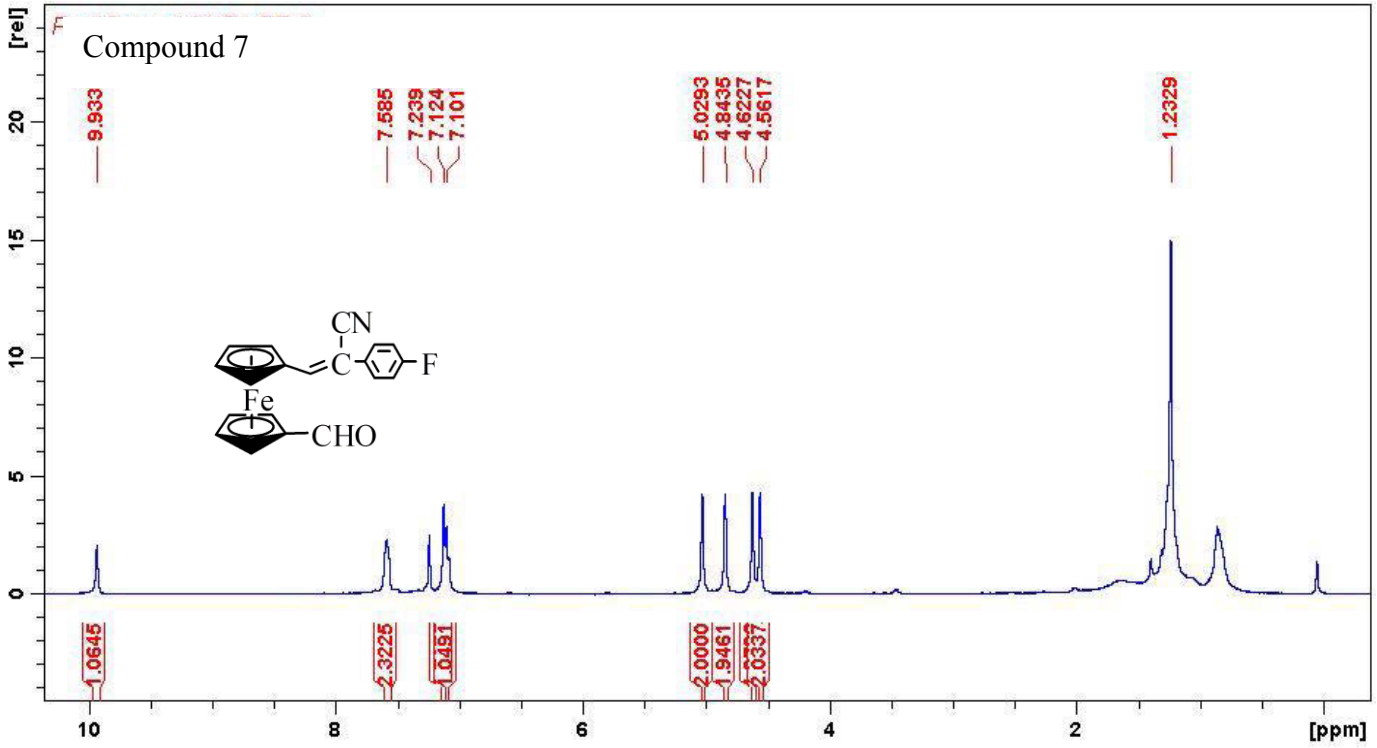


**Figure 21: proton NMR for Compound 7**

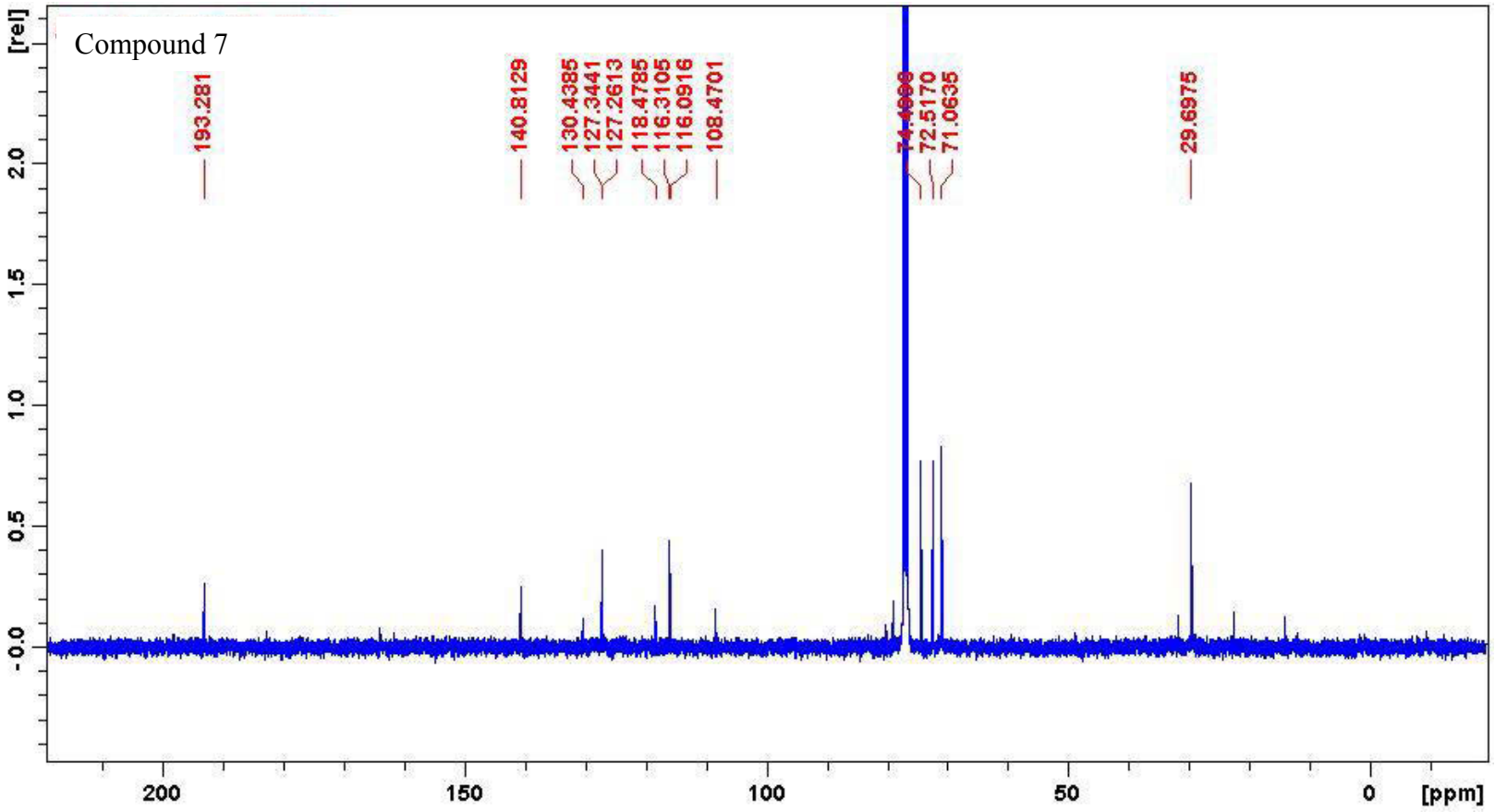


**Figure 22: $^{13}$carbon NMR for compound 7**

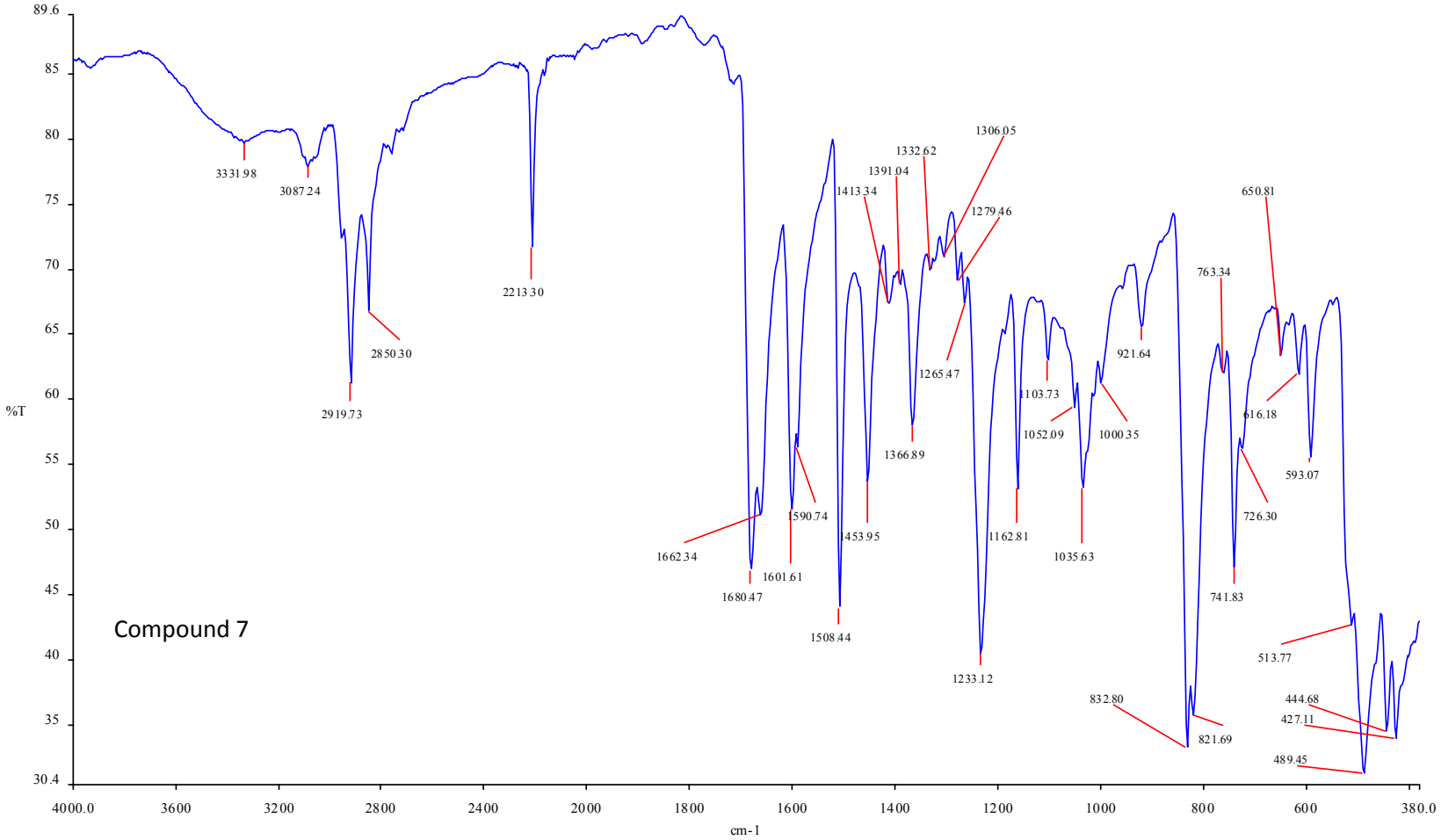


**FT-IR 23: spectrum for compound 7**

## Elemental Composition Report



### Single Mass Analysis

Tolerance = 5.0 PPM / DBE: min = -1.5, max = 100.0
Element prediction: Off
Number of isotope peaks used for i-FIT = 3

Monoisotopic Mass, Odd and Even Electron Ions
82 formula(e) evaluated with 1 results within limits (up to 50 best isotopic matches for each mass)
Elements Used:
C: 20-25 H: 10-15 N: 0-5 O: 0-5 F: 1-1 Fe: 0-2

Compound 1D(2) 2 (0.017) Cm (1:30)
TOF MS ES+

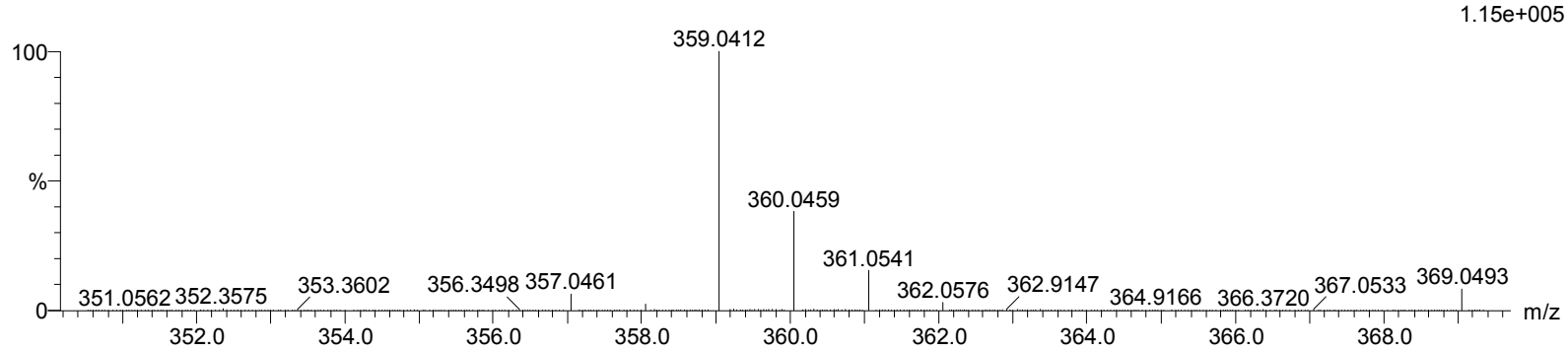


| | | | | | | | |
|---|---|---|---|---|---|---|---|
| Minimum: | | | | -1.5 | | | |
| Maximum: | | 5.0 | 5.0 | 100.0 | | | |
| Mass | Calc. Mass | mDa | PPM | DBE | i-FIT | i-FIT (Norm) | Formula |
| 359.0412 | 359.0409 | 0.3 | 0.8 | 14.0 | 547.2 | 0.0 | C20 H14 N O F Fe |

**Figure 24: HR-MS for compound 7**

***Phenylene-3,3'-bis-(ferrocenyl)-diacrylonitrile (compound 9)***

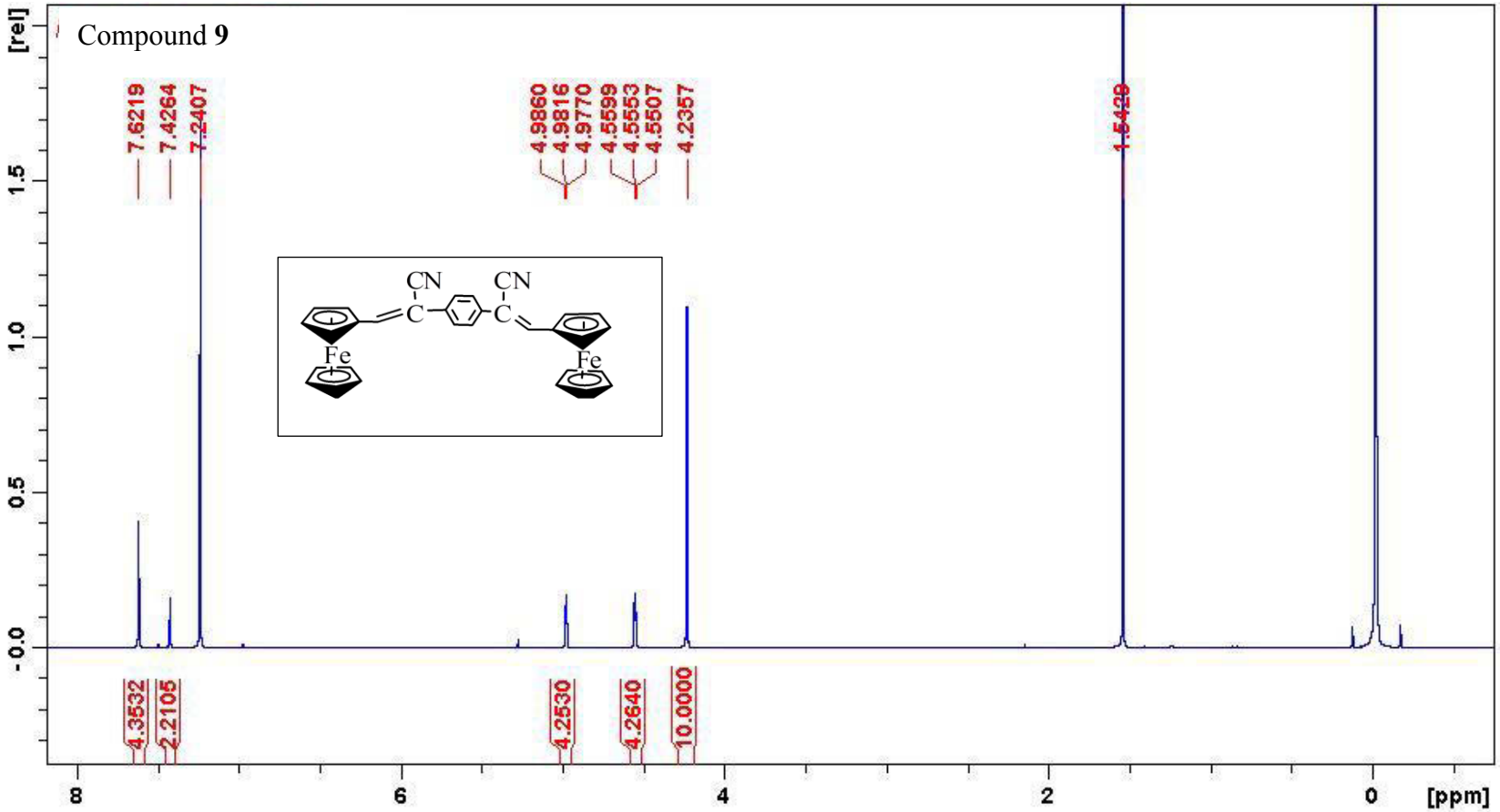


**Figure 25: Proton NMR of compound 9**

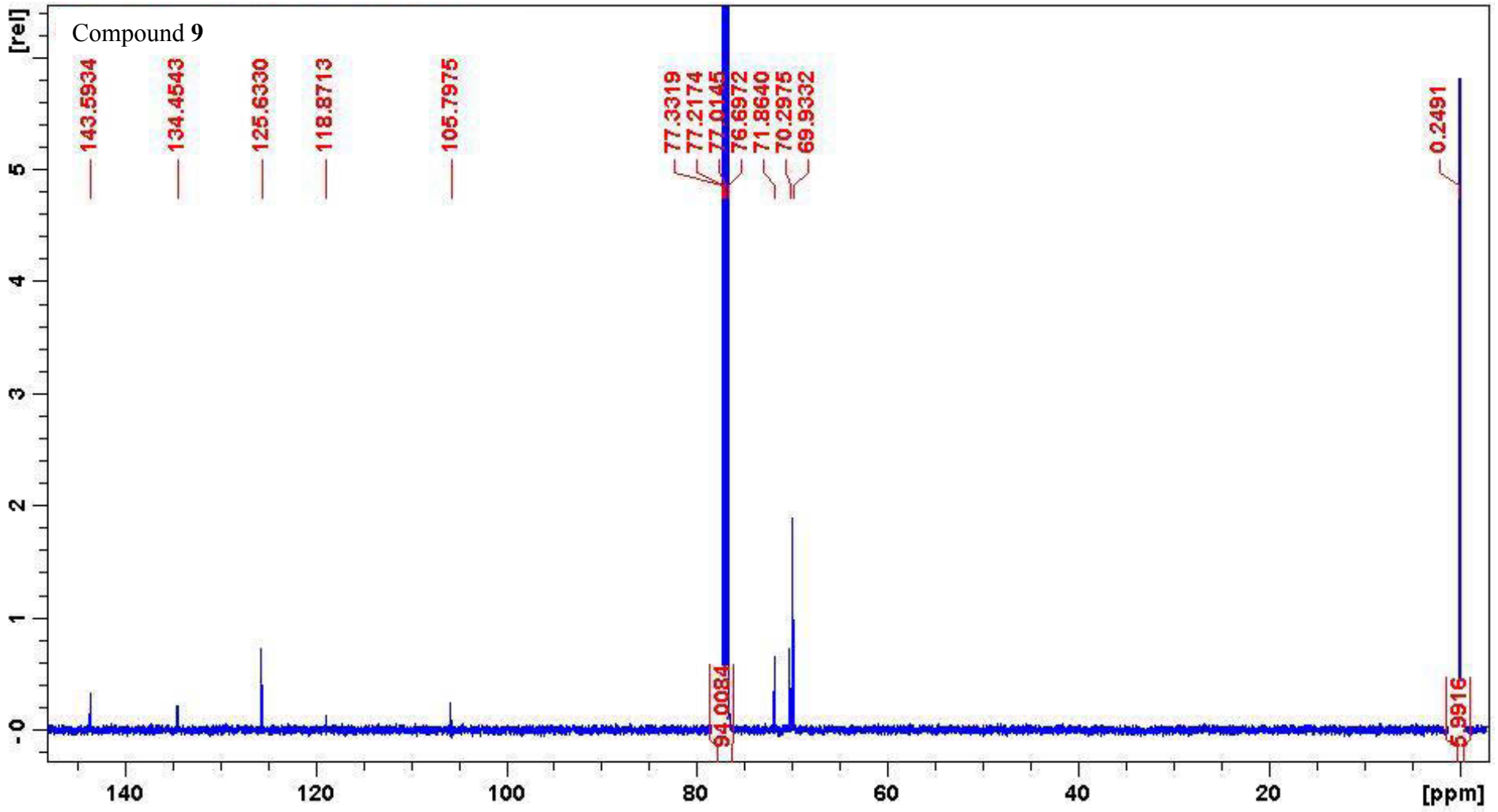


**Figure 26: $^{13}$Carbon NMR for compound 9**

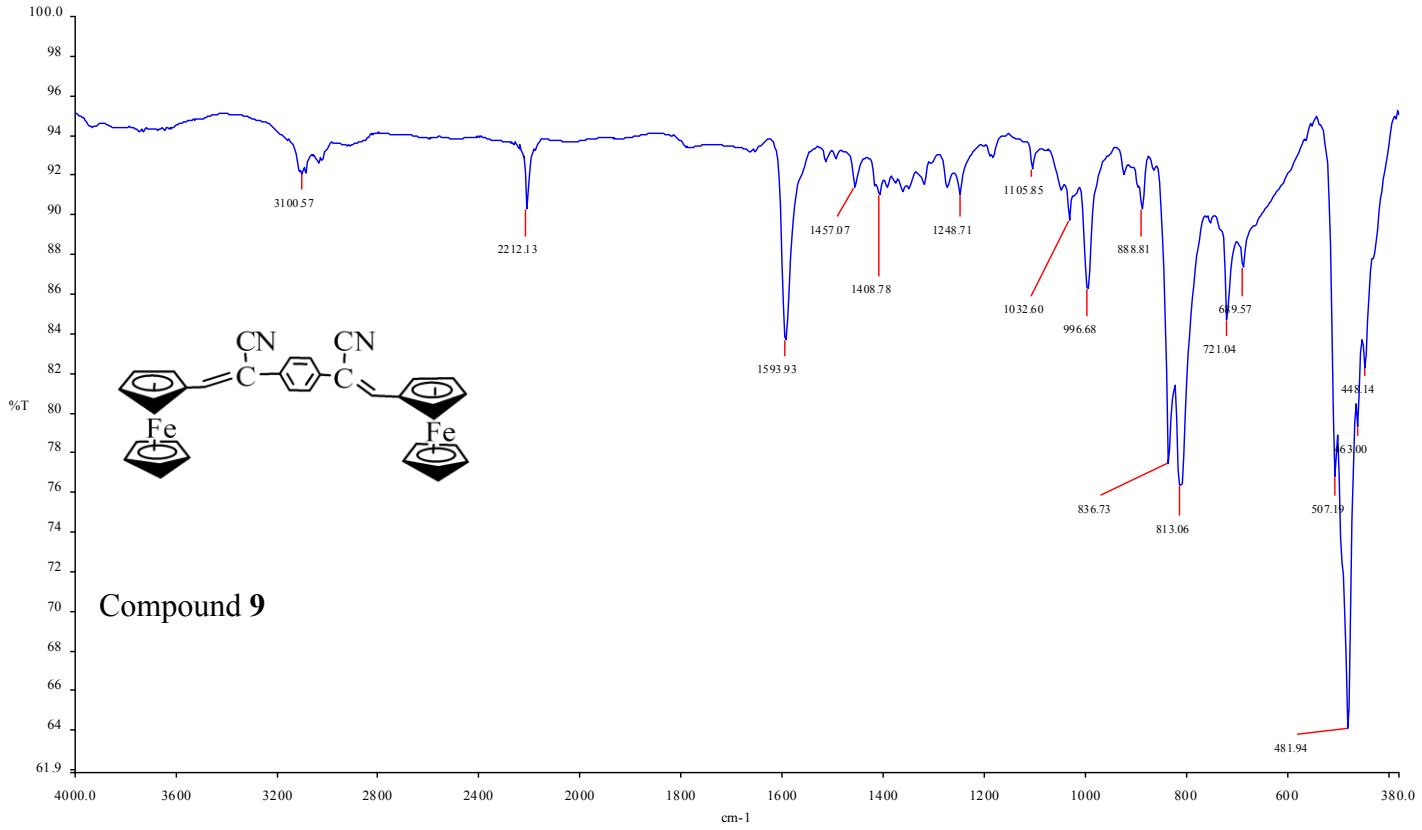


**Figure 27: FT-IR spectra of compound 9**

## Elemental Composition Report



### Single Mass Analysis

Tolerance = 4.0 PPM / DBE: min = -1.5, max = 50.0
Element prediction: Off
Number of isotope peaks used for i-FIT = 3

Monoisotopic Mass, Odd and Even Electron Ions
10 formula(e) evaluated with 1 results within limits (up to 50 best isotopic matches for each mass)
Elements Used:
C: 30-35 H: 20-25 N: 0-5 Na: 0-1 Fe: 0-2

Compound 2A 27 (0.443) Cm (2:30)
TOF MS ES+

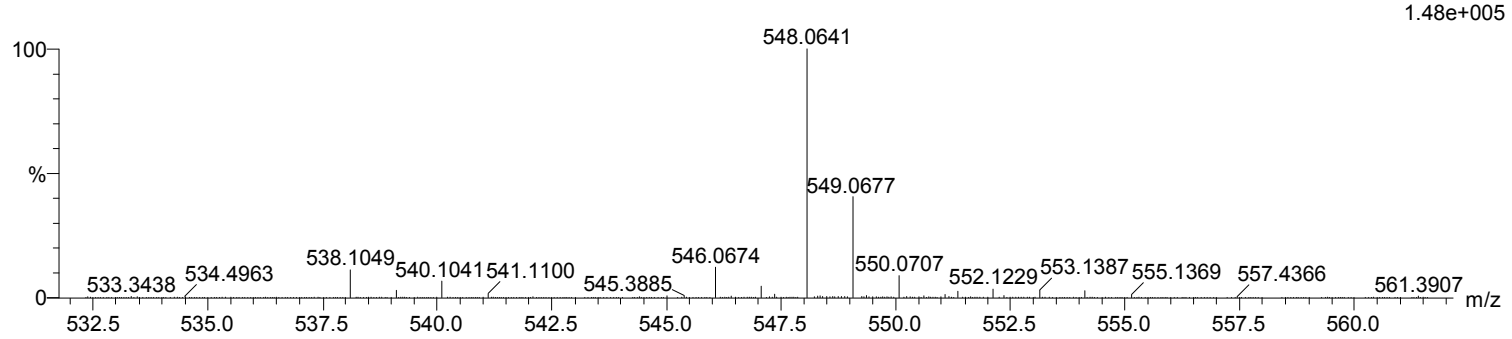


| | | | | | | | |
|---|---|---|---|---|---|---|---|
| Minimum: | | | | -1.5 | | | |
| Maximum: | | 5.0 | 4.0 | 50.0 | | | |
| Mass | Calc. Mass | mDa | PPM | DBE | i-FIT | i-FIT (Norm) | Formula |
| 548.0641 | 548.0638 | 0.3 | 0.5 | 22.0 | 613.5 | 0.0 | C32 H24 N2 Fe2 |

**Figure 28: HR-MS for compound 9**

3-Ferrocenyl-2(acetonitrophenyl)acrylonitrile (compound 10)

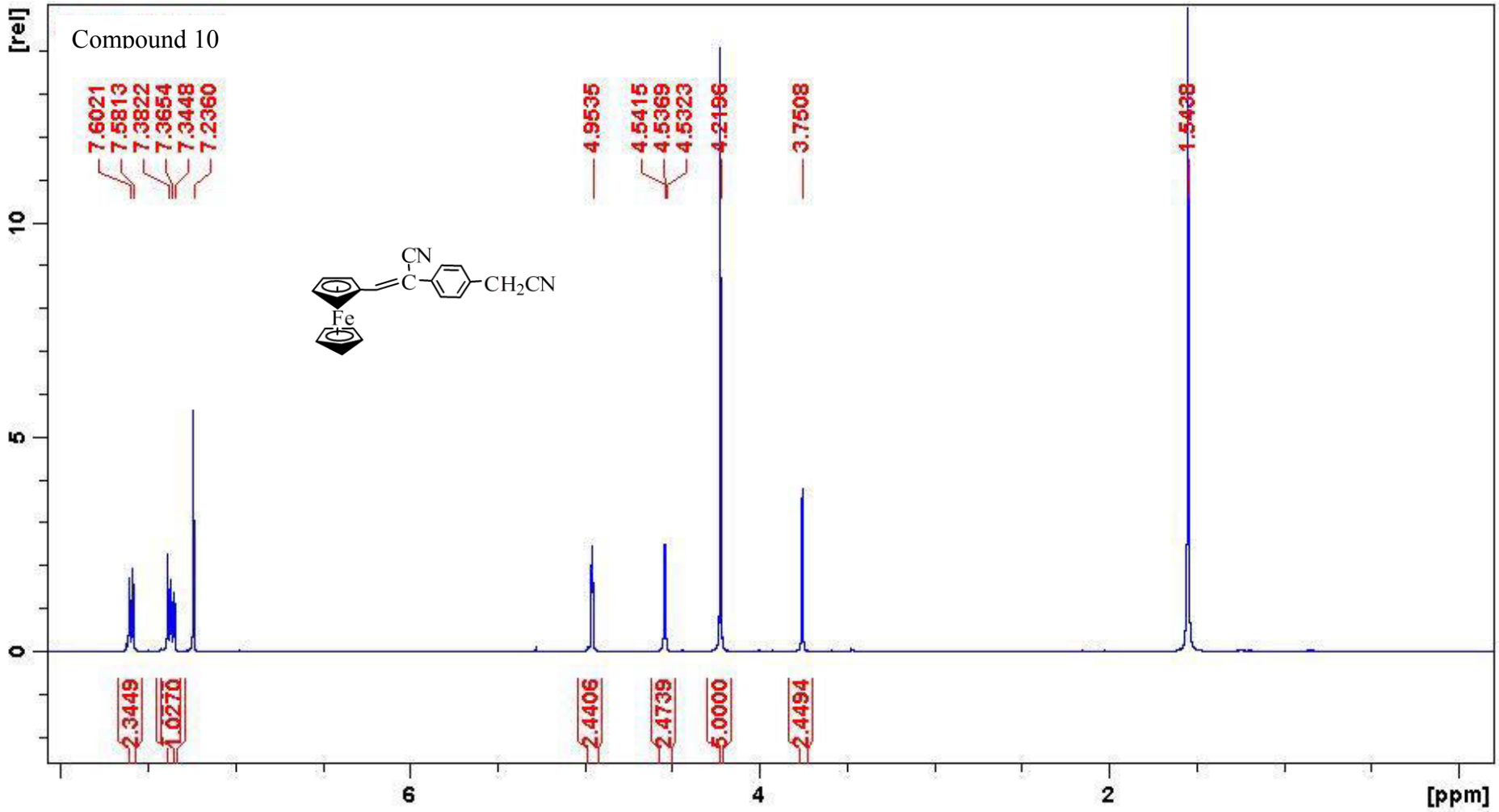


**Figure 29: Proton NMR for compound 10**

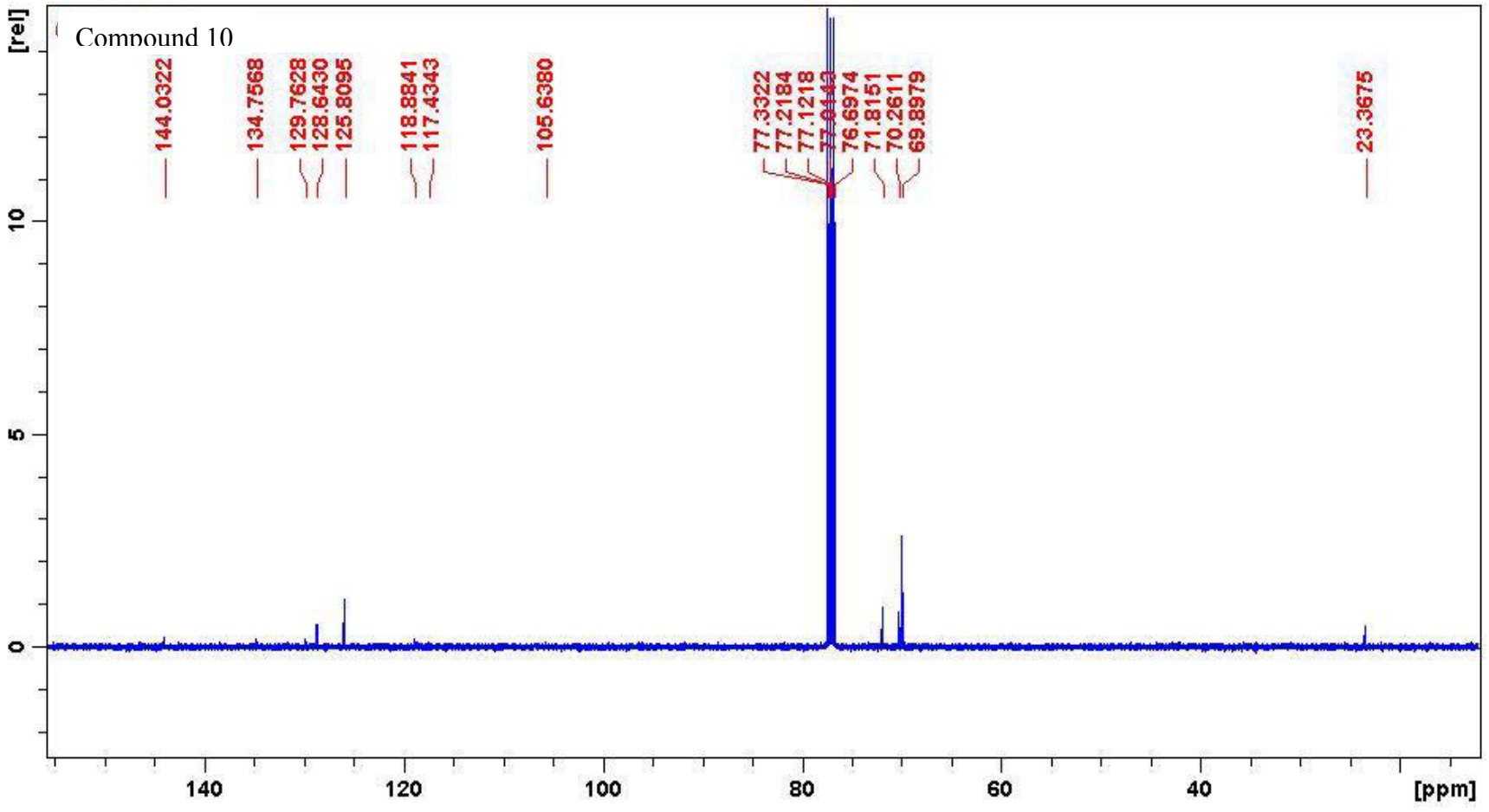


Figure:

**Figure 30: 13Carbon-NMR for compound 10**

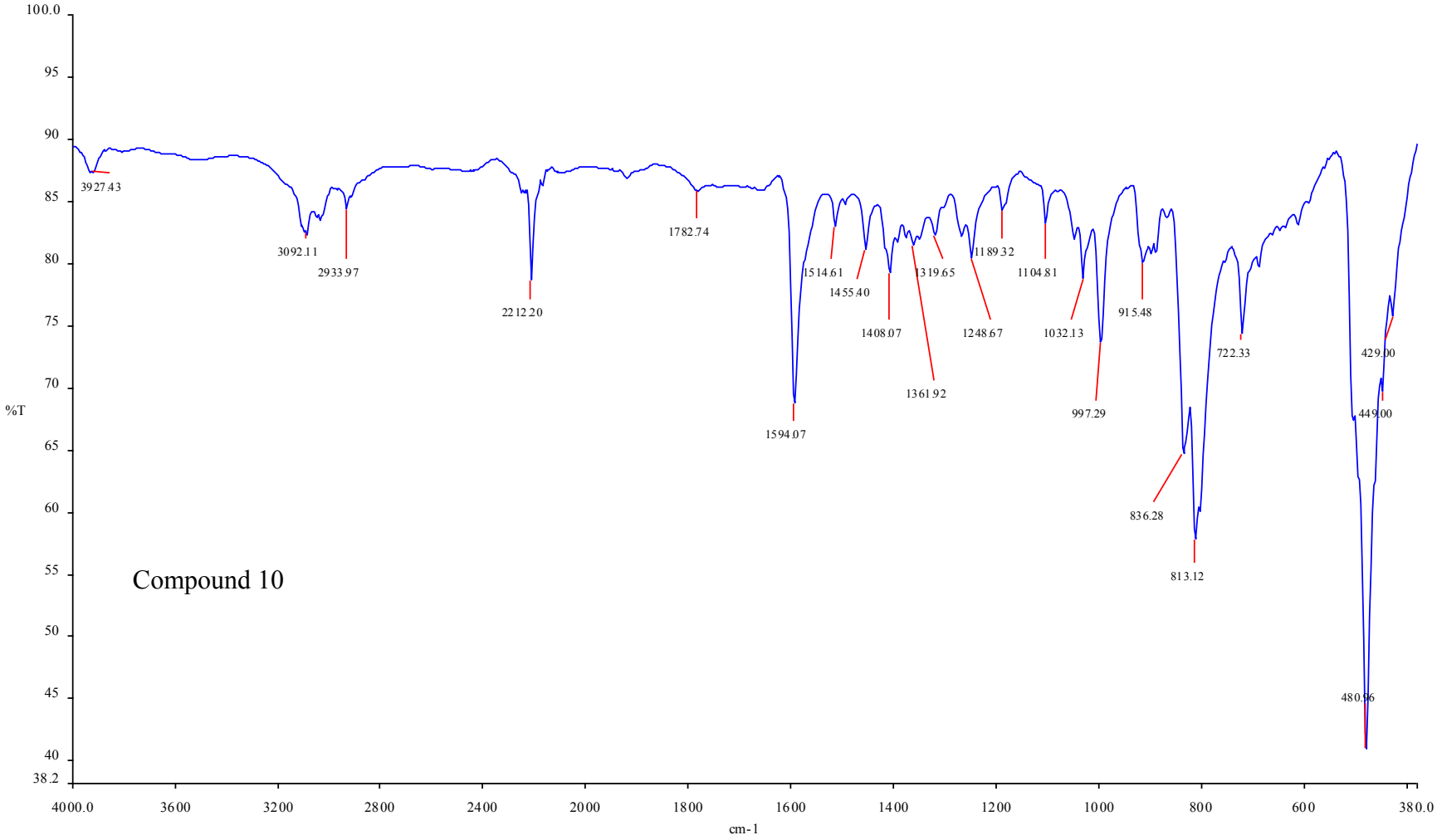


**Figure 31: FT-IR spectra of compound 10**

## Elemental Composition Report



### Single Mass Analysis

Tolerance = 4.0 PPM / DBE: min = -1.5, max = 50.0
Element prediction: Off
Number of isotope peaks used for i-FIT = 3

Monoisotopic Mass, Odd and Even Electron Ions
23 formula(e) evaluated with 1 results within limits (up to 50 best isotopic matches for each mass)
Elements Used:
C: 20-25 H: 15-20 N: 0-5 Na: 0-1 Fe: 0-2

Compound 2B 31 (0.512) Cm (1:31)
TOF MS ES+

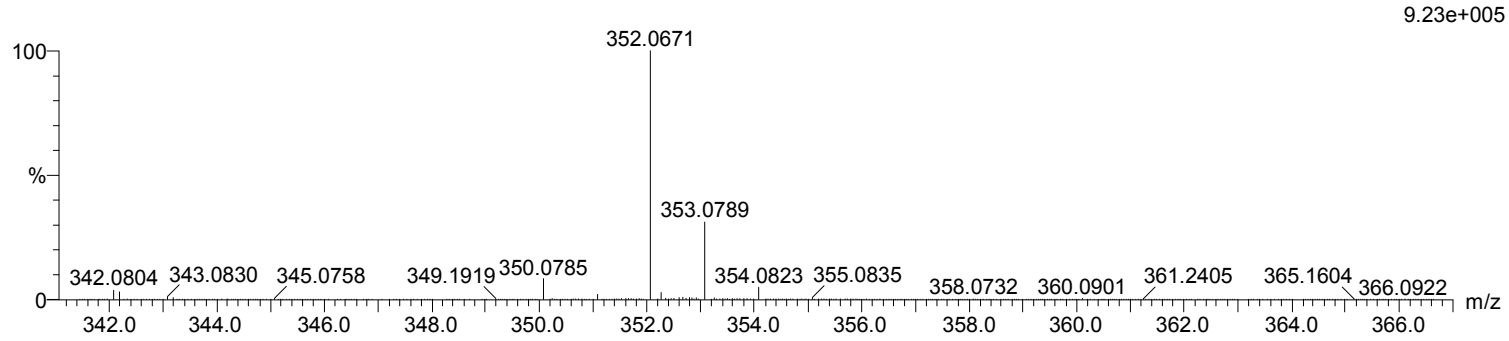


| | | | | | | | |
|---|---|---|---|---|---|---|---|
| Minimum: | | | | -1.5 | | | |
| Maximum: | | 5.0 | 4.0 | 50.0 | | | |
| Mass | Calc. Mass | mDa | PPM | DBE | i-FIT | i-FIT (Norm) | Formula |
| 352.0671 | 352.0663 | 0.8 | 2.3 | 15.0 | 740.4 | 0.0 | C21 H16 N2 Fe |

**Figure 32: HR-MS of compound 10**

# APPENDIX 2: Supporting Information for Chapter Five

## Supplementary Information S1

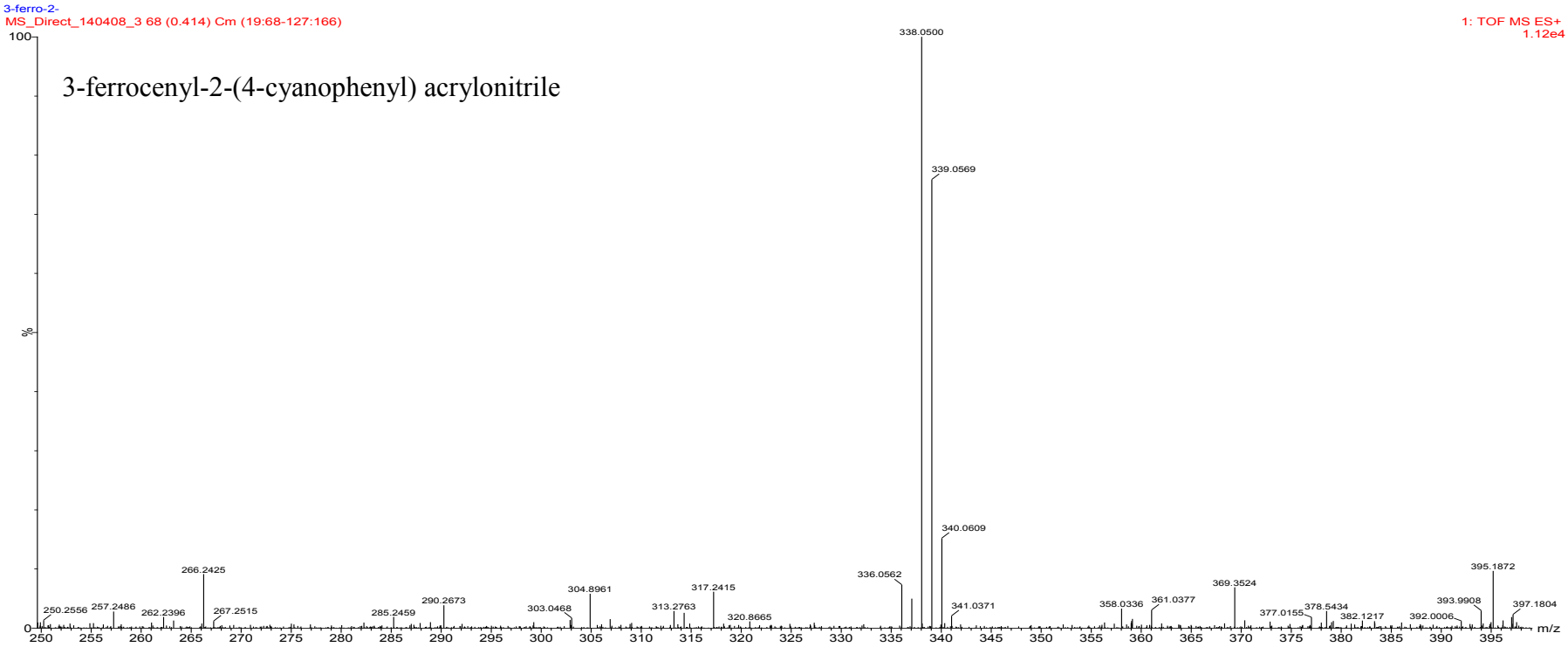


**Supplementary Information S1** HR-MS of 3-ferrocenyl-2-(4-cyanophenyl)acrylonitrile used as the catalyst in synthesis of N-CNTs

**Supplementary Information S2**

Summary of oxygen and nitrogen percentages in acetonitrile solution

| Mass of ethylbenzoate (g) in 10 g of solution | Ethylbenzoate (wt.%) in solution | Moles of oxygen in 10 g of solution | Oxygen (wt.%) in acetonitrile solution | Moles of nitrogen in 10 g of solution | nitrogen (wt.%) in acetonitrile solution |
|---|---|---|---|---|---|
| 0 | 0 | 0 | 0 | 0.239 | 33.5 |
| 0.50 | 5 | 0.009 | 1 | 0.226 | 31.7 |
| 1.00 | 10 | 0.018 | 2 | 0.211 | 29.6 |
| 1.50 | 15 | 0.027 | 3 | 0.202 | 28.3 |
| 2.00 | 20 | 0.036 | 4 | 0.190 | 26.6 |
| 2.50 | 25 | 0.044 | 5 | 0.178 | 24.9 |
| 3.00 | 30 | 0.053 | 6 | 0.166 | 23.2 |

**Supplementary Information S3**

Effect of oxygen on the yield of N-CNTs synthesized by using acetonitrile at 850 °C and 3-ferrocenyl-2-(4-cyanophenyl)acrylonitrile as the catalyst

| wt.% oxygen | N-CNTs yield (mg) |
|---|---|
| 0 | 140.1 |
| 1 | 130.5 |
| 2 | 120.7 |
| 3 | 118.2 |
| 4 | 102.4 |
| 5 | 96.6 |

**Supplementary Information S4**

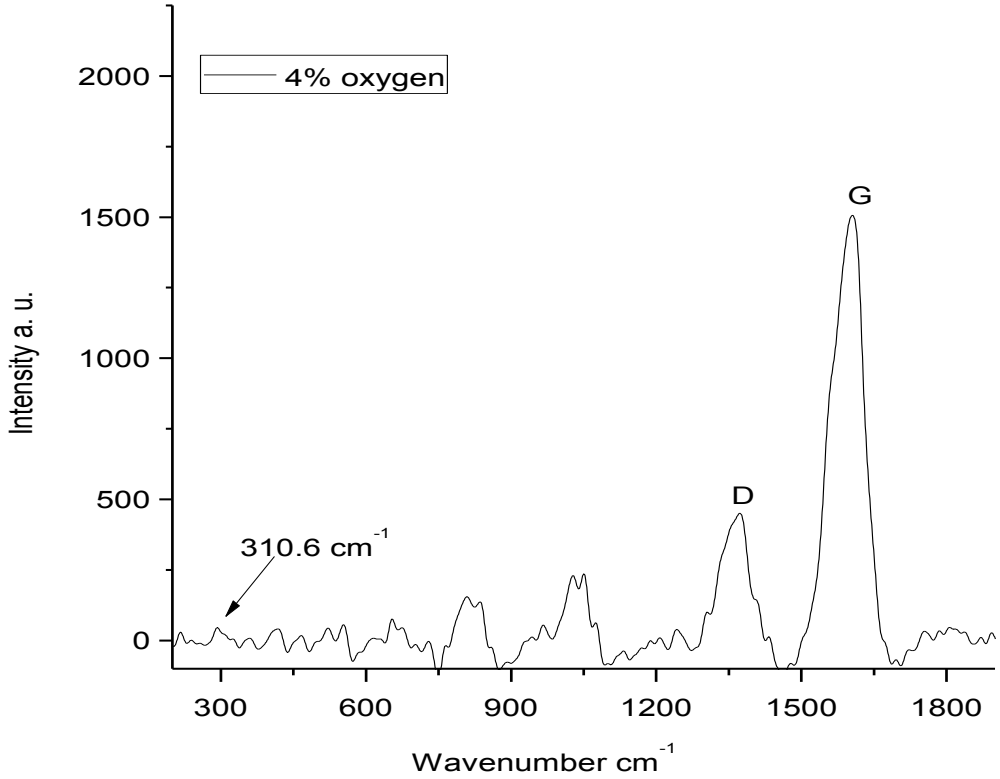


**Supplementary Information S4:** Raman spectra of N-CNTs synthesized by using 4 wt.% of oxygen in acetonitrile at 850 °C and 3-ferrocenyl-2-(4-cyanophenyl)acrylonitrile as the catalyst

# APPENDIX 3: Supporting Information for Chapter Six

## Pyrrolic nitrogen-doped carbon nanotubes: Physicochemical properties, interactions with Pd and their role in the selective hydrogenation of nitrobenzophenone

Lucy M. Ombaka, Patrick G. Ndungu and Vincent O. Nyamori*
School of Chemistry and Physics, University of KwaZulu-Natal, Westville Campus, Private Bag X54001, Durban, 4000, South Africa

### Supporting Information S1

### Materials used to synthesize 3-ferrocenyl-2-(4-cyanophenyl)acrylonitrile and the synthetic procedure

Ferrocenecarboxaldehyde 98%, 4-cyanophenylacetonitrile 97%, piperidine 99%, diethyl ether 99.8% and hexane 97% were purchased from Sigma Aldrich. All reagents and solvents were of analytical grade and were used as received from the suppliers. Aluminium-backed silica gel 60 $F_{254}$ plates purchased from Merck were used to carry out thin layer chromatography in solvents of varying polarity. Column chromatography was accomplished by using Merck silica gel 60, 0.063-0.2 mm.

The catalyst, 3-ferrocenyl-2-(4-cyanophenyl)acrylonitrile, was synthesized *via* a mechanochemical approach under solvent-free conditions following the procedure outlined by Imrie *et al*. Ferrocenecarboxaldehyde (200.0 mg, 0.93 mmol) and 4-cyanophenyl-acetonitrile (132.0 mg, 0.93 mmol) were ground together in the presence of 2 drops of piperidine to yield a maroon paste. The paste was first dried in air, then under vacuum to obtain a maroon product. The maroon product was purified by means of column chromatography on silica gel with a solvent system of (1:1) hexane/diethyl ether to obtain 3-ferrocenyl-2-(4-cyanophenyl)acrylonitrile as dark red crystals. Yield (311.0 mg; yield of 98%); m. p. 139 ºC (lit [Imrie *et al*]: 140 ºC). IR ($cm^{-1}$) 3099, 3050, 2943, 2225, 2207, 1609, 1585, 1452, 1408, 1367, 1312, 1252, 1178, 1103, 1032, 998, 920, 833, 826, 543, 501, 487, 432; $^{1}$H-NMR (ppm) in $CDCl_3$: 7.68 (4H, s, ArH), 7.50 (1H, s, CH), 4.99 (2H, t, *J* 1.9, $C_5H_4$), 4.61 (2H, t, *J* 1.8, $C_5H_4$), 4.24 (5H, s, $C_5H_5$); $^{13}$C-NMR (ppm) in $CDCl_3$ 132.85, 125.45, 146.60, 139.12, 118.56, 118.34, 111.36, 104.52, 77.18, 72.56, 70.68, 70.10. MS ($C_{20}H_{14}FeN_2$) ES: $[M]^+$ *m/z* calcd 338.050638, found 338.0500.

## Conditions for GC-FID and GC-MS analysis

Quantitative analysis of nitrobenzophenone (NBP) and aminobenzophenone (ABP) was conducted on the GC-FID. The GC-FID was fitted with a SGE BP X5 column (0.25 mm inner diameter, 30 m length, 0.25 μM film thickness). The carrier gas used was nitrogen and it was pumped at a flow rate of 30.0 mL $min^{-1}$. The oven temperature used for NBP and ABP analysis was 250 °C. A splitless injection mode was used, and for each analysis 3 μL of the quenched product was injected at a temperature of 110 °C. The identity of NBP and ABP were determined by comparing their retention times with that of purchased commercial samples used as external standards. The integrated peak areas of each sample were used to determine the concentration of NBP and ABP at different time intervals. The calibration range used for both NBP and ABP was 5, 20, 40, 80 and 100 ppm. The NBP calibration curve had an $R^2$ value of 0.9884, while the ABP calibration curve had an $R^2$ value of 0.9981. Further qualitative analysis of the hydrogenation product was conducted on the GC-MS. The GC-MS was fitted with an InertCap 5MS/Sil column (0.25 mm inner diameter, 30 m length, 0.25 μM film thicknesses). The carrier gas used was helium and it was pumped at a flow rate of 30.0 mL $min^{-1}$. The oven temperature used for NBP and ABP analysis was 250 °C. A splitless injection mode was used, for each analysis, 1 μL of the quenched product was injected at a temperature of 110 °C. The identity of NBP and ABP was determined by comparing their masses with the hit-targets obtained from the mass spectrometer library.

## ICP-OES analysis

Triplicate analyses were performed for each catalyst. For all analyses, an external standard was used to create a calibration line ($R^2$ = 0.994). The calibration standards used were prepared in nitric acid solutions at concentrations of 0, 20, 40, 60 and 100 ppm from a palladium ICP-OES standard stock solution (Johnson Matthey, prepared in South Africa, guaranteed to be 1000 ppm ± 0.2% Pd in 0.5 M $HNO_3$). For each ICP-OES measurements, three measurements were conducted. The results were analysed using a Perkin Elmer WinLab 32 software.

**Raman analysis**

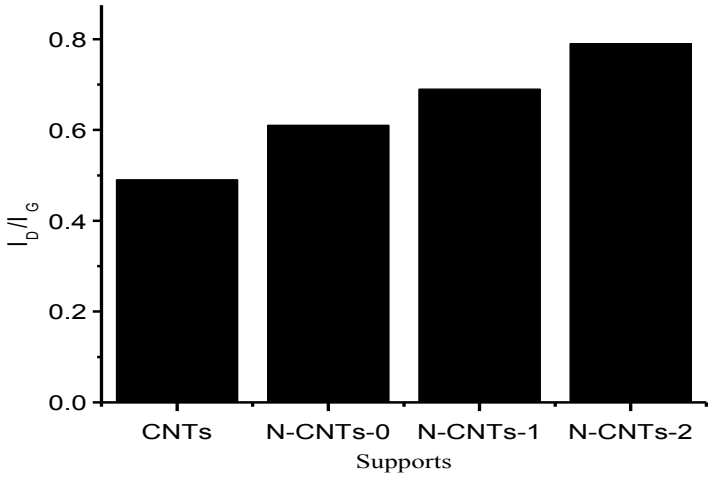


Figure S1: $I_D/I_G$ ratios of N-CNTs and CNTs: Note the higher ratios indicate more disordered materials

**Supporting Information S2**

Table S2. Summary of oxygen and nitrogen percentages in acetonitrile solution used to synthesize N-CNTs.

| Sample | Mass of ethyl benzoate (g) in 10 g of solution | Moles of oxygen in 10 g of solution | Oxygen (%) in acetonitrile solution | Moles of nitrogen in 10 g of solution | nitrogen (%) in acetonitrile solution |
|---|---|---|---|---|---|
| N-CNTs-0 | 0 | 0 | 0 | 0.239 | 33.5 |
| N-CNTs-1 | 0.50 | 0.009 | 1 | 0.226 | 31.7 |
| N-CNTs-2 | 1.00 | 0.018 | 2 | 0.211 | 29.6 |

## Supporting Information S3

### S3 (1). Summary of XPS analysis of all Pd/CNTs and Pd/N-CNTS

| Sample | Element | Atomic Concentration (%) | Binding energy (eV) |
|---|---|---|---|
| Pd/N-CNTs-0 | O | 10.48 | 532 |
| | N | 4.36 | 398.5 (21.43%)<br>400.3 (63.08%)<br>404.1 (15.49%) |
| | Pd | 1.31 | 335 |
| | C | 83.85 | 284 |
| Pd/N-CNTs-1 | O | 8.34 | 532 |
| | N | 3.48 | 398.4 (16.68%)<br>400.6 (72.87%)<br>404.7 (10.46%) |
| | Pd | 0.67 | 336 |
| | C | 87.51 | 284 |
| Pd/N-CNTs-2 | O | 13.46 | 534 |
| | N | 2.53 | 398.4 (11.64%)<br>400.3 (80.37%)<br>405.1 (7.98%) |
| | Pd | 0.94 | 337 |
| | C | 83.07 | 285 |
| Pd/CNTs | O | 6.66 | 532 |
| | Pd | 1.13 | 335 |
| | C | 92.22 | 284 |

**S3(2). XPS analysis of Pd/N-CNTs-0**

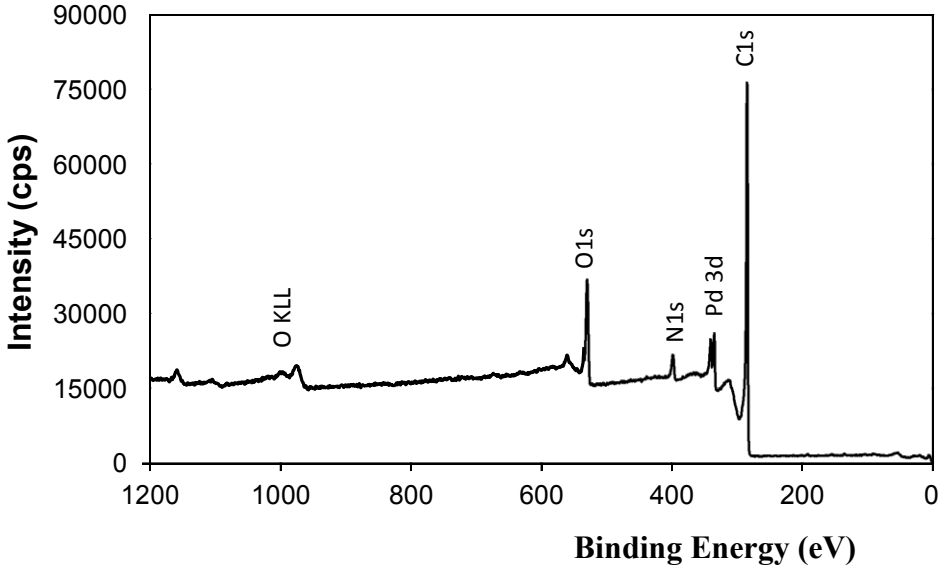


Figure S3 (2a). XPS spectra of Pd/N-CNTs-0

Table S3 (2a). Summary of XPS spectra of Pd/N-CNTs-0

| Peak | Position BE (eV) | FWHM (eV) | Raw Area (cps eV) | RSF | Atomic Mass | Atomic Conc % | Mass Conn % |
|---|---|---|---|---|---|---|---|
| C 1s | 285 | 2.610 | 254430.0 | 0.278 | 12.011 | 83.85 | 73.24 |
| N 1s | 399 | 4.222 | 23168.0 | 0.477 | 14.007 | 4.36 | 4.44 |
| Pd 3d | 335 | 3.291 | 77012.0 | 5.356 | 106.534 | 1.31 | 10.13 |
| O 1s | 532 | 4.082 | 92125 | 0.780 | 15.999 | 10.48 | 73.24 |

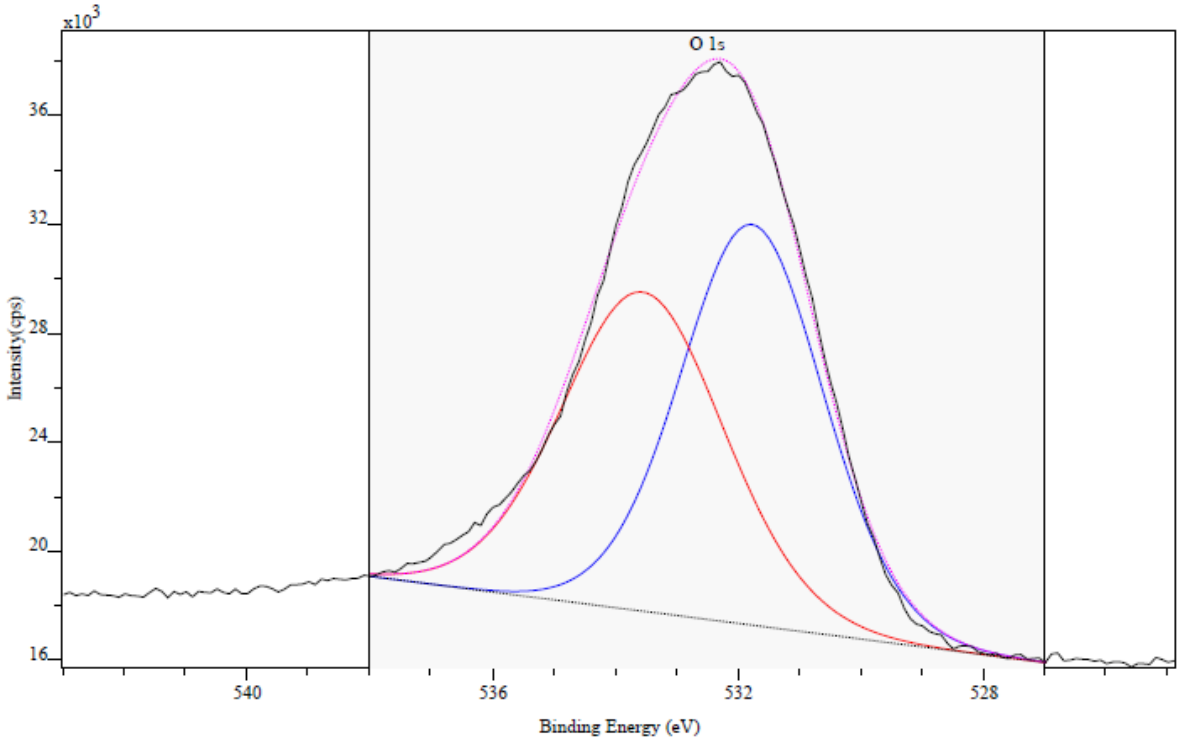


Figure S3 (2b). O 1s spectra of Pd/N-CNTs-0

Table S3 (2b). Summary of O 1s spectra of Pd/N-CNTs-0

| Band | Position BE (eV) | FWHM (ev) | Raw Area (cps eV) | RSF | Atomic Mass | Atomic Conc % | Mass Conc % |
|---|---|---|---|---|---|---|---|
| 1 | 531.883 | 2.817 | 44351.3 | 0.780 | 15.999 | 53.03 | 53.03 |
| 2 | 533.520 | 3.322 | 39294.8 | 0.780 | 15.999 | 46.97 | 46.97 |

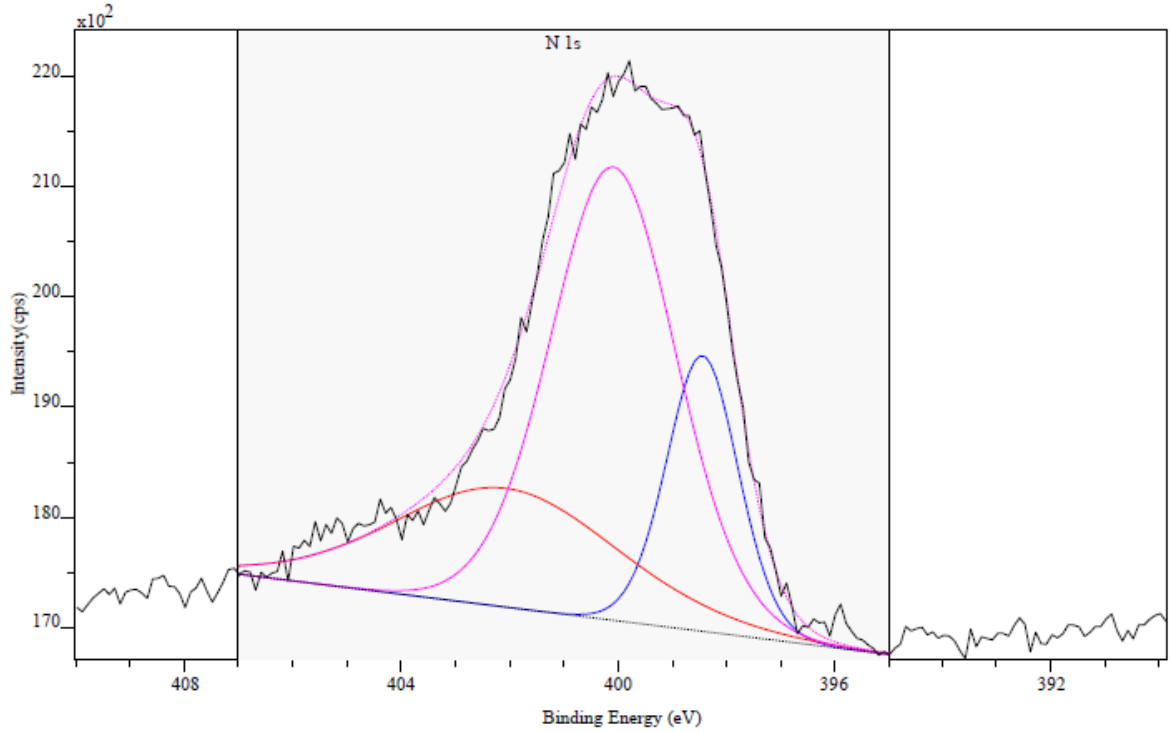


Figure S3 (2c). N 1s spectra of Pd/N-CNTs-0

Table S3 (2c). Summary of N 1s spectra of Pd/N-CNTs-0

| Band | Position BE (eV) | FWHM (ev) | Raw Area (cps eV) | RSF | Atomic Mass | Atomic Conc % | Mass Conc % |
|---|---|---|---|---|---|---|---|
| 1 | 398.512 | 1.687 | 5031.7 | 0.477 | 14.007 | 21.43 | 21.43 |
| 2 | 404.059 | 4.149 | 3636.6 | 0.477 | 14.007 | 15.49 | 15.49 |
| 3 | 400.291 | 2.898 | 14809.6 | 0.477 | 14.007 | 63.08 | 63.08 |

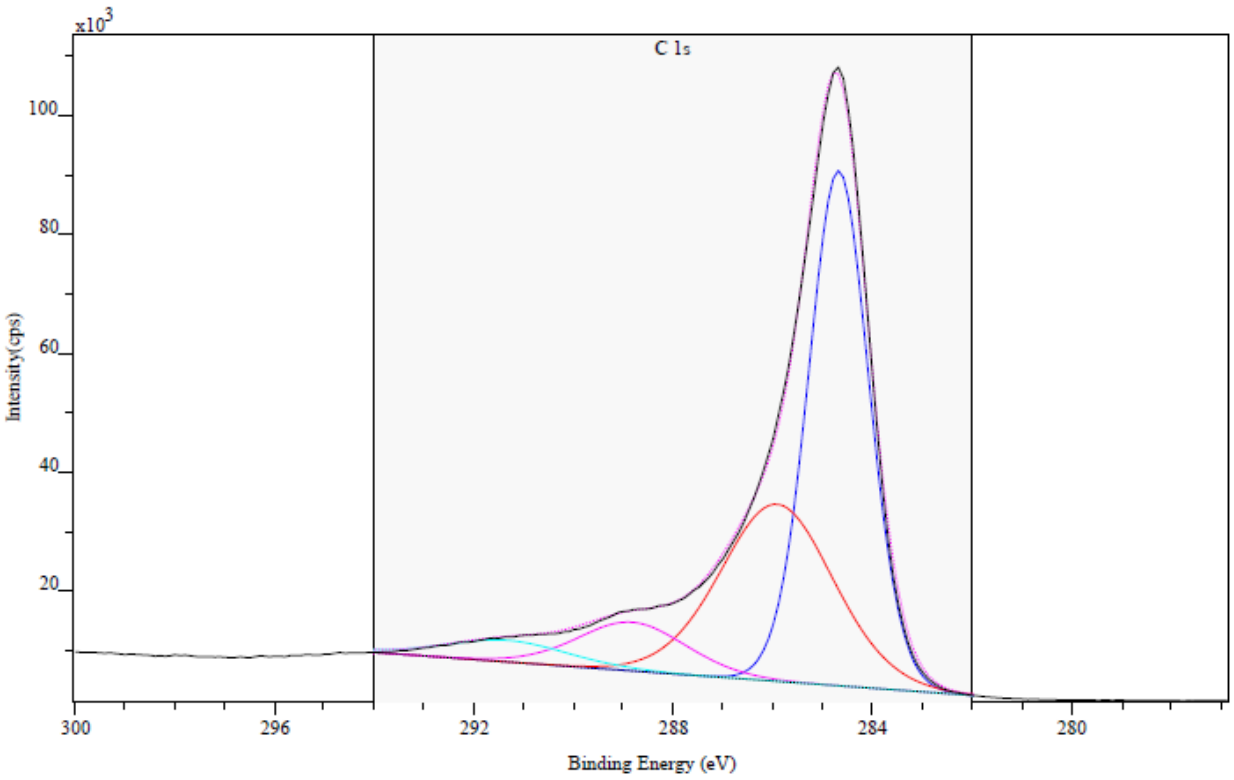


Figure S3 (2d). C 1s spectra of Pd/N-CNTs-0

Table S3 (2d). Summary of C 1s spectra of Pd/N-CNTs-0

| Band | Position BE (eV) | FWHM (ev) | Raw Area (cps eV) | RSF | Atomic Mass | Atomic Conc % | Mass Conc % |
|---|---|---|---|---|---|---|---|
| 1 | 284.683 | 1.400 | 133171.5 | 0.278 | 12.011 | 52.74 | 52.74 |
| 2 | 285.939 | 2.606 | 85347.5 | 0.278 | 12.011 | 33.81 | 33.81 |
| 3 | 288.826 | 2.510 | 22557.5 | 0.278 | 12.011 | 8.94 | 8.94 |
| 4 | 291.336 | 2.860 | 11371.4 | 0.278 | 12.011 | 4.51 | 4.51 |

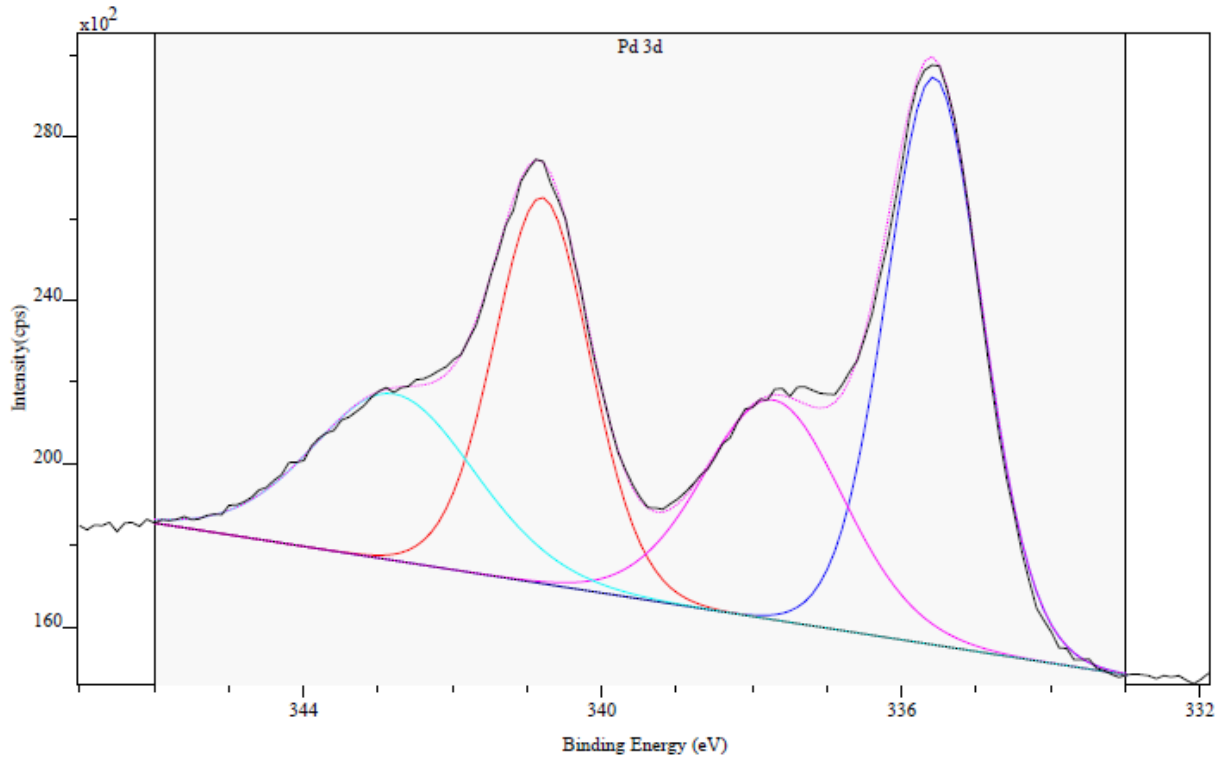


Figure S3 (2e). Pd 3d spectra of Pd/N-CNTs-0

Table S3 (2e). Summary of Pd 3d spectra of Pd/N-CNTs-0

| Band | Position BE (eV) | FWHM (ev) | Raw Area (cps eV) | RSF | Atomic Mass | Atomic Conc % | Mass Conc % |
|---|---|---|---|---|---|---|---|
| 1 | 335.555 | 1.500 | 22918.0 | 5.356 | 106.534 | 36.53 | 36.53 |
| 2 | 340.796 | 1.500 | 15600.5 | 5.356 | 106.534 | 24.83 | 24.83 |
| 3 | 337.746 | 2.178 | 12918.9 | 5.356 | 106.534 | 20.58 | 20.58 |
| 4 | 342.795 | 2.532 | 11353.2 | 5.356 | 106.534 | 18.06 | 18.06 |

**S3(3). XPS spectra of Pd/N-CNTs-1**

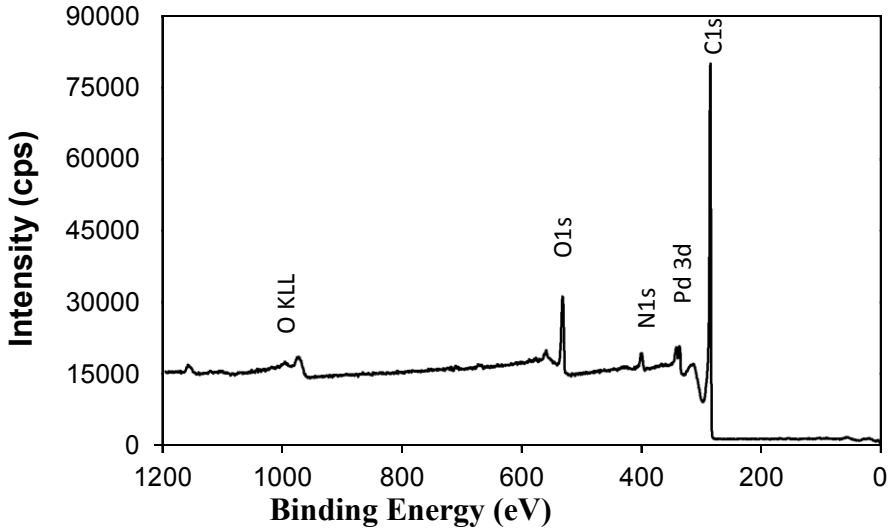


Figure S3 (3a). XPS spectra of Pd/N-CNTs-1

Table S3 (3a). Summary of XPS spectra of Pd/N-CNTs-1

| Peak | Position BE (eV) | FWHM (eV) | Raw Area (cps eV) | RSF | Atomic Mass | Atomic Conc % | Mass Conn % |
|---|---|---|---|---|---|---|---|
| C 1s | 284 | 2.573 | 278652.0 | 0.278 | 12.011 | 87.51 | 80.53 |
| N 1s | 400 | 4.944 | 19421.0 | 0.477 | 14.007 | 3.48 | 3.74 |
| Pd 3d | 336 | 4.460 | 41703.0 | 5.356 | 106.534 | 0.67 | 5.51 |
| O 1s | 532 | 4.646 | 76876.0 | 0.780 | 15.999 | 8.34 | 10.22 |

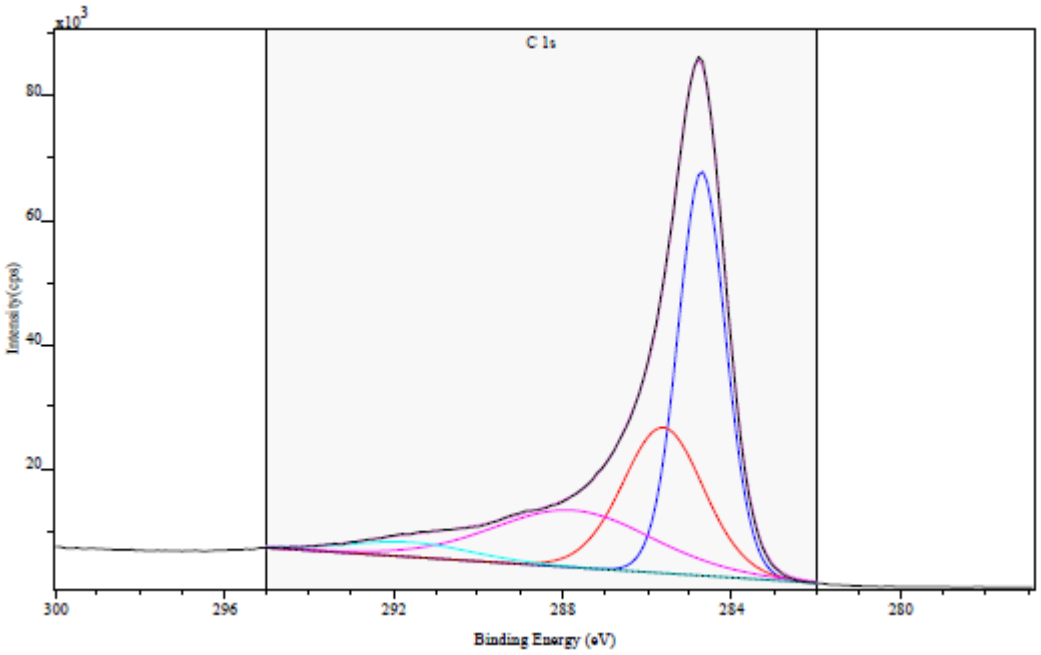


Figure S3 (3b). C 1s spectra of Pd/N-CNTs-1

Table S3 (3b). Summary of C 1s spectra of Pd/N-CNTs-1

| Band | Position BE (eV) | FWHM (ev) | Raw Area (cps eV) | RSF | Atomic Mass | Atomic Conc % | Mass Conc % |
|---|---|---|---|---|---|---|---|
| 1 | 284.743 | 1.297 | 92897.4 | 0.278 | 12.011 | 45.87 | 45.87 |
| 2 | 285.625 | 2.213 | 56818.4 | 0.278 | 12.011 | 28.06 | 28.06 |
| 3 | 287.777 | 4.371 | 43967.5 | 0.278 | 12.011 | 21.73 | 21.73 |
| 4 | 291.599 | 3.391 | 8777.8 | 0.278 | 12.011 | 4.34 | 4.34 |

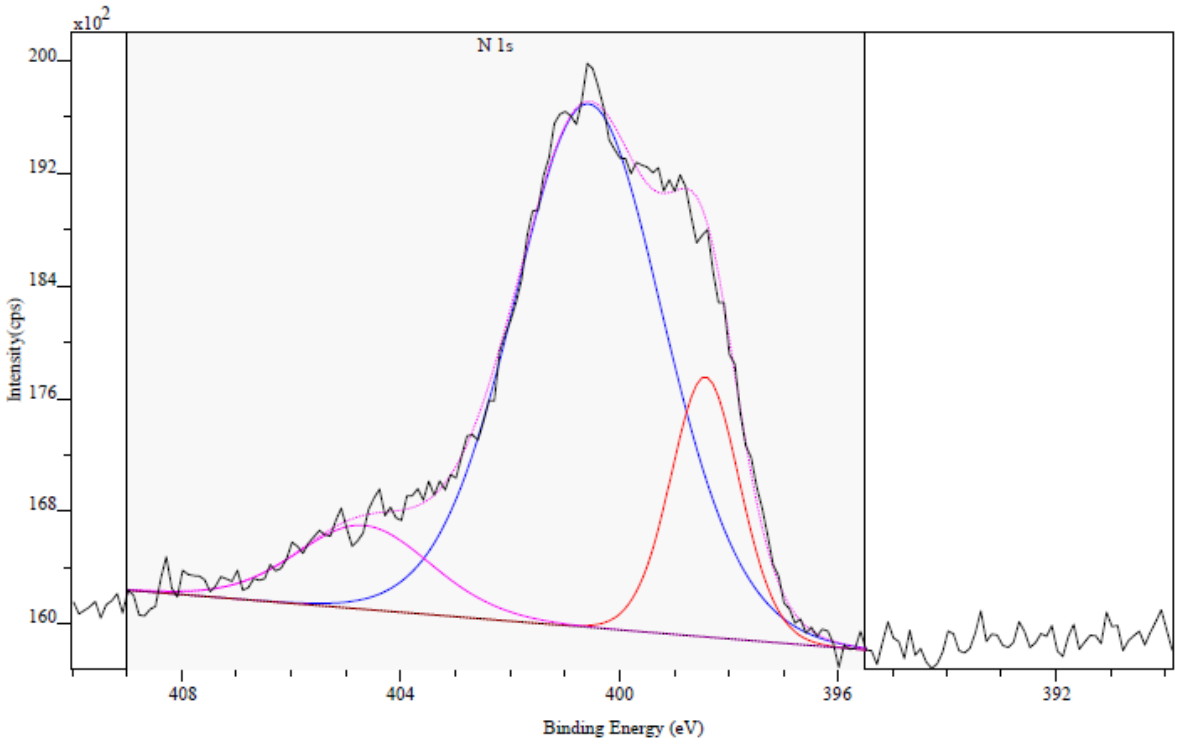


Figure S3 (3c). N 1s spectra of Pd/N-CNTs-1

Table S3 (3c). Summary of N 1s spectra of Pd/N-CNTs-1

| Band | Position BE (eV) | FWHM (ev) | Raw Area (cps eV) | RSF | Atomic Mass | Atomic Conc % | Mass Conc % |
|---|---|---|---|---|---|---|---|
| 1 | 400.595 | 3.182 | 12996.5 | 0.477 | 14.007 | 72.87 | 72.87 |
| 2 | 398.416 | 1.471 | 2974.7 | 0.477 | 14.007 | 16.68 | 16.68 |
| 3 | 404.712 | 2.854 | 1864.9 | 0.477 | 14.007 | 10.46 | 10.46 |

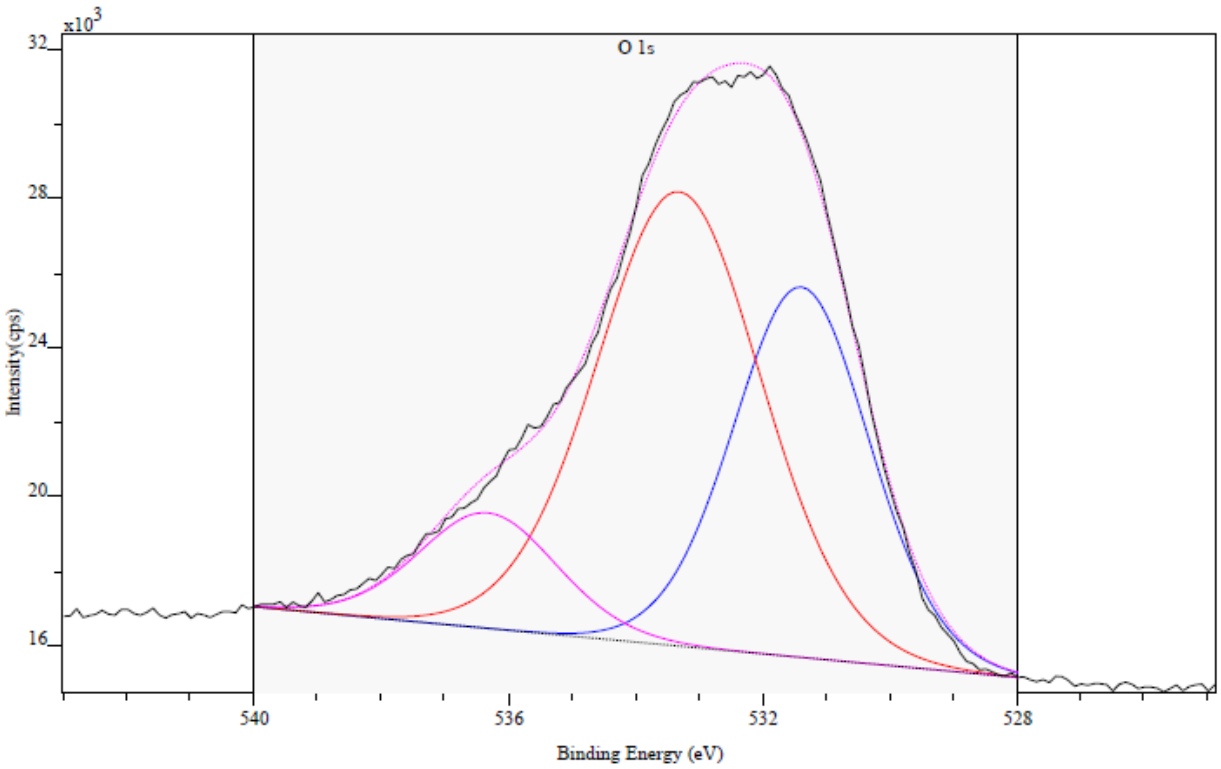


Figure S3 (3d). O 1s spectra of Pd/N-CNTs-1

Table S3 (3d). Summary of O 1s spectra of Pd/N-CNTs-1

| Band | Position BE (eV) | FWHM (ev) | Raw Area (cps eV) | RSF | Atomic Mass | Atomic Conc % | Mass Conc % |
|---|---|---|---|---|---|---|---|
| 1 | 531.393 | 2.487 | 27160.2 | 0.780 | 15.999 | 35.68 | 35.68 |
| 2 | 533.329 | 3.017 | 40417.0 | 0.780 | 15.999 | 53.08 | 53.08 |
| 3 | 536.334 | 2.516 | 8564.2 | 0.780 | 15.999 | 11.24 | 11.24 |

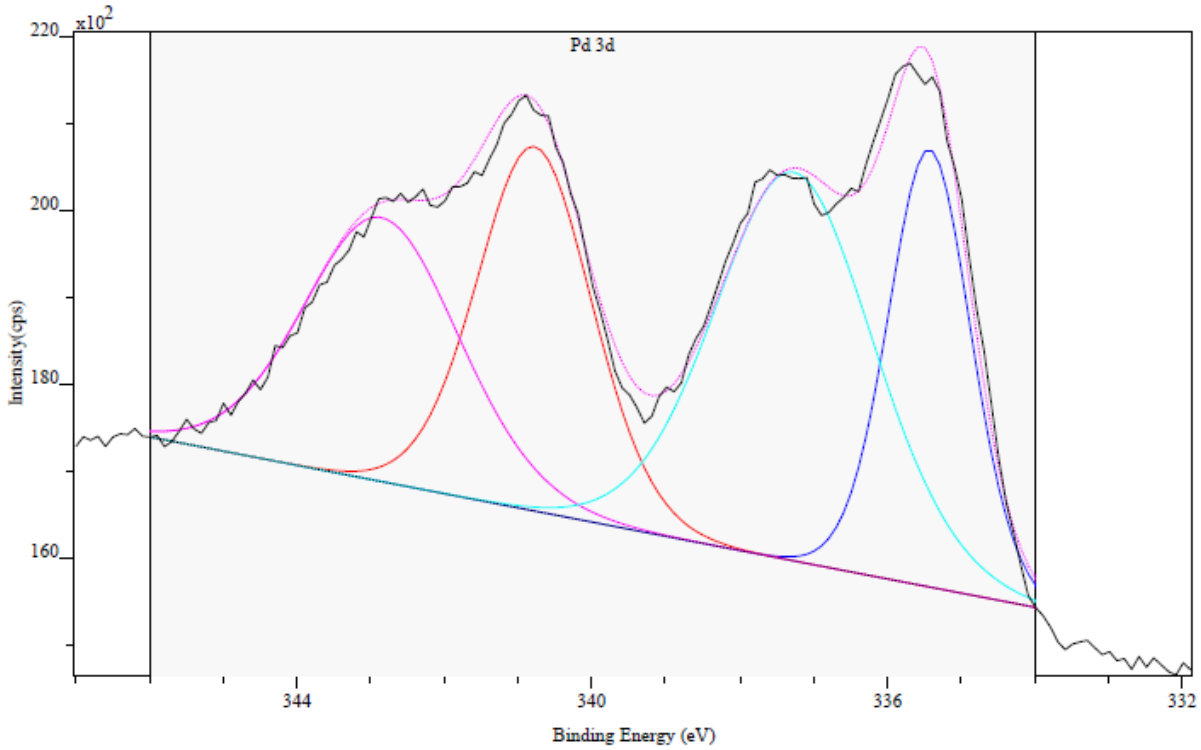


Figure S3 (3e). Pd 3d spectra of Pd/N-CNTs-1

Table S3 (3e). Summary of Pd 3d spectra of Pd/N-CNTs-1

| Band | Position BE (eV) | FWHM (ev) | Raw Area (cps eV) | RSF | Atomic Mass | Atomic Conc % | Mass Conc % |
|---|---|---|---|---|---|---|---|
| 1 | 335.435 | 1.300 | 7198.1 | 5.356 | 106.534 | 20.01 | 20.01 |
| 2 | 340.779 | 1.810 | 8332.6 | 5.356 | 106.534 | 23.13 | 23.13 |
| 3 | 342.848 | 2.458 | 8193.3 | 5.356 | 106.534 | 22.73 | 22.73 |
| 4 | 337.289 | 2.499 | 12289.0 | 5.356 | 106.534 | 34.14 | 34.14 |

**S3(4). XPS spectra of Pd/N-CNTs-2**

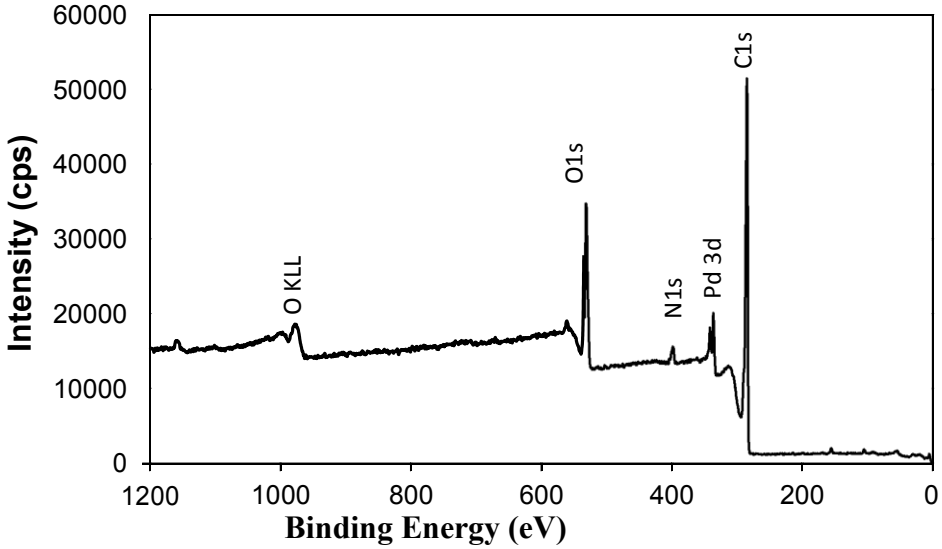


Figure S3 (4a). XPS spectra of Pd/N-CNTs-2

Table S3 (4a). Summary of XPS spectra of Pd/N-CNTs-2

| Peak | Position BE (eV) | FWHM (eV) | Raw Area (cps eV) | RSF | Atomic Mass | Atomic Conc % | Mass Conn % |
|---|---|---|---|---|---|---|---|
| C 1s | 285 | 3.653 | 209690.0 | 0.278 | 12.011 | 83.07 | 73.96 |
| N 1s | 399 | 4.828 | 10807.0 | 0.477 | 14.007 | 2.53 | 2.62 |
| Pd 3d | 337 | 2.678 | 44772.0 | 5.356 | 106.534 | 0.94 | 7.46 |
| O 1s | 532 | 4.082 | 92125.0 | 0.780 | 15.999 | 10.48 | 10.22 |

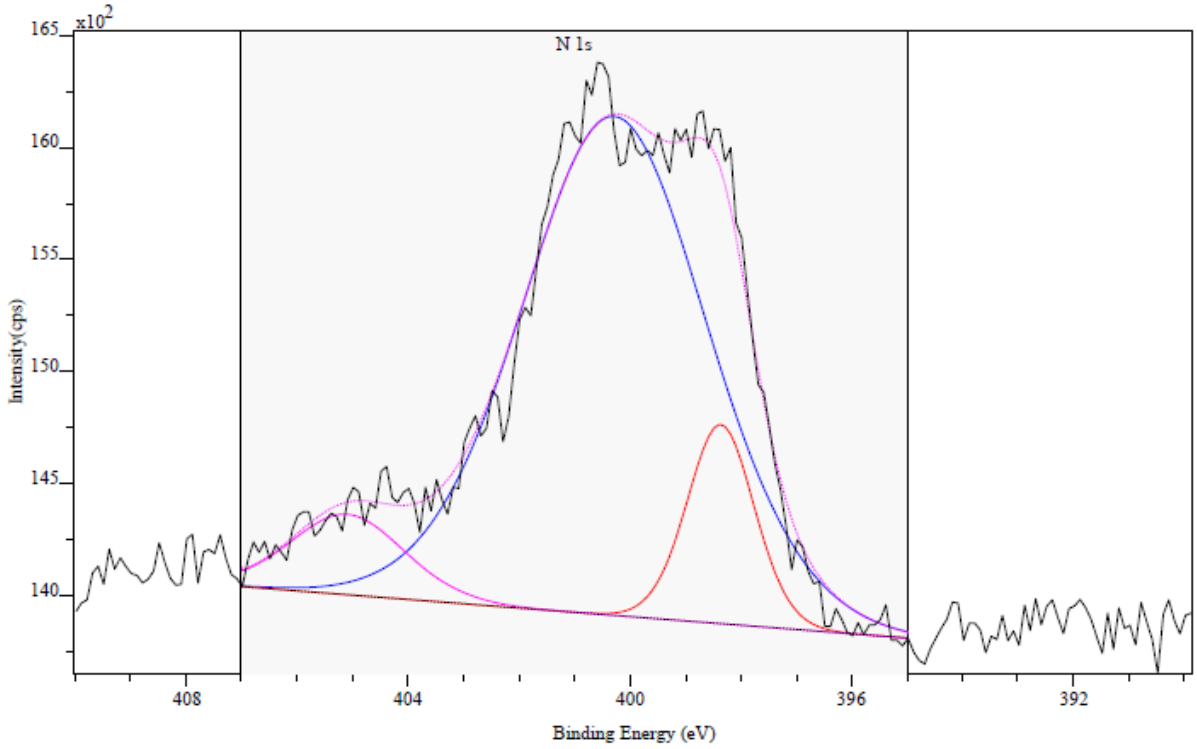


Figure S3 (4b). N 1s spectra of Pd/N-CNTs-2

Table S3 (4b). Summary of N 1s spectra of Pd/N-CNTs-2

| Band | Position | FWHM | Raw Area | RSF | Atomic | Atomic | Mass |
|---|---|---|---|---|---|---|---|
| 1 | 400.312 | 3.859 | 9431.7 | 0.477 | 14.007 | 80.37 | 80.37 |
| 2 | 398.387 | 1.397 | 1366.6 | 0.477 | 14.007 | 11.64 | 11.64 |
| 3 | 405.125 | 2.377 | 936.7 | 0.477 | 14.007 | 7.98 | 7.98 |

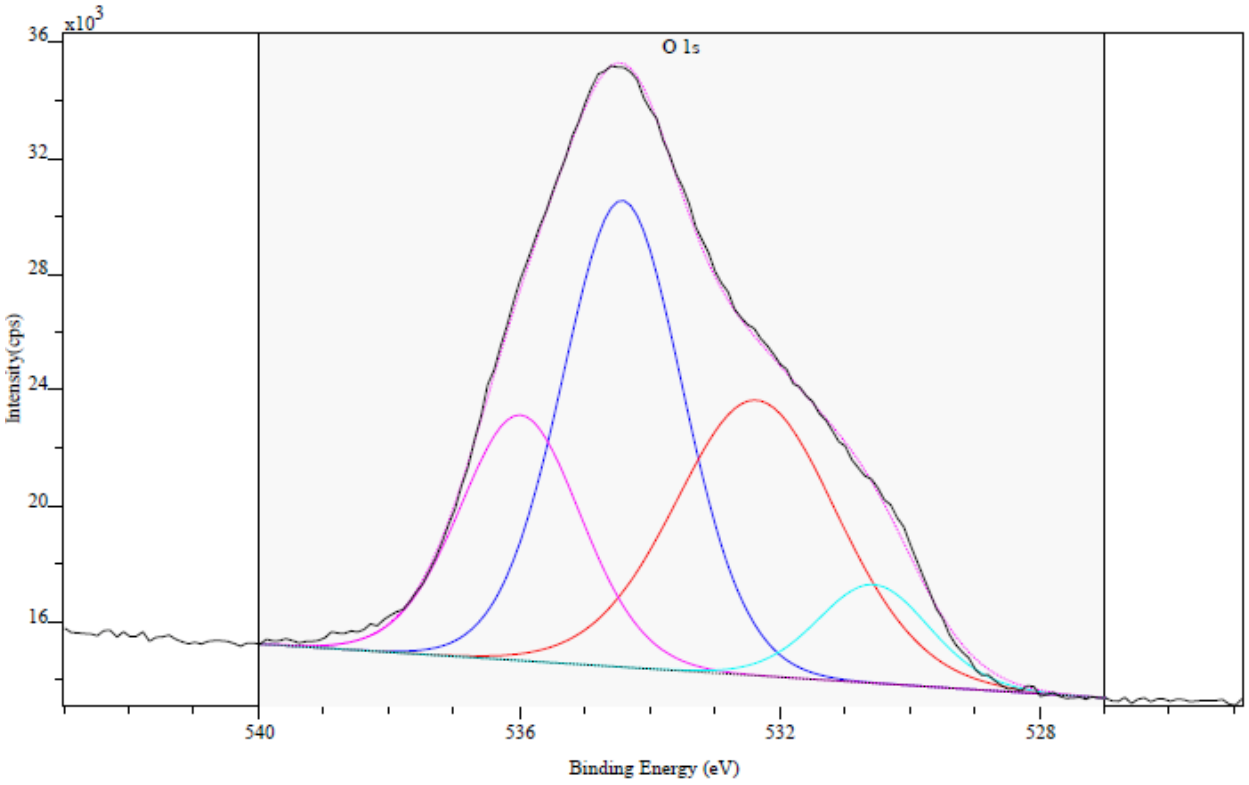


Figure S3 (4c). O 1s spectra of Pd/N-CNTs-2

Table S3 (4c). Summary of O 1s spectra of Pd/N-CNTs-2

| Band | Position BE (eV) | FWHM(eV) | Raw Area (cps eV) | RSF | Atomic Mass | Atomic Conc % | Mass Conc |
|---|---|---|---|---|---|---|---|
| 1 | 534.431 | 2.165 | 38249.0 | 0.780 | 15.999 | 39.77 | 39.77 |
| 2 | 532.370 | 2.911 | 30330.1 | 0.780 | 15.999 | 31.55 | 31.55 |
| 3 | 536.000 | 2.165 | 20134.2 | 0.780 | 15.999 | 20.93 | 20.93 |
| 4 | 530.559 | 2.000 | 7454.0 | 0.780 | 15.999 | 7.75 | 7.75 |

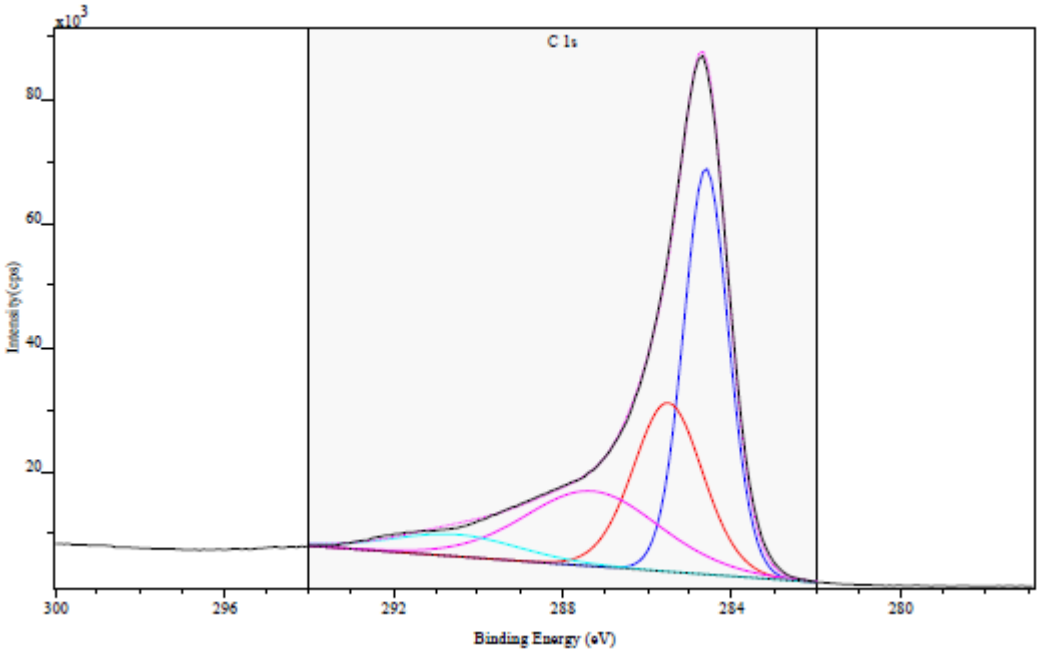


Figure S3 (4d). C 1s spectra of Pd/N-CNTs-2

Table S3 (4d). Summary of C 1s spectra of Pd/N-CNTs-2

| Band | Position BE (eV) | FWHM (ev) | Raw Area (cps eV) | RSF | Atomic Mass | Atomic Conc % | Mass Conc % |
|---|---|---|---|---|---|---|---|
| 1 | 284.626 | 1.231 | 88666.3 | 0.278 | 12.011 | 42.62 | 42.62 |
| 2 | 285.524 | 1.900 | 56800.8 | 0.278 | 12.011 | 27.31 | 27.31 |
| 3 | 287.319 | 3.687 | 48917.9 | 0.278 | 12.011 | 23.53 | 23.53 |
| 4 | 290.561 | 3.500 | 13561.4 | 0.278 | 12.011 | 6.53 | 6.53 |

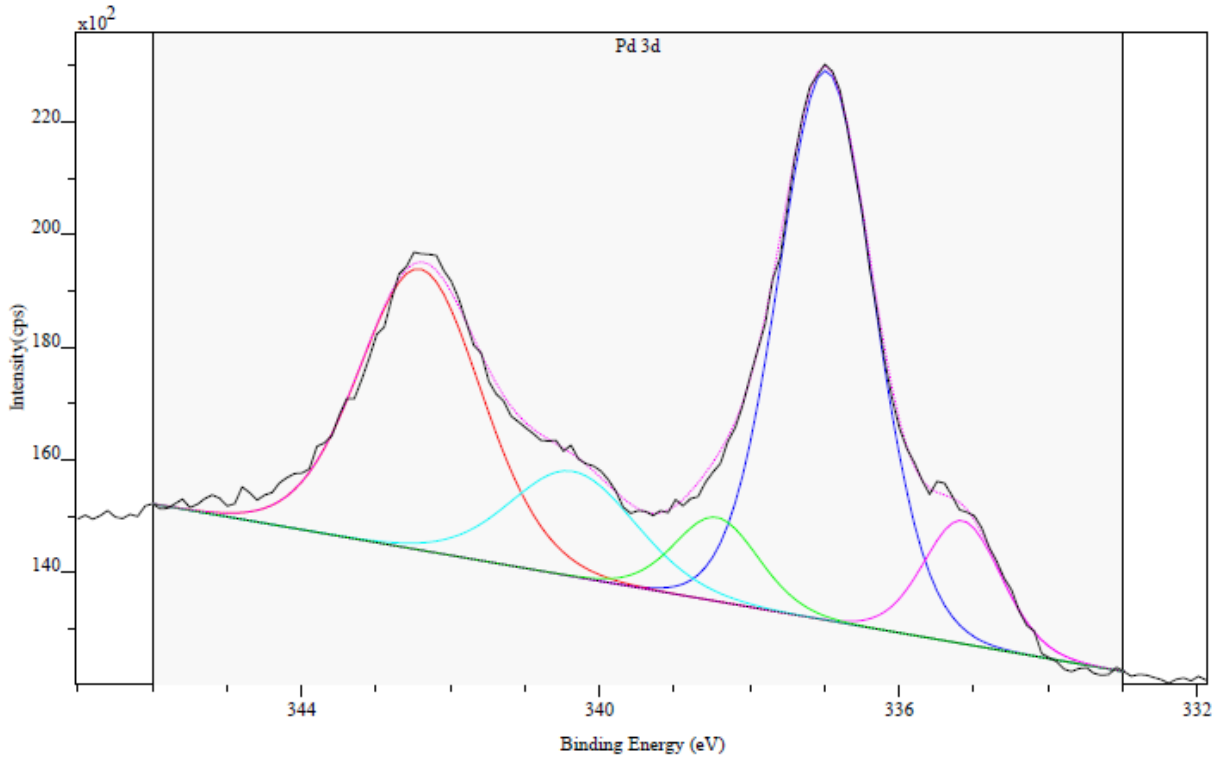


Figure S3 (4e). Pd 3d spectra of Pd/N-CNTs-2

Table S3 (4e). Summary of Pd 3d spectra of Pd/N-CNTs-2

| Band | Position BE (eV) | FWHM (ev) | Raw Area (cps eV) | RSF | Atomic Mass | Atomic Conc % | Mass Conc % |
|---|---|---|---|---|---|---|---|
| 1 | 336.966 | 1.500 | 16093.2 | 5.356 | 106.534 | 45.29 | 45.29 |
| 2 | 342.409 | 1.902 | 10429.3 | 5.356 | 106.534 | 29.30 | 29.30 |
| 3 | 335.166 | 1.200 | 2897.6 | 5.356 | 106.534 | 8.16 | 8.16 |
| 4 | 340.372 | 1.953 | 4010.6 | 5.356 | 106.534 | 11.27 | 11.27 |
| 5 | 338.455 | 1.291 | 2125.9 | 5.356 | 106.534 | 5.98 | 5.98 |

**S3(5). XPS spectra of Pd/CNTs**

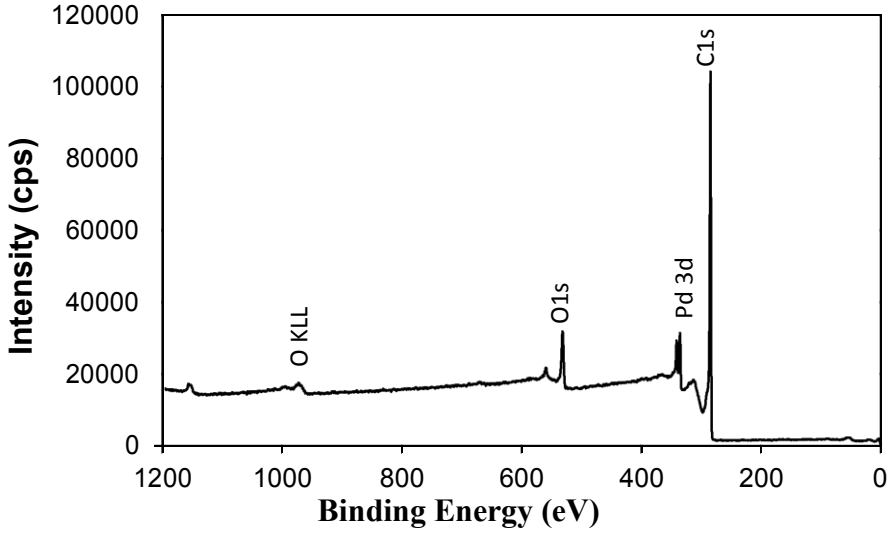


Figure S3 (5a). XPS spectra of Pd/CNTs

Table S3 (5a). Summary of XPS spectra of Pd/CNTs

| Peak | Position BE (eV) | FWHM (eV) | Raw Area (cps eV) | RSF | Atomic Mass | Atomic Conc % | Mass Conn % |
|---|---|---|---|---|---|---|---|
| C 1s | 284 | 2.144 | 293844.0 | 0.278 | 12.011 | 92.22 | 83.03 |
| Pd 3d | 335 | 2.383 | 69642.0 | 5.356 | 106.534 | 1.13 | 8.99 |
| O 1s | 532 | 3.860 | 61397.0 | 0.780 | 15.999 | 6.66 | 7.98 |

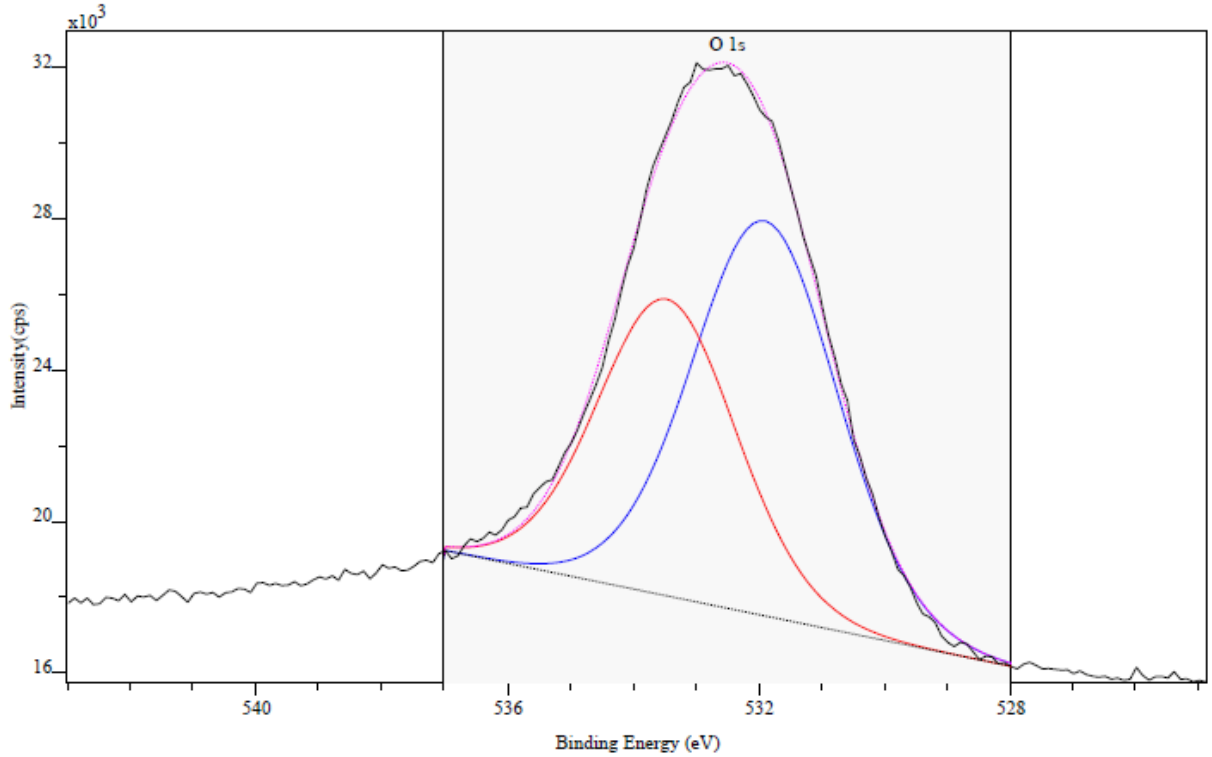


Figure S3 (5b). O 1s spectra of Pd/CNTs

Table S3 (5b). Summary of O 1s spectra of Pd/CNTs

| Band | Position BE (eV) | FWHM (ev) | Raw Area (cps eV) | RSF | Atomic Mass | Atomic Conc % | Mass Conc % |
|---|---|---|---|---|---|---|---|
| 1 | 531.925 | 2.690 | 30860.6 | 0.780 | 15.999 | 58.24 | 58.24 |
| 2 | 533.486 | 2.568 | 22129.1 | 0.780 | 15.999 | 41.76 | 41.76 |

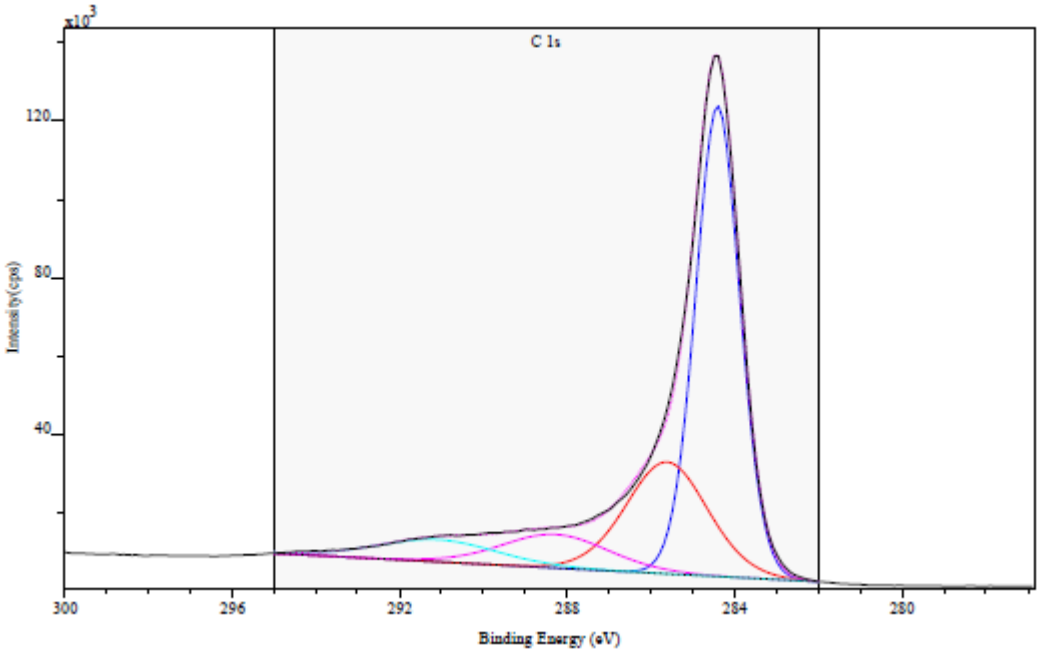


Figure S3 (5c). C 1s spectra of Pd/CNTs

Table S3 (5c). Summary of C 1s spectra of Pd/CNTs

| Band | Position BE (eV) | FWHM (ev) | Raw Area (cps eV) | RSF | Atomic Mass | Atomic Conc % | Mass Conc % |
|---|---|---|---|---|---|---|---|
| 1 | 284.418 | 1.208 | 159796.3 | 0.278 | 12.011 | 57.48 | 57.48 |
| 2 | 285.627 | 2.235 | 69976.4 | 0.278 | 12.011 | 25.18 | 25.18 |
| 3 | 288.298 | 2.948 | 27689.2 | 0.278 | 12.011 | 9.97 | 9.97 |
| 4 | 291.105 | 3.301 | 20465.8 | 0.278 | 12.011 | 7.37 | 7.37 |

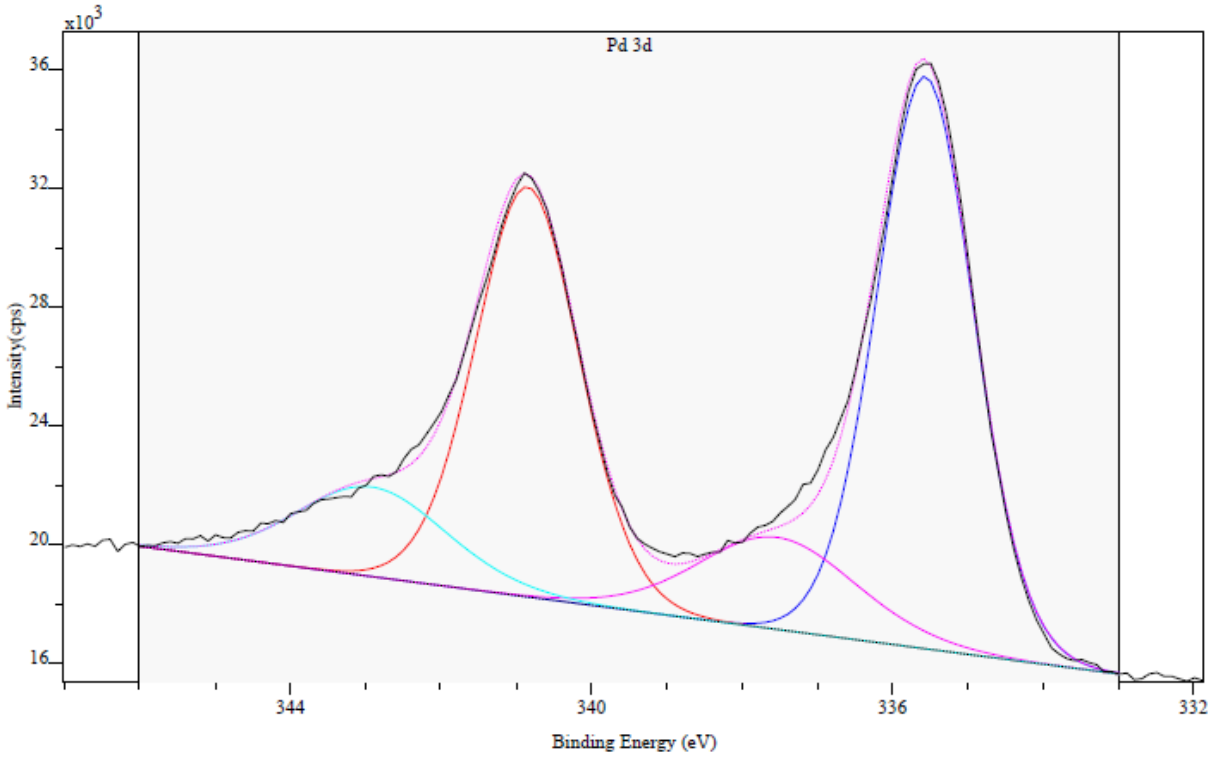


Figure S3 (5d). Pd 3d spectra of Pd/CNTs

Table S3 (5d). Summary of Pd 3d spectra of Pd/CNTs

| Band | Position BE (eV) | FWHM (ev) | Raw Area (cps eV) | RSF | Atomic Mass | Atomic Conc % | Mass Conc % |
|---|---|---|---|---|---|---|---|
| 1 | 335.561 | 1.500 | 31746.3 | 5.356 | 106.534 | 44.11 | 44.11 |
| 2 | 340.882 | 1.600 | 24318.1 | 5.356 | 106.534 | 33.74 | 33.74 |
| 3 | 337.564 | 2.437 | 8300.4 | 5.356 | 106.534 | 11.53 | 11.53 |
| 4 | 342.957 | 2.307 | 7658.1 | 5.356 | 106.534 | 10.62 | 10.62 |

## Supporting Information S4

### O 1s analysis

The O 1s spectra of N-CNTs and CNTs exhibited broad peaks between 531-536 eV as depicted in Figure S4 (1). Deconvolution of these broad peaks revealed that N-CNTs-1 and N-CNTs-2 had an extra peak at 536.0-536.3 eV coded as O1, which was assigned to oxygen present in esters (Supporting Information S3). Increase in the quantity of C3 directly correlated with the increase of O1 (Table 1). Since both species were only present in N-CNTs-1 and N-CNTs-2, it is possible that they originated from the same compound present in N-CNTs-1 and N-CNTs-2 alone. This compound was possibly a lactone because, C3 was assigned to carbonyls in quinones, lactones or ketones and O1 was ascribed to oxygen in esters. Lactones have been known to be introduced into N-CNTs and CNTs by acid treatment with nitric acid.[14] However, in this case, a similar procedure was used in the acid treatment of all supports; therefore, the possibility of introducing lactone groups in N-CNTs-1 and N-CNTs-2 by only acid treatment was ruled out. Thus, we propose that the lactones originated from the reaction between oxygen present in ethylbenzoate and hydrocarbons present in the synthesis precursors.

**Table S4 (1).** Summary of C 1s and O 1s XPS spectra of Pd/N-CNTs and Pd/CNTs.

| Sample | C at.% | | | | O at.% | |
|---|---|---|---|---|---|---|
| | C1 | C2 | C3 | C4 | O Total | O1 |
| Pd/N-CNTs-0 | 52.7 | 33.8 | - | 8.9 | 10.4 | - |
| Pd/N-CNTs-1 | 45.9 | 28.6 | 21.7 | - | 8.3 | 11.2 |
| Pd/N-CNTs-2 | 42.4 | 27.3 | 23.5 | - | 13.5 | 20.9 |
| Pd/CNTs | 57.4 | 25.1 | - | 10.0 | 6.6 | - |

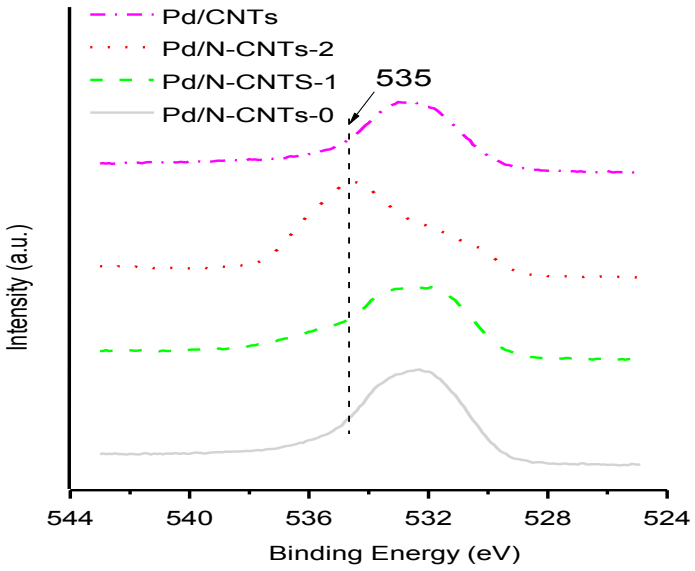


**Figure S4 (1).** O 1s XPS spectra of CNTs and N-CNTs synthesized by using 0-2 wt.% oxygen in acetonitrile.

**$N_2$-adsoption-desortion analysis**

**Table S4 (2).** Textural properties of as-synthesized and purified supports.

| Support | SA of as-synthesized support ($m^2g^{-1}$) | SA of purified support ($m^2g^{-1}$) | Pore size distribution of as-synthesized support (nm) | Pore size distribution of purified support (nm) |
|---|---|---|---|---|
| CNTs | 14 | 40 | 2.8 | 4.1 |
| N-CNTs-0 | 24 | 38 | 3.8 | 4.5 |
| N-CNTs-1 | 14 | 64 | 3.9 | 4.1 |
| N-CNTs-2 | 15 | 33 | 3.9 | 4.1 |

SA: surface area

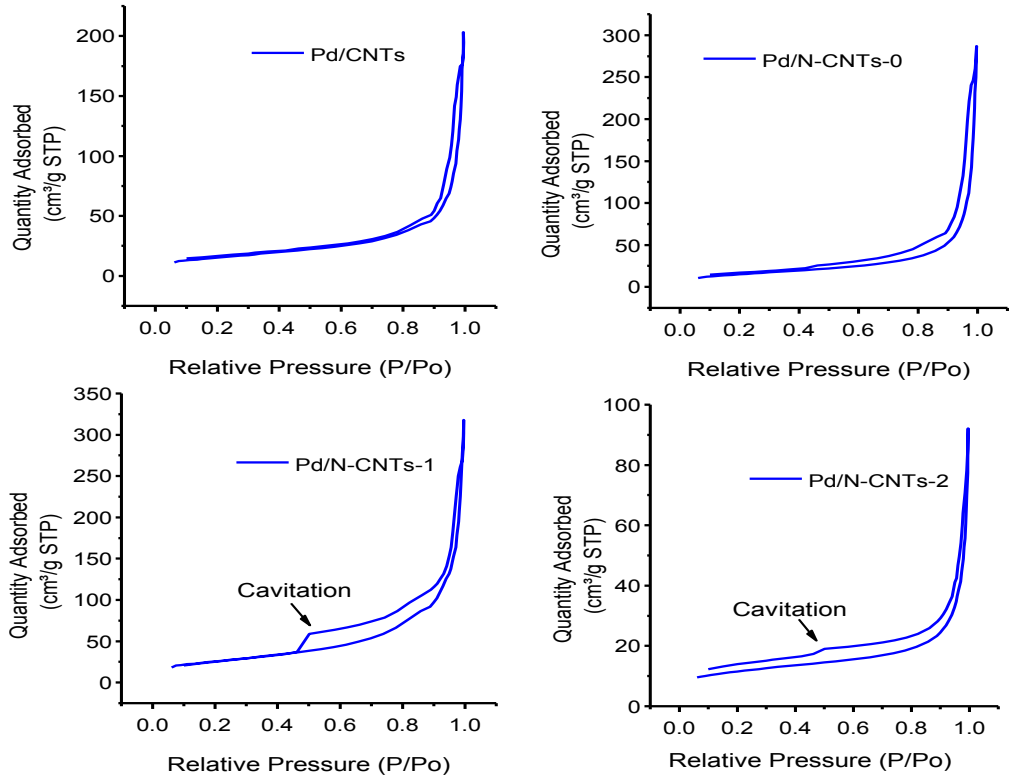


**Figure S4 (2).** $N_2$ adsorption–desorption isotherms of Pd/CNTs and Pd/N-CNTs.

**Supporting Information S5**

Table S5(a): The surface area and pore size distribution of Pd/AC.

| Catalyst | Surface area ($m^2g^{-1}$) | Pore size distribution (nm) |
|---|---|---|
| Pd/AC | 890 | 3.9 |

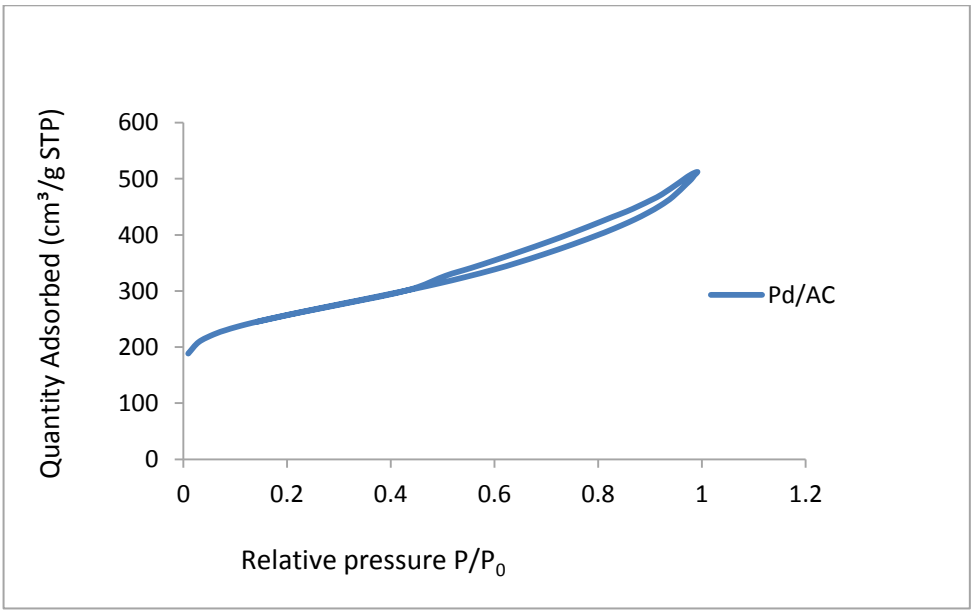


Figure S5 (b): The $N_2$ adsorption–desorption isotherms of Pd/AC.

## Supporting Information S6

## TEM analysis of Pd/AC

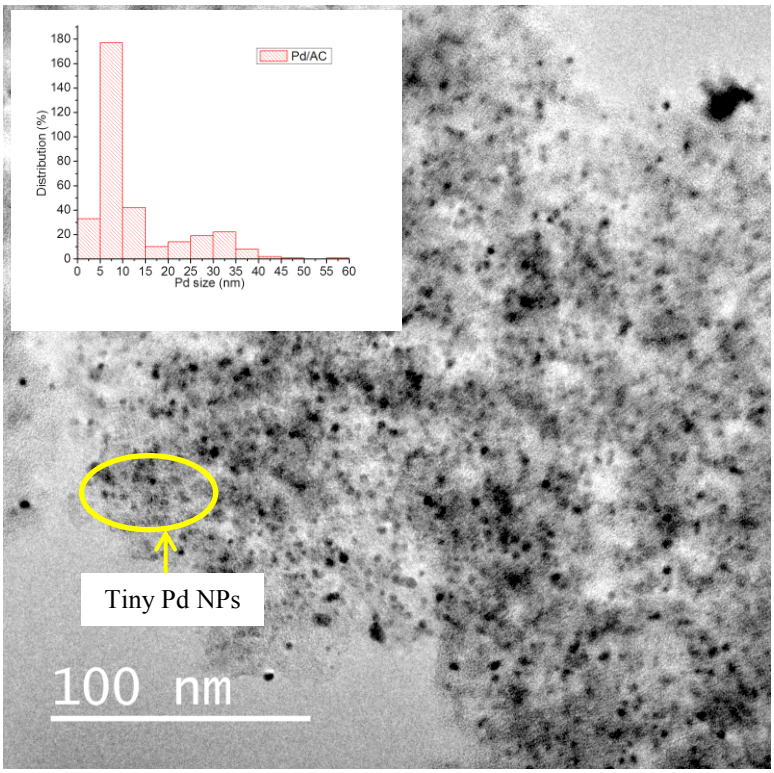


Figure S6 (a): TEM image of Pd/AC.

**Hydrogenation over Pd/AC**

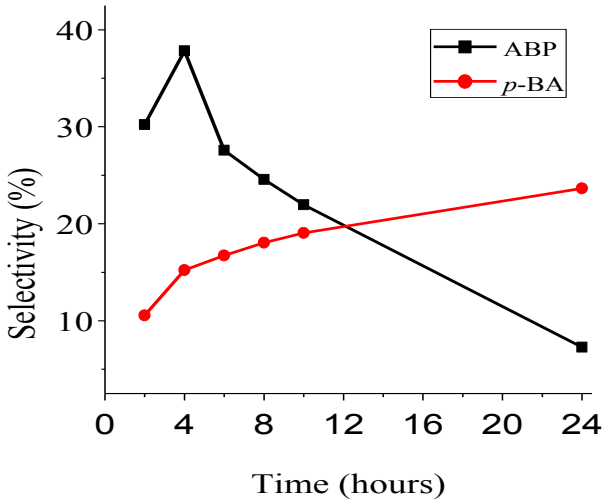


Figure S6 (b): Selectivity towards aminobenzophenone (ABP) and *p*-benzylaniline (*p*-BA) over Pd/AC.

**Supporting Information S7**

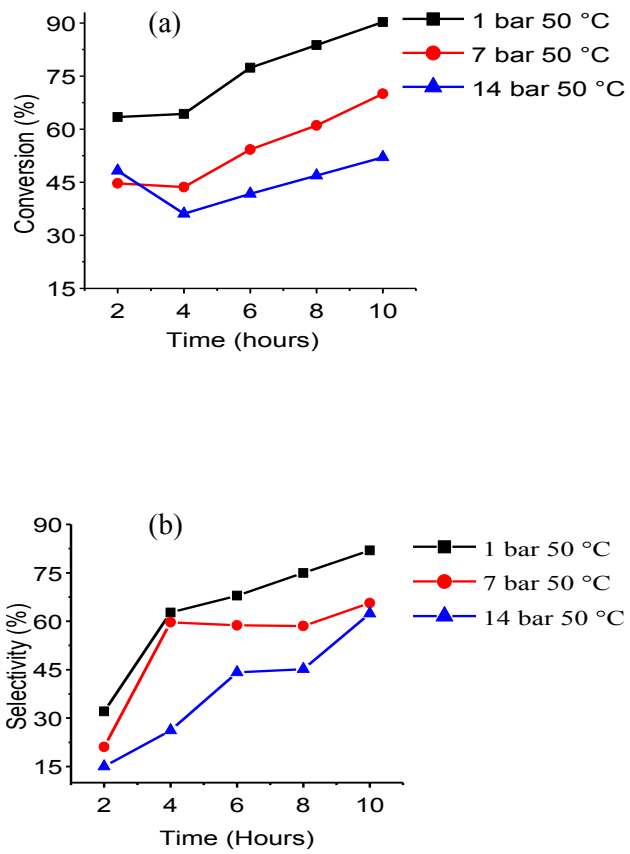


Figure S7. The effect of pressure on (a) catalytic activity of Pd/N-CNTs-2 and (b) selectivity over Pd/N-CNTs-2.

**Supporting Information S8**

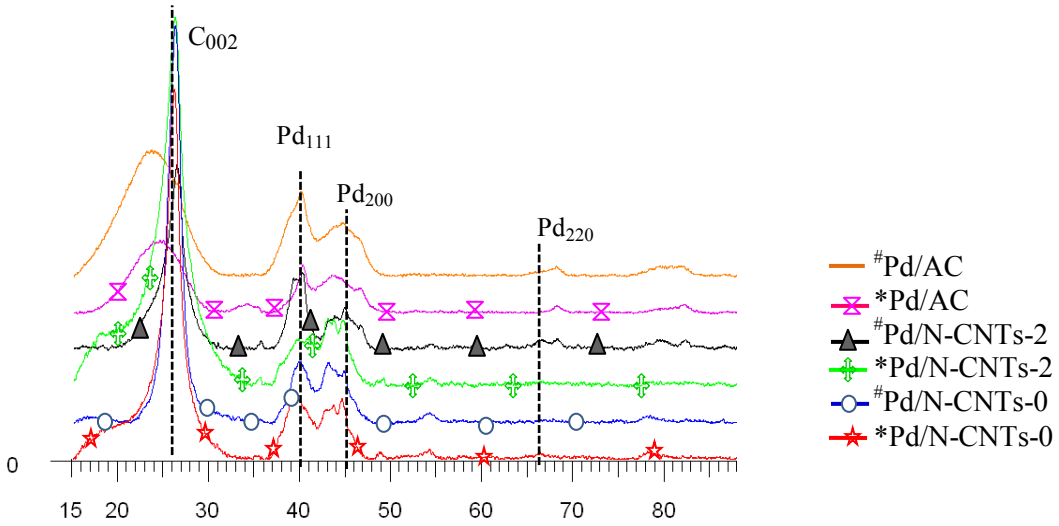


Figure S8. XRD diffractograms of used and unused Pd/AC, Pd/N-CNTs-0 and Pd/N-CNTs-2. (*): Fresh catalyst and (#): used catalyst.